

The Effects of Pressure Gradient and Roughness on Pressure Fluctuations Beneath High Reynolds Number Boundary Layers

Daniel J. Fritsch

Dissertation submitted to the Faculty of the
Virginia Polytechnic Institute and State University
in partial fulfillment of the requirements for the degree of

Doctor of Philosophy
in
Aerospace Engineering

William J. Devenport, Co-chair
Christopher J. Roy, Co-chair
K. Todd Lowe
Craig A. Woolsey
William C. Tyson

10 August, 2022
Blacksburg, Virginia

Keywords: Turbulent Boundary Layers, Pressure Fluctuations, Pressure Gradient,
Roughness, RANS CFD

Copyright 2022, Daniel J. Fritsch

The Effects of Pressure Gradient and Roughness on Pressure Fluctuations Beneath High Reynolds Number Boundary Layers

Daniel J. Fritsch

(ABSTRACT)

High Reynolds number turbulent boundary layers over both smooth and rough surfaces subjected to a systematically defined family of continually varying, bi-directional pressure gradient distributions are investigated in both wind tunnel experiments and steady 2D and 3D Reynolds-Averaged-Navier-Stokes (RANS) computations. The effects of pressure gradient, pressure gradient history, roughness, combined roughness and pressure gradient, and combined roughness and pressure gradient history on boundary growth and the behavior of the underlying surface pressure spectrum are examined. Special attention is paid to how said pressure spectra may be effectively modeled and predicted by assessing existing empirical and analytical modeling formulations, proposing updates to those formulations, and assessing RANS flow modeling as it pertains to successful generation of spectral model inputs.

It is found that the effect of pressure gradient on smooth wall boundary layers is strongly non-local. The boundary layer velocity profile, turbulence profiles, and associated parameters and local skin friction at a point that has seen non-constant upstream pressure gradient history will be dependent both on the local Reynolds number and pressure gradient as well as the Reynolds number and pressure gradient history. This shows itself most readily in observable downstream lagging in key observed behaviors. Steady RANS solutions are capable of predicting this out-of-equilibrium behavior if the pressure gradient distribution is captured correctly, however, capturing the correct pressure gradient is not as straightforward as may have previously been thought. Wind tunnel flows are three-dimensional, internal problems dominated by blockage effects that are in a state of non-equilibrium due to the presence of corner and juncture flows. Modeling a 3D tunnel flow is difficult with the standard eddy viscosity models, and requires the Quadratic Constitutive Relation for all practical simulations. Modeling in 2D is similarly complex, for, although 3D effects can be ignored, the absence of two walls worth of boundary layer and other interaction flows causes the pressure gradient to be captured incorrectly. These effects can be accounted for through careful setup of meshed geometry.

Pressure gradient and history effects on the pressure spectra beneath smooth wall boundary layers show similar non-locality, in addition to exhibiting varying effects across different spectral regions. In general, adverse pressure gradient steepens the slope of the mid-frequency region while favorable shallows it, while the high frequency region shows self-similarity under viscous normalization independent of pressure gradient. The outer region is dominated by history effects. Modeling of such spectra is not straightforward; empirical models fail to incorporate the subtle changes in spectral shape as coherent functions of flow variables

without becoming overly-defined and producing non-physical spectral shapes. Adopting an analytical formulation based on the pressure Poisson equation solves this issue, but brings into play model inputs that are difficult to predict from RANS. New modeling protocols are proposed that marry the assumptions and limitations of RANS results to the analytical spectral modeling.

Rough surfaces subjected to pressure gradients show simplifications over their smooth wall relatives, including the validity of Townsend's outer-layer-Reynolds-number-similarity Hypothesis and shortened history effects. The underlying pressure spectra are also significantly simplified, scaling fully on a single outer variable scaling and showing no mid-frequency slope pressure gradient dependence. This enables the development of a robust and accurate empirical model for the pressure spectra beneath rough wall flows. Despite simplifications in the flow physics, modeling rough wall flows in a steady RANS environment is a challenge, due to a lack of understanding of the relationship between the rough wall physics and the RANS model turbulence parameters; there is no true physical basis for a steady RANS roughness boundary condition. Improvements can be made, however, by tuning a shifted wall distance, which also factors heavily into the mathematical character of the pressure spectrum and enables adaptations to the analytical model formulations that accurately predict rough wall pressure spectra.

This work was sponsored by the Office of Naval Research, in particular Drs. Peter Chang and Julie Young under grants N00014-18-1-2455, N00014-19-1-2109, and N00014-20-2821. This work was also sponsored by the Department of Defense Science, Mathematics, and Research for Transformation (SMART) Fellowship Program and the Naval Air Warfare Center Aircraft Division (NAWCAD), in particular Mr. Frank Taverna and Dr. Phil Knowles.

The Effects of Pressure Gradient and Roughness on Pressure Fluctuations Beneath High Reynolds Number Boundary Layers

Daniel J. Fritsch

(GENERAL AUDIENCE ABSTRACT)

Very near to a solid surface, air or water flow tends to be highly turbulent: chaotic and random in nature. This is called a boundary layer, which is present on almost every system that involves a fluid and a solid with motion between them. When the boundary layer is turbulent, the surface of the solid body experiences pressures that fluctuate very rapidly, and this can fatigue the structure and create noise that radiates both into the structure to passengers and out from the structure to observers far away. These pressure fluctuations can be described in a statistical nature, but these statistics are not well understood, particularly when the surface is rough or the average pressure on the surface is changing. Improving the ability to predict the statistics of the pressure fluctuations will aid in the design of vehicles and engineering systems where those fluctuations can be damaging to the structure or the associated noise is detrimental to the role of the system. Wind turbine farm noise, airport community noise, and air/ship-frame longevity are all issues that stand to benefit from improved modeling of surface pressure fluctuations beneath turbulent boundary layers.

This study aims to improve said modeling through the study of the effects of changing average surface pressure and surface roughness on the statistics of surface pressure fluctuations. This goal is accomplished through a combination of wind tunnel testing and computer simulation. It was found that the effect of gradients in the surface pressure is not local, meaning the effects are felt by the boundary layer at a different point than where the gradient was actually applied. This disconnect between cause and effect makes understanding and modeling the flow challenging, but adjustments to established modeling ideas are proposed that prove more effective than what exists in the literature for capturing those effects. Roughness on the surface causes the flow to become even more turbulent and the surface pressure fluctuations to become louder and more damaging. Fortunately, it is found that the combination of roughness with a gradient in surface pressure is actually simpler than equivalent smooth surfaces. These simplifications offer significant insight into the underlying physics at play and enable the development of the first analytically based model for rough wall pressure fluctuations.

Dedication

*For Lauren, who shows me everyday the
kind of person and scientist I hope to
become.*

Acknowledgments

First and foremost, thank you to my family and friends for your eternal support and the many opportunities you have provided me.

Thank you to Jeremy Smith. You taught me what it means to push myself, to work hard, and to have a passion and drive that goes beyond surface level. You teach so much more than physics, and I carry the lessons I learned from your class with me to this day, and intend to for a long time to come.

Thank you to my advisor, Dr. William Devenport. It has been an extraordinary privilege to be your student. I cannot imagine a finer research leader, teacher, or mentor, and you have had a profound impact on how I want to build my career. Thank you to my co-advisor Dr. Chris Roy. I have learned so much from you and have grown immensely as a researcher under your guidance. Thank you to my committee, Dr. Todd Lowe, Dr. Craig Woolsey, and Dr. Will Tyson. Your guidance and support were instrumental in my journey.

Thank you to CREATE and all my amazing colleagues at VT. The list is long and spans several generations of students: Dr. Agastya Balantrapu, Dr. Matt Szoke, Dr. Christopher Hickling, Aldo Gargiulo, Julie Duetsch-Patel, Dr. Nandita Hari, Shishir Damani, Jarrod Banks, Humza Butt, Jeremiah Welchel, Surabhi Srivastava, Russel Repasky, and many others. It has been empowering to watch CREATE grow during my time here, and though I'm passing the torch with a heavy heart, I know the group is in excellent hands. Thank you to the many incredible undergraduate researchers who made this work possible: Surabhi Srivastava, Mason Fitzsimmons, Jared Minionis, Emily Sellards, Sasha Mintz, Chase Leuchtmann, Josh Pinkos, and Kyle Casey.

Thank you to Bill Oetjens, Dr. Aurelien Borgoltz, John Burleson, James Lambert, Cameron Hollandsworth, and Scott Patrick for your support of wind tunnel testing and development. Thank you to the AOE staff, Kelsey, Courtney, Erin, Sherry, and Cory for helping with countless purchases, reimbursements, and forms.

Thank you to Frank Taverna, Dr. Phil Knowles, Amber Geisz, and Dr. Will Tyson from the Naval Air Warfare Center for your support, and thank you to the DoD SMART program. A very special thank you to Dr. Bobby Nichols for putting up with my endless emails and requests for coding changes.

Finally, thank you from the very bottom of my heart to Vidya Vishwanathan. You are the best co-worker a person could ask for and you deserve a huge amount of credit for the work in this dissertation. It isn't an exaggeration to say I could not have done it without you.

Thank you all,

Danny

Contents

List of Figures	xii
List of Tables	xix
1 Introduction	1
1.1 Motivation	1
1.2 Scope and Aims of Present Work	2
1.3 Key Findings	3
1.4 Structure and Contents	5
2 Review of Literature	7
2.1 Boundary Layers	7
2.1.1 General Boundary Layer Theory and the Laminar Boundary Layer	7
2.1.2 Turbulence and the Turbulent Boundary Layer	9
2.1.3 Turbulent Boundary Layers in Pressure Gradient	15
2.1.4 Rough Wall Turbulent Boundary Layers	19
2.2 Turbulent Wall Pressure Fluctuations	24
2.2.1 Theory	24
2.2.2 Experimental Measurement	32
2.2.3 Pressure Gradient Effects	34
2.2.4 Roughness Effects	34
2.2.5 Modeling	35
2.3 Computational Fluid Dynamics	39
2.3.1 Theory and RANS Turbulence Modelling	39
2.3.2 Roughness Modelling	42
2.4 Summary of Literature	43
3 Fluctuating Pressure Beneath Smooth Wall Boundary Layers in Non-Equilibrium	

Pressure Gradients	45
3.1 Abstract	46
3.2 Nomenclature	46
3.3 Introduction	46
3.4 Methods	47
3.4.1 Experimental Setup	47
3.4.2 Mean Parameters	48
3.4.3 Fluctuating Pressure Measurements	49
3.4.4 Wall Shear Stress	49
3.4.5 Test Cases	50
3.4.6 Uncertainty Quantification	50
3.5 Results and Discussion	50
3.5.1 Pressure Gradient Cases	50
3.5.2 Velocity Profiles	51
3.5.3 Skin Friction	53
3.5.4 Boundary Layer Development	53
3.5.5 Fluctuating Pressure	55
3.5.6 Autospectral Scalings	57
3.5.7 Microphone Based Shear Sensor	58
3.5.8 Space-Time Correlation	59
3.5.9 Pressure Convection Velocity	59
3.5.10 Discussion of Historical and Non-Equilibrium Effects	61
3.6 Conclusions	62
Acknowledgements	63
References	63
4 Experimental and Computational Study of 2D Smooth Wall Turbulent Bound- ary Layers in Pressure Gradients	65
4.1 Abstract	66
4.2 Nomenclature	67

4.3	Introduction	67
4.4	Flow Case	68
4.5	Methods	70
4.5.1	Collaboration	70
4.5.2	Grid Development	71
4.5.3	Grid Refinement	71
4.5.4	Virginia Tech Simulations	72
4.5.5	DLR Simulations	73
4.5.6	University of Melbourne Simulations	73
4.5.7	Chalmers University of Technology Simulations	77
4.5.8	MARIN/IST Simulations	79
4.5.9	Sirehna Naval Group Simulations	80
4.6	Results	83
4.6.1	Solution Comparisons	83
4.6.2	Turbulence Model	88
4.7	Discussion	89
4.7.1	Variations in CFD Solvers	89
4.7.2	Variations in Turbulence Model	91
4.7.3	Agreement with Experiment	94
4.8	Conclusion	95
4.9	Appendix	96
4.9.1	VT Grid Convergence	96
4.9.2	UofM Airfoil Section Domain Grid Convergence	96
	Acknowledgements	96
	References	98
5	Turbulence and pressure fluctuations in rough wall boundary layers in pressure gradients	101
5.1	Abstract	102
5.2	Introduction	103

5.3	Methods	106
5.3.1	Experiments	106
5.3.2	Computations	110
5.4	Measured Boundary Layer Development	111
5.5	Surface Pressure Statistics	116
5.6	Modeling Considerations	123
5.7	Conclusions	127
	Acknowledgements	129
	References	129
6	Modeling the Surface Pressure Spectrum Beneath Turbulent Boundary Layers in Pressure Gradients	135
6.1	Abstract	136
6.2	Nomenclature	136
6.3	Introduction	138
6.4	Flow Case	139
6.4.1	Experiment	139
6.4.2	Numerical Simulations	140
6.5	Empirical Modeling	141
6.5.1	Review of Existing Models	141
6.5.2	Assessment at Pressure Gradient Conditions	144
6.5.3	Development of New Empirical Modeling with GEP	144
6.6	Analytical TNO Modeling	157
6.6.1	Overview	157
6.6.2	Source Sensitivities	161
6.6.3	Recommended Practices and Performance in Pressure Gradient	168
6.7	Conclusions	173
	Acknowledgements	175
	References	175
7	Modeling the Surface Pressure Spectrum on Rough Walls in Pressure Gradients	180

7.1	Abstract	181
7.2	Nomenclature	181
7.3	Introduction	183
7.4	Flow Case	184
7.5	Numerical Methods	186
7.6	Flow Modeling	187
7.6.1	Spalart-Allmaras	187
7.6.2	Menter SST	190
7.7	Empirical Pressure Spectrum Modeling	193
7.7.1	Review of Existing Models	193
7.7.2	New Model	193
7.7.3	Results	194
7.8	Analytical TNO Modeling	196
7.8.1	Baseline Model	198
7.8.2	Adjustments for Roughness	200
7.8.3	Rough Wall Analytical Model	200
7.9	Conclusions	203
	Acknowledgements	206
	References	206
8	Findings	210
9	Outlook	213
	Bibliography	216

List of Figures

2.1	Typical boundary layer velocity profile with various regions highlighted [67].	12
2.2	Low speed streaks in sub- and buffer layers visualized by hydrogen bubbles [72]. . . .	13
2.3	Vortical structure generating sweeps and ejections as it rotates and convects [107]. .	13
2.4	Schematic of outer-region vortical structures: Loop (a), Horseshoe (b), and Hairpin (c) [67].	14
2.5	Sketch of the four layers of turbulent boundary layers; inner viscous layer (I), stress-gradient balance layer (II), viscous/advection balance meso-layer (III), and inertial/advection balance outer layer (IV) as described by Wei <i>et al.</i> (2005) [131]. . . .	15
2.6	Equilibrium relation of Mellor & Gibson (1966) [89].	17
2.7	Various experimental data of equilibrium APG boundary layers on Schofield-Perry defect scaling [114].	18
2.8	Illustration of near wall flow in D-Type (a) and K-Type (b) roughness, flow left to right [66].	20
2.9	Smooth vs. rough wall Law of the Wall velocity profiles [96].	21
2.10	Isocontours of vorticity for hemispherical (a), cylindrical (b), and cuboid (c) roughness elements [141].	23
2.11	Sketch of a dual hairpin-necklace vortex structure observed in three-dimensional roughness sublayer [11].	23
2.12	Viscous boundary layer scaling (left) and defect scaling (right) for a variety of smooth and rough boundary layer flows [44].	24
2.13	Frequency spectrum of wall pressure fluctuations [67].	33
2.14	Wall pressure autospectral densities from both smooth and various rough walls scaled on classical viscous inner scaling (a) and the rough wall viscous scaling of Meyers <i>et al.</i> (2015) (b),(c) [91].	36
3.1	Top-down view of test section with NACA0012 model installed showing coordinate system, major dimensions, and locations of boundary layer trip and model quarter chord. Black stations correspond to boundary layer rake measurements gray to the origins of the linear microphone array	48
3.2	Modular hardwall showing nominal locations of surface pressure taps. Adapted with permission from Duetsch-Patel <i>et al.</i> 2020	48

3.3	Boundary layer rake (a) and associated wall normal probe positions (b)	49
3.4	Positions (a) and corresponding separations (b) of the six HBK 1/8th inch microphones used in the fluctuating pressure sensor array	49
3.5	Example spectral calibrations in ZPG conditions at both tested Reynolds number	50
3.6	Mean pressure coefficient (a) and pressure gradient parameter β (b) developing downstream	51
3.7	Mean boundary layer velocity profiles under viscous scaling	52
3.8	Coles wake strength parameter at each location and angle of attack	53
3.9	Coles wake strength parameter as measured and as predicted from (a) Coles and (b) Durbin and Reif	53
3.10	Skin friction coefficient (a) and corresponding wall shear stress (b) as calculated from the Clauser plot method using boundary layer rake data	54
3.11	Boundary layer thickness developing on test wall - 99% edge velocity, (a) displacement (b), and momentum (c)	54
3.12	$\delta^+ = Re_\tau = \delta u_\tau / \nu$ developing downstream on test wall. Panel (a) shows all data collected; (b) shows averages for each Reynolds number case with a linear fit of the form of Eq. 3.8	55
3.13	Root mean square of fluctuating wall pressure, dimensional (a) and normalized on wall shear stress τ_w (b)	55
3.14	Autospectral density of fluctuating pressure expressed in decibels per Hertz relative to 20 micro-Pascals as a function of frequency, Reynolds number, model angle, and downstream position	56
3.15	Slope of mid-frequency region of the autospectra of fluctuating pressure measured at each location and model angle of attack	57
3.16	Slope of mid-frequency region of the autospectra of fluctuating pressure measured at each location and model angle of attack displayed as a function of local skin friction coefficient. Marker styles found in Table 3.4	57
4.1	Flow case system showing coordinate system origin, primary dimensions, model and trip locations.	69
4.2	Pressure coefficient (a) and pressure gradient parameter (b) distributions for flow cases at twelve angles of attack.	69
4.3	Displacement thickness growth for flow cases at twelve angles of attack.	70
4.4	Geometry layout of 2D CFD grids used for common collaborative grid family.	71
4.5	Arithmetic average and root-mean-square cell areas for each grid level.	72

4.6	Grid levels 1 —, 3 —, and 5 —. Full grid for GL5 shown in (a) zoomed image corresponding to green box for all three levels shown in (b)	72
4.7	Grid convergence test on the reduced domain comparing the baseline RANS on the wall-friction velocity (u_τ) the displacement thickness (δ^*) and the wall-scaled velocity for location P7.	75
4.8	Comparison of the baseline RANS to the new Reynolds stress-closure (using u^+ as the cost function) on the wall-friction velocity (u_τ), the displacement thickness (δ^*), and the wall-scaled velocity for location P7.	76
4.9	Comparison of the streamwise evolution of c_p c_f and β between the baseline RANS (legend R) and the machine-learnt model using u^+ as the cost-function.	76
4.10	Comparison of the wall-normal profiles of u/U_e and u^+ between the baseline RANS (legend R) and the machine-learnt model using u^+ as the cost-function.	77
4.11	Comparison of the wall-normal profiles of $\overline{u'v'}^+$ and k^+ between the baseline RANS (legend R) and the machine-learnt model using u^+ as the cost-function. Red data point represents point below which data is known to be attenuated.	78
4.12	Example L2 norms of steady residuals from Chalmers OpenFOAM simulations. . . .	78
4.13	Iterative convergence of the MARIN/IST calculations performed with the Spalart-Allmaras one-equation eddy-viscosity model.	81
4.14	Iterative convergence of the MARIN/IST calculations performed with the $k-\omega$ SST two-equation eddy-viscosity model.	82
4.15	Sirehna STAR-CCM+ L2 norm residuals for -10° (a) and 12° (b) cases.	82
4.16	Pressure (a) and skin friction (b) coefficients as computed for the 12° case using all solvers with Menter SST.	83
4.17	95% edge velocity (a), displacement (b), and momentum (c) thicknesses and shape factor (d) as computed for the 12° case using all solvers with Menter SST.	84
4.18	Clauser paramter (a) and defect shape factor as a function of Clauser paramter (b) as computed for the 12° case using all solvers with Menter SST.	85
4.19	Velocity (a-c), TKE (d-f), and Reynolds shear stress (g-i) profiles at the three primary assessment locations P3, P5, and P7 (left, middle, right columns respectively) as computed for the 12° case using all solvers with Menter SST. Linear sublayer and Law of the Wall with $\kappa = 0.41$ and $B = 5.1$ marked with black dashes.	86
4.20	Pressure (a) and skin friction (b) coefficients as computed for the -10° case using all solvers with Menter SST.	87
4.21	95% edge velocity (a), displacement (b), and momentum (c) thicknesses and shape factor (d) as computed for the -10° case using all solvers with Menter SST.	88

4.22	Clauser paramter (a) and defect shape factor as a function of Clauser parameter (b) as computed for the -10° case using all solvers with Menter SST.	89
4.23	Velocity (a-c), TKE (d-f), and Reynolds shear stress (g-i) profiles at the three primary assessment locations P3, P5, and P7 (left, middle, right columns respectively) as computed for the -10° case using all solvers with Menter SST. Linear sublayer and Law of the Wall with $\kappa = 0.41$ and $B = 5.1$ marked with black dashes.	90
4.24	Pressure (a) and skin friction (b) coefficients as computed for the 12° case using various turbulence models	91
4.25	95% edge velocity (a), displacement (b), and momentum (c) thicknesses and shape factor (d) as computed for the 12° case using various turbulence models	92
4.26	Clauser parameter (a) and defect shape factor as a function of Clauser parameter (b) as computed for the 12° case using various turbulence models.	93
4.27	Velocity (a-c), TKE (d-f), and Reynolds shear stress (g-i) profiles at the three primary assessment locations P3, P5, and P7 (left, middle, right columns respectively) as computed for the 12° case using various turbulence models. Linear sublayer and Law of the Wall with $\kappa = 0.41$ and $B = 5.1$ marked with black dashes.	94
4.28	Comparison of main outputs c_p , c_f , and δ^* across systematically refined grid family from VT Kestrel simulations.	96
4.29	Residual convergence for VT Kestrel simulation of $\alpha = -10^\circ$ Menter SST on GL3.	97
4.30	Grid convergence of the streamwise evolution of C_p , C_f and β	97
4.31	Grid convergnce of the wall-normal profiles of U^+	97
5.1	Top-down view of test-section with installed NACA0012 model showing coordinate system, major dimensions, and measurement locations.	107
5.2	Rough surface layout	108
5.3	Microphone array layout for streamwise orientation. Gray marks show locations of roughness elements.	109
5.4	Measured mean pressure coefficient (a), skin friction coefficient (b), and Clauser parameter (c) distributions.	112
5.5	Measured mean velocity profiles under viscous normalization at each measurement location.	113
5.6	Measured mean velocity profiles under outer normalization for inflow (a) and outflow (b) measurement planes and change in outer normalized velocity between Reynolds number cases at outflow plane (c).	114
5.7	Measured boundary layer 99% edge velocity (a), displacement (b), and momentum (c) thicknesses.	115

5.8	Measured autospectral densities of fluctuating wall pressure.	117
5.9	Pressure spectra under viscous scaling of Meyers <i>et al.</i> (2015) [91]. Comparison with smooth wall data of Fritsch <i>et al.</i> [49] (2022) shown in (b).	119
5.10	Viscous scale u_ν of Meyers <i>et al.</i> (2015) [91] presented as ratios of U_e (a) and u_τ (b).	120
5.11	Pressure spectra under outer scaling.	122
5.12	Local pressure convection velocity distributions for each model angle at $x/h = 1.34$	122
5.13	Measured broadband convection velocity distributions.	123
5.14	Displacement thickness growth measured and predicted at $\alpha = 12^\circ$	124
5.15	Outer normalized velocity profiles as measured and predicted at $x/h = 0.68$, $\alpha = 12^\circ$	125
5.16	Roughness function as a function of roughness Reynolds number as computed against the curve of Nikuradse (1956) [94].	125
5.17	Roughness function as a direct function of wall BC parameter SR for both measured Reynolds numbers.	127
6.1	Flow case system showing coordinate system origin, primary dimensions, and model and trip locations (a) and corresponding distributions of Clauser pressure gradient parameter (b). Taken with permission from Fritsch <i>et al.</i> (2022) [50]	140
6.2	Representative diagram of CFD grid domain. Taken with permission from Fritsch <i>et al.</i> (2022) [51]	141
6.3	Measured and empirically modeled surface pressure spectra at ZPG (a), APG (b), FPG (c), and APG-FPG (d) conditions	145
6.4	Sensitivity studies of nine Goody-style model parameters	147
6.5	Tuned Goody model parameters and experimental data used for tuning at ZPG (a), APG (b), FPG (c), and APG-FPG (d) conditions	149
6.6	Flowchart showing the GEP algorithm.	151
6.7	Prediction at APG (a) and FPG (b) conditions compared with experimental data and existing empirical model of Hu (2018) [64].	153
6.8	Sensitivity of performance of GEP model on different experimental data training sets at APG (a) and FPG (b) conditions.	154
6.9	Contributions of each GEP model sub-function.	155
6.10	Validation of GEP model at training (a) and non-training (b) conditions.	156
6.11	Performance of experiment based GEP model at ZPG (a), APG (b), FPG (c), and APG-FPG cross (d) conditions.	157

6.12	Performance of RANS based GEP model at ZPG (a), APG (b), FPG (c), and APG-FPG cross (d) conditions.	158
6.13	Reynolds stress distributions (a) and corresponding TNO model spectra (b).	162
6.14	Velocity spectrum distributions at $y/\delta = 0.55$ (a) and corresponding TNO model spectra (b).	164
6.15	Length scale distributions (a) and corresponding TNO model spectra (b).	167
6.16	TNO model spectra with varying U_c	169
6.17	Pressure spectra at ZPG (a), APG (b), FPG (c), and APG-FPG (d) conditions as predicted using both final TNO models, Goody model, and as measured.	171
6.18	Pressure spectrum at ZPG conditions predicting using TNO RANS model showing uncertainty bounds from associated RANS uncertainty in velocity and TKE profiles	172
6.19	ZPG spectra predicted from full TNO model and using TM term only	173
7.1	Flow case diagram showing layout dimensions, roughness extent, and key measurement locations (a) and corresponding Clauser parameter distributions (b). Taken with permission from Fritsch <i>et al.</i> (2022) [50]	185
7.2	Computational domain layout (a), coarse grid (b), zoomed view of fine —, medium —, and coarse — grids (c)	187
7.3	Roughness function as a function of Reynolds number for new and old Spalart-Allmaras boundary conditions compared with data of Nikuradse (1950) [94].	188
7.4	Roughness function as a function of roughness Reynolds number for constant Reynolds number, increasing k_s and constant k_s , increasing Reynolds number compared with data of Nikuradse (1950) [94].	189
7.5	Outer normalized velocity profiles as measured experimentally and as simulated with SA model with constant k_s and increasing free-stream Reynolds number.	189
7.6	Viscous normalized velocity profiles as measured experimentally and as simulated with SA model using experimental k_s and k_s tuned to match Δu^+	190
7.7	Roughness function as a function of Reynolds number for new and old Menter SST boundary conditions compared with data of Nikuradse (1950) [94].	191
7.8	Roughness function as a function of roughness Reynolds number for constant Reynolds number, increasing k_s and constant k_s , increasing Reynolds number compared with data of Nikuradse (1950) [94].	191
7.9	Outer normalized velocity profiles as measured experimentally and as simulated with SST model with constant k_s and increasing free-stream Reynolds number.	192
7.10	Viscous normalized velocity profiles as measured experimentally and as simulated with SA model using experimental k_s and k_s tuned to match Δu^+	192

7.11	Proposed empirical pressure spectrum model shown against experimental data of Fritsch <i>et al.</i> (2022) [50].	194
7.12	Newly proposed model compared with data of Joseph (2017) [67] for various rough surfaces and Reynolds numbers	195
7.13	Empirical models of Catlett <i>et al.</i> [25], Joseph <i>et al.</i> [68], and proposed model shown against experimental data of Fritsch <i>et al.</i> [50] for ZPG (a), APG (b), FPG (c), and APG-FPG cross (d) conditions.	197
7.14	ZPG spectra predicted using baseline PPE model from Fritsch <i>et al.</i> (2022) [47] with SST and SA data and with new empirical model compared against experiment. . . .	199
7.15	ZPG spectra predicted using baseline PPE model from Fritsch <i>et al.</i> (2022) [47] with SST data and with new empirical model compared against experiment and newly proposed rough wall model using SST and SA data.	201
7.16	Pressure spectra as measured and predicted using new rough wall PPE model and new empirical model for ZPG (a), APG (b), FPG (c), and APG-FPG cross (d) conditions	204

List of Tables

2.1	<i>a-c</i> parameters for empirical Goody-style empirical models corresponding to Eq. 2.78.	37
2.2	<i>d-f</i> parameters for empirical Goody-style empirical models corresponding to Eq. 2.78.	37
2.3	<i>g-i</i> parameters for empirical Goody-style empirical models corresponding to Eq. 2.78.	38
2.4	Scalings for empirical Goody-style empirical models corresponding to Eq. 2.78. . . .	38
3.1	Average ambient conditions	50
3.2	Primary instrument uncertainties	50
3.3	Quantified experimental uncertainties in major variables of interest	51
3.4	Markers used for Fig. 3.9 3.16 ?? and ??	53
3.5	Markers used for autospectral density scaling Fig. ??-??	58
4.1	Grid metrics for systematically refined 2D grid family	71
4.2	Estimates of uncertainties due to discretization error for Kestrel simulations.	73
4.3	Details of grids of the reduced domain tested. Each subsequent grid starts the calculation from the converged solution of the previous RANS grid level.	74
5.1	Estimates of uncertainty in measured quantities. dB relative to $p_{ref} = 20\mu Pa$	110
5.2	Marker styles	111
5.3	Select quantities from rough and smooth walls for $Re = 2M$ quantifying history effects	116
6.1	<i>a-c</i> parameters for empirical Goody-style empirical models.	143
6.2	<i>d-f</i> parameters for empirical Goody-style empirical models.	143
6.3	<i>g-i</i> parameters for empirical Goody-style empirical models.	143
6.4	Scalings for empirical Goody-style empirical models.	143
6.5	Empirical model input parameters as computed from RANS data.	144
6.6	Root-mean-square decibel error of empirical model spectra ($RMS[10 \log_{10}(G_{pptrue}) - 10 \log_{10}(G_{ppmodel})]$).	146
6.7	Select Goody model parameters - original and tuned to measured data.	148

7.1	Coefficients for Goody style model for Goody [54], Catlett <i>et al.</i> [25], Jospeh <i>et al.</i> [68], and new proposed models.	196
-----	--	-----

Nomenclature

β	Clauser parameter ($\frac{\delta^*}{\tau_w} \frac{dp}{dx}$)
δ	Boundary layer thickness
δ^*	Displacement thickness
δ_{ij}	Dirac Delta function
Δ_{RC}	Rotta-Clauser length scale ($\delta^* \sqrt{c_f/2}$)
Δ_{ZS}	Zagarola-Smits parameter (δ/δ^*)
ϵ	Turbulence dissipation rate
κ	von Kármán constant
Λ	Longitudinal integral length scale
λ	Roughness density or Taylor microscale
μ	Dynamic viscosity
∇	Gradient operator
ν	Kinematic viscosity
ω	Frequency OR specific turbulence dissipation rate
\bar{U}	Joseph velocity scale ($U_e(1 - \delta^*/\delta)$)
ϕ_{ij}	Spectral density of variables i, j
Π	Wake strength parameter
ρ	Density
τ_w	Wall shear stress
τ_{ij}	Reynolds stress tensor
θ	Momentum thickness
$\tilde{\nu}$	Spalart-Allmaras working variable
ξ_l	Catlett pressure gradient parameter ($\frac{l}{q} \frac{dp}{dx}$)
c_f	Skin friction coefficient

c_p	Pressure coefficient
f	Time frequency
G	Defect shape factor($\frac{1-1/H}{u_\tau/U_e}$)
G_{ij}	One sided spectral density of variables i,j
H	Shape factor (δ^*/θ)
K	Acceleration parameter ($\frac{\nu}{U_e^2} \frac{dU_e}{dx}$)
k	Wavenumber magnitude or turbulent kinetic energy
k^+	Roughness Reynolds number
k_g	Roughness height
k_i	ith component of wavenumber
k_s	Sandgrain roughness height
L	Length scale
M	Mach number
p	Pressure
q	Dynamic pressure ($\frac{1}{2}\rho U_\infty^2$)
Re	Reynolds number
SR	Wilcox roughness variable
T	Temperature or period
t	Time
t_{ij}	Stress tensor
u	Streamwise velocity
u^+	Viscous normalized velocity
u_ν	Meyers modified friction velocity
u_τ	Friction velocity
U_c	Convection velocity
U_e	Boundary layer edge velocity
u_i	ith component of velocity vector

U_{cb}	Broadband convection velocity
v	Wall-normal velocity
x	Streamwise direction
x_i	ith component of position vector
y	Wall-normal direction
y^+	Viscous normalized wall-normal direction

Chapter 1

Introduction

1.1 Motivation

The World Health Organization classifies noise from wind turbine farms as a health hazard, citing studies that show living and working near a wind farm can cause stress, sleep deprivation, and even mild hearing loss [1]. The noise produced by wind turbines comes primarily from the generation on each blade of a turbulent boundary layer (TBL), a thin region of airflow that is decelerated compared to the average wind speed due to viscous, adhesive forces between the air and the surface of the blade. Regardless of how clean and steady the oncoming wind may be, the flow of air in the boundary layer will become turbulent, meaning that it will swirl and fluctuate randomly. When this turbulence interacts with the edge of the blade, it produces noise that will radiate away from the turbine to nearby homes and offices, creating the background noise that is so undesirable.

Companies that design and manufacture wind turbines invest heavily in noise reduction, tasking their engineers with designing new blade shapes and mitigating technologies to reduce the nearby perceived noise levels. To do this, the engineers require a rapid, low cost method for predicting the sound generated by a given blade design, which ultimately relies on the statistics of the turbulent flow-field developing in the blade's turbulent boundary layer. Let's put ourselves in the shoes of such an engineer - we've just been tasked with determining the potential noise reduction of a new blade shape, how can we know this for less time and money than building and installing the new blade? We would need three things:

1. A method for predicting the development of the blade's turbulent boundary layer, ideally in a simulated environment, that we trust to be accurate
2. A robust physical understanding of the relationship between the predicted boundary layer flow and the pressure statistics on the blade's surface
3. A robust and accurate mathematical model that relates the two and outputs a prediction for the pressure statistics

Item 1 exists, and is called Computational Fluid Dynamics (CFD). Unfortunately, fully resolved simulations of a turbulent flow are prohibitively expensive and will likely remain so for many decades to come [37]. In 2022, we rely instead on models for the effects of a turbulent flow on the mean behavior of a given system, models that are imperfect and fail to accurately predict several key phenomena: three-dimensionality, non-equilibrium, and surface roughness effects, to name a few. Item 2 is settled, but only for simple, canonical flows like flat plates. Our physical understanding is

lacking when considering the effects of changing pressure and velocity, surface curvature, or surface roughness. Item 3 is similarly lacking for complex flows, and the most robust models that have been proposed are largely academic in nature and have yet to be employed in such a way that is both robust and applicable in an industry setting.

There is a need for research that embraces the complexities of real-world flow cases, shows how they behave across a wide range of conditions, and develops methods by which they can be accurately modeled within the limitations of modern computational power, and for many reasons beyond wind farm noise. Turbulent boundary layer noise presents itself in all mechanical, aerospace, and marine engineering problems in which boundary layer flows are present, and the statistics of the pressure fluctuations at the surface have effects beyond noise. Fluctuating surface pressure beneath turbulent boundary layer flows affects the underlying structure, potentially exciting resonant frequencies and generating cyclical fatigue. Robust prediction protocols for the fluctuating surface pressure are a requirement for advancing our understanding of fluid-structure-interaction problems, providing the necessary boundary conditions for a dynamic structural analysis that incorporates external aero/hydrodynamic effects.

1.2 Scope and Aims of Present Work

This work aims to provide fundamental insight into the wall pressure spectrum beneath high Reynolds number turbulent boundary layer flows that can be considered under non-equilibrium effects: continually varying pressure gradient and surface roughness. In addition to revealing the fundamental physics at play, this work seeks to meaningfully advance the ability to model and predict these surface pressure spectra working within the limitations of industry-standard practices, i.e., working from Reynolds-Averaged-Navier-Stokes (RANS) data rather than higher fidelity, less practically accessible simulations. To this end, this work has three specific aims:

1. Understand the effects of continually varying pressure gradients of adverse, favorable, and mixed signs on both smooth and rough wall boundary layers and their underlying surface pressure spectra
 - (a) Design and implement a new experimental flow case that captures non-equilibrium effects to a greater degree than existing benchmark databases
 - (b) Perform this experiment to the level of documentation and completeness required for validation experiments as described by Oberkampf & Smith 2017 [95]
 - (c) Study in great detail the boundary layer development, turbulence development, and surface pressure statistics beneath these boundary layer flows
 - (d) Identify scaling laws and quantifiable flow-driven effects of the pressure spectra
2. Assess the current state-of-the-art in RANS CFD prediction for these flows to determine new best-practices for generating requisite data for pressure spectrum modeling
 - (a) Open the experimental data from Aim 1 to the international turbulence modeling community for their verification and validation efforts

- (b) Create digital twins for the flow case and verify and validate these simulations to the highest level of completeness
 - (c) Identify, implement, and publish proper best-practices for simulating these flows
 - (d) Critically assess the produced pressure spectrum model inputs for their accuracy compared to experiment
3. Develop new modeling protocols for the wall pressure spectrum that interface seamlessly with RANS flow data and offer more accurate and robust prediction across a wide range of non-equilibrium flow conditions than the current state-of-the-art
- (a) Assess current state-of-the art in spectral models against validation database
 - (b) Assess sensitivities of existing RANS based prediction of model inputs
 - (c) Where necessary, develop new protocols for model derivations, definitions, or input prediction
 - (d) Identify, implement, and publish proper best-practices for predicting the wall pressure spectrum

1.3 Key Findings

The key findings of this work are summarized below. Data generated in pursuit of these findings has been made publicly available through the Virginia Tech Library [48].

- The effect of pressure gradient on boundary layer development is strongly non-local. Under the presence of continually varying pressure gradient, the boundary layer growth lags downstream of the pressure gradient distribution. This lag appears to be independent of pressure gradient sign or magnitude and of the free-stream Reynolds number, but is dependent on surface treatment; history lags are shortened in rough wall flows. This is most likely due to intensification of inner motions in the rough wall boundary layer, which are shown to respond more rapidly to pressure gradient than their outer layer counterparts.
- The effect of pressure gradient on the smooth wall pressure spectrum is complex and region dependent. The high frequency behavior scales on classical viscous variables and appears largely pressure gradient and history independent. The mid-frequency slope is highly dependent on pressure gradient and features similar lagging behavior to the boundary layer development. This variation was shown to be strongly correlated ($\rho = 0.96$) with the local skin friction coefficient, and it is hypothesized that this is due to the movement towards/-away from the wall of the location of bulk pressure fluctuation sources, which will drive the mid-frequency decay and is strongly dependent on local Reynolds number.
- Standard eddy-viscosity RANS is capable of replicating the effects of continually varying pressure gradient on the boundary layer very accurately if the pressure gradient is captured correctly. However, this is a surprisingly large *if*. Wind tunnel flows are complex, internal, three-dimensional problems that are not as well understood as was once thought. Accurately

replicating the pressure gradient in a 2D environment requires careful attention to the meshing and simulation design. This is helped immensely by collaboration between experimental and computational teams from the beginning of the effort. Accurately replicating the flow in 3D requires careful choice of turbulence model; the standard Boussinesq hypothesis appears incapable of replicating corner and juncture flows and should be replaced by the Quadratic Constitutive Relation (QCR).

- Empirical models for smooth walls in pressure gradients fail to balance *flexibility* (accurate changes with changing pressure gradient behavior) with *robustness* (maintenance of physical behavior across a wide range of flow cases). This is due primarily to the sensitivity of the empirical formulation, which requires the correlation of an infinite dimensional space of flow variables to minute changes in input parameters.
- An analytical formulation for the pressure spectrum can be derived, albeit with questionably valid assumptions. This formulation does not automatically interface well with RANS flow modeling, but new protocols have been proposed for the prediction of Reynolds stresses, velocity spectra, length scales, and anisotropy within the confines of RANS data. These spectral models show improvement in both flexibility and robustness over empirical modeling as well as capturing spectral features that empirical models cannot.
- Rough wall flows in pressure gradients are simplified in many ways compared to equivalent smooth wall flows. They exhibit Reynolds number similarity, shortened history effects (due, it is hypothesized, to the disruption of large-scale turbulent motions and a corresponding reduction in convection speed), and simple pressure spectra with no mid-frequency pressure gradient dependence. The pressure spectra beneath rough walls scale universally on an outer variable scaling, suggesting a dominance of outer motions and their respective pressure gradient effects in combination with a universal viscous behavior and k_s dependence fully describe the pressure fluctuations.
- The modified viscous scaling of Meyers *et al.* (2015) [91] appears to hold validity in pressure gradient and pressure gradient history. The Meyers scale, u_ν , can be interpreted as the shear due to viscous effects, which are un-affected by the presence of roughness, implying that the increase in shear over a rough surface is driven by a new mechanism that is not present in a smooth wall flow. It is hypothesized that this mechanism is the production of turbulent motions at the canopy height.
- RANS simulations of rough wall flows are fundamentally flawed; there is no physical basis for the current state-of-the-art in rough wall boundary condition modeling. This would be acceptable if the existing models produced results that agreed with experimental data across a wide range of cases, but this does not appear true for several widely accepted models. More consistent models have been proposed more recently, but a consistent picture of which models should be employed in which circumstances is lacking.
- A novel empirical model for rough wall pressure spectra is proposed that contains no flow dependent inputs on a classical outer-variable scaling. The lack of Reynolds number dependence on outer scaling is reminiscent of Townsend's hypothesis.

- The analytical pressure spectrum model requires adaptation for rough walls. This comes in two primary changes: an increase in the magnitude of the velocity spectra and a wall shift in the integration, effectively shifting the pressure sources upwards by some function of the roughness height. This formulation proves effective at modeling rough wall pressure spectra, even in pressure gradient, but is difficult to interface with RANS due to a disconnect between the real and simulated values of the roughness height.

1.4 Structure and Contents

This is a manuscript-style dissertation, meaning the bulk chapters are scientific articles that have been or will be published in peer-reviewed journals.

Chapter 1 describes the motivation and key results of this work as well as an outline of the dissertation.

Chapter 2 contains an in-depth review of the current literature relevant to the work to be discussed.

Chapter 3 is the first manuscript, entitled “Fluctuating Pressure Beneath Smooth Wall Boundary Layers in Non-Equilibrium Pressure Gradients,” published in *AIAA Journal*. This chapter discusses experimentally observed effects of pressure gradient and pressure gradient history on the development of turbulent boundary layers and their underlying surface pressure spectra.

Chapter 4 is a joint NATO special session paper presented at the 2022 *AIAA Science and Technology Forum* entitled “Experimental and Computational Study of 2D Smooth Wall Turbulent Boundary Layers in Pressure Gradients.” This chapter discusses an internationally collaborative effort to simulate the flow case presented in Chapter 3 using steady RANS, including verification and validation of methods, results, and models.

Chapter 5 is a third manuscript, entitled “Turbulence and pressure fluctuations in rough wall boundary layers in pressure gradients,” published in a Topical Collection on rough wall boundary layer flows in *Experiments in Fluids*. This chapter discusses experimentally observed effects of pressure gradient and pressure gradient history on the development of rough wall boundary layers and their underlying pressure spectra, as well as many of the challenges associated with modeling these flows.

Chapter 6 is a fourth manuscript, entitled “Modeling the Surface Pressure Spectrum Beneath Turbulent Boundary Layers in Pressure Gradients.” A version of this paper was published at the *28th AIAA/CEAS Aeroacoustics Conference* in June, 2022 and is currently under review by *AIAA*

Journal. This chapter takes an in-depth look at various methods for modeling the surface pressure spectrum, including empirical models, analytical models, and the potential for machine learning.

Chapter 7 is the final manuscript, entitled “Modeling the Surface Pressure Spectrum Beneath Rough Wall Boundary Layers in Pressure Gradients,” intended to be submitted to *AIAA Journal*. This chapter discusses how rough wall flows can most accurately be modeled, and how these modeled flow data can be utilized to model the underlying surface pressure spectra.

Chapter 8 presents an overview and summary of the work completed and the key findings.

Chapter 9 concludes the dissertation with some final remarks on what has been learned through the course of this work as well as some thoughts on what may come next.

Formatting will vary chapter-to-chapter. Chapters 1, 2, 8, and 9 will use the standard dissertation formatting, while Chapters 3-7 are presented in their respective journal formats.

Chapter 2

Review of Literature

2.1 Boundary Layers

2.1.1 General Boundary Layer Theory and the Laminar Boundary Layer

The concept of the boundary layer was first proposed by German physicist Ludwig Prandtl in 1904 [103], within a year of the Wright brothers' first successful sustained, powered flight. This early work had profound impacts still felt today – Prandtl was the first to put forth the ideas of skin friction drag, streamlining, flow separation, and stall. He proposed dividing the flow over a solid surface into two regions: the boundary layer, in which viscous forces dominate, and the free-stream, where viscosity can be neglected. This leads to a closed form solution for the boundary layer flow where, outside the boundary layer, an inviscid form of the Navier-Stokes equations can be solved and, inside the boundary layer, for an incompressible, laminar, two-dimensional flow, the Navier-Stokes equations can be approximated as:

$$\frac{\partial u}{\partial x} + \frac{\partial v}{\partial y} = 0 \quad (2.1)$$

$$\frac{\partial u}{\partial t} + u \frac{\partial u}{\partial x} + v \frac{\partial u}{\partial y} = -\frac{1}{\rho} \frac{\partial p}{\partial x} + \nu \frac{\partial^2 u}{\partial y^2} \quad (2.2)$$

$$\frac{\partial p}{\partial y} \approx 0 \quad (2.3)$$

The key differences between the boundary layer approximation and the full Navier-Stokes equations are the effective lack of a wall-normal momentum equation and the simplification of the stress term. By adopting these simplifications, generating solutions for the flow inside the boundary layer becomes much more straightforward, at least for steady, laminar flows. Much of the early work in boundary layer theory was on solving this closed-form equation to develop models for the growth of a boundary layer.

The general physics of the boundary layer phenomenon are captured in the no-slip condition: the concept that the velocity of the fluid exactly at the wall relative to the wall is zero, due to the adhesion between the wall and the fluid being stronger than the cohesion between the molecules

of the fluid. Above the no-slip wall, the streamwise velocity will increase through the boundary layer until reaching the free-stream value. Typically, the thickness of the boundary, δ , is defined as the distance away from the wall at which the velocity has recovered 99% of its free-stream value. While simple to visualize, this description of the boundary layer is lacking in physical meaning and is prone to error, as the velocity in the outer region of the boundary layer changes very slowly as will be discussed later. Instead, boundary layers are typically characterized by two parameters, the displacement and momentum thicknesses. The displacement thickness:

$$\delta^* = \int_0^\infty \left(1 - \frac{u}{U_e}\right) dy \quad (2.4)$$

is the distance the wall would have to be displaced in an inviscid flow (i.e., no boundary layer) in order to see the same reduction in mass flow as is created by the presence of the boundary layer and thus is a measure of mass flow lost to the boundary layer. The momentum thickness:

$$\theta = \int_0^\infty \frac{u}{U_e} \left(1 - \frac{u}{U_e}\right) dy \quad (2.5)$$

is the same concept for momentum loss. The ratio of displacement to momentum thickness is called the shape factor, which broadly indicates the character of the boundary layer, that is, whether the boundary layer is laminar, transitioning to turbulent, or fully turbulent, but there are no hard values of shape factor for these regimes, as the shape factor is also dependent on other effects, such as pressure gradient, which will be covered later. As described by Clauser [31], for flat plate laminar boundary layers in zero pressure gradient, the boundary layer parameters are linked to each other such that $\delta/\delta^* = 9$ and $\delta^*/\theta = 2.6$.

The origin of the boundary layer parameters is the early work of von Kármán [128] and Pohlhausen [102], both of whom derived a simplified, solvable version of the weak (integral) form of the boundary layer momentum equation. The resulting equation can be expressed:

$$\frac{d}{dx} \int_0^\delta [u(U_\infty - u)] dy + \frac{dU_\infty}{dx} \int_0^\delta (U_\infty - u) dy = \frac{\tau_w}{\rho} \quad (2.6)$$

By substituting the definitions of the displacement and momentum thicknesses into this form of the momentum equation, the integrals vanish leaving:

$$\frac{d}{dx} (U_\infty^2 \theta) + \delta^* U_\infty \frac{dU_\infty}{dx} = \frac{\tau_w}{\rho} \quad (2.7)$$

This form of the governing equation provides a simple, straightforward way of calculating the flow of a developing boundary layer on a smooth, flat plate in zero pressure gradient.

The nature of turbulence and the turbulent boundary layer will be covered in the next section, but for now we require a definition for the laminar boundary layer for context. In essence, a laminar flow is simply one without the presence of turbulence, but as we have not yet defined turbulence, this definition is not useful. Formally, a laminar flow is one that consists entirely of laminae, meaning layers of fluid that move nearly perfectly parallel to one another with no contamination between

layers. In a laminar boundary layer, then, all the fluid motion is in the streamwise direction, and the wall-normal and transverse velocities are zero everywhere.

The specifics of laminar boundary layer research are outside the scope of this review, but the concept is of great historical importance. The early works on boundary layer theory focused on finding closed-form solutions to the boundary layer equations for simple, laminar, flat-plate cases. While inappropriate and inaccurate for practical flow cases, the solutions of, for instance, Blasius [18] and Thwaites [124] form the basis out of which modern boundary layer research will grow. More thorough reviews of laminar boundary layer theories and solutions to the boundary layer equations are given by Schlichting [112] and Schetz [111].

2.1.2 Turbulence and the Turbulent Boundary Layer

Turbulence has many subtly differing definitions, but has several agreed upon characteristics: it is random and chaotic, exists on a broad spectrum of scales, and is irreversible in time. All of this adds up to a significant challenge: turbulent flow is unpredictable by its very definition, and, as such, the nature of turbulence has stymied researchers for centuries. One of the earliest important turbulence studies was the pipe flow experiments of Osborne Reynolds in 1883. Reynolds observed the behavior of dye in a transparent pipe flowing at various speeds and saw that at low speeds the dye continued in an unbroken line. As the speed was increased, the dye path would begin to waver downstream until, eventually, upon reaching sufficient speed and distance through the pipe, the dye would disperse into a turbulent cloud. This is the first demonstration of a very important concept: flow does not become turbulent until crossing some critical point. This point is defined by the Reynolds number:

$$Re = \frac{\rho U L}{\mu} \quad (2.8)$$

where U is a characteristic velocity and L is a characteristic length. At sufficiently high Reynolds number, all flows naturally become turbulent.

This does not, however, tell us anything about what exactly turbulence is. One of the first meaningful concepts of the nature of turbulence is given by Lewis Fry Richardson in 1922 when he postulated the idea of the energy cascade [106]. Based almost entirely on the simple observation of clouds on a windy day, Richardson observed that the fundamental nature of turbulence can be described by the generation of large structures, called eddies, which in turn spawn small eddies, which generate still smaller eddies and so on, and that energy and momentum are transported from the mean free-stream flow down to viscous dissipation through that cascade of ever shrinking eddies. Or more elegantly, he is famously quoted as saying, “...big whirls have little whirls that feed on their velocity, little whirls have smaller whirls and so on to viscosity.” These two ideas, that turbulence is made up of structures or eddies at many scales and that energy and momentum cascade down through those scales, form the basis of everything we know about turbulence.

There are two very important early works that define the scales of these structures and their role in the production and dissipation of turbulence. In 1923, Geoffrey Ingram Taylor performed a novel experiment visually observing the flow between concentric cylinders, revealing that turbulent

structures are strongly characterized by vorticity, i.e., rotational motion [122]. He also put forth a length scale for the turbulence, called the Taylor microscale, which represents the divide between eddies driven by viscous and inertial forces. At scales smaller than the Taylor scale, viscosity plays a large role in the dynamics of the turbulent eddies, but at larger scales viscosity can be neglected and inertia dominates in what is called the inertial range. Formally, Taylor's microscale is defined as:

$$\lambda = [-\frac{1}{2} \frac{\partial^2 f}{\partial x^2} |_{x=0}]^{-1/2} \quad (2.9)$$

$$f = \frac{R_{11}}{u'^2} \quad (2.10)$$

where R_{11} is the autocorrelation of the turbulent velocity fluctuations in the streamwise direction. For homogenous, isotropic turbulence, it can be shown that the Taylor microscale can be expressed as:

$$\lambda = [\frac{30\nu\overline{u'^2}}{\epsilon}]^{-1/2} \quad (2.11)$$

Soviet mathematician Andrey Kolmogorov defined two other length scales, the integral length scale, which is the size of the largest eddies in a given flow, and the Kolmogorov length scale, which is the size of the smallest eddies just before they are dissipated to heat by viscosity [123]. The Kolmogorov length scale is defined as:

$$\eta = (\frac{\nu^3}{\epsilon})^{\frac{1}{4}} \quad (2.12)$$

For a boundary layer flow, the integral length scale can be taken to be of the order of the boundary layer thickness, δ . Kolmogorov's 1941 theory of turbulence is a large part of our foundation of knowledge on the behavior of turbulent flows, in which he postulates that the smallest scales of turbulence are dependent on the viscosity of the fluid and the rate of dissipation of turbulent energy to heat, and that the behavior of these smallest scales is universal [74]. The largest scales, then, are dependent on the production of turbulence and the relationship between the large and small scales is driven by the Reynolds number.

A flow-field containing turbulence is characterized by fluctuations in the fluid variables, whereby the properties of the fluid vary in both space and time such that the exact quantities cannot be predicted with precision. However, turbulent flows often display predictable statistics within the pseudo-randomness of the instantaneous field. A fluctuating variable can be decomposed into its mean and fluctuating parts via a Reynolds decomposition, such that:

$$x = X + x' \quad (2.13)$$

where the variable x is a summation of its local mean, X , and its zero-mean fluctuation, x' . Many turbulent flows of interest are steady, meaning that the local means are not changing in time,

simplifying their statistical analyses. One of the most important statistics of a turbulent flow is its mean-square velocity fluctuations, $\overline{u'_i u'_j}$, where the overbar represents a mean, the ' indicates a zero-mean fluctuation of a variable, u is the velocity in component directions i, j . The mean-square velocity fluctuations are proportional to the Reynolds stress:

$$\tau_{ij} = \overline{\rho u'_i u'_j} \quad (2.14)$$

which effectively represents the effect of the present turbulence on the flow-field, and will be discussed in more detail in Section 2.3.1.

Turbulence in a boundary layer contains all of the above characteristics plus a few behaviors unique to wall bounded flows. The first major work on turbulent boundary layers, and certainly one of the most important, is that of Theodore von Kármán in 1930 [129]. In this work, von Kármán puts forth the Law of the Wall: an empirical relationship which describes how, in the inner region of the boundary layer, velocity will grow logarithmically with wall distance as a function of viscosity and wall shear stress:

$$u^+ = \frac{1}{\kappa} \ln y^+ + B \quad (2.15)$$

$$u^+ = \frac{u}{u_\tau} \quad (2.16)$$

$$y^+ = \frac{y u_\tau}{\nu} \quad (2.17)$$

where κ and B are constants, typically taken as $\kappa = 0.41$ and $B = 5.0$. Since then, the validity of this profound relation has been confirmed over and over again. The outer region of the boundary layer velocity profile is typically considered more difficult to completely describe and more dependent on the specifics of the flow case, most importantly that the value of y^+ at which the outer region begins increases with increasing Reynolds number [31]. The general framework, however, is described by Donald Coles in 1956 in his Law of the Wake, which describes a defect law for the outer region as it defects from the Law of the Wall [32]:

$$u^+ = f(y^+) + \frac{\Pi}{\kappa} w\left(\frac{y}{\delta}\right) \quad (2.18)$$

where $f(y^+)$ is the Law of the Wall, Π is Coles' wake strength parameter, and $w(y/\delta)$ is the Law of the Wake. The exact formulations of Π and w are unsettled, but must have the properties:

$$w(0) = 0 \quad (2.19)$$

$$w(1) = 2 \quad (2.20)$$

$$\int_0^2 dw = 1 \quad (2.21)$$

It has also been observed that, beneath the Log Layer (where the Law of the Wall applies) there is a region very near the surface where velocity varies linearly with wall distance, called the viscous sublayer [31]. The overlap between the sublayer and log layer is called the buffer layer. A complete description of the velocity profile in the inner region is given by Spalding (1961) [120]. An illustration of the turbulent boundary layer profile is given in Figure 2.1.

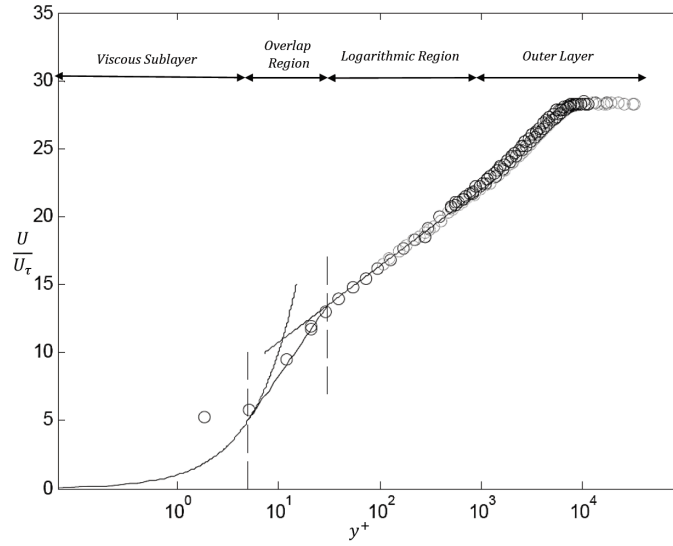


Figure 2.1: Typical boundary layer velocity profile with various regions highlighted [67].

The first major review of turbulent boundary layers is given by Clauser in 1956 [31]. Clauser carefully compares and contrasts laminar and turbulent boundary layers, describing how the turbulent boundary layer is thicker and imparts greater shear stress to the wall, but is also more stable and less prone to separation. He also compares the Blasius [18] universal velocity distribution for the laminar boundary layer to von Kármán’s Law of the Wall [129] and describes how the velocity will rise much more rapidly with wall distance in the turbulent boundary layer than the laminar. Additionally, the non-dimensional laminar boundary layer profile (U/U_e vs. y/δ) is universal, whereas the same for the turbulent boundary layer shows a clear Reynolds number dependency (this is accounted for by plotting instead on viscous scales, i.e., u^+ vs. y^+). The clear interpretation of this observation is that laminar boundary layers are driven by the mean outer motion whereas turbulent boundary layers are driven largely by the effects of friction and viscosity.

The importance of structures (or eddies) to the nature of turbulence cannot be overstated. In 1967, Kline & Reynolds used a combination of hydrogen bubbles and dye injection to observe the formation of coherent structures in a turbulent boundary layer [72]. They observed the production of “streaky” structures (Figure 2.2) in the inner layer which oscillated between low and high speeds in patterns correlated with the parameters of the Law of the Wall. The streaks would then burst as

they were pulled from the wall and Kline and Reynolds postulated that this is the main means by which turbulence is generated and imparted into the boundary layer. Our understanding of these low-speed streaks received an upgrade in 1980 with the work of Falco, who performed simultaneous visual observation and hotwire anemometry measurements of a turbulent boundary layer [39]. Falco observed that the streaks had two major patterns: motion *toward* the wall, which he called sweeps, and motion *away from* the wall, called ejections, as shown in Figure 2.3. Falco correlated the observed sweeping and ejection of the streaky structures with simultaneously observed perturbations in the velocity and velocity gradients.

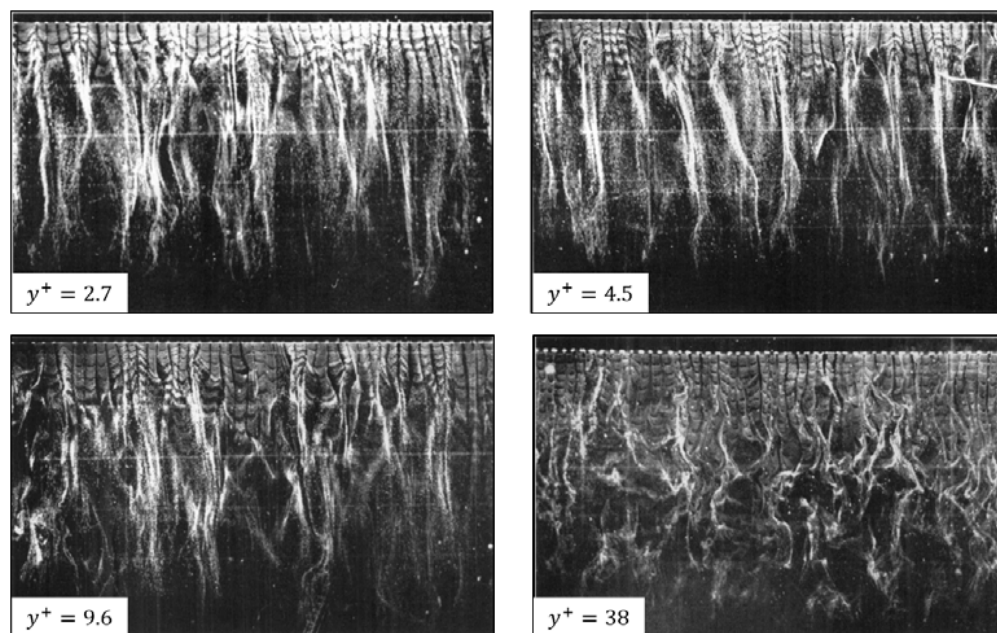


Figure 2.2: Low speed streaks in sub- and buffer layers visualized by hydrogen bubbles [72].

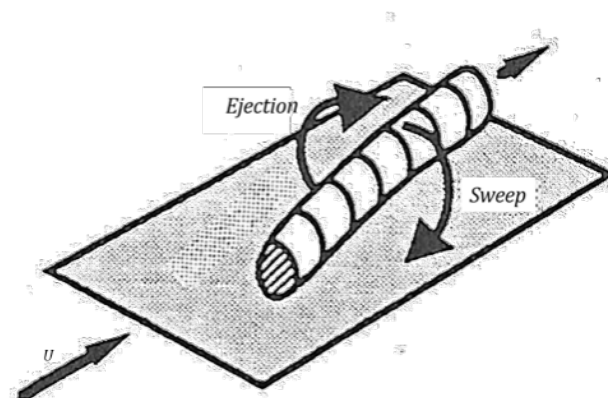


Figure 2.3: Vortical structure generating sweeps and ejections as it rotates and convects [107].

The nature of vortical structures in the outer regions of the boundary layer is, by comparison, still hotly debated, but a good overview is given by Robinson (1990) [107], who completed one of the first major DNS databases of turbulent boundary layer flows. Vortical structures in the boundary layer have a complex, but reasonably distinct, three-dimensional shape. The vortical structures begin as vortex tubes aligned transverse to the flow, then the center of the tube lifts from the surface and accelerates forward, away from the ends, creating a distinctive looping shape, the exact characteristics of which are dependent on the Reynolds number. At low Reynolds number, the tube is thick and has a wide radius of curvature and is called a Loop (Figure 2.4a). At moderate Reynolds number, the tube becomes thinner and shows a decreased radius of curvature and is referred to as a Horseshoe Vortex (Figure 2.4b). At high Reynolds number, the tube becomes very thin, and its radius of curvature approaches zero (i.e., an instantaneous 180° turn), which is called a Hairpin Vortex (Figure 2.4c). This is still an ongoing area of research, but it's generally agreed that the turbulence in a high Reynolds number turbulent boundary layer consists of packets of Hairpin Vortices, and this hypothesis has a good deal of empirical evidence; see, for example, Adrian *et al.* (2000) [2].

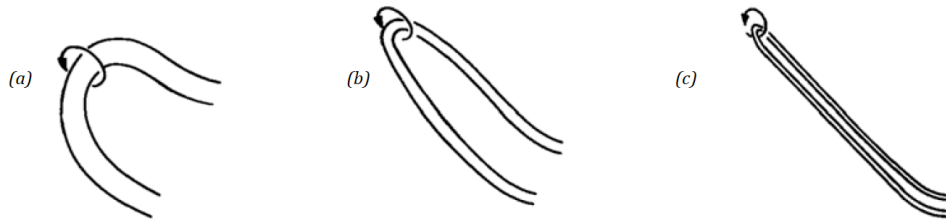


Figure 2.4: Schematic of outer-region vortical structures: Loop (a), Horseshoe (b), and Hairpin (c) [67].

One aspect of turbulence research that warrants special attention is that of non-dimensional scalings. Due to the inherent unpredictability of turbulence, our descriptions of turbulent flow must be statistical in nature. In order to draw meaningful conclusions about how these statistics inform us of the underlying physics, it is important to uncover how these statistics may be described non-dimensionally, that is, scaled, much like how Blasius [18] showed that the velocity profile of the laminar boundary layer is universal when plotted as U/U_e vs. y/δ as opposed to U vs. y . For turbulent boundary layers, the velocity profile instead may collapse on a defect scaling $((u - U_\infty)/u_\tau$ vs. y/δ), as described by Clauser [31], and the logarithmic region is known to collapse on viscous variables as described previously. A major review of proposed turbulent boundary layer scalings was given by Panton (1990) [97]. It's generally agreed that the two-layer (outer and inner) description of the turbulent boundary layer is a good one, and the most common way to scale these flows is using so-called outer and inner variables for the behavior of the two regions respectively, where “outer” variables are things like the edge velocity and boundary layer thickness and “inner” variables may be the friction velocity and viscosity. In 1997, George & Castillo effectively argued for the validity of these scalings based on first principles (specifically the RANS equations) [53]. Scaling has proved particularly effective at uncovering the physics of turbulent flows in pipes (see, for example, Zagarola & Smits 1998 [142] or Hultmark *et al.* 2010 [65]) and will be an important

point later in the discussion of the turbulent wall pressure spectrum.

A novel and potentially ground-breaking description of the turbulent boundary layer is provided by Wei *et al.* (2005), who propose describing the regions of the boundary layer, not by the mean velocity, but by the mean dynamics, specifically the ratio of viscous to turbulent forces [131]. They claim that this shows that viscosity plays an important role in the behavior of the boundary layer much farther from the wall than previously thought and propose a four-region boundary layer, with the typical inner and outer regions and their associated scalings, but with the addition of two middling regions where viscosity is of equal or dominant order and where mixed scalings are more appropriate, as shown in Figure 2.5. This interpretation of the boundary layer proved powerful, particularly in describing the physics of transitionally turbulent boundary layers, a regime that previously stymied researchers, as described by Klewicki *et al.* (2011) [71].

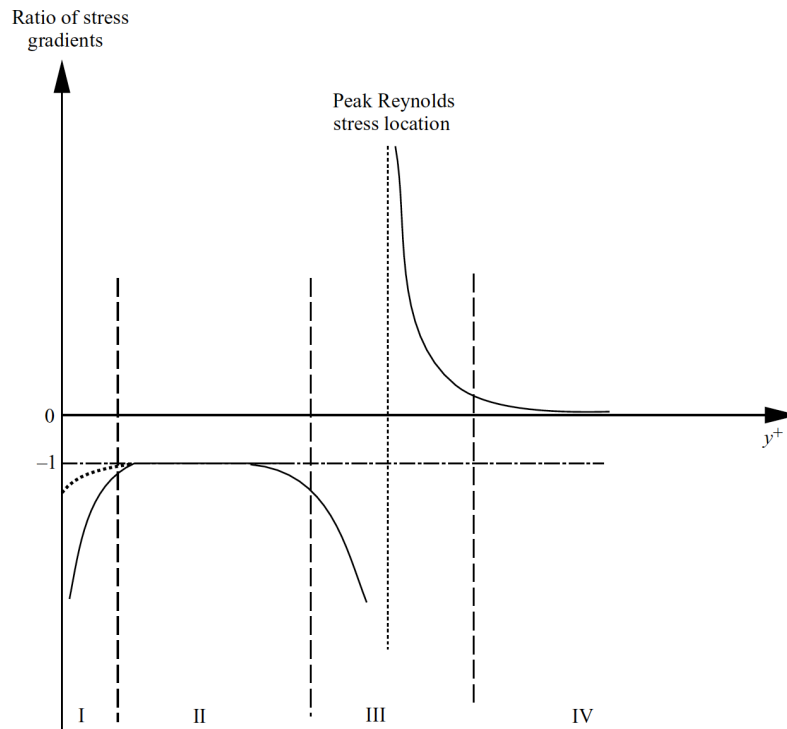


Figure 2.5: Sketch of the four layers of turbulent boundary layers; inner viscous layer (I), stress-gradient balance layer (II), viscous/advection balance meso-layer (III), and inertial/advection balance outer layer (IV) as described by Wei *et al.* (2005) [131].

2.1.3 Turbulent Boundary Layers in Pressure Gradient

The presence of a streamwise gradient in the mean wall pressure is a phenomenon common in many engineering applications and which is known to greatly impact the development of the boundary layer on said wall. The first major review of adverse pressure gradient effects on boundary layers is

given by Clauser (1954) [30] who proposed that the effect of the pressure gradient could be classified based on a non-dimensionalization of the pressure gradient:

$$\beta = \frac{\delta^*}{\tau_w} \frac{dp}{dx} \quad (2.22)$$

The origin of the Clauser parameter is an extension of the aforementioned integral momentum equation, now including pressure gradient:

$$\frac{d\theta}{dx} = \frac{1}{2} c_f \left[1 + (H + 2) \frac{\theta}{\tau_w} \frac{dp}{dx} \right] \quad (2.23)$$

It can be seen that if the term $(\theta/\tau_w)(dp/dx)$ is constant, then the growth of the boundary layer and its skin friction are tied very simply together by a first order partial differential equation. This produces an “equilibrium” pressure gradient boundary layer, meaning that the flow ought to be self-similar. A true equilibrium turbulent flow will exhibit self-similarity and self-preservation [36], but true equilibrium in an external turbulent boundary layer flow is not physical, due to the effects of three-dimensionality and fluid entrainment and given that the inner and outer scales are de-coupled. However, region-specific self-similarity should be observed in an equilibrium case, but Clauser observed that this was not always the case, due, most likely, to the three-dimensionality of boundary layers subjected to pressure gradients, resulting in a narrow band of velocity profiles but not a true collapse [30]. A better classification of the pressure gradient is achieved using the displacement thickness as the length scale rather than the momentum thickness because, with increasing Reynolds number, δ^* asymptotically approaches a constant ratio of δ faster than θ , making it a more stable predictor of equilibrium behavior. Early results show that when β is held constant, regardless of if $(\theta/\tau_w)(dp/dx)$ is constant, the boundary layer behavior is very closely self-similar, indicating a state of equilibrium. Mellor & Gibson (1966) observed that boundary layers in equilibrium show a universal and definable relationship between the Clauser parameter and a defect shape factor, G , and postulated that the presence and deviation from equilibrium are quantifiable by the agreement with this relation, shown in Figure 2.6 [89].

The Clauser parameter is still widely used to classify pressure gradient boundary layer flows, with the hope that the Reynolds number and β would be sufficient to characterize them. One of the major findings of early work on pressure gradient flows is that boundary layers subjected to adverse pressure gradient become unstable and can separate if subjected to a sufficiently strong APG for sufficient distance. It is for this reason that adverse pressure gradient has been subjected to significantly more research than favorable. The adverse pressure gradient similarly had a large impact on the observed boundary layer growth, thickening the boundary layer and increasing the skin friction. With the exception of the Law of the Wall, early attempts to define the functional dependencies of boundary layers to pressure gradients proved impossible, as was demonstrated by Samuel & Joubert (1974) [109].

The first reasonable model for the outer mean velocity profile in a pressure gradient boundary layer is that of Schofield & Perry (1981) [114]. The Schofield-Perry defect law is similar to Coles’ defect law, but the exact formulation is restated to incorporate empirically observed adverse pressure gradient effects:

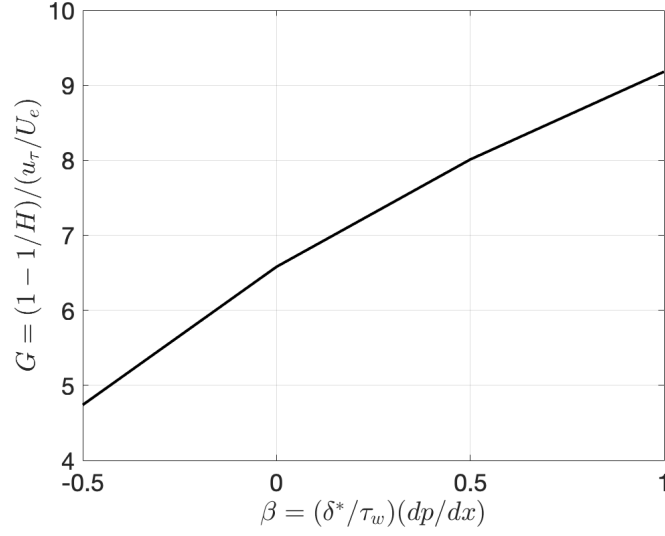


Figure 2.6: Equilibrium relation of Mellor & Gibson (1966) [89].

$$\frac{U_\infty - u}{U_s} = 1 - 0.4\left(\frac{y}{B}\right)^{\frac{1}{2}} - 0.6 \sin\left(\frac{\pi y}{2B}\right) \quad (2.24)$$

$$U_s = 8\left(\frac{B}{L}\right)^{\frac{1}{2}} U_m \quad (2.25)$$

$$B = 2.86\delta^* \frac{U_\infty}{U_s} \quad (2.26)$$

where L is the distance from the wall to the location of peak Reynolds shear stress and U_m is the velocity scale associated with this stress, $U_m = \sqrt{\tau_{max}/\rho}$. This model was shown to agree well with experimental data from adverse pressure gradient boundary layers, with the not-insignificant caveat that the pressure gradients were in equilibrium (constant β) (Figure 2.7). In the process, they defined the limits of the equilibrium APG boundary layer by quantifying the ratios of τ_{max} to τ_w that resulted in collapse of the Schofield-Perry law.

Another model is presented by Barenblatt *et al.* (2002) [12], who propose that pressure gradient boundary layers are self-similar when scaled with the non-dimensionalized pressure gradient parameter using the viscous length scale:

$$P = \frac{\nu/u_\tau}{\tau_w} \frac{dp}{dx} \quad (2.27)$$

and an “effective” Reynolds number. This model shows good agreement with data but is suspect due to the self-fulfillment of the effective Reynolds number, which is chosen empirically *posteriori*.

The effects of adverse pressure gradient on turbulent boundary layers are reviewed by Nagano *et al.* (1991) [93], which paints the following general picture: boundary layers subjected to adverse

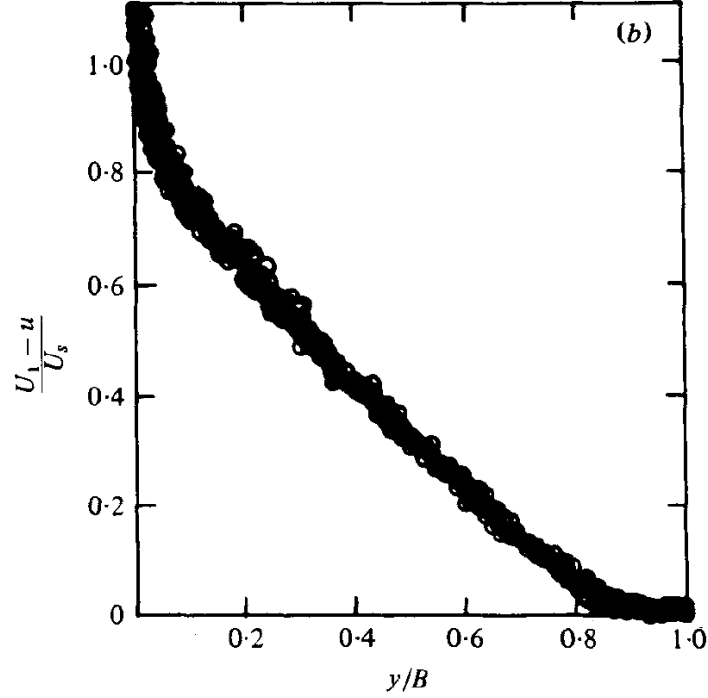


Figure 2.7: Various experimental data of equilibrium APG boundary layers on Schofield-Perry defect scaling [114].

pressure gradient become thicker and slower and move towards instability and separation, though the size of the sublayer shrinks. Additionally, the turbulent stresses and turbulent intensity increase in adverse pressure gradient. An updated picture of APG boundary layers is given by Aubertine & Eaton (2005) [6], which adds the following observations: the near wall region is self-similar with ZPG experiments, indicating that the inner regions may be pressure gradient independent, while the outer region cannot be collapsed except in equilibrium conditions.

Adverse pressure gradient also has an impact on the coherent structures in the boundary layer. Lee & Sung (2008) [80] and Harun *et al.* (2013) [59] found that the addition of adverse pressure gradient energizes the structures, particularly in the outer region of the boundary layer, causing them to rotate with increased vorticity and contribute to increased turbulent stresses. However, the geometry of the structures appears largely unaffected.

Scaling the adverse pressure gradient boundary layer proved challenging for many decades. Contrary to the hope of Clauser, Re and β are insufficient to characterize a pressure gradient flow unless the flow is in equilibrium. However, Maciel *et al.* (2018) [86] showed that the inclusion of one more parameter, the inertial parameter:

$$\alpha = \frac{U_e V_e}{U_0} \quad (2.28)$$

(where U_e and V_e are the streamwise and wall normal edge velocities and U_0 is some, as of yet unde-

terminated, characteristic velocity scale) closes the model and allows for true self-similar description of a wide range of non-equilibrium pressure gradient flows. They suggest that the proper choice of U_0 is the Zagarola-Smits velocity scale [142]. Another interesting scaling was proposed by Schatzman & Thomas (2017) [110], who postulated (and gave evidence for) the existence of an embedded shear layer between the wall and the boundary layer edge. They found that the length and velocity scales implied by this embedded shear layer fully collapsed a wide variety of pressure gradient flows. This observation was confirmed by Balantrapu *et al.* (2021) for axisymmetric boundary layers in strong APG [9].

There are two glaring gaps in the above literature: the effect of favorable pressure gradient and the effect of mixing pressure gradient behavior. The intense focus on adverse pressure gradient does make sense, but a more realistic approach to pressure gradient studies is likely needed to improve physical understanding. There have been a few favorable pressure gradient studies (see, e.g., Schloemer (1966) [113] which will be discussed in detail later), but for the most part these are not as thoroughly studied as it is known that they tend to re-laminarize the boundary layer and have fewer negative effects. There has been at least one interesting study on history effects in pressure gradient flows, that of Bobke *et al.* (2017) [19]. This work showed that there is a downstream lag in boundary layer parameters in a non-equilibrium pressure gradient flows that takes around seven boundary layer thicknesses to resolve, however, the viscous normalized boundary layer thickness, δ^+ , grows independent of pressure gradient. They also showed that a flat plate flow and an airfoil flow have very different turbulence characteristics, even with identical pressure gradients and Reynolds numbers. However, Bobke *et al.* only considered adverse pressure gradient.

2.1.4 Rough Wall Turbulent Boundary Layers

To be incredibly precise, there is no such thing as a smooth wall boundary layer. All surfaces have imperfections that could be considered roughness, even if only on a microscopic level. Surface roughness can present in many ways; some surfaces, particularly in marine applications, have rough characteristics simply as a result of their manufacturing, like large container ships. Others develop roughness characteristics over time due to use: smashed insects, barnacles, or surface rust, for example, and some roughness can develop temporarily due to environmental conditions, like leading edge icing. Still others have roughness characteristics that are included purposefully, like submarines, which must coat the top deck in a grippy surface such that is safe to walk on while at sea

The first important topic to discuss in the realm of surface roughness is the characterization of rough wall flows. First and foremost, we need a way of quantifying how “rough” or “smooth” a given surface is. One of the earliest works in rough wall boundary layers is that of Nikuradse (1950) [94], who studied the effect of various graded sand surfaces on the fully developed boundary layer in a pipe. He defined the roughness Reynolds number as:

$$k^+ = \frac{k_s u_\tau}{\nu} \quad (2.29)$$

and found that the rough flows could be broken into three regimes: hydraulically smooth ($k^+ \leq 5$) where the flow shows no deviation from smooth wall behavior, transitionally rough ($5 < k^+ \leq 70$)

where the flow shows clear deviation from smooth wall behavior, but that cannot be described entirely in terms of k^+ and the traditional Reynolds number also has an effect, and fully rough ($k^+ > 70$) where the flow can be described entirely in terms of the roughness Reynolds number. Ligrani & Moffat (1986) showed that, in the transitionally rough regime, flow behavior asymptotically approached smooth and rough behavior respectively and that the transitional effects are due to the combination of viscous drag and form drag that occur in these flows, leading to geometric dependencies that are not fully characterized by k_s alone [84]. Physically, then, a fully rough flow is one in which the form drag of individual elements can be neglected in favor of an integrated roughness effect characterized by k_s . These categorizations are important and effective, but the vast majority of rough surfaces do not fall under the description of sand grain. A more general description of roughness is based on its height (k_g and $k_g^+ = k_g u_\tau / \nu$) and sparseness ratio (λ).

Surface roughness can exist in infinite combinations and patterns, but can broadly be categorized a few ways. Roughness patterns can be either *regularly* or *randomly* distributed; most practically applicable rough surfaces will be random in nature, but rough wall experiments typically use a regular, ordered surface in order to eliminate contradictory effects and ensure complete control over the roughness effects. It is generally agreed that flows of equivalent k_s height will contain the same physics, regardless of roughness pattern, but this is still being explored [43].

Roughness elements can be of any shape, size, and pattern; in a research setting a rough surface is typically described by its height, k_g , shape, pattern, and pattern density, which can be quantified a few different ways, including pitch-to-height ratio [13], pitch-to-width ratio [38], total-area-to-frontal-area ratio [117], and sparseness ratio (frontal-area-to-planform-area ratio) [67]. The density of rough surface can also be broadly characterized in two types: D- and K-Type roughness. Originally put forth by Perry *et al.* [101], the difference between roughness type is shown in Figure 2.8.

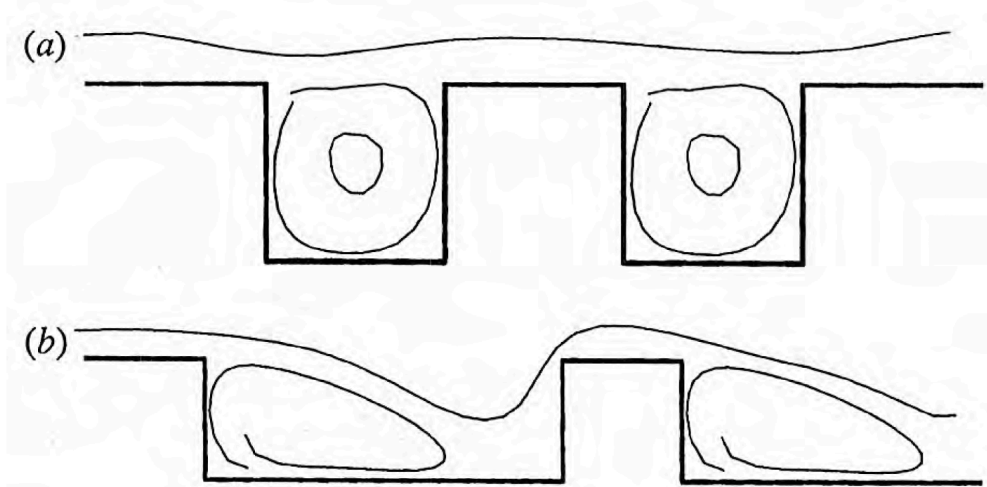


Figure 2.8: Illustration of near wall flow in D-Type (a) and K-Type (b) roughness, flow left to right [66].

For a sparse (i.e., K-Type) rough surface, each element will form its own wake that will then interact with the next downstream element. As roughness density increases, it will eventually pass some

critical threshold at which point the inter-roughness flow becomes mutually sheltered, effectively isolating the roughness above and beneath the canopy. This can be thought of as the difference between a smooth surface made rough by protrusions *up from the wall* (K-Type) and a smooth surface made rough by porous holes protruding *into the wall* (D-Type). The exact value of this threshold is dependent on the roughness geometry, flow properties, and roughness pattern, but a good estimate is $\lambda g > 4$ [140].

The main general effect of roughness on the boundary layer, as described by Nikuradse (1950) [94] and Dvorak (1969) [38] and shown in Figure 2.9 is a distinct shift in the mean velocity profile. Compared to the smooth wall Law of the Wall, the velocity profile of the rough wall boundary layer shows the same slope in the log region but at lower values of u^+ , thus the Law of the Wall for rough wall boundary layers can be written:

$$u^+ = \frac{1}{\kappa} \ln(y^+) + B - \Delta u^+ \quad (2.30)$$

The velocity profile shift, Δu^+ , is the most effective way to characterize a rough wall flow as it describes precisely how much of an effect the roughness is having on the development of the boundary layer, provided that the roughness is fully developed and consistent. Later, Schlichting (1979) would bring together a large database of rough wall flows and correlate the shift to the effective sand grain roughness, thus giving us the first comprehensive way to categorize the rough wall boundary layer (i.e., $\Delta u^+ \propto k_s$ even for non-sand-grain flows) [112].

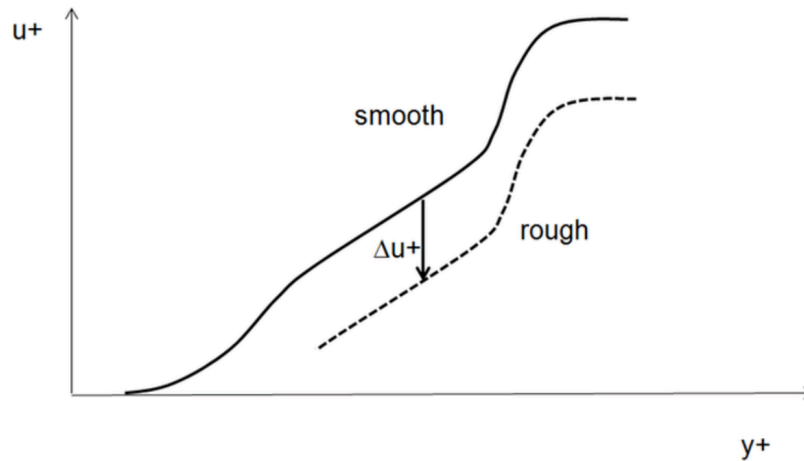


Figure 2.9: Smooth vs. rough wall Law of the Wall velocity profiles [96].

The general effect of roughness on boundary layer flows was reviewed by Raupach *et al.* (1991) [105], Krogstad *et al.* (1992) [76], and Jimenez (2004) [66]. In addition to the velocity profile shift, rough wall boundary layers have a larger wake region and are thicker than their smooth wall counterparts. They also exhibit a large increase in turbulent kinetic energy and a moderate increase in Reynolds stresses, corresponding to an increase in skin friction drag. Rough wall boundary layers do not have a viscous sublayer, instead they can be divided into two regimes existing respectively above

and below the “roughness canopy,” which extends just beyond the tops of the roughness elements. Beneath the canopy, in the roughness sublayer, the flow is characterized by the interaction with individual elements of roughness, generating local separations and highly chaotic flow, though Ligrani & Moffat (1986) hypothesized that, in a mean sense, the flow beneath the canopy is linear and effectively behaves identically to the smooth-wall sublayer [84]. Above the canopy, the flow is qualitatively similar to a smooth wall boundary layer with distinct quantitative differences driven by scale separation, i.e., the value of the roughness Reynolds number and the ratio of the boundary layer thickness to the roughness height. This is Townsend’s Hypothesis (Townsend (1976)), which states that, beyond the canopy, rough wall boundary layers display Reynolds number similarity [125].

Much of the work on rough wall boundary layers focuses on correlating the easily known characteristics of the rough surface (i.e., k_g and λ) with those that actually drive the flow (i.e., k_s and Δu^+). Dvorak proposed the first roughness correlation function in 1969 and it was quite effective, both at predicting the velocity shift and at extrapolating to other flow characteristics like the skin friction coefficient [38]. In 1973, Simpson generalized these correlation functions by using an alternate definition of the roughness density (based on an element’s height and length rather than frontal and planform area) and saw improved agreement with experiment [117]. A new and more complex form of the roughness correlation function was presented by Sigal & Danberg (2012), which introduced a new roughness parameter and saw even better agreement with a wide range of experimental conditions [116]. In addition, Antonia & Krogstad (2001) showed that the anisotropy of turbulence in a rough wall boundary layer is closely correlated with roughness density [4].

The structures in the outer regions of a rough wall boundary layer are similar to those in smooth wall boundary layers, that is, the outer region is dominated by packets of hairpin vortices as described by Blake (1971) [17] and Bandyopadhyay & Watson (1988) [11], however, these structures are found to be more active and carry more turbulent energy than in smooth wall flows. The structure near the surface is far more complex and varies greatly with roughness pattern, height, and density, as shown in Figure 2.10. Grass (1971) [56] postulated that sweeps and ejections are a universal feature and are the main mode of turbulent momentum transport in both smooth and rough walls and, indeed, Raupach (1981) [104] found that, just as in the smooth wall, sweeps are responsible for the bulk of turbulent stresses near the roughness canopy. The structures within the roughness canopy are difficult to study, but Bandyopadhyay & Watson (1988) showed that for two-dimensional roughness the roughness sublayer is composed predominantly of hairpin vortices as they begin to grow into the boundary layer [11]. However, for three-dimensional roughness, each element contained what was coined a necklace vortex, which wrapped around the element and stayed within the canopy, interacting with subsequent elements and necklace vortices, pictured in Figure 2.11.

Scaling of rough wall flows is not straightforward, given the nearly infinite variety of surface configurations and corresponding flow behaviors that fall under the heading of “rough wall flows”. Blake (1971) argued that the proper scaling is that based on the displacement thickness and friction velocity, and this has proven reasonably effective though not universal [17]. Schultz & Flack (2007) proposed a defect law scaling for the rough wall boundary layer which successfully collapsed the mean velocity and Reynolds stress profiles of a variety of rough wall flows as seen in Figure 2.12 [115]. Mehdi *et al.* (2013) [88] extended the mean dynamics description of the boundary layer of Wei *et al.* (2005) [131] to rough surfaces with surprisingly consistent results, suggesting the

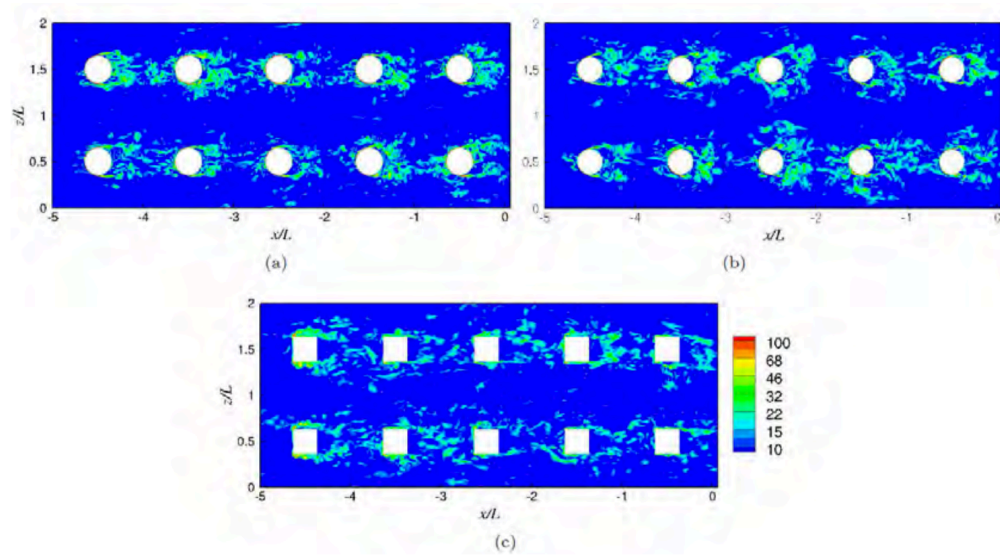


Figure 2.10: Isocontours of vorticity for hemispherical (a), cylindrical (b), and cuboid (c) roughness elements [141].

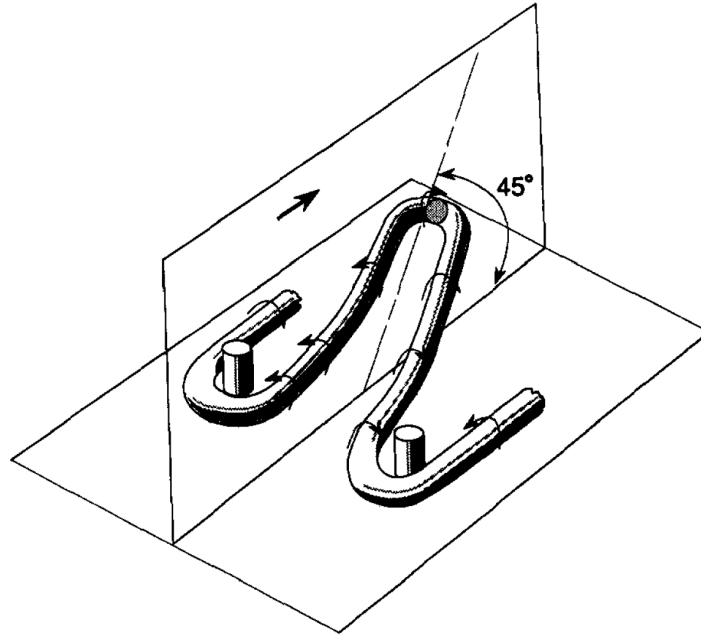


Figure 2.11: Sketch of a dual hairpin-necklace vortex structure observed in three-dimensional roughness sublayer [11].

universality (at least between smooth and rough walls) of the peak Reynolds stress length scaling.

There is still debate as to the nature of rough wall boundary layers and very little is understood about the combined effects of roughness and pressure gradient.

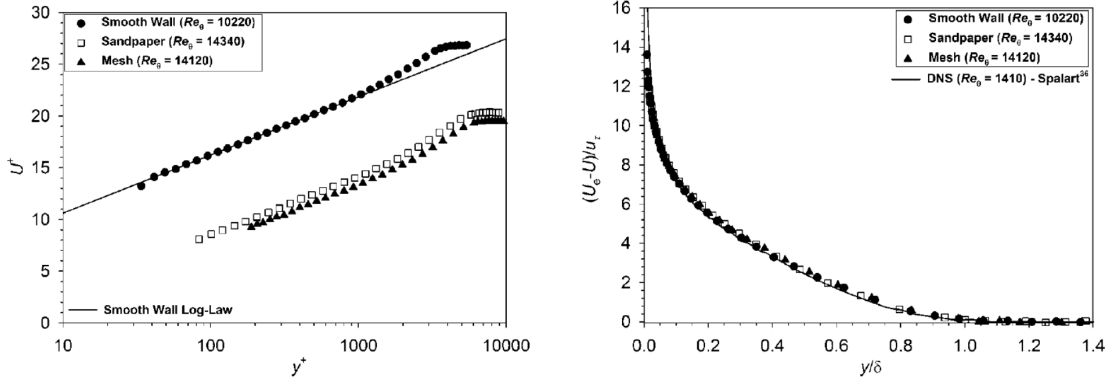


Figure 2.12: Viscous boundary layer scaling (left) and defect scaling (right) for a variety of smooth and rough boundary layer flows [44].

2.2 Turbulent Wall Pressure Fluctuations

2.2.1 Theory

The fluctuating pressure field in an incompressible turbulent boundary layer is governed by the pressure Poisson equation (PPE). The derivation for the PPE begins with the incompressible form of the conservation of momentum Navier-Stokes equation:

$$\rho \frac{\partial \vec{u}}{\partial t} + \rho(\vec{u} \cdot \nabla) \vec{u} = \mu \nabla^2 \vec{u} - \nabla p + \vec{f} \quad (2.31)$$

where \vec{u} is the velocity vector, p is the pressure, \vec{f} is the body force tensor and μ is the dynamic viscosity. We begin by neglecting the body forces, and then take the divergence of the remaining equation:

$$\nabla \cdot \left[\rho \frac{\partial \vec{u}}{\partial t} + \rho(\vec{u} \cdot \nabla) \vec{u} \right] = \nabla \cdot (\mu \nabla^2 \vec{u} - \nabla p) \quad (2.32)$$

This can be simplified by noting that the divergence of the velocity vector, $\nabla \cdot \vec{u}$ must be zero. We begin with the left-hand-side:

$$L.H.S. = \nabla \cdot \left[\rho \frac{\partial \vec{u}}{\partial t} + \rho(\vec{u} \cdot \nabla) \vec{u} \right] = \rho \frac{\partial}{\partial t} (\nabla \cdot \vec{u}) + \rho \nabla \cdot (\vec{u} \cdot \nabla) \vec{u} \quad (2.33)$$

The first term is identically zero, since $\nabla \cdot \vec{u} = 0$, leaving:

$$L.H.S. = \rho \nabla \cdot (\vec{u} \cdot \nabla) \vec{u} \quad (2.34)$$

Now, we consider the right-hand-side:

$$R.H.S. = \nabla \cdot (\mu \nabla^2 \vec{u} - \nabla p) = \mu \nabla^2 (\nabla \cdot \vec{u}) - \nabla^2 p \quad (2.35)$$

The first term is identically zero, since $\nabla \cdot \vec{u} = 0$, leaving:

$$R.H.S. = -\nabla^2 p \quad (2.36)$$

We have now, by simply assuming incompressibility and lack of body forces, reduced the momentum equation to:

$$\rho \nabla \cdot (\vec{u} \cdot \nabla) \vec{u} = -\nabla^2 p \quad (2.37)$$

which can be rearranged to show:

$$\frac{1}{\rho} \nabla^2 p = -\nabla \cdot [(\vec{u} \cdot \nabla) \vec{u}] \quad (2.38)$$

At this point in the derivation, it becomes easier to manipulate the terms in tensor, as opposed to vector, notation. This accomplished by:

$$\vec{u} \cdot \nabla = \begin{pmatrix} u \\ v \\ w \end{pmatrix} \cdot \begin{pmatrix} \frac{\partial}{\partial x} \\ \frac{\partial}{\partial y} \\ \frac{\partial}{\partial z} \end{pmatrix} = u_j \frac{\partial}{\partial x_j} \quad (2.39)$$

Thus, the right-hand-side becomes:

$$R.H.S. = -\nabla \cdot [(\vec{u} \cdot \nabla) \vec{u}] = -\nabla \cdot (u_j \frac{\partial u_i}{\partial x_j}) = -\frac{\partial}{\partial x_i} (u_j \frac{\partial u_i}{\partial x_j}) \quad (2.40)$$

Applying the chain rule:

$$R.H.S. = -\frac{\partial^2 (u_i u_j)}{\partial x_i \partial x_j} \quad (2.41)$$

We have now converted the pressure equation from vector to tensor notation:

$$\frac{1}{\rho} \nabla^2 p = -\frac{\partial^2}{\partial x_i \partial x_j} (u_i u_j) \quad (2.42)$$

Next, we will apply a Reynolds decomposition, separating each variable into its mean and fluctuating parts:

$$\begin{aligned} u &= U + u' \\ p &= P + p' \end{aligned} \quad (2.43)$$

where capital variables represent the mean and the ' superscript denotes the fluctuating component. Our pressure equation can thus be re-stated:

$$\frac{1}{\rho} \nabla^2 (P + p') = - \frac{\partial^2}{\partial x_i \partial x_j} [(U_i + u'_i)(U_j + u'_j)] \quad (2.44)$$

We expand the term in brackets:

$$(U_i + u'_i)(U_j + u'_j) = U_i U_j + u'_j U_i + u'_i U_j + u'_i u'_j \quad (2.45)$$

So:

$$\frac{1}{\rho} \nabla^2 (P + p') = - \frac{\partial^2}{\partial x_i \partial x_j} (U_i U_j + u'_j U_i + u'_i U_j + u'_i u'_j) \quad (2.46)$$

We are interested only in the fluctuating pressure field and its statistics, and so need to eliminate the time average pressure field, P . If we take the time average of Eq. 2.46, we are left with:

$$\frac{1}{\rho} \nabla^2 P = - \frac{\partial^2}{\partial x_i \partial x_j} (U_i U_j + \overline{u'_i u'_j}) \quad (2.47)$$

We can then subtract this mean equation from the full equation of Eq. 2.46 to achieve:

$$\frac{1}{\rho} \nabla^2 p' = - \frac{\partial^2}{\partial x_i \partial x_j} (u'_j U_i + u'_i U_j + u'_i u'_j - \overline{u'_i u'_j}) \quad (2.48)$$

The first two terms inside the derivative can be pulled out and simplified to one term by the application of the chain rule. This brings us to the final form of the PPE:

$$\frac{1}{\rho} \nabla^2 p' = -2 \frac{\partial u'_j}{\partial x_i} \frac{\partial U_i}{\partial x_j} - \frac{\partial^2}{\partial x_i \partial x_j} (u'_i u'_j - \overline{u'_i u'_j}) \quad (2.49)$$

an exact (assuming incompressible flow with no body forces), analytical partial differential equation for the fluctuating pressure field in an arbitrary turbulent flow. The first term is the *rapid* term, representing the interaction between turbulence and the mean shear. This term has a linear dependency on fluctuating velocity. The second term is the *slow* term, representing the turbulence-turbulence interaction. This term has a non-linear dependency on the velocity fluctuations. Fundamentally, we see that the fluctuating pressure field has a complex, non-linear dependency on the flow through the entire boundary layer. For more on the pressure Poisson equation, see, e.g., Lilley & Hodgson (1960) [85], Panton & Linebarger (1974) [98], Lee *et al.* (2005) [82], Grasso *et al.* (2019) [57].

To this point, our derivation has been largely algebraic manipulation, making only the assumptions of incompressible flow without body forces. However, we now need to transform the Laplacian

of the fluctuating pressure field into the associated power spectral density at the wall surface, for which there is no true analytical solution. To begin, let us assume that the right-hand-side of the PPE is a single source term for the pressure fluctuations, such that:

$$\nabla^2 p' = q(x_i, t) \quad (2.50)$$

where q is the source of the pressure fluctuations, dependent on space, x_i , and time, t . Now, we will assume that this pressure fluctuation source can be approximated as an infinitely thin harmonic wave at some finite location above the surface of the wall, which is essentially the assumption that the turbulence in the boundary layer is frozen and composed of an infinite number of infinitely thin homogeneous wall-parallel planes. This harmonic can be expressed:

$$q(x_i, t) = Q(y_0, k_1, k_3, \omega) \delta(x_2 - y_0) \exp[-i\omega t + ik_1 x_1 + ik_3 x_3] \quad (2.51)$$

where Q is the amplitude of the fluctuating velocity at the location of the pressure source, y_0 is the location of the pressure source, δ is the Dirac Delta function, effectively isolating the source of the pressure fluctuations to a single location, $x_2 = y_0$, and ω , k_1 , and k_3 are the time, streamwise, and transverse frequencies respectively. We have eliminated dependence on k_2 by assuming each harmonic is infinitely thin in the x_2 direction and thus effectively isotropic in k_2 .

This gives us an expression for the harmonic source at any given location above the wall. The wall pressure fluctuations will be an integrated effect of the entire boundary layer flow, which can be expressed as the integrated effect of the whole field of harmonics:

$$\nabla^2 p' = \oint_V q(x_i, t) = \int_{-\infty}^{\infty} \int_{-\infty}^{\infty} \int_{-\infty}^{\infty} \int_0^{\infty} Q(y_0, \omega, k_1, k_3) \delta(x_2 - y_0) \exp[-i\omega t + ik_1 x_1 + ik_3 x_3] dy_0 d\omega dk_1 dk_3 \quad (2.52)$$

Prior to solving this integral, we must consider what we expect the final form of p' to look like. We can assume that it will have a harmonic dependency, such that it could be expressed:

$$p'(x_i, t) = \hat{p}(x_2) \exp[-i\omega t + ik_1 x_1 + ik_3 x_3] \quad (2.53)$$

where \hat{p} is the amplitude of the fluctuating pressure, dependent only on x_2 as we have assumed homogeneity in each x_2 plane. By substituting this form into Eq. 2.50, we can show:

$$\nabla^2 \hat{p} - (k_1^2 + k_3^2) \hat{p} = Q(y_0, \omega, k_1, k_3) \delta(x_2 - y_0) \quad (2.54)$$

which can be rearranged to show:

$$\nabla^2 \hat{p} = Q(y_0, \omega, k_1, k_3) \delta(x_2 - y_0) + (k_1^2 + k_3^2) \hat{p} \quad (2.55)$$

We now need to eliminate the Laplacian and arrive at an expression for the pressure amplitude by itself. To do this, we make use of the fact that Eq. 2.55 is the form of a tailored Green's function in order to perform the necessary integration. The general solution to this equation is:

$$\hat{p}(x_2) = \frac{1}{2\sqrt{k_1^2 + k_3^2}} Q(y_0, \omega, k_1, k_3) [\exp[-\sqrt{k_1^2 + k_3^2}|x_2 - y_0|] + \exp[-\sqrt{k_1^2 + k_3^2}(x_2 + y_0)]] \quad (2.56)$$

Now we are ready to isolate the pressure fluctuations at the wall, by setting $x_2 = 0$:

$$\hat{p}_{wall} = \frac{1}{\sqrt{k_1^2 + k_3^2}} Q(y_0, \omega, k_1, k_3) \exp[-\sqrt{k_1^2 + k_3^2}y_0] \quad (2.57)$$

This can then be substituted back into Eq. 2.53 to show:

$$p'_{wall}(t) = \frac{1}{\sqrt{k_1^2 + k_3^2}} Q(y_0, \omega, k_1, k_3) \exp[-i\omega t + k_1x_1 + k_3x_3 - \sqrt{k_1^2 + k_3^2}y_0] \quad (2.58)$$

Eq. 2.58 represents the form we expect for the time-dependent wall pressure fluctuations, based on harmonic sources of the form Q . We can now substitute this source form into Eq. 2.52 to eliminate the Laplacian and show:

$$p'_{wall}(t) = \int_{-\infty}^{\infty} \int_{-\infty}^{\infty} \int_{-\infty}^{\infty} \int_0^{\infty} \frac{1}{\sqrt{k_1^2 + k_3^2}} Q(y_0, \omega, k_1, k_3) \exp[-i\omega t + ik_1x_1 + ik_3x_3 - \sqrt{k_1^2 + k_3^2}y_0] dy_0 d\omega dk_1 dk_3 \quad (2.59)$$

Earlier, we stated that we would assume Taylor's hypothesis, i.e., that the turbulence can be assumed frozen. Frozen turbulence implies that the turbulent field does not evolve in time or space and simply convects downstream. Making this assumption allows us to state that all dependence on t , x_1 , and x_3 can be re-formulated as dependence on the associated frequencies ω , k_1 , and k_3 respectively. This allows us to eliminate the time and spatial dependence and re-formulate Eq. 2.59 as:

$$p'_{wall}(\omega, k_1) = \int_{-\infty}^{\infty} \int_0^{\infty} \frac{1}{\sqrt{k_1^2 + k_3^2}} Q(y_0, \omega, k_1, k_3) \exp[-\sqrt{k_1^2 + k_3^2}y_0] dy_0 dk_3 \quad (2.60)$$

We now have an expression for the wall pressure fluctuations that is a function only of frequency and the source term, Q . We can now perform a spectral analysis to achieve the spectral density of these pressure fluctuations. The formal definition of the spectral density is the Fourier transform of the correlation function. We do not have enough information to know the correlation behavior of p'_{wall} , however, there is a quasi-exact estimator for the spectral density:

$$\phi_{pp}(\omega, k_1) = \frac{2\pi}{T} E[\tilde{p}^* \tilde{p}] \quad (2.61)$$

where \tilde{p} is the Fourier transform of p'_{wall} , the $*$ denotes a complex conjugate, E is the expected value, and T is the period over which the Fourier transform is taken. This gives us an expression for the spectral density:

$$\phi_{pp}(\omega, k_1) = \frac{2\pi}{T} \int_{-\infty}^{\infty} \int_0^{\infty} \int_{-\infty}^{\infty} \int_0^{\infty} \frac{E[\tilde{Q}^*(y'_0, \omega, k_1, k'_3) \tilde{Q}(y_0, \omega, k_1, k_3)]}{\sqrt{k_1^2 + k_3^2} \sqrt{k_1'^2 + k_3'^2}} \exp[-\sqrt{k_1^2 + k_3^2} y_0 - \sqrt{k_1'^2 + k_3'^2} y'_0] dy_0 dk_3 dy'_0 dk'_3 \quad (2.62)$$

At this point, let us pause and recap. From Eq. 2.50 to Eq. 2.62 we have arrived at an expression for the reduced wavenumber-frequency spectral density of wall pressure that is a function of the Fourier transform of some source term, Q , and its corresponding position, y_0 , and the complex conjugate of that Transform and *its* corresponding position, y'_0 . We have done this without relating Q back to the PPE in any way. Now, however, we must return our attention to the PPE in order to replace the place-holder Q with actual flow physics.

We will need to isolate the rapid and slow terms, and will begin with an analysis of the rapid, turbulence-mean-shear (TM) term. Recalling our source definition in Eq. 2.51:

$$q_{TM}(x_i, t) = Q_{TM}(y_0, \omega, k_1, k_3) \exp[-i\omega t + ik_1 x_1 + ik_3 x_3] = -2\rho \frac{\partial u'_j}{\partial x_i} \frac{\partial U_i}{\partial x_j} \quad (2.63)$$

In order to solve this, we will need to greatly simplify the partial derivatives. This can be accomplished by applying the classical boundary layer assumptions, chiefly that the velocity in non-streamwise components is negligible compared to the streamwise component and that all velocity gradients are negligible compared to the wall-normal component, i.e.:

$$\begin{aligned} U_1 &\gg U_2, U_3 \\ \frac{\partial U_1}{\partial x_2} &\gg \frac{\partial U_1}{\partial x_1}, \frac{\partial U_1}{\partial x_3} \end{aligned} \quad (2.64)$$

This allows us to state:

$$q_{TM}(x_i, t) = -2\rho \frac{\partial u'_j}{\partial x_i} \frac{\partial U_i}{\partial x_j} \approx -2\rho \frac{\partial u'_2}{\partial x_1} \frac{\partial U_1}{\partial x_2} \quad (2.65)$$

Next, recall that we have established the source term is an integrated effect and that the application of Taylor's hypothesis allows us to restate a dependence in space as a dependence in spatial frequency, thus:

$$q_{TM}(t) = \oint_V q_{TM}(x_i, t) dx_i = \int_{-\infty}^{\infty} \int_{-\infty}^{\infty} \int_{-\infty}^{\infty} Q(y_0, \omega, k_1, k_3) \exp[-i\omega t + ik_1 x_1 + ik_3 x_3] d\omega dk_1 dk_3 \quad (2.66)$$

Eq. 2.66 is the definition of the inverse Fourier transform of Q . We then can rearrange it to show:

$$Q_{TM}(y_0, \omega, k_1, k_3) = \frac{1}{(2\pi)^2} (ik_1) \int_{-\infty}^{\infty} \int_{-\infty}^{\infty} \int_{-\infty}^{\infty} \left[\int_{-\infty}^{\infty} q_{TM}(x_i, t) dx_i \right] \exp[i\omega t - ik_1 x_1 - ik_3 x_3] dt dk_1 dk_3 \quad (2.67)$$

Next, by assuming that we will evaluate this expression only at $x_2 = y_0$, we can say:

$$\int_{-\infty}^{\infty} q(x_i, t) dx_i = \oint_V -2\rho \frac{\partial u'_2}{\partial x_1} \frac{\partial U_1}{\partial y_0} = -2\rho \frac{\partial U_1}{\partial y_0} \int_{-\infty}^{\infty} \frac{\partial u'_2}{\partial x_1} dx_1 = -2\rho \frac{\partial U_1}{\partial y_0} u'_2(t, y_0, x_3) \quad (2.68)$$

We can substitute this into Eq. 2.67 to achieve:

$$Q_{TM}(y_0, \omega, k_1, k_3) = -\frac{2\rho}{(2\pi)^2} \frac{\partial U_1}{\partial y_0}(ik_1) \int_{-\infty}^{\infty} \int_{-\infty}^{\infty} \int_{-\infty}^{\infty} u'_2(t, y_0, x_3) \exp[i\omega t - ik_1 x_1 - ik_3 x_3] dt dk_1 dk_3 \quad (2.69)$$

We now have an expression for Q_{TM} and know it depends on the wall-normal gradient of streamwise velocity and the fluctuating wall normal velocity. Thus, we can say:

$$E[Q_{TM}^*(y'_0, \omega, k_1, k'_3) Q_{TM}(y_0, \omega, k_1, k_3)] \propto E[u_2'^*(t, y'_0, x_3) \tilde{u}'_2(t, y_0, x_3)] \quad (2.70)$$

The right-hand-side of this equation is the definition of the autocorrelation, i.e.:

$$E[u_2'^*(t, y'_0, x_3) \tilde{u}'_2(t, y_0, x_3)] \equiv R_{22}[(t' - t), y_0, y'_0, (x'_3 - x_3)] \quad (2.71)$$

We can use this to write out an exact formulation for $E[Q_{TM}^* Q_{TM}]$:

$$\begin{aligned} E[Q_{TM}^*(y'_0, \omega, k_1, k'_3) Q_{TM}(y_0, \omega, k_1, k_3)] = \\ \left[\frac{2\rho}{(2\pi)^2} (ik_1) \right]^2 \frac{\partial U_1}{\partial y_0} \frac{\partial U_1}{\partial y'_0} \\ \times \int_{-T}^T \int_{-T}^T \int_{-\infty}^{\infty} \int_{-\infty}^{\infty} R_{22}[(t' - t), y_0, y'_0, (x'_3 - x_3)] \exp[-i\omega(t' - t) - ik_3(x'_3 - x_3)] dx_3 dx'_3 dt dt' \end{aligned} \quad (2.72)$$

The quad integral in this equation is the Fourier transform of an autocorrelation, which is the analytical definition of the autospectral density. Thus, this can be re-written:

$$E[Q_{TM}^*(y'_0, \omega, k_1, k'_3) Q_{TM}(y_0, \omega, k_1, k_3)] = 4\rho^2 \frac{T}{2\pi} k_1^2 \frac{\partial U_1}{\partial y_0} \frac{\partial U_1}{\partial y'_0} \phi_{22}(y_0, y'_0, k_1, k_3) \quad (2.73)$$

Finally, this can be substituted into Eq. 2.62 to obtain a model for the spectral density of wall pressure due to the rapid term of the PPE:

$$\phi_{pp}^{TM}(k_1, k_3) = 4\rho^2 \int_0^{\infty} \int_0^{\infty} \frac{k_1^2}{k_1^2 + k_3^2} \frac{\partial U_1}{\partial y_0} \frac{\partial U_1}{\partial y'_0} \phi_{22}(y_0, y'_0, k_1, k_3) \exp[-\sqrt{k_1^2 + k_3^2}(y_0 + y'_0)] dy_0 dy'_0 \quad (2.74)$$

In arriving at this expression, we have made the following assumptions:

- Incompressible flow with no body forces
- $U_1 \gg U_2, U_3$
- $\frac{\partial U_1}{\partial x_2} \gg \frac{\partial U_1}{\partial x_1}, \frac{\partial U_1}{\partial x_3}$
- Taylor's hypothesis of frozen turbulence [122]
- Source terms exist in otherwise homogeneous, wall parallel planes

These assumptions and their ramifications warrant further discussion and research; some of which is the topic of this dissertation, but much of the knowledge and research in this area is reviewed thoroughly by Grasso *et al.* (2019) [57].

We now turn our attention to the slow, turbulence-turbulence interaction term. This term is far more difficult to transform into the associated wall pressure spectrum owing to the non-linearity of the pressure-velocity relation. Many authors [82, 85, 98] simply neglect the TT term, citing evidence that it accounts for less than 10% of the total energy of the pressure spectrum, however, for the sake of rigor, it seems better to include the effects of this term, if possible. Grasso *et al.* (2019) show a derivation for a TT model, but this relies on significantly more assumptions than the above TM model derivation [57]. Grasso *et al.*'s model assumes that the boundary layer turbulence is homogeneous and isotropic and that the velocity correlations can be of an assumed form, either an exponential or Gaussian distribution. The full derivation will not be shown, as it is long and not this author's intellectual work; we will skip to the final model equation:

$$\begin{aligned} \phi_{pp}^{TT}(k_1, k_3) = & \\ & \frac{\rho^2 L^2}{128\pi} (k_1^2 + k_3^2) [28 + L^2(k_1^2 + k_3^2)] \exp[-L^2(k_1^2 + k_3^2)/8] \\ & \times \int_0^\infty \int_0^\infty \frac{4}{9} k_T(y_0) k_T(y'_0) \exp[-(y_0 + y'_0) \sqrt{k_1^2 + k_3^2}] \mathcal{F}^2 dy_0 dy'_0 \end{aligned} \quad (2.75)$$

Here, \mathcal{F} is the assumed correlation distribution, and L is the associated length scale. The accuracy of this model is highly questionable, due to the invalid assumptions used to derive it, but it produces a model spectrum that is small relative to the TM model and of a robust form.

The combined model form, $\phi_{pp} = \phi_{pp}^{TM} + \phi_{pp}^{TT}$, can be transformed to the autospectral density of fluctuating pressure in the time-frequency domain by integrating over k_3 and then assuming that k_1 is related to ω via Taylor's hypothesis of frozen turbulence [122], wherein the eddies are convecting at some constant speed, U_c , such that:

$$k_1 = \frac{\omega}{U_c} \quad (2.76)$$

$$G_{pp}(\omega) = 2 \frac{\int_{-\infty}^{\infty} \phi_{pp}(k_1, k_3) dk_3}{U_c} \quad (2.77)$$

These equations provide an excellent framework for understanding and predicting turbulent pressure fluctuations from first principles, but as will be discussed throughout, modeling is still required and robust guidelines for how these equations can and should be utilized in a practical setting are still not settled.

2.2.2 Experimental Measurement

One of the first major works on fluctuating wall pressure was that of Kraichnan (1956) [75]. Kraichnan's work was largely theoretical; he attempted to derive the Reynolds and Mach number dependencies of the root-mean-square pressure based on similarity arguments and compared these to early experimental results. These results were extremely limited due to the limitations of fluctuating pressure transducers at that time [137]. More time resolved measurements of the fluctuating wall pressure were not possible until the early 1960's; Willmarth & Woolridge (1962) gathered some of the first high quality measurements of wall pressure fluctuations [136] and this work was instrumental in uncovering some of the two-point statistics and correlations within the fluctuating pressure field, including the variation of pressure convection velocity with separation, that is, the pressure convection velocity increases with the separation over which the convection data is obtained, asymptotically approaching some broadband value, the exact value of which is claimed to be between 80 and 85% of the free-stream velocity, depending on which author is read.

As the 1960's progressed, researchers focused on pushing the envelope of experimental techniques to higher frequencies (see the work of Corcos 1963 [33], Bull 1963 [21], Corcos 1964 [34], Corcos 1967 [35], and Bull 1967 [22]). Our understanding to this point was thoroughly reviewed by Willmarth (1975) [135]; it was understood that the turbulent wall pressure spectrum presented as a positive slope in the low frequencies and a negative slope in the high frequencies, the coherence in frequency and space presented as an arrowhead shape, and the space-time correlation map as an oval. These results showed the qualitative behavior of fluctuating pressure and provided a baseline on which all modern research in the area is based.

One issue of special relevance was (and still is) the ability of transducers to resolve the smallest eddies. The smallest pressure imparting eddies have a length scale of ν/u_τ , on the order of $10 \mu m$ in air. Creating sensors that can effectively measure high frequency turbulent pressure fluctuations without significant spatial averaging is one of the greatest challenges of fluctuating pressure measurement. One common method is to use a pinhole cap on top of a larger transducer. This changes the effective sensing area from that of the transducer to that of the pinhole, but it does not come without cost. Firstly, the pinhole will attenuate high frequency pressure fluctuations; the exact frequency at which this attenuation occurs is investigated and documented by Gravante *et al.* (1998) [58]. Corcos proposed a correction to recover data at attenuated frequencies (Corcos 1963, 1967 [33, 35]), however such corrections could be construed as self-fulfilling and are largely unnecessary provided that there is sufficient non-attenuated data to capture the slope of the high frequency region of the spectrum. The second problem with pinhole caps is that they function as Helmholtz resonators, corrupting the measured spectra with a tonal resonance that is a function of the pinhole geometry, acoustic impedance, and the grazing flow conditions. The problem of calibrating for this resonance is still a topic of much debate and the effect of grazing flow is not understood [10, 46, 126].

As technology progressed, researchers were able to both measure the same flows more exactly and push the measured flows to higher Reynolds numbers. As the scale separation (i.e., Reynolds number) of the flows and the frequency resolution of the sensors increased, it became clear that the turbulent wall pressure spectrum was actually a three-region spectrum, showing a distinction between the moderate decay at mid-frequencies and the steep roll-off at high frequencies. In

addition, our understanding of the space-time correlation of the pressure field increased, showing us that there is variation in the coherence and correlation slopes at varying separations, implying both that convection velocity varies with turbulent scale and that large scale pressure imparting structures are dissipating energy through turbulent mixing in the outer region near the boundary layer edge (Choi & Moin 1990 [29], Farabee & Casarella 1991 [41]).

Understanding of turbulent pressure fluctuations was reviewed thoroughly by Bull in 1996 [23]. According to Bull, the autospectrum exists as three distinct regions, a low frequency region ($\omega\delta^*/U_e < 0.03$) with slope ω^2 , a high frequency region ($\omega\nu/u_\tau^2 > 0.3$) of slope ω^{-5} , and a mid-frequency region of slope ω^{-1} . Bull argues (based largely on his own works and the works of Panton & Linebarger 1974 [98] and Farabee & Casarella 1991 [41]) that the low frequency region should scale on outer variables, $G_{pp}\delta/q^2U_e$ vs. $\omega\delta/U_e$ (where $q = 0.5\rho U_e^2$ is the dynamic pressure), the high frequencies should scale on inner variables, $G_{pp}\nu/\tau_w^2u_\tau^2$ vs. $\omega\nu/u_\tau^2$, and the mid-frequency region is an “overlap” region, which will scale on both. An illustration of the spectrum, its regions, and the corresponding scaling behaviors are shown in Figure 2.13. The slope of the mid-frequency region is hotly debated; many authors (e.g., Goody 2004 [54], Tsuji *et al.* 2007 [126]) argue that it is more in the range of $\omega^{-0.8}$. The existence of the overlap region is also widely disputed and appears to only truly exist in equilibrium, smooth wall, ZPG boundary layers with relatively small scale separation.

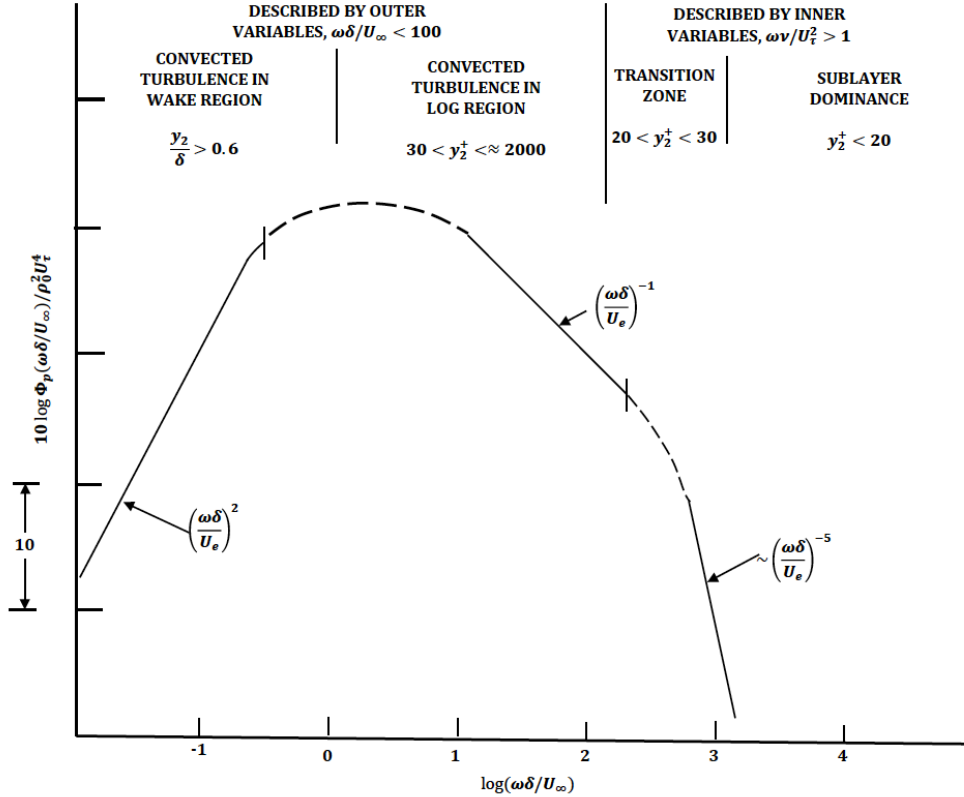


Figure 2.13: Frequency spectrum of wall pressure fluctuations [67].

2.2.3 Pressure Gradient Effects

There is surprisingly little literature on the topic of the fluctuating wall pressure behavior in flows with pressure gradients, so much so that some empirical models which will be discussed later are based primarily on DNS, not experiment [108]. Major strides were made early by Schloemer in 1966, who performed a novel experiment involving a half-cut airfoil section, which displaced a continually varying pressure gradient (adverse and then favorable downstream) onto a flat test wall [113]. Despite its age, this work is still considered the seminal work on pressure fluctuations in pressure gradient. Schloemer found that the impact of the pressure gradient on the spectra was complex; for example, adverse pressure gradient increased the spectral amplitude at low frequencies but decreased it at higher frequencies while the opposite was true in favorable pressure gradient. Schloemer also observed a strong decrease in pressure convection velocity in adverse pressure gradient flows and an increase in favorable.

In 1987, McGrath & Simpson showed that the spectra in zero and mild favorable pressure gradient both collapse at high frequency on viscous variables and fairly well at low and mid-frequencies on outer variables [87]. They also found that, while the coherence in the ZPG case was very nearly exponential in behavior, the favorable pressure gradient case showed a deviation from exponential behavior that was accounted for by Corcos' similarity parameter ($\omega\Delta x/U_c$) [35].

In 2021, Balantrapu *et al.* studied fluctuating pressure under a strong, axisymmetric turbulent boundary layer and found that the entire spectrum collapsed on outer variables [9]. This was attributed to extreme intensification of outer scale motions in the flow of interest as evidenced by hotwire measurements and was not considered a universally applicable finding.

Several experiments have been made investigating pressure fluctuations at the trailing edge of airfoils, a classic adverse pressure gradient case, due to the applicability to trailing edge noise (see, e.g., Catlett *et al.* 2016 [26]). Unfortunately, most of these works fail to sufficiently characterize the pressure gradient behavior of the flow so as to be more generally applicable (the work of Catlett *et al.* being an exception) and none consider the potential effects of favorable pressure gradient at the leading edge on the trailing edge spectra.

2.2.4 Roughness Effects

In 1970, William Blake studied the difference in the fluctuating wall pressure between smooth and rough walls using the smallest area sensors available at that time [15]. He independently varied the density and height of the considered rough surface in order to de-couple their effects on the wall pressure spectrum and found that roughness density has a large impact on the large scale, low frequency pressure imparting eddies while the height more impacted the mid- and high frequency regions of the spectra. The RMS pressure levels increased on the rough wall and were strongly dependent on the height of the roughness elements. Blake also proposed a new spectral scaling based on the roughness height as the primary length scale.

Aupperle & Lambert (1970) found that only the autospectral density was affected by roughness size; cross-spectra, coherence, and correlations were consistent across varying flow cases [8]. They also found that large scale, low frequency, pressure imparting structures ($L \gg k_s$) were largely

unaffected by the presence of roughness, with the exception that they decayed much faster than their smooth wall counterparts

Bhaganagar *et al.* (2007) performed extensive DNS of rough wall channel flows and found that the presence of roughness intensifies fluctuating pressure throughout the boundary layer and modifies the length scales implied by the 2-point correlation of pressure [14]. They also found that the definitions of the roughness sublayer based on velocity fluctuations and pressure fluctuations were very different, implying a potential decoupling of roughness effects on the velocity and pressure fields, at least very near the surface within the canopy.

Varano (2010) found that, for sparse rough flows, the friction and edge velocities are directly proportional, thus the edge velocity, which is more easily measured, can be used as an effective velocity scaling [127]. Forest (2012) proposed an alternate form of the viscous inner scaling that better collapses the high frequency region of rough wall pressure spectra based on a geometric combination of the traditional viscous scaling and the roughness Reynolds number [45]. He also observed that the spectrum in rough wall flows decays significantly faster, $\omega^{-4/3}$ in the mid-frequencies and ω^{-8} in the high frequency region. He postulated that there was, in fact, a universal overlap region in rough wall flows, which would follow a double-scaling rather than a triple, which would be needed in other non-equilibrium flows. Meyers *et al.* (2015) [91] improved on the high frequency scaling of Forest (2012) [45] by defining a viscous scaling that is adjusted for pressure drag on the roughness elements by defining an alternate form of the friction velocity that asymptotes to u_τ as the wall becomes smooth, demonstrated in Figure 2.14. The value of this alternate friction velocity was chosen *posteriori* in order to collapse the spectrum, however, since there are two degrees of freedom in the spectrum and velocity scaling affects only one, the subsequent collapse is considered to have strong physical meaning. Joseph (2017) confirmed this scaling and provided it with physical meaning and an *a priori* determination [67]. In addition, she postulated two low-frequency scalings, which are physically interpreted as showing that the pressure imparting eddies in the outer regions are driven and sustained by a defect velocity from the edge velocity. She also observed that the mid-frequency slope was largely determined by element density and that no universal overlap region exists.

Joseph also measured the surface pressure spectrum at the roughness canopy and found that such a spectrum exhibits smooth wall behavior [67]. This observation appears to indicate that spectral features that can be considered to be due to roughness effects are driven by the flow inside the canopy. Alternatively, this could be interpreted as a shift, k_s , in the wall-normal point at which the bulk pressure fluctuations are produced.

2.2.5 Modeling

Models for the turbulent wall pressure spectrum can be classified in two varieties: purely empirical and what will could be referred to as “semi-empirical” (meaning also semi-analytical). The first purely empirical model is that of Chase (1980) [27], expanded upon in 1987 [28]. This model fails to incorporate the high frequency roll-off of the point spectrum but has the advantage of incorporating the full wavenumber-frequency dependency, and captures both the acoustic cone and convective ridge behavior of the full spectrum for smooth, ZPG flows. Witting (1986) presented an interesting model based on the presence and behavior of coherent structures; bursts and sweeps

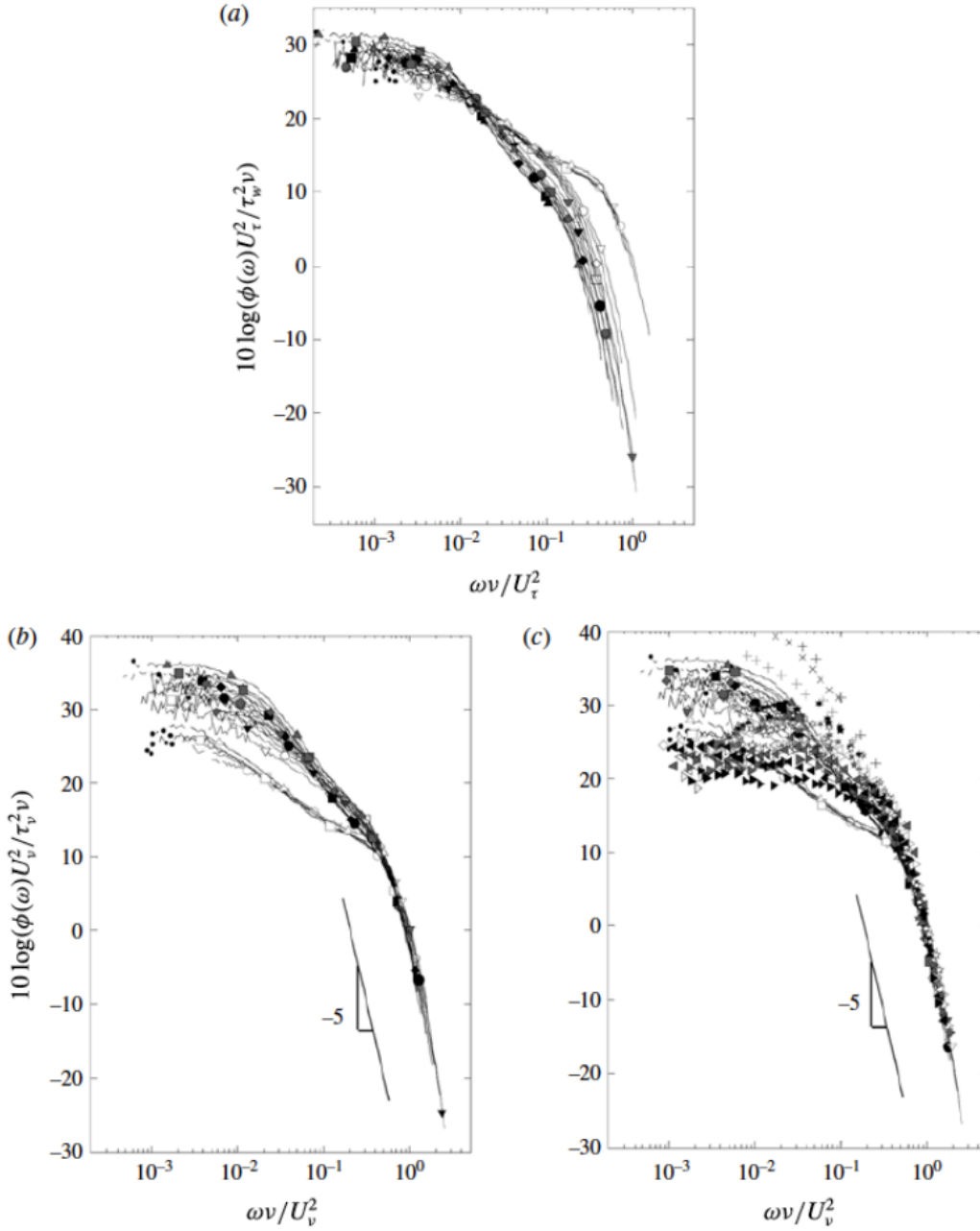


Figure 2.14: Wall pressure autospectral densities from both smooth and various rough walls scaled on classical viscous inner scaling (a) and the rough wall viscous scaling of Meyers *et al.* (2015) (b),(c) [91].

were modeled as dipole sources, which collectively generated the full pressure spectrum [139]. A similar structure-based model was proposed by Ahn *et al.* (2004) [3]. Early models were reviewed thoroughly by Graham (1997), from the perspective of cabin noise prediction, and he determined that these early models were generally not effective, particularly in the convective domain [55].

Perhaps the most well-known empirical pressure spectrum model is that of Goody (2004) [54]. Goody's model has repeatedly been confirmed to predict with good accuracy the fluctuating pressure spectrum for smooth, ZPG, equilibrium boundary layers. Goody's work spawned a variety of what could be called "Goody-Type" models, where the Goody Type Model is an empirical approximation of the shape of the wall pressure spectrum:

$$G_{pp}(\omega FS)SS = \frac{a(\omega FS)^b}{[i(\omega FS)^c + d]^e + [fR_T^g(\omega FS)]^h} \quad (2.78)$$

where SS is a spectral scaling, FS is a frequency scaling, and a - h are constants that are unique to each model. Models in the Goody-Type family include those of Howe (1998) [61], Rozenburg *et al.* (2012) [108], Kamruzzaman *et al.* (2015) [69], Catlett *et al.* (2016) [26], Hu & Herr (2016) (re-published as Hu 2018) [63], Hu (2017) [62], Lee (2018) [81], Hu (2018) [64], Catlett *et al.* (2022) [25], and Joseph *et al.* (2022) [68], all of which attempt to extend the Goody model to flows beyond the smooth wall zero pressure gradient. Unfortunately, the Goody spectrum proves fairly sensitive to changes in the constants; while it is possible to tune the model parameters to match empirically with varying flows, none of the aforementioned models have proven to be broadly applicable. The tuned parameters of the aforementioned models are shown in Tables 2.1-2.4.

Model	a	b	c
Howe [61]	2.0	2.0	2.0
Goody [54]	3.0	2.0	0.75
Rozenburg <i>et al.</i> [108]	$[2.82\Delta_{ZS}^2(6.13\Delta_{ZS}^{-0.75} + d)^e][4.2(\frac{\Pi}{\Delta_{ZS}}) + 1]$	2.0	0.75
Kamruzzaman <i>et al.</i> [69]	$0.45[1.75(\Pi^2\beta^2)^m + 15]$, $m = 0.5(\frac{H}{1.31})^{0.3}$	2.0	1.637
Catlett <i>et al.</i> Smooth [26]	$3.0 + \exp[7.98(\xi_{\Delta_{RC}} Re_{\Delta_{RC}})^{0.131} - 10.7]$	2.0	$0.912 + 20.9(\xi_{\delta} Re_{\delta}^{0.05})^{2.76}$
Hu (2017) [62]	3.1×10^{-9}	1.0	$1.5(1.169 \ln[H] + 0.642)^{1.6}$
Lee [81]	$\max[a_{Rozenburg}, (0.25\beta_{\theta} - 0.52)a_{Rozenburg}]$	2.0	0.75
Hu (2018) [64]	$(81.004d + 2.154) \times 10^{-7}$	1.0	$1.5h^{1.6}$
Catlett <i>et al.</i> Rough [25]	$3.0 + 1.028(k^+u^+)^{0.426}$	2.0	$0.75 + 0.059(k^+u^+)^{0.329}$
Joseph <i>et al.</i> [68]	$\frac{u_{\tau}}{U_e - \bar{U}} \frac{u_{\tau}}{u_{\nu}}$	2.0	$0.56(\bar{U}/U_e)^{-1.63}$

Table 2.1: a - c parameters for empirical Goody-style empirical models corresponding to Eq. 2.78.

Model	d	e	f
Howe [61]	0.0144	1.5	0.0
Goody [54]	0.5	3.7	1.1
Rozenburg <i>et al.</i> [108]	$4.76(\frac{1.4}{\Delta_{ZS}})^{0.75}[0.375e - 1]$	$3.7 + 1.5\beta_{\theta}$	8.8
Kamruzzaman <i>et al.</i> [69]	0.27	2.47	$1.15^{-2/7}$
Catlett <i>et al.</i> Smooth [26]	$0.397 + 0.328(\xi_{\Delta_{RC}} Re_{\Delta_{RC}}^{0.35})^{0.310}$	$3.872 - 19.3(\xi_{\delta} Re_{\delta}^{0.05})^{0.628}$	$2.19 - 2.57(\xi_{\delta} Re_{\delta}^{0.05})^{0.224}$
Hu (2017) [62]	0.07	$1.13/(1.169 \ln[H] + 0.642)^{0.6}$	$7.645(\sqrt{2/c_f})^g$
Lee [81]	$\max[1.0, d_{Rozenburg}]$	$3.7 + 1.5\beta_{\theta}$	8.8
Hu (2018) [64]	$10^{-5.8 \times 10^{-5} Re_{\theta} H - 0.35}$	$\frac{1.3}{h^{0.6}}$	$7.645\sqrt{2/c_f}^g$
Catlett <i>et al.</i> Rough [25]	$0.5 + 0.126(k^+u^+)^{0.317}$	3.7	$1.1 + 0.761(k^+u^+)^{0.368}$
Joseph <i>et al.</i> [68]	1.5	5.0	$(U_e - \bar{U})/u_{\nu}$

Table 2.2: d - f parameters for empirical Goody-style empirical models corresponding to Eq. 2.78.

Model	g	h	i
Howe [61]	0.0	0.0	1.0
Goody [54]	-0.57	7.0	1.0
Rozenburg <i>et al.</i> [108]	-0.57	$\min[3.0, (\frac{19}{\sqrt{R_T}})] + 7.0$	4.76
Kamruzzaman <i>et al.</i> [69]	-2/7	7.0	1.0
Catlett <i>et al.</i> Smooth [26]	$-0.5424 + 38.1(\xi_\delta H^{-0.5})^{2.11}$	$7.31 + 0.797(\xi_{\Delta_{RC}} Re_{\Delta_{RC}}^{0.35})^{0.0724}$	1.0
Hu (2017) [62]	-0.411	6.0	1.0
Lee [81]	-0.57	$\min[3.0, (0.139 + 3.104\beta_\theta)] + 7.0$	4.76
Hu (2018) [64]	-0.411	$1.169 \ln(H) + 0.642$	1.0
Catlett <i>et al.</i> Rough [25]	-0.57	7.0	1.0
Joseph <i>et al.</i> [68]	$-\frac{4}{7} - 0.24(\frac{k_g}{\delta})^{0.16}$	7.0	1.0

Table 2.3: g - i parameters for empirical Goody-style empirical models corresponding to Eq. 2.78.

Model	SS	FS
Howe [61]	$U_e/\tau_w^2\delta^*$	δ^*/U_e
Goody [54]	$U_e/\tau_w^2\delta$	δ/U_e
Rozenburg <i>et al.</i> [108]	$U_e/\tau_w^2\delta^*$	δ^*/U_e
Kamruzzaman <i>et al.</i> [69]	$U_e/\tau_w^2\delta^*$	δ^*/U_e
Catlett <i>et al.</i> Smooth [26]	$U_e/\tau_w^2\delta$	δ/U_e
Hu (2017) [62]	$u_\tau/(q^2 \times 1m)$	θ/U_e
Lee [81]	$U_e/\tau_w^2\delta^*$	δ^*/U_e
Hu (2018) [64]	$u_\tau/q^2\theta$	θ/U_e
Catlett <i>et al.</i> Rough [25]	$U_e/\tau_w^2\delta$	δ/U_e
Joseph <i>et al.</i> [68]	$\overline{U}/(U_e - \overline{U})^4 \rho^2 \delta$	δ/\overline{U}

Table 2.4: Scalings for empirical Goody-style empirical models corresponding to Eq. 2.78.

Semi-empirical or fully analytical modelling is far more desirable, but the former proves difficult and the latter impossible, due to the complexity of generating solutions to the pressure Poisson equation. Most semi-empirical models are based on the equations presented in Section 2.2.1 Early researchers (e.g., Kraichnan 1956 [75], Panton & Linebarger 1974 [98]) attempted to derive the fundamental nature of the wall pressure from the pressure Poisson equation, but their efforts were stymied by the lack of general turbulence modelling ability of their time. In modern research, semi-empirical models for the wall pressure spectrum are obtainable if a model is known or can be obtained for the spectrum of fluctuating wall normal velocity, ϕ_{22} , which started largely in the TNO-Blake style modelling, originally put forth by Blake (1986) [16] and later implemented successfully by Parchen (1998) [99] of the TNO Institute of Applied Physics.

Lee *et al.* (2005) estimated ϕ_{22} from the empirical formulation of Chase (1980) [27] and the experimental data of Farabee (1986) [40] and then accounted for the anisotropy of these formulations by averaging the anisotropy factors from the smooth wall data of Klebanoff and the rough wall data of Corssin as taken from Hinze (1975) [60]. Peltier & Hambric (2007) [100] estimated the ϕ_{22} term

by applying Gavin's (2002) [52] Simplified Anisotropic Model (SAM) for the covariance of velocity. Fischer *et al.* (2017) [42] proposed an improvement of the TNO-Blake model by making different assumptions than Blake (1986) [16] when developing their model for ϕ_{22} ; Blake (and Parchen) used the von Kármán spectrum [130], but Fischer expanded the correlation behavior of the PPE solution using equations developed by Kraichnan [75].

2.3 Computational Fluid Dynamics

2.3.1 Theory and RANS Turbulence Modelling

The governing equations of fluid dynamics are the Navier-Stokes equations, elegant re-statements of the classical conservation laws of mass, momentum, and energy as they apply to a purely fluid system:

$$\begin{aligned} \frac{\partial \rho}{\partial t} + \frac{\partial(\rho u_i)}{\partial x_i} &= 0 \\ \frac{\partial(\rho u_i)}{\partial t} + \frac{\partial}{\partial x_j}(\rho u_i u_j) &= -\frac{\partial p}{\partial x_i} + \frac{\partial t_{ij}}{\partial x_j} \\ \frac{\partial}{\partial t}[\rho(e + \frac{1}{2}u_i^2)] + \frac{\partial}{\partial x_j}[\rho u_j(h + \frac{1}{2}u_i^2)] &= \frac{\partial}{\partial x_j}(u_i t_{ij}) - \frac{\partial q_j}{\partial x_j} \end{aligned} \quad (2.79)$$

Here, e is the internal energy, $h = e + p/\rho$ is the enthalpy, q_j is the heat flux, and t_{ij} is the stress tensor:

$$t_{ij} = \mu \left(\frac{\partial u_i}{\partial x_j} + \frac{\partial u_j}{\partial x_i} - \frac{2}{3} \frac{\partial u_k}{\partial x_k} \delta_{ij} \right) \quad (2.80)$$

Spatially and temporally resolved simulations of these equations (referred to as Direct Numerical Simulations or DNS) are possible, from a numerical algorithm standpoint, but they are sufficiently computationally expensive as to be completely impractical in an industry setting. Commercial and government solvers predominantly solve the steady, Reynolds Averaged Navier-Stokes (RANS) equations instead, which require that the impact of turbulence be modelled. After performing a Reynolds average, Eq. 2.79 reduces to:

$$\begin{aligned} \frac{\partial \bar{\rho}}{\partial t} + \frac{\partial}{\partial x_i}(\bar{\rho} U_i) &= 0 \\ \frac{\partial \bar{\rho} U_i}{\partial t} + \frac{\partial \bar{\rho} U_i U_j}{\partial x_j} &= -\frac{\partial \bar{P}}{\partial x_i} + \frac{\partial}{\partial x_j}[\bar{T}_{ij} - \overline{\rho u'_i u'_j}] \\ \frac{\partial}{\partial t}[\bar{\rho}(E + \frac{1}{2}(U_i^2 + \rho u_i'^2))] + \frac{\partial}{\partial x_j}[\bar{\rho} U_j(H + \frac{1}{2}(U_i^2 + \rho u_i'^2))] &= \frac{\partial}{\partial x_j}[-q_{Lj} - \overline{\rho u'_j h'} + t_{ij} u'_i - \frac{1}{2} \overline{\rho u_i'^2 u'_j} + U_i(\bar{T}_{ij} - \overline{\rho u'_i u'_j})] \end{aligned} \quad (2.81)$$

Here, capital letters and overbars denote averaged quantities. Thus, the turbulent fluctuation of the velocity has been confined to a single term and the stress in the fluid is now captured in the mean strain rate tensor:

$$T_{ij} = \mu \left(\frac{\partial U_i}{\partial x_j} + \frac{\partial U_j}{\partial x_i} - \frac{2}{3} \frac{\partial U_k}{\partial x_k} \delta_{ij} \right) \quad (2.82)$$

and the Reynolds stress tensor:

$$\tau_{ij} = -\overline{\rho u'_i u'_j} \quad (2.83)$$

The primary challenge of RANS is the prediction of the Reynolds stress tensor, Eq. 2.83. Most turbulence models rely on the Boussinesq linear eddy viscosity hypothesis, which states that the effect of turbulence on a flowfield is analogous to an increase in effective viscosity, such that $\mu = \mu_L + \mu_T$, where L and T refer to laminar and turbulent respectively [20]. Further, Boussinesq purports that the Reynolds stress tensor is linearly related to this turbulent viscosity, such that:

$$\tau_{ij} = \mu_T \left(\frac{\partial U_i}{\partial x_j} + \frac{\partial U_j}{\partial x_i} - \frac{2}{3} \frac{\partial U_k}{\partial x_k} \delta_{ij} \right) - \frac{2}{3} \rho k \delta_{ij} \quad (2.84)$$

Thus, it is possible to model the effects of turbulence on the flow if we have equations for the turbulent viscosity, μ_T , and kinetic energy, k . The majority of turbulence models utilize two transport equations, one for k and one for some other representative variable, the combination with k of which reveals μ_T . The most common variable used in the second transport equation is the turbulent dissipation rate, ϵ . The primary drawback of k - ϵ models is they are known to have numerical issues very near the wall in boundary layer flows, as the ratio of ϵ to k becomes very large. A common solution to this problem is to instead model the transport of the specific dissipation rate, $\omega = \epsilon/C_\mu k$ (where C_μ is a constant). Unsurprisingly, k - ω models have opposing pros and cons to k - ϵ models, performing well near the wall but suffering when modeling free-stream turbulence, free-shear layers, and jets. The most common two-equation model used today is the Menter Shear Stress Transport (SST) model, which balances the strengths of both k - ϵ and k - ω models by employing a blending function that transitions the model from k - ω at the wall to k - ϵ when far from it [90]. The other most common model employed in industry today is the Spalart-Allmaras model [119]. The SA model is a single transport equation for an effective working variable, $\tilde{\nu}$, which is related directly to both μ_T and τ_{ij} , eliminating the need for k . A good review of commonly used turbulence models is given by Catalano & Amato (2003) [24].

For the purposes of this discussion, we want to approach the problem of turbulence modelling from the standpoint of the problem we wish to solve, that is, how RANS could be used to predict the fluctuating wall pressure spectrum. Recall from Section 2.2.1 that our ability to predict the pressure spectrum is entirely dependent on our ability to predict the spectrum of wall normal velocity, ϕ_{22} . For now, let us focus on the modelling of ϕ_{22} , which will eventually bring us back to a discussion of RANS modelling. The first, and most commonly cited model for the velocity spectrum is the von Kármán spectrum (1948) [130]. A generalized form of this spectrum is given by Wilson (1997) [138]:

$$\phi_{22}(k, x_2, x'_2) = \frac{\sqrt{u_2'^2(x_2)u_2'^2(x'_2)} l^4 k^2 \zeta^{\nu+2}}{\Gamma(\nu) \pi 2^{\nu+1} (1 + l^2 k^2)^{\nu+2}} K_{\nu+2}(\zeta) \quad (2.85)$$

$$\zeta = \frac{|x_2 - x'_2|}{l} \sqrt{1 + l^2 k^2} \quad (2.86)$$

where K is the Bessel K function. The beauty of this formulation is the tuning parameter, ν , which makes the spectrum form generalized. Setting $\nu = 1/3$ results in the original von Kármán spectrum and choosing $\nu = 1/2$ results in the spectrum of Liepmann *et al.* (1951) [83]. According to Grasso *et al.* (2019), setting $\nu = 7/6$ results in a spectrum that matches well with predictions from Rapid Distortion Theory [57]. This spectrum tells us what we need from our RANS solver in order to estimate the fluctuating pressure spectrum. First, we need the specific wall normal Reynolds stress, $\overline{u_2'^2}$. Typically, this is found from a RANS solution using the Boussinesq approximation (Eq. 2.84) [20]. Setting $i = j = 2$:

$$\overline{u_2'^2} = \frac{2}{3}k - 2\frac{\mu_T}{\rho}\frac{\partial U_2}{\partial x_2} \quad (2.87)$$

However, it is well known that, while eddy viscosity models are decent at predicting over-all turbulent effects, Eq. 2.87 is a poor, effectively isotropic prediction of the wall-normal Reynolds stress component. Accounting for the anisotropy of the Boussinesq equation is one of the remaining challenges in effective pressure spectrum modeling.

There are also alternatives to the eddy viscosity hypothesis; first, it is possible to model the transport of the Reynolds stress tensor components directly, known as Reynolds Stress Transport Modelling (RSTM) (see, e.g., Launder *et al.* 1975 [79], Launder 1989 [78]), though this is not an option typically used in industry, as RSTM is more computationally expensive than RANS and, if extra computational power is available, one would typically use it to move from RANS to Large Eddy Simulation (LES). Second, there are other ways to estimate the Reynolds stress other than the Boussinesq approximation, although they are confined mostly to research rather than industry at this time, for example the Quadratic Constitutive Relation (QCR) Reynolds stress modelling technique (see, e.g., SAQCR2000 [121]).

The second thing we need to pull from our RANS model is an estimate for the length scale:

$$l = \frac{1}{k_e} = \Lambda \frac{\sqrt{\pi}\Gamma(v+1/2)}{\Gamma(v)} \quad (2.88)$$

Properly estimating the longitudinal integral length scale remains one of the most difficult aspects of semi-empirical pressure spectra modelling. Formally, it is defined:

$$\Lambda = \int_{-\infty}^{\infty} \rho_{uu}(x, \xi) d\xi \quad (2.89)$$

where ρ_{uu} is the two-point correlation coefficient and ξ is the separation between the two points. Correlations are not obtainable from a RANS solution, and so the length scale too must be modelled. Integral length scales can be estimated from the turbulence model, e.g., for k - ϵ models:

$$\Lambda = C_\mu^{\frac{3}{4}} \frac{k^{\frac{3}{2}}}{\epsilon} \quad (2.90)$$

or for k - ω models:

$$\Lambda = C_\mu^{-\frac{1}{4}} \frac{\sqrt{k}}{\omega} \quad (2.91)$$

where $C_\mu = 0.09$. There are also a variety of proposed length scales in the literature, e.g. Michel (1968) [92], Wilcox (1993) [133], Kamruzzaman *et al.* (2011) [70], and Lane *et al.* (2021) [77], just to name a few. Which of these length scales may be a valid model for the pressure spectrum length scale has yet to be truly assessed anywhere in the literature.

2.3.2 Roughness Modelling

It is neither efficient nor effective to include roughness geometry in a CFD grid; instead, roughness is typically applied as a boundary condition on the wall of interest. The question of how this boundary condition is applied is one still up for major debate. As described by Wilcox (2006) [134], the general principle is this: the user inputs some parameters that represent the roughness and the solver uses those parameters to enforce the Δu^+ that corresponds with that roughness by correlating the $\Delta u^+ \propto k^+$ relationship to turbulence model parameters. The simplest roughness function is to simply query the user for the equivalent sandgrain roughness, k_s , and use the relationship of Nikuradse (1950) [94], Schlichting (1979) [112] or similar to convert to Δu^+ . This is effective, and such schemes match experimental data well, but it is self-fulfilling. If the user already knows k_s , and by extension Δu^+ , why are they calculating this case? Additionally, such "wall-function" simulations produce less data fidelity than a fully resolved simulation and are known to break down in pressure gradient [118]. It would be far more practical to query the user for parameters representing the pure geometry of the roughness, perhaps k_g and λ , for instance, and calculate the roughness effect from there. This relies on the existence a good, universal roughness correlation function, something that is currently lacking in the literature. Roughness correlation functions do, of course, exist, as discussed in Section 2.1.4, but they are derived from flat plates in zero pressure gradient with homogeneous roughness patterns.

For wall-resolved simulations, the equivalent sandgrain roughness is instead correlated to the turbulence model parameters at or near the wall. The most well-known of these models is the Wilcox (1988, updated 2006) model for k - ω models [132, 134]. The Wilcox model correlates the roughness height to the specific dissipation rate at the wall:

$$\omega_{wall} = SR(k^+) \frac{\rho u_\tau^2}{\mu} \quad (2.92)$$

Recall from Section 2.3.1 that $\omega = \epsilon/C_\mu k$. The no-slip condition implies that $k_{wall} = 0$, which implies that $\omega_{wall} = \infty$. Computers do not handle infinite values, so the typical practice for a smooth wall k - ω simulation is to set ω_{wall} to some arbitrary, very large value. Thus, the philosophy behind Wilcox's model is to reduce this value, which will decrease the dissipation of near wall turbulence, increasing the kinetic energy in this region and simulating the effects of roughness. The Wilcox model is known to correlate well for moderate roughness Reynolds numbers, but has been shown to break down at high k^+ [7, 73]. Knopp (2009) proposed adding an additional $k_{wall} \neq 0$ boundary condition to continue the increase of turbulent kinetic energy near the wall to

higher values of k^+ [73]. Aupoix (2014) proposed abandoning the boundary condition in favor of an enforced value of ω^+ in the cell-center of the first cell from the wall [7]. Both of these models have shown better high k^+ behavior for k - ω simulations than the original Wilcox formulation.

The one-equation Spalart-Allmaras model also has a roughness modification, which alters the effective wall distance, $\tilde{\nu}$ source term, and $\tilde{\nu}$ wall boundary condition to simulate the effect of roughness on the flow.

The struggles of roughness modelling are described well by Apsley (2007) [5] and Song *et al.* (2020) [118]. In essence, our current methods for computing flows over rough walls are sorely lacking, particularly for flows with varying roughness and pressure gradients.

2.4 Summary of Literature

A wide range of papers covering several relevant topics have been reviewed. Despite a wide body of literature investigating boundary layer flows, there is a lack of consensus on the precise effects of non-equilibrium pressure gradient, pressure gradient history, and roughness on boundary layer behavior. Adverse pressure gradient increases boundary layer thickness and turbulence intensity, as does roughness in zero pressure gradient, while favorable pressure gradient confines and relaminarizes the flow. The effect of varying or switching pressure gradient signs and magnitudes is less well understood, but it is known that the flow is dependent on variation of the pressure gradient upstream.

Turbulence in the boundary layer imparts a distinctive three-region spectrum of fluctuating pressure onto the immersed surface. The high frequency portion of this spectrum is known to be fully described by viscous variables (i.e., μ and u_τ), while (in zero pressure gradient) the low frequency region is described by outer region variables (e.g., U_e and δ). The effect of pressure gradient on the spectrum is not straightforward; effecting different regions in different ways, though it is known that the universality of the high frequency viscous behavior holds. Roughness increases the peak of the spectrum in correspondence with the increasing turbulent energy in the overlying flow, while the high frequencies still collapse on a modified viscous scaling.

A variety of empirical models for the spectrum exist that are known to predict well for smooth wall, zero pressure gradient flows, but struggle to capture pressure gradient and roughness effects. Analytical modeling could potentially improve predictive capability in these regimes, but the form of analytical models relies on either high fidelity knowledge of the flow behavior (that is prohibitively expensive with the current state-of-the-art in flow modeling) or further sub-models to close the model, the form of which is unsettled.

Successful implementation of any given model for the surface pressure spectrum would rely on knowledge of the overlying boundary layer behavior. The ability of current RANS models to predict non-equilibrium pressure gradient and roughness effects is in doubt, and this capability is a prerequisite for successful prediction of the inputs required for pressure spectrum modeling.

There are four primary gaps in the literature that should be addressed: 1) an understanding of the effects of non-equilibrium pressure gradient on the surface pressure spectrum, 2) an understanding of

the combined effects of roughness and pressure gradient on the surface pressure spectrum, 3) robust and accurate models for the spectrum under the effects of roughness and/or pressure gradient, and 4) robust and accurate prediction methods/protocols for the requisite input variables for the models in point 3.

Chapter 3

Fluctuating Pressure Beneath Smooth Wall Boundary Layers in Non-Equilibrium Pressure Gradients

This chapter includes a manuscript published in *AIAA Journal* that presents the setup and results for a wind tunnel experiment studying smooth wall boundary layers in pressure gradients and their underlying pressure spectra.

Attributions

Daniel J. Fritsch is the primary contributor and first author. All figures and text are his original work, except where noted by citation.

Vidya Vishwanathan partnered in the design and setup of the experiment as well as collecting and processing the data.

K. Todd Lowe and William J. Devenport secured the funding for this work and advised the data collection and analysis and writing.



Fluctuating Pressure Beneath Smooth Wall Boundary Layers in Nonequilibrium Pressure Gradients

Daniel J. Fritsch,* Vidya Vishwanathan,[†] K. Todd Lowe,[‡] and William J. Devenport[§]
Virginia Tech, Blacksburg 24060, Virginia

<https://doi.org/10.2514/1.J061431>

An experimental investigation is made of smooth wall turbulent boundary layers under a family of continually varying streamwise pressure gradient distributions. In general, the effects of these pressure gradient cases on the boundary layer are found to be nonlocal and dependent on upstream history effects. However, the friction Reynolds number grows independent of applied pressure gradient and appears to be dependent only on the origin of the turbulent boundary layer. Special attention is paid to the statistics of the fluctuating pressure on the immersed surface, and it is found that there is a spectral-region-dependent relationship between pressure gradient and the fluctuating wall pressure, indicating the lack of a universal overlap region and providing insight into the impact of pressure gradient history on turbulence evolution. The classical viscous inner scaling of the pressure spectra appears universal as does a proposed mixed variable low-frequency scaling. The impact of the pressure gradients on the pressure space-time correlations and convection velocities is more locally dependent. The implications of these observations on our understanding of nonequilibrium flows are explored, and it is postulated that such flows may be describable as a three-dimensional space governing the mean growth, pressure gradient effect, and nonequilibrium effect, respectively.

Nomenclature

c_f	=	skin friction coefficient
c_p	=	pressure coefficient
f	=	time frequency, Hz
G	=	defect shape factor, $(1 - 1/H)/(u_\tau/U_e)$
G_{pp}	=	autospectral density of pressure, (f) Pa ² /Hz, (ω) Pa ² · s/rad
H	=	shape factor, δ^*/θ
h	=	tunnel height, 1.85 m
K	=	acceleration parameter, $(\nu/U_e^2)(dU_e/dx)$
p	=	pressure, Pa
q	=	dynamic pressure, $1/2\rho U_e^2$, Pa
Re	=	Reynolds number
T	=	temperature, K
U_c	=	convection velocity, m/s
U_{cb}	=	broadband convection velocity, m/s
U_e	=	edge velocity, m/s
u	=	velocity, m/s
u_τ	=	friction velocity, m/s
u^+	=	viscous normalized velocity, u/u_τ
x	=	streamwise coordinate, m
y	=	wall normal coordinate, m
y^+	=	viscous normalized wall distance, yu_τ/ν
β	=	Clauser parameter, $(\delta^*/\tau_w)(dp/dx)$
δ	=	boundary-layer thickness, m
δ^*	=	displacement thickness, m
θ	=	momentum thickness, m
ν	=	kinematic viscosity, m ² /s

ξ	=	spanwise separation, m
Π	=	Coles wake strength parameter
ρ	=	density, kg/m ³
ρ_{pp}	=	pressure correlation coefficient
τ	=	time delay, s
τ_w	=	wall shear stress, Pa
ω	=	frequency, rad/s

I. Introduction

TURBULENT boundary layers (TBLs) are present in effectively all vehicles and practical applications involving fluid flow over solid bodies. Turbulence in the boundary-layer region causes the pressure on the immersed surface to fluctuate over a wide range of amplitudes and time and length scales, radiating noise to the far field and potentially exciting resonant frequencies in the structure of the solid body, generating fatigue.

As such, fluctuating pressure under laboratory boundary-layer flows, mainly flat, smooth, zero pressure gradient (ZPG), equilibrium TBLs, has been a major focus of study since as early as the 1950s and is fairly thoroughly documented. One of the first comprehensive reviews of TBL fluctuating pressure theory was given by Lilley and Hodgson, at which point the bridge between experimental data and theory was just beginning to be crossed [1]. At this time, the shape of the wall pressure spectrum was understood to be of two regions: a low-frequency region of positive slope and a high-frequency region of negative slope. In the early 1960s, fluctuating pressure transducers made major leaps forward, revolutionizing the study of turbulent pressure fluctuations. For the first time, sensors had the spatial and temporal resolution to correctly capture the high-frequency portion of the surface pressure spectrum, revealing a three-region spectrum with a high-frequency roll-off. Corcos observed that the inner region of the boundary layer is largely free of pressure sources and thus may have no impact on the turbulent wall pressure [2]. It was later determined by Panton and Linebarger in 1974 that, in actuality, the inner region of the boundary layer is largely responsible for the high-frequency portion of the spectrum and that the lack of pressure sources in this region means that the high-frequency spectra are driven by dissipation due to viscosity, and thus will be universal when scaled on viscous variables with a slope of ω^{-5} [3]. This observation has been confirmed by many authors and is considered a cornerstone of our understanding of turbulence-induced fluctuating pressure [4].

Much work since has focused on determining the functional dependencies of the spectrum to various flow variables and the

Received 4 November 2021; revision received 17 February 2022; accepted for publication 14 April 2022; published online 16 May 2022. Copyright © 2022 by The Authors. Published by the American Institute of Aeronautics and Astronautics, Inc., with permission. All requests for copying and permission to reprint should be submitted to CCC at www.copyright.com; employ the eISSN 1533-385X to initiate your request. See also AIAA Rights and Permissions www.aiaa.org/randp.

*Graduate Research Assistant, Crofton Department of Aerospace and Ocean Engineering; dannyf96@vt.edu. Student Member AIAA (Corresponding Author).

[†]Graduate Research Assistant, Crofton Department of Aerospace and Ocean Engineering. Student Member AIAA.

[‡]Professor, Crofton Department of Aerospace and Ocean Engineering. Associate Fellow AIAA.

[§]Professor, Crofton Department of Aerospace and Ocean Engineering. Fellow AIAA.

relationship between these and the observable statistics of the pressure fluctuations, e.g., Chase [5], Choi and Moin [6], or Farabee and Casarella [7]. The work to this point is thoroughly reviewed by Bull [4], and paints the following picture: the spectral density of fluctuating pressure presents as a three-region spectrum, a low-frequency region ($\omega\delta^*/U_e < 0.3$) of positive slope ending in a peak amplitude and transition to negative slope, which scales on outer variables; a high-frequency region ($\omega\nu/u_\tau^2 > 0.3$) of steeply negative slope approximately ω^{-5} , which scales on viscous variables; and midfrequency overlap region, which scales on both inner and outer variables and has a slope of ω^{-1} , though some authors dispute the exact value, claiming it is more on par with $\omega^{-0.8}$. More modern studies have pushed these observations to higher Reynolds numbers with a corresponding increased scale separation [8,9]. As Reynolds number (scale separation) increases, the extent of the midfrequency region grows, creating a more distinctive three-region spectrum as the entire spectrum shifts to higher amplitudes and frequencies.

Several models have been proposed that describe the dependency of the pressure spectrum on flow characteristics, starting with that of Chase [5]. A review of early models is provided by Graham [10], at which time modeling efforts struggled to properly capture the convective behavior. Perhaps the most well-known pressure spectra model is that of Goody [11], which empirically describes the shape of the autospectral density and shows good agreement with ZPG equilibrium boundary-layer datasets. Some efforts have been made to derive a fundamental model from first principles [12,13], but significant challenges remain.

Lacking in the majority of the studies listed above is consideration of real-world, nonidealized conditions such as curvature, pressure gradient, or roughness. One or more of these effects are present in most practical applications and should impact the development of the TBL. Several studies have focused on the impact of strong adverse pressure gradients (APGs) [14–17] and have found that APG expands the boundary layer, increases turbulence intensity (particularly of the outer scale motions), and pushes the boundary layer toward separation. Schatzman and Thomas proposed that, in pressure gradients of sufficient magnitude, APG caused the formation of a secondary shear layer, the location of which serves as an important scaling for the boundary-layer behavior [17], an observation also made by Balantrapu et al. [18].

However, pressure gradient effects on the fluctuating wall pressure have rarely been studied experimentally. In 1966, Schloemer performed a study of TBL pressure fluctuations in the presence of mild favorable and APGs and found that, in general, the strength of low-frequency fluctuating pressure increases in APG and decreases in favorable pressure gradient (FPG) while having negligible impact on high-frequency content, which appeared universal under viscous scaling regardless of applied pressure gradient [19], an observation that was later repeated by McGrath and Simpson [20]. Schloemer also observed that pressure convection velocity increases in FPG and decreases in APG [19].

Relatively few studies have considered favorable pressure gradients, flows of nonconstant or mixed pressure gradient character, or the effect of pressure gradient history. Bobke et al. studied history effects in TBLs and observed that the friction Reynolds number, $\delta^+ = \delta u_\tau/\nu$, grows independently of applied pressure gradient where no other measured parameters did, but did not consider favorable pressure gradients or the fluctuating wall pressure [21]. Hu and Erbig observed history effects on pressure spectra; however, their concern was primarily in the effect on sensor resolution and correction rather than the implications to the fundamental flow physics [22]. Similarly, several models have been proposed for pressure spectra under APGs [23–26], but none consider the effects of FPG or the possible history effects that would make the spectra dependent on more than local conditions.

A flow that has dependencies beyond the local conditions may be considered to be not in a state of “equilibrium.” As described by Bradshaw and Ferris, in a purely mathematical sense, an equilibrium flow is one in which the convective terms of the turbulent transport equation are negligible—information is not convecting in the flow and the properties will be dependent only on local conditions [27].

This is a valid description of a fully developed pipe or channel flow but will almost never be the case for an external boundary-layer flow due to growth, entrainment, and three-dimensionality. In boundary-layer flows, a more practical definition of equilibrium is a flow that exhibits self-similarity in the mean flow and turbulence structure. It is generally agreed upon that a prerequisite for equilibrium in boundary-layer flows is a constant nondimensional pressure gradient:

$$\beta = \frac{\delta^*}{\tau_w} \frac{dp}{dx} \quad (1)$$

This follows from the analysis of Clauser, who showed that if the pressure gradient term of the integral momentum equation was constant, the development of the boundary layer became a simple linear relationship relating the wall shear stress to boundary-layer growth [28]. Thus, it can be assumed that in a boundary-layer flow in which β is not constant there will be observable nonequilibrium or history effects that must be quantified in order to understand the underlying physics of such a flow case.

A possible measure of the deviation from equilibrium of a given flow is given by Mellor and Gibson [29], who showed that for a range of equilibrium boundary-layer flows, there was a universal correlation between the Clauser parameter and the defect shape factor:

$$G = \frac{1 - 1/H}{u_\tau/U_e} = G(\beta) \quad (2)$$

Thus, the deviation of a boundary-layer flow from equilibrium could be quantified by how far off the equilibrium curve it lies.

This work explores the effects of a systematic family of mean pressure gradient flow cases, involving APG and FPG as well as both characters in the same flow case, on low Mach number, high Reynolds number, smooth wall TBLs. The development of the boundary-layer family will be investigated in order to understand the effects of the varied pressure gradient cases, both local and historical. A key point of discussion will be the impact of these pressure gradients on the fluctuating surface pressure beneath the boundary layer. In Sec. II, the flow cases and the methods used to investigate them will be described in detail. Results will be presented and discussed in Sec. III, and finally conclusions will be drawn in Sec. IV.

II. Methods

A. Experimental Setup

Experiments were performed in the Virginia Tech Stability Wind Tunnel (VTSWT). As described by Devenport et al. [30], the VTSWT is a closed-circuit, subsonic wind tunnel with 1.85 m \times 1.85 m \times 7.32 m test section and 9:1 ratio contraction, powered by a 0.45 MW motor driving a 4.3-m-diam fan, capable of producing freestream test section speeds of up to 80 m/s, or a Reynolds number of 5 million per meter. The freestream turbulence levels are low, 0.020% at 20 m/s and 0.031% at 57 m/s, and the inflow is uniform across the inlet area due to the installation of turbulence screens and a contraction liner for flow quality improvement [31].

A 0.914 m chord NACA0012 airfoil model is installed in the geometric center of the test section, spanning the full 1.85 m height. The function of the model is to displace continually varying pressure distributions onto the side walls of the test section, where the boundary layers of interest will grow, via the balancing of lift, drag, and blockage produced by the model. The leading edge of the model has a 0.5-mm-high zigzag tape boundary-layer trip at 5% chord to ensure that the airfoil boundary layer is fully turbulent, delaying separation and allowing the model to be pushed to higher angles of attack, expanding the generated flow regimes.

The test section-model system is shown in Fig. 1. The coordinate system is defined such that $x = 0$ at the junction between the test section and contraction and is positive in the flow direction, $y = 0$ at the surface of the port side wall (left when standing in the test section looking upstream toward the contraction) and points normal to the surface into the tunnel, and $z = 0$ at the geometric spanwise center of the port wall, equally 0.925 m from the floor and ceiling, and points

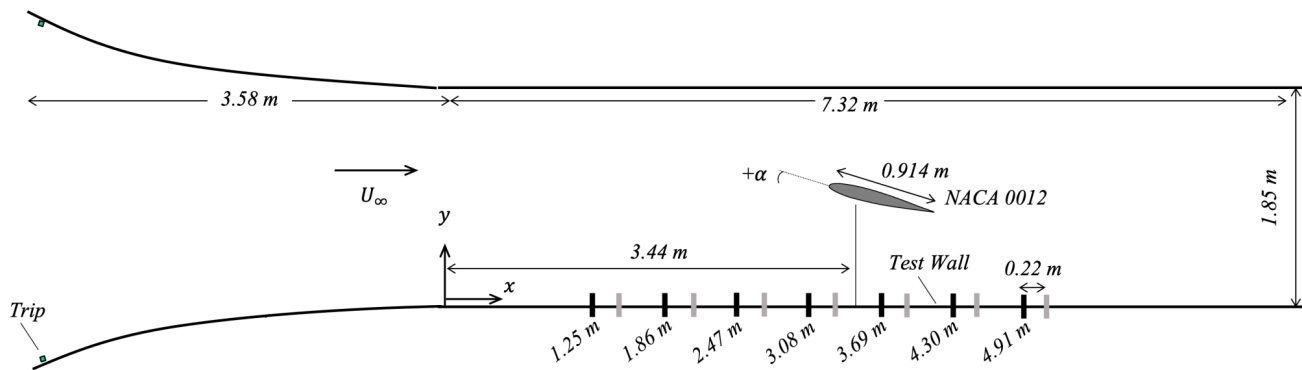


Fig. 1 Top-down view of test section with NACA0012 model installed showing coordinate system, major dimensions, and locations of boundary-layer trip and model quarter chord. Black stations correspond to boundary-layer rake measurements, and gray to the origins of the linear microphone array.

up as per the right-hand-rule about the x and y axes. In this coordinate system the quarter chord of the airfoil model, which is its axis of rotation, is located at $x = 3.44$, $y = 0.925$ m. The airfoil angle of rotation is defined by the right-hand rule about the negative z axis, such that positive angles of attack produce positive lift in the positive y direction.

To ensure that the tested boundary layer is fully turbulent and free of step effects, the boundary layer on all four walls is tripped in the contraction at $x = -3.58$ m, where the contraction to test section area ratio is 1.66. The contraction trip is a zigzag pattern 3.18 mm high and 20.39 mm wide in the streamwise direction, and it has 27.6° angle in the pattern. The first boundary-layer measurements are taken at $x = 1.25$ m, 1500 trip heights downstream, sufficient to ensure the lack of step effects in the boundary-layer turbulence.

The boundary-layer wall is a modular hard wall consisting of twenty-seven 2 ft \times 2 ft (0.61 m \times 0.61 m) aluminum panels in a 3×9 array, pictured in Fig. 2 and designed and documented by Duetsch-Patel et al. [32]. The leading edge of the first panel is located at $x = 1.11$ m. Each panel in the array is, by default, instrumented with an array of 1.0-mm-diam static pressure taps as shown in the orange dots in Fig. 2 but can be swapped for any compatible 2 ft \times 2 ft panel, enabling a wide variety of instrumentation to be equipped. Steps and gaps between panels were a concern during experimental setup; a protocol was developed by which the steps between panels were smoothed by shimming behind each panel until the step between the panels read zero on a micrometer with a resolution of $1/1000$ in. = 0.0254 mm. With this uncertainty, the wall is considered smooth to within a $y^+ \approx \pm 4$ at a freestream velocity of 35 m/s. Gaps between panels were sealed with 40- μ m-thick tape (40 μ m $\approx y^+ = 7$ at 35 m/s). The effects of panel steps in the wall were thoroughly documented by Duetsch-Patel et al. [32] by observing the effect of systematically varied panel step height on the velocity profile and corresponding displacement thickness at the measurement location, 3.5 in. (88.9 mm) downstream of the panel

edge, and it was concluded that an uncertainty of $y^+ \approx \pm 7$ in the smoothness at the leading edge of the panel had negligible impact on boundary-layer measurements made on the panel as it resulted in the measurement location being greater than 2500 step heights downstream in the worst-case scenario and was typically on the order of >5000 step heights.

B. Mean Parameters

Mean static pressure measurements are made on both test section side walls, all four contraction walls, and the airfoil surface. Each 1.0 mm pressure tap is connected via Tygon tubing to a 4'' H₂O DTC Initium ESP 32-HD or 10'' H₂O Esterline 9816 (walls), 20'' H₂O DTC Initium 64 HD (contraction), or 2.5 psi Esterline 9816 (airfoil) pressure transducer. For each test run, mean pressures were taken in all taps and averaged over 25 records, where each record is the average of samples acquired at 600 Hz for 0.94 s. Mean pressure coefficients on the walls were then corrected in a two-step process, involving a previous measurement of the c_p distribution in the empty tunnel. This calibration is necessary due to a repeatable bias error observed in each individual tap associated with small imperfections in its shape and installation. First, the empty tunnel c_p values for each tap were subtracted from the raw data in order to eliminate this bias error from individual probes. However, this assumes that each tap ought to read nominally zero in the empty tunnel case, which is not true due to the growth of the boundary layers on the four walls of the test section acting as a pseudocontraction and imparting a small dc_p/dx . This dc_p/dx is quantified from the empty tunnel data and added back into the experimental data.

Mean tunnel freestream velocity at the inlet was calculated by comparing static pressure measurements made in the contraction and settling chamber at approximately $x = -2.07$ m and $x = -10$ m, respectively, and applying a calibration factor determined from a previous calibration experiment involving a Pitot-static measurement made in the test section geometric center.

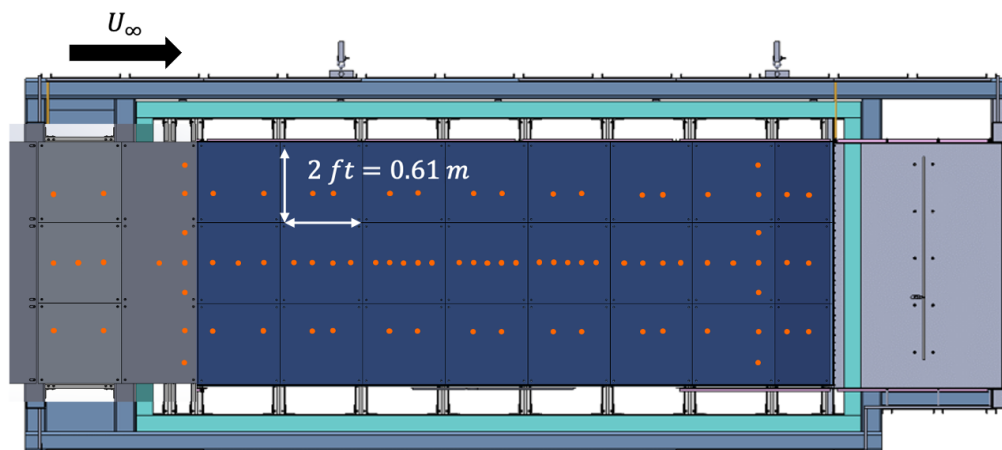


Fig. 2 Modular hard wall showing nominal locations of surface pressure taps. Adapted with permission from Duetsch-Patel et al. [32].

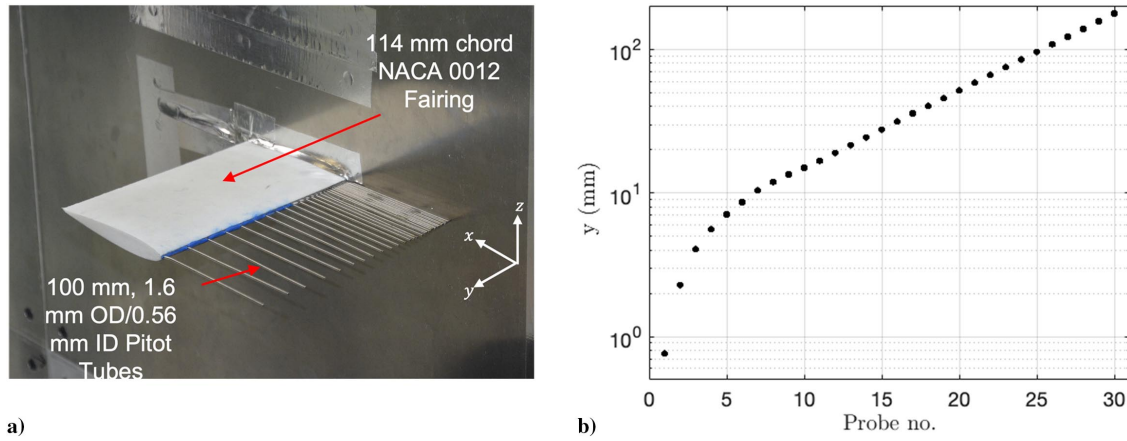


Fig. 3 Boundary-layer rake (a) and associated wall-normal probe positions (b).

Mean temperature in the test section was measured with an Omega Thermistor type 44004 thermocouple on the boundary-layer wall downstream of the test area at approximately $x = 7.5$, $y = 0$, and $z = 0.7$ m. Freestream density was obtained via the constitutive relationship knowing the freestream static pressure and temperature. Similarly, kinematic viscosity was determined from the measured temperature using Sutherland's relationship.

Measurements of the mean velocity in the boundary layer were made using a Pitot-static pressure rake installed in a modular panel on the port wall of the test section at the streamwise locations indicated in Fig. 1. The rake, pictured in Fig. 3, consists of 30 Pitot tubes of 0.56 mm inner diameter protruding 100 mm forward from a 114 mm chord NACA0012 aerodynamic fairing. The Pitot tubes are arranged between $y = 0.8$ mm and $y = 178$ mm with distribution shown in Fig. 3b. Static pressure measurements were also taken on the rake panel surface averaged between measurements taken at $\Delta z = \pm 0.1$ m from the rake location. Pressure was sampled in the static taps and Pitot probes using a 20'' H2O DTC ESP 32HD pressure scanner. For the determination of boundary-layer displacement and momentum thicknesses, 10,000 points were added a posteriori beneath the rake data following the Spalding profile [33].

C. Fluctuating Pressure Measurements

Fluctuating pressure data were acquired with an array of six flush mounted Hottinger Brüel and Kjaer (HBK) type 4138 A-015 1/8th-in. pressure field condenser microphones. The sensors are arranged as pictured in Fig. 4a, resulting in the separation vector shown in Fig. 4b. Before each test, the sensitivity of each sensor was measured using a HBK type 4228 pistonphone calibrator. Data were acquired using an HBK 24-bit Pulse LAN-XI data acquisition

system at 65,536 Hz for 32 s, high-pass filtered at 0.7 Hz, and anti-alias low-pass filtered at 25.6 kHz.

Each sensor is equipped with a 1/2-mm-diam pinhole cap to reduce spatial averaging of small-scale turbulence; however, the pinhole cap creates errors in the acquired pressure measurements requiring adjustment. Pinhole caps attenuate high-frequency pressure fluctuations requiring the discarding of certain high-frequency data depending on the maximum resolvable frequency, which is a function of effective pinhole diameter, $d^+ = du_\tau/\nu$ [34]. The pinhole cap also creates a cavity between itself and the microphone diaphragm, which acts as a Helmholtz resonator. This is accounted for by assuming that the microphone response is a second-order dynamic system, the exact nature of which is determined from the transfer function between the pinhole microphone response and the response of a flat-response microphone in an anechoic, quiescent environment in the presence of white noise. The second-order transfer is fit to the form

$$C(\omega) = \frac{1}{a_1\omega^2 + ia_2\omega + 1} \quad (3)$$

where C is the calibration and a_1 and a_2 are empirically determined coefficients. The dynamic response characteristics change in the presence of grazing flow as a function of wall shear stress [35]. This is accounted for a posteriori using an optimization algorithm that minimizes the deviations of spectral slope in the high-frequency portion of the pressure autospectrum by optimizing the values of a_1 and a_2 . The final spectrum is then expressed:

$$G_{pp}(\omega)_{\text{calibrated}} = \frac{G_{pp}(\omega)_{\text{raw}}}{C_{\text{opt}}^* C_{\text{opt}}} \quad (4)$$

where C_{opt} is the optimized calibration and C_{opt}^* is its complex conjugate. More details on the basis, derivation, and implementation of this scheme are found in [35]. Examples of these data before and after calibration are shown in Fig. 5. In the lower-Reynolds-number case, the correction is relatively mild, but the higher-Reynolds-number case shows a Helmholtz resonance of approximately 12 dB.

The autospectral and cross-spectral densities were determined using the Welch algorithm utilizing a Hanning window of record length 8192 with 50% overlap. Autospectra were then octave binned using 20 points per octave. Measurements were taken at the seven streamwise locations shown in Fig. 1 with the array oriented both parallel to the flow (streamwise) and rotated 90° (spanwise).

D. Wall Shear Stress

Estimates of the wall shear stress were made by fitting the logarithmic region of the boundary-layer velocity profile to that of Spalding [33] in a Clauser plot method. The efficacy of this estimate relies on the assumption that the slope of the logarithmic region of the velocity profile (i.e., the von Kármán constant) will be constant and equal to the ZPG value through the entire pressure gradient family.

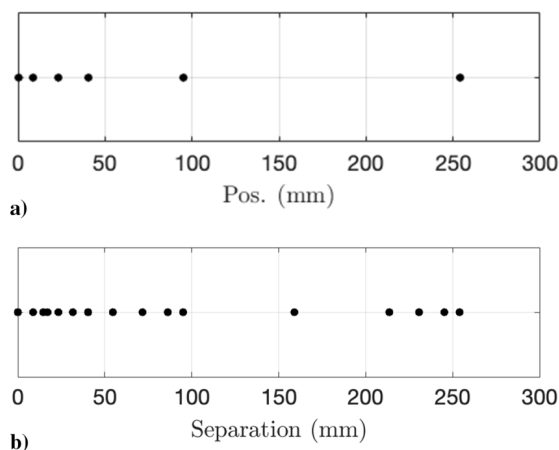


Fig. 4 Positions (a) and corresponding separations (b) of the six HBK 1/8th-in. microphones used in the fluctuating pressure sensor array.

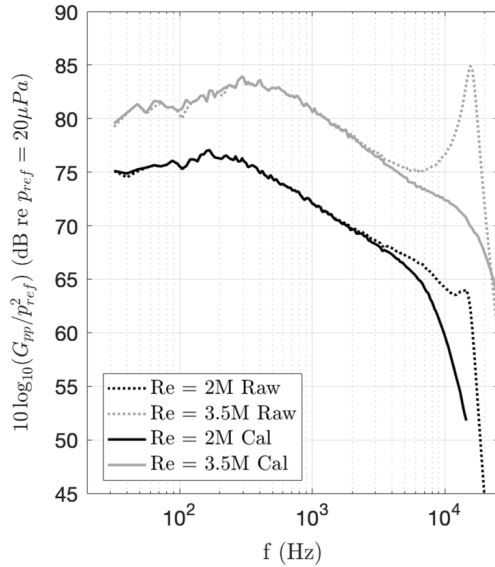


Fig. 5 Example spectral calibrations in ZPG conditions at both tested Reynolds numbers.

This is considered a valid assumption for this flow family based on the observations of Dixit and Ramesh, who found that the standard Clauser method requires no significant modifications for magnitudes of the acceleration parameter, $K = (\nu/U_e^2)(\partial U_e/\partial x)$, less than 1.0×10^{-7} [36]. The highest magnitude of K observed in these pressure gradient cases was 3.04×10^{-8} . Based on the skin friction results obtained using the classical Clauser method, this would give a Dixit and Ramesh pressure gradient parameter, $\Delta p = -K/(c_f/2)^{3/2}$, of 7.0×10^{-4} , an order of magnitude smaller than the mildest pressure gradients observed therein. Nevertheless, there is uncertainty in this method, accounted for in Sec. II.F.

E. Test Cases

Data were acquired at two freestream Reynolds numbers based on the inflow velocity and airfoil model chord length of 2 and 3.5 million, corresponding approximately to $U_\infty = 32$ and 56 m/s respectively. For each Reynolds number, data were acquired with the model positioned at twelve angles of attack ranging from -10° to $+12^\circ$ in 2° increments. This generated a total family of 24 unique flow cases. Within each flow case, boundary-layer data were acquired at seven streamwise locations ranging from $0.70 < x/h < 2.77$. These data were acquired in midwinter in Blacksburg, VA, at an elevation of around 600 m, and had the average ambient conditions shown in Table 1.

F. Uncertainty Quantification

The primary sources of uncertainty in this experiment are the instruments themselves, which have the nominal uncertainties shown in Table 2. These uncertainties can be carried through the various computations to estimate uncertainty in final reported values, in the manner of

$$\begin{aligned} \delta(X(v_1, v_2, \dots)) \\ = \sqrt{\delta(X(v_1 + \delta v_1, v_2, \dots))^2 + \delta(X(v_1, v_2 + \delta v_2, \dots))^2 + \dots} \end{aligned} \quad (5)$$

Table 1 Average ambient conditions

T , K	ρ , kg/m ³	p , kPa	ν , m ² /s
282	1.156	93.0	1.53×10^{-5}

Table 2 Primary instrument uncertainties

Instrument	Uncertainty
Esterline pressure scanner	$\pm 0.05\%$ full range
DTC pressure scanner	$\pm 0.03''$ H ₂ O
Omega T/C	± 0.2 K
HBK 1/8'' Mic	± 1 mV
Rake probe y	$\pm 3\%$ nominal

where δ indicates an uncertainty, X is the derived parameter of interest, and v_1, v_2, \dots are the primary variables on which X depends.

Random uncertainty is also estimated as ± 1 standard deviation of a range of repeated measurements taken with each instrument.

In addition, there are a few other special considerations. Firstly, the uncertainty in the airfoil angle of attack is $\pm 0.1^\circ$. A sensitivity analysis was performed using both repeat experimental measurements and 2D Reynolds-averaged Navier–Stokes computations to show that this corresponds to an additional uncertainty in the static pressure on the test section of ± 1.5 Pa with a corresponding uncertainty in boundary-layer velocities.

Secondly, more details must be considered in order to estimate final uncertainty in the fluctuating pressure data. The sensitivity of the microphone is calibrated as described above and is uncertain due to the uncertainty in the measurement of the ambient pressure correction, measured using a calibrated barometer provided by HBK with the pistonphone calibrator. In addition, the subtraction of background acoustics and calibration of Helmholtz resonance introduce uncertainties into the final autospectral density that exist only in certain frequency domains; hence spectral uncertainty is broken into low-, mid-, and high-frequency regions, where the midfrequency region has no additional uncertainty; the low-frequency region has an additional uncertainty due to background acoustic contamination, estimated based on the canonical low-frequency behavior as described by Bull [4]; and the high-frequency region has an additional uncertainty due to the Helmholtz calibration, estimated based on repeat measurements of the calibration values and the canonical high-frequency behavior described by Bull [4]. Next, the Welch algorithm itself contains numerical uncertainties as it uses the FFT estimator for the Fourier transform. Finally, Hu and Erbig showed that, when flush mounting a fluctuating pressure sensor, mounting accuracy is critical because steps in the microphone mounting of 0.3 mm resulted in a spectral error of 3 dB [22]. Measurements taken with a micrometer indicated that the fluctuating pressure sensors were mounted with less than 0.1 mm of step to the wall; coupled with the data of Hu and Erbig, the uncertainty due to mounting error is thought to be on the order of 1 dB.

Uncertainty in wall shear stress as measured in the Clauser chart method is more difficult to estimate. The estimates of wall shear stress uncertainty are a best guess based on the deterministic uncertainty in the velocity profile and the results of Dixit and Ramesh [36]. Additionally, the probe diameter of 0.56 mm causes the uncertainty in boundary-layer velocity to grow very near the wall due to the spatial averaging in regions of higher velocity gradient. By comparing to the Spalding profile, the error in the first probe from the wall is estimated to be $\pm 6\%$, but this results in less than $\pm 1\%$ change in the calculated skin friction and, as such, no corrections are made.

Considering all these factors, the final uncertainty estimates for major quantities are estimated, converted to percentages of measured values, and shown in Table 3.

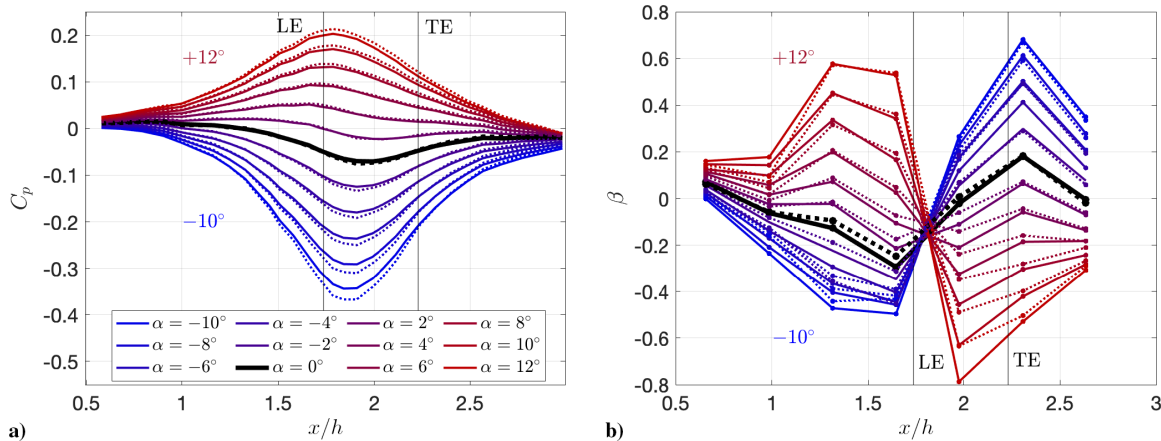
III. Results and Discussion

A. Pressure Gradient Cases

This experimental case generates a family of continuously varying mean wall pressure distributions featuring both favorable (negative sign) and adverse (positive sign) streamwise gradients. The mean pressure coefficient (Fig. 6a) begins at nominally zero at the inflow

Table 3 Quantified experimental uncertainties in major variables of interest

p	ρ	ν	U_∞	u	δ	δ^*	θ	τ_w	β	G_{ppLow}	G_{ppMid}	G_{ppHigh}
$\pm 0.1\%$	$\pm 0.1\%$	$\pm 0.1\%$	$\pm 0.1\%$	$\pm 0.9\%$	$\pm 3.0\%$	$\pm 3.0\%$	$\pm 4.0\%$	$\pm 8.0\%$	$\pm 8.0\%$	± 2.5 dB	± 1.5 dB	± 1.75 dB

**Fig. 6** Mean pressure coefficient (a) and pressure gradient parameter β (b) developing downstream. Streamwise locations of leading and trailing edges marked. Blue curves are negative model angles of attack, and red are positive. Solid lines are $Re_c = 2M$, and dotted lines are $Re_c = 3.5M$.

plane and then either increases or decreases as the flow progresses downstream, reaching its maximum magnitude as the flow passes beneath the quarter chord of the airfoil model, and is positive when the model is at a positive angle of attack and vice versa. Downstream of the model quarter chord, the pressure coefficient magnitude decreases until returning to nominally zero at the test section exit. In Fig. 6, red curves correspond to positive airfoil angles of attack, blue to negative, and the zero-degree case is shown in bold black. The solid curves are data at $Re_c = 2M$ and the dotted lines are data at $Re_c = 3.5M$. These color and line style schemes will apply to all of the upcoming figures.

The mean pressure gradient is best represented in nondimensional form by the Clauser parameter, $\beta = (\delta^*/\tau_w)(dp/dx)$ (Fig. 6b). Each flow case features a roughly sinusoidal pressure gradient exhibiting one character upstream of the airfoil quarter chord and the other downstream. The flow cases contain what is dubbed a “cross-over point” beneath the quarter chord, where the curves from the various angle-of-attack cases show the same value of β , which is not exactly ZPG due to the small, but not negligible, favorable pressure gradient generated by the growth of the boundary layer on the four walls of the test section, effectively acting as a very small area ratio contraction. Across the family of flows, pressure gradients are observed on the order of $\beta = \pm 0.7$. These are relatively mild pressure gradients compared to some practical cases; however, this systematic and dense family offers a multitude of valuable insights. By studying repeated pressure gradient values with different streamwise locations and upstream histories, the effects of mean pressure, pressure gradient, and pressure gradient history can be decoupled and quantified independently.

Freestream Reynolds number appears to have negligible impact on the normalized mean pressure coefficient or pressure gradient in these cases. The discrepancies that do arise, predominantly at the peak mean pressure magnitude in the extremes of the angle-of-attack range, are attributed to small structural deformations in the model and tunnel walls at high speeds and lift forces. This nondimensional Reynolds number similarity is advantageous as it allows for the decoupling of Reynolds number and pressure gradient effects.

B. Velocity Profiles

Figure 7 shows velocity profiles at seven streamwise locations on the boundary-layer wall as measured by the boundary-layer rake under viscous normalization (u^+ vs y^+). In each plot, curves are

shown for each model angle of attack, colored blue-to-red as in the previous figures. In the first two measurement locations (Figs. 7a and 7b), there is negligible angle-of-attack dependency, but by the point of maximum pressure gradient in Fig. 7c there are clear differences developing in the various angle-of-attack cases. The logarithmic region is well-collapsed, but there is a pressure gradient effect in the wake. While, dimensionally, favorable pressure gradient will increase boundary-layer edge velocity, under viscous scaling FPGs (blue curves) push the value of u^+ down. This indicates that favorable pressure gradient has a greater impact on the wall shear stress than it has on the edge velocity, or that the opposite is true in APG, or some combination of both. This trend sustains through the maximum mean pressure coefficient magnitude in Fig. 7d.

Moving further downstream to the point of maximum secondary pressure gradient in Fig. 7e, the trend appears to begin reversing and the wake regions of Fig. 7e look similar to those in Fig. 7c. This would appear to indicate that the deviation in the wake is following the mean pressure, which would follow logically from Bernoulli’s principle.

In Fig. 7e, at the point of maximum secondary pressure gradient, a dip develops in the velocity profiles between $y^+ = 70$ and $y^+ = 300$. For this short extent within the boundary layer, the profile deviates down from the logarithmic region for cases that previously passed through APG and are now in favorable pressure gradient (red curves). The trend continues downstream as shown in Figs. 7f and 7g; at all three of the most downstream locations, the downward dip between the logarithmic and wake regions can be seen, becoming more pronounced farther downstream. This feature is more evident in the positive-angle-of-attack cases (red curves), flows that passed through an initially APG and are now experiencing a favorable one. This flow feature was not observed in the initial pressure gradient region shown in Figs. 7a–7d, meaning that it may be a feature unique to this kind of mixed-character, bidirectional pressure gradient flow.

From the data shown in Figs. 7a–7e, it seemed that the defects observed in the wake region were following the local mean pressure distribution. When combined with the data in Figs. 7f and 7g, however, it becomes clear that this is not the case. In Figs. 7f and 7g, the defect in the wake does not return toward a collapse, as seen in Fig. 7a, but rather reverses its trend, with the negative-angle-of-attack cases (blue curves) now showing higher values of u^+ . This new trend increases downstream to the most downstream profile location; the boundary layer is not returning toward an equilibrium state, even as it

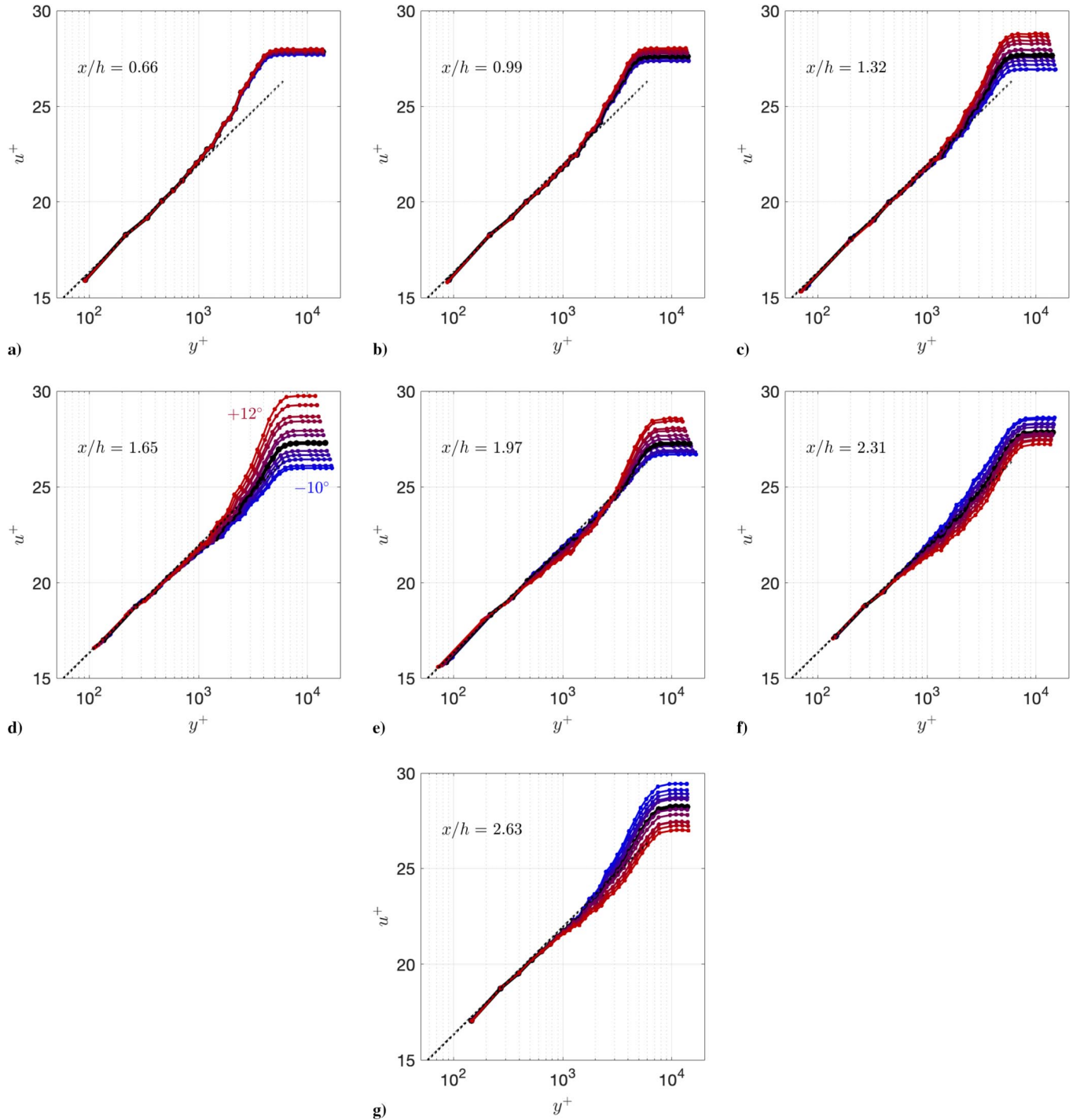


Fig. 7 Mean boundary-layer velocity profiles under viscous scaling. Blue curves are negative model angles of attack, red are positive, and black dots are law of the wall, $u^+ = (1/\kappa) \ln(y^+) + B$, with $\kappa = 0.41$ and $B = 5.0$. Data shown for $Re_c = 2M$, but under this normalization data are qualitatively the same for $Re_c = 3.5M$.

passes into a region that is experiencing close to ZPG, indicating that the effect of pressure gradient sustains downstream after its point of application, what will be termed “history effects.”

The behavior of the wake observed in Fig. 7 can be more directly quantified by considering Coles’s law of the wake [37]:

$$u^+ = \frac{1}{\kappa} \ln(y^+) + B + \frac{\Pi}{\kappa} W\left(\frac{y}{\delta}\right) \quad (6)$$

Here, κ and B are the classical von Kármán constants, taken to be $\kappa = 0.41$ and $B = 5$, Π is the wake strength parameter, and W is the law of the wake. The exact nature of W is still debated, but it is agreed upon that $W(1) = 2$, which implies

$$\Pi = \frac{\kappa}{2} \left[U_e^+ - \frac{1}{\kappa} \ln(\delta^+) - B \right] \quad (7)$$

The measured distribution of the wake strength is given in Fig. 8. At the inflow, $\Pi \approx 0.45$, which then generally increases in APG and decreases in FPG, reaching a maximum deviation upstream of the leading edge near the point of maximum mean pressure coefficient. Π drops to around -0.1 in FPG and climbs to 0.7 in APG, matching the respective suppression and expansion of the wake seen in Fig. 7d. The wake strength responds to the secondary pressure gradient downstream of the quarter chord with a clear lag, also consistent with the observations of the velocity profiles.

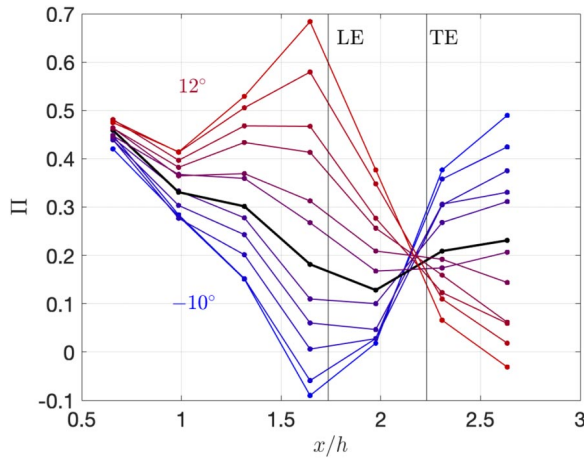


Fig. 8 Coles [37] wake strength parameter measured at each location and angle of attack for $Re_c = 2M$.

The measured wake strength parameters are compared to two proposed a priori relations in Fig. 9, for which marker styles are found in Table 4. The predictor of Coles [37] in Fig. 9a is a linear relationship with a von Kármán constant slope growing with the parameter $U_e^+ \delta^* / \delta$. The measured data very closely match the predicted $\kappa = 0.41$ slope, but show consistently lower values of Π than the Coles relation.

Durbin and Reif [38] postulated that, for pressure gradient flows, $\Pi = 0.8(\beta_\theta + 0.5)^{3/4}$, where β_θ is the Clauser parameter using the momentum thickness as the length scale. As shown in Fig. 9b, the measured data do not appear at first glance to be functionally dependent with β . At most stations, taken individually (e.g., the Δ markers), Π increases with β_θ in a trend roughly parallel to the curve of Durbin and Reif but consistently low, similar to the comparison with the Coles prediction in Fig. 9a. At $x/h = 1.97$, where the secondary pressure gradient is strongest (indicated with the \diamond markers), however, the trend is almost perfectly opposing the Durbin and Reif curve. The reversal of the pressure gradient appears to impart some perturbation to the boundary layer that disrupts the normal wake behavior and pressure gradient effect. This perturbation works out of the flow, however, by the next station (\square markers). These effects will be explored more in Sec. III.J.

C. Skin Friction

The family of cases generates skin friction coefficients in the range of $0.0022 < c_f < 0.0030$. Here, the skin friction coefficient is defined using the local boundary-layer edge velocity as its reference velocity for each case. The skin friction coefficient distribution (Fig. 10a) shows an increase in the initially favorable pressure gradient case and a decrease in the initially adverse case from the inflow value, reaching

Table 4 Markers used for Figs. 9,16,27, and 28

Location	Marker
$x/h = 0.66/0.79$	+
0.99/1.12	*
1.32/1.45	×
1.65/1.78	Δ
1.97/2.11	\diamond
2.31/2.44	\square
2.63/2.77	\circ

a maximum deviation around the leading edge of the model. Another crossover point is observed; however, the crossover point in the skin friction coefficient is further downstream than the pressure gradient, occurring close to the trailing edge of the model. It appears that there is not perfect correlation between either mean edge velocity or pressure gradient and skin friction alone. Instead, there is a combined dependency on both the local flow velocity and pressure gradient and the upstream flow history, whereby the skin friction at a given point on the surface is a function both of the local flow velocity and pressure gradient above that point and the behavior the boundary layer has previously passed through to get there.

The higher-freestream-Reynolds-number case exhibits lower values of skin friction coefficient, as is typically observed for flat plate boundary layers. The dimensional wall shear stress follows a different trend than the skin friction coefficient: the trend in the initial pressure gradient region is the same, increasing in FPG and decreasing in APG, reaching a maximum deviation around the leading edge of the airfoil and then returning with the change of pressure gradient sign. Downstream, there is a crossover point, but it is now located farther downstream, around half a chord length downstream of the airfoil. Wall shear stress is evidently predominantly dependent on the local boundary-layer edge velocity, but is also moderately sensitive to upstream flow history.

D. Boundary-Layer Development

The 99% edge velocity boundary-layer thickness (Fig. 11a) grows in APG and shrinks in favorable, as might be expected. The boundary-layer thickness also shrinks with increasing freestream Reynolds number. The general trend is a quasi-linear increase downstream with a deviation off that line caused by the presence of pressure gradient. This quasi-linear growth, closely represented by the $\alpha = 0^\circ$ case, can be thought of as the baseline boundary-layer growth that would be expected under ZPG conditions. This deviation then is corrected downstream of the model quarter chord when the pressure gradient behavior reverses. At the quarter chord, where the deviation is maximum, there is a 20% variation in δ , indicating that, despite the mildness of the applied pressure gradients, their impact on the boundary layer is strong.

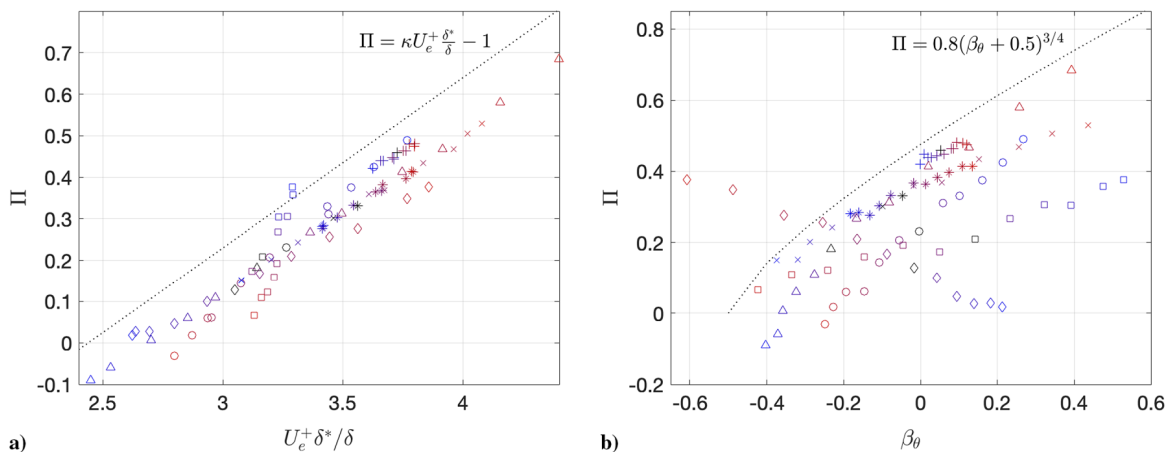


Fig. 9 Coles wake strength parameter as measured (symbols, Table 4) and as predicted (lines) from a) Coles [37] and b) Durbin and Reif [38].

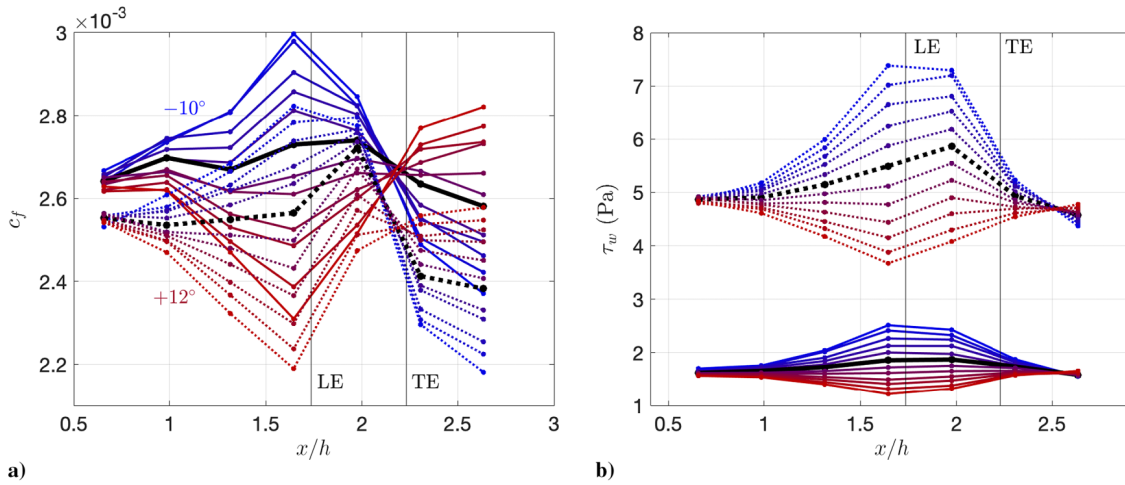


Fig. 10 Skin friction coefficient (a) and corresponding wall shear stress (b) as calculated from the Clauser plot method using boundary-layer rake data.

The displacement and momentum thicknesses (Figs. 11b and 11c, respectively) show similar trends to each other. They also reach a maximum deviation from the baseline growth of the $\alpha = 0^\circ$ case around the quarter chord location and then return toward baseline downstream; however, in these parameters there exists a crossover point, now at another new location. While the boundary-layer thickness appears to respond locally to the applied mean pressure (i.e., local freestream velocity), the displacement and momentum thicknesses have more dependence on upstream history, and that dependence is not the same as the skin friction.

At this point it is interesting to put forth the idea of an effect lag. One possible interpretation of the above observations is that there is a lag between various important parameters, most notably between pressure gradient and skin friction, which can be thought of as the local contribution to drag, and then again between skin friction and displacement or momentum thickness, which is representative of the total experienced drag. Such lag effects could be instrumental in understanding complex flow cases, since most cases of practical interest contain pressure gradients of both character along a given streamline similar to this family, and thus will contain flow dependencies that contain upstream history effects as well.

The boundary-layer thickness can be normalized and expressed in viscous wall units as $\delta^+ = \delta u_\tau / \nu$, a parameter that represents the ratio of outer to inner length scales in the boundary layer, i.e., the friction Reynolds number Re_τ . Interestingly, δ^+ appears to grow completely independent of pressure gradient or pressure gradient history (Fig. 12). This suggests that the impact of pressure gradient is universal across the various scales of the boundary-layer turbulence; i.e., if the pressure gradient increases the size of the outer scales, it will increase the size of the inner scales by the same amount.

Furthermore, if the observed trend in δ^+ is extended upstream as a linear fit with downstream distance (Fig. 12b), the x intercept of that line is very nearly the location of the boundary-layer trip. It is not believed that this is a coincidence, but rather a fundamental insight

into how the TBL develops downstream from its origin. If the origin of the TBL imparts some scale or scales of turbulent motion, the effect of downstream development is to increase the ratio of the largest to smallest scales linearly with the length of that development. The effect of pressure gradient then serves to expand or compress the TBL as a whole, leaving the ratio of outer to inner scales intact and a function only of downstream distance and some freestream parameter that drives the slope. A similar observation was recently made by Bobke et al., who found that an instantaneous shift from ZPG to strong APG had no effect on the development of δ^+ [21].

The work of Bobke et al. did not, however, consider the range of freestream Reynolds numbers considered here. By looking at these two Reynolds number cases, we see that there is, in fact, some dependence on the freestream condition in the slope of that development. It may follow logically that, for a tripped boundary layer as considered here, this ought to be a function of the local conditions at the tripping point. By considering the area ratio between the test section and the trip location and utilizing Bernoulli's relationship, the freestream velocity at the trip point can be easily estimated as ≈ 24.8 m/s for the 2M Reynolds number case and ≈ 43.5 m/s for the 3.5M Reynolds number case. The TBL origin has some representative length scale, which also serves as an effective initial condition, taken in this case to be the height of the trip, $h_{\text{trip}} = 3.18$ mm. These parameters are empirically fit to the slopes of the curve fits in Fig. 12b and it is found that the slopes for both Reynolds numbers are described by $0.04 \sqrt{U_\infty / \delta_0 \nu}$, meaning that the nondimensionalized boundary-layer growth can be expressed as

$$\delta^+ = 0.04 \sqrt{\frac{U_\infty}{\delta_0 \nu}} x \quad (8)$$

where U_∞ is the freestream velocity at the boundary-layer origin and δ_0 is the representative integral length scale of the boundary-layer

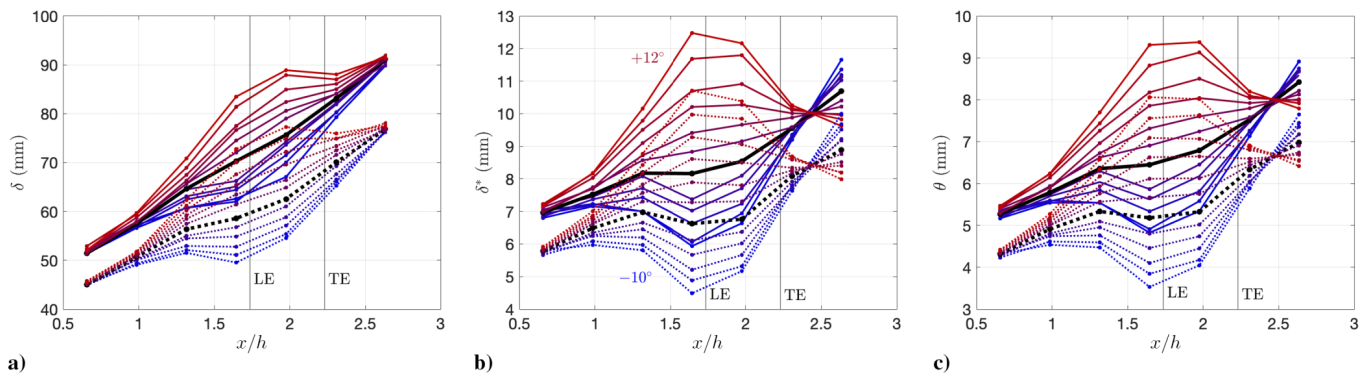


Fig. 11 Boundary-layer thickness developing on test wall: 99% edge velocity (a), displacement (b), and momentum (c).

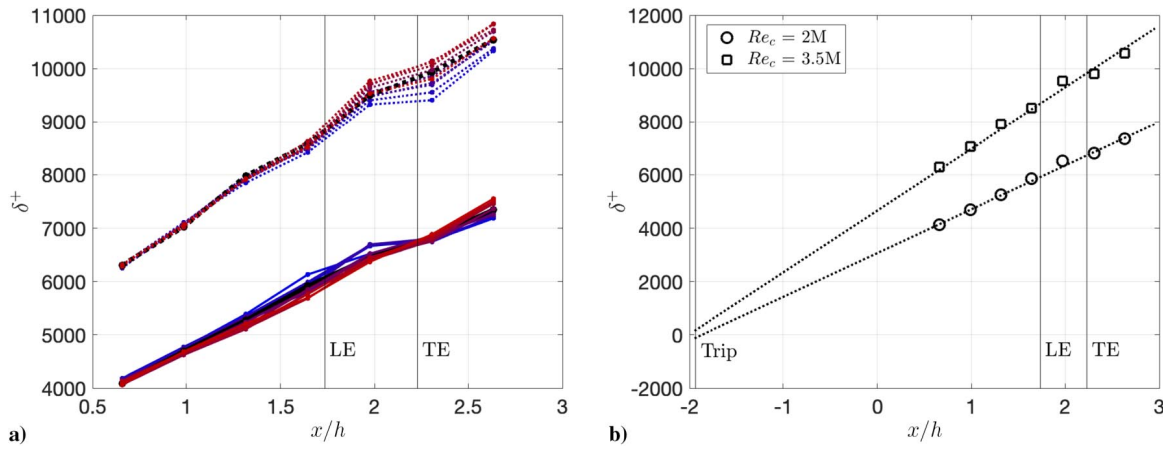


Fig. 12 $\delta^+ = Re_\tau = \delta u_\tau / \nu$ developing downstream on test wall. Panel (a) shows all data collected; panel (b) shows averages for each Reynolds number case with a linear fit of the form of Eq. (8).

origin, hypothesized to be the trip height h_{trip} for a tripped boundary-layer origin.

E. Fluctuating Pressure

The root mean square (rms) of the fluctuating pressure on the boundary-layer wall is inversely correlated with the mean static pressure (Fig. 13a), where the mean pressure coefficient increases, the rms of fluctuating surface pressure decreases. The streamwise location of maximum deviation is quite interesting; in the negative-angle-of-attack cases (blue curves, initially favorable pressure gradient), the rms pressure reaches a peak around the leading edge of the model. In the positive-angle-of-attack cases (red curves, initially APG), however, the rms pressure reaches a minimum around the 3/4 chord. This seems to indicate how rapidly the turbulence responds to the pressure gradient (i.e., how strong the history effects are) is somehow dependent on the character of the applied gradient.

The increase in freestream Reynolds number has a reasonably large effect on the rms of the pressure fluctuations, a roughly 160% increase in rms pressure with a 75% increase in Reynolds number. Given that the trend observed in the rms pressure is similar to that of the wall shear stress, one might expect that normalizing the rms pressure on τ_w would result in a straight line, which was the observation of Farabee and Casarella [7]. However, when normalized this way, the rms pressure retains a clear flow case dependency (Fig. 13b). Interestingly, the normalized rms pressure increases with initially APG rather than decreasing. The streamwise dependency now has a crossover point observed around the 3/4 chord. Much like the wall shear stress, the streamwise and pressure gradient dependency of the rms pressure depends on how (or if) the value is normalized, meaning that careful choice of normalizing parameters is of the utmost importance.

The autospectral density of the fluctuating pressure shows a variety of interesting behaviors throughout this flow family, shown in Fig. 14. The Reynolds number effect is clear; moving from the lower- to higher-freestream-Reynolds-number cases results in a 5–10 dB increase in spectral level across the frequency range and shifts the observed spectra to higher frequencies by approximately 200 Hz, though it is most likely that the frequency shift is due simply to the increased flow velocity. How the spectra scale with the associated flow variables will be explored in the next section.

An interesting paradox arises when considering the frequency range of the various spectra across Reynolds numbers. The lower-Reynolds-number case results in a much lower viscous normalized frequency, meaning that much of the data that are present below the Nyquist frequency must be thrown out due to pinhole attenuation, as described by Gravante et al. [34]. In the lower-Reynolds-number case, the cutoff frequency fell between 14 and 18 kHz, above which no data is plotted in Fig. 14. In the higher-Reynolds-number case, the cutoff frequency is above the Nyquist frequency of 25.6 kHz, meaning that no data must be discarded. This would seem, at first, to indicate that a greater range of turbulent scales can be observed in the higher-Reynolds-number data. This is not, however, the case. As the increasing Reynolds number pushes the spectra to higher frequencies, the amount of high-frequency turbulence that is captured beneath the Nyquist frequency decreases and does so faster than the benefit of increasing pinhole resolution can keep up with, resulting in the strange predicament of seeing a greater range of turbulent structures in the lower-Reynolds-number data, despite the decreased frequency range. Because the high-frequency behavior is well captured, even with the highest frequencies discarded, no corrections were applied to the spectra.

The pressure gradient effect on the spectra is more complex; different spectral regions exhibit different behaviors as the flow

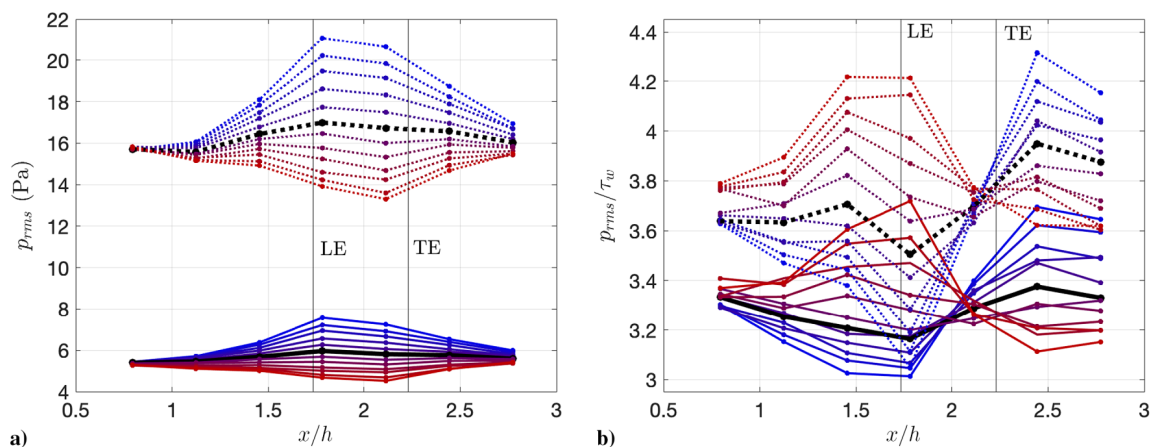


Fig. 13 Root mean square of fluctuating wall pressure, dimensional (a) and normalized on wall shear stress τ_w (b).

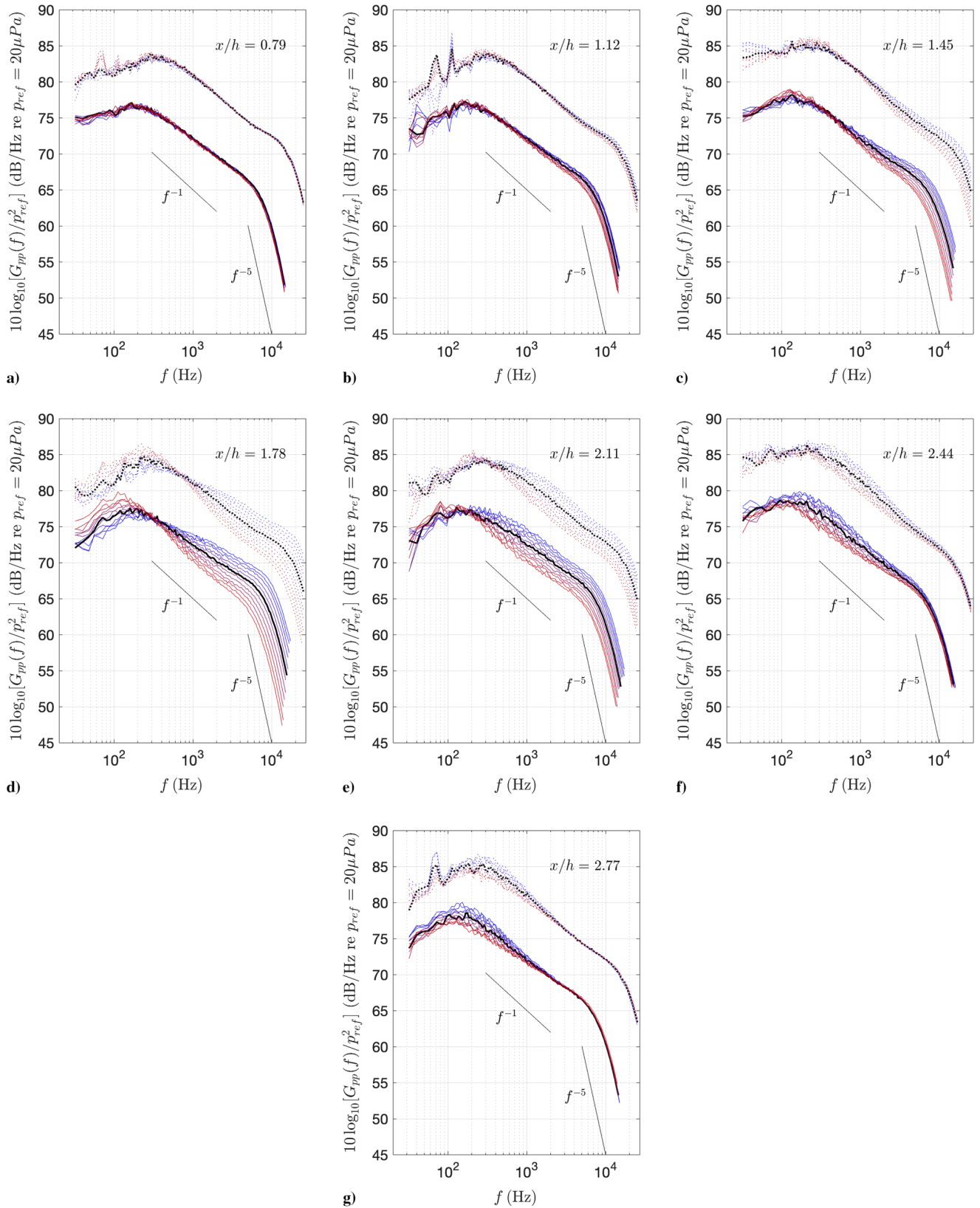


Fig. 14 Autospectral density of fluctuating pressure expressed in decibels per hertz relative to 20 μPa as a function of frequency, Reynolds number, model angle, and downstream position. Color and line-style scheme is standard.

progresses downstream and through the family of cases. The predominant effect of pressure gradient is on the slope of the mid-frequency region; favorable pressure gradient decreasing the slope and adverse steepening it, in keeping with the observations of Schloemer [19]. The slope of the high-frequency region is a constant f^{-5} , the amplitude affected only by the varying mid-frequency slopes.

As the flow progresses farther downstream, it becomes clear that the pressure gradient effect on the midfrequency slope is also historically dependent, most strongly observable in the parallel slopes in Fig. 14e, at the point of strong return pressure gradient rather than one station upstream where the pressure gradient has relaxed. By the most downstream station, the high-frequency region has recollapsed to a single curve. The low-frequency region, however, does not, retaining

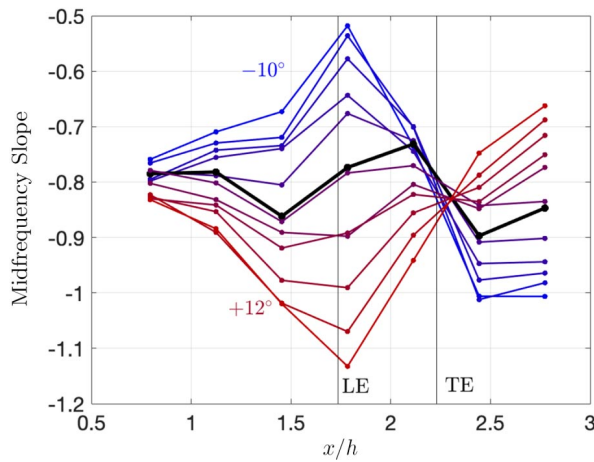


Fig. 15 Slope of midfrequency region of the autospectra of fluctuating pressure measured at each location and model angle of attack.

some angle-of-attack dependency, but that dependency has changed. Whereas in the more upstream regions a higher angle of attack (red curves) corresponded to higher low-frequency amplitudes, this behavior reverses between $x/h = 2.11$ and 2.44 (Figs. 14e and 14f). This behavior is reminiscent of what was observed in δ^* and θ .

Throughout the entirety of the spectral development, it seems that the midfrequency slope is the most sensitive to applied pressure gradient. Figure 15 shows the midfrequency spectral slopes plotted in the same style as the other boundary-layer parameters. The slopes of the midfrequency regions were determined by isolating each spectrum between $0.6 < \omega \delta^*/U_e < 5$ and applying a curve fit of the form $a\omega^b$, where a and b are coefficients determined from the curve fitting algorithm. This distribution looks similar to that of the skin friction coefficient in Fig. 10, increasing in favorable pressure gradient and decreasing in adverse, reaching a maximum deflection around the leading edge of the model ($x/h = 1.75$), and returning in opposing gradient, experiencing a crossover point around the model trailing edge ($x/h = 2.25$) before finally reversing its trend toward the outflow. It is possible that this relationship is causal; i.e., the skin friction directly drives the energy decay in the midfrequency region. However, it is also possible, and perhaps more likely, that the similarities arise due to the skin friction and midfrequency fluctuating pressure decay simply having similar pressure gradient and history dependencies.

Figure 16 shows the midfrequency pressure spectra slopes plotted as a function of local skin friction coefficient. The marker styles for Fig. 16 are shown in Table 4. This relationship collapses to a reasonably narrow band displaying what appears to be a roughly

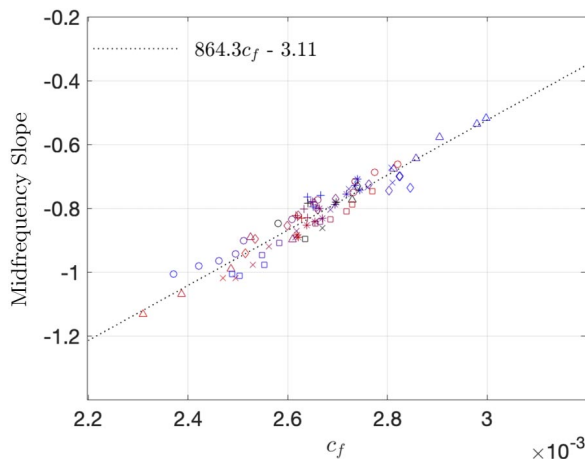


Fig. 16 Slope of midfrequency region of the autospectra of fluctuating pressure measured at each location and model angle of attack displayed as a function of local skin friction coefficient. Marker styles found in Table 4.

linear relationship. A linear fit is applied through these data for demonstrative purposes; however, this relationship is most likely not physical, as it would imply midfrequency slopes never before observed at well documented skin friction values. It is clear, however, that these two variables are correlated; specifically they show a correlation coefficient of 0.96. The observed relationship, however, is opposite to that observed in rough wall flows, where increased skin friction is correlated with steeper slope [39]. It is currently hypothesized that this discrepancy is due to the differing manner by which rough walls and favorable pressure gradients produce increased skin friction; rough walls increase the total turbulent motion, thus driving a higher dissipation rate (assuming that dissipation rate is proportional to kinetic energy), while favorable pressure gradients increase skin friction by increasing the velocity while simultaneously driving the turbulence toward relaminarization, thus driving a reduced dissipation rate.

The various regional dependencies of the pressure spectra reveal much about the nature of the turbulence in these cases. In APG, the strength of the fluctuating pressure due to large, low-frequency structures increases. This enlarged peak connects to a suppressed high-frequency roll-off via a steepened midfrequency slope. Assuming that the turbulence is frozen (Taylor's hypothesis), i.e., that the temporal frequency is directly proportional to a spatial frequency, this steepened slope can be interpreted as an acceleration of the dissipation rate of the large-scale structures to the small. The variation in midfrequency slope suggests quite strongly that there cannot be a universal overlap region in these spectra, because although spectral scaling may capture the variations in spectral level or frequency dependency, it cannot account for changes in slope, which would effectively represent a rotation in the spectra where scaling can only translate.

F. Autospectral Scalings

Scaling is still a valuable tool, however, for isolating the various correlations between the behavior of the turbulent structures and mean flow variables. The high-frequency portion of these spectra has been observed to collapse on variables representing the viscous forces at play in the boundary layer: the fluid viscosity and wall shear stress. This is often referred to as the "classical" inner viscous scaling [4] and is shown in Fig. 17 for all of the measured spectra. Marker styles for Figs. 17–19 are found in Table 5. The spectra collapse to what appears to be a single curve above normalized frequencies of $\omega\nu/u_\tau^2 = 0.3$, indicating the universality of viscous effects on the smallest scales of turbulence and their dissipation. This dissipation is captured in the universal frequency decay as ω^{-5} , in keeping with what has been repeatedly observed in the literature [4].

While visual observation seems to indicate that the spectra in Fig. 17 are collapsed, a more rigorous evaluation is needed. To ascertain whether an autospectral scaling is truly meaningful, a 95% confidence band can be defined knowing the uncertainty in the spectral level and

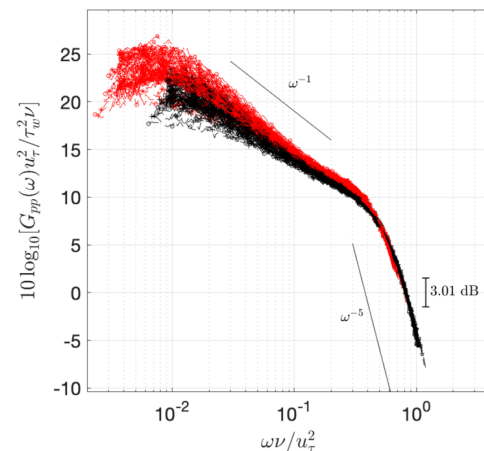


Fig. 17 Classical inner autospectral scaling applied to all measured spectra: black curves are $Re_c = 2M$, red are $Re_c = 3.5M$, and markers are found in Table 5.

the respective scaling variables (see Table 3). This confidence band represents the maximum expected statistical uncertainty of the scaled spectra. The maximum uncertainty of the inner scaled spectra is 2.13 dB, giving a 95% confidence band of 3.01 dB. This band is included in Fig. 17 as an uncertainty bar and it is clear that all of the high-frequency spectra collapse to within a band smaller than 3.01 dB, confirming that this scaling is statistically significant.

By coloring the spectra in Fig. 17 by freestream Reynolds number, it appears that there is a Reynolds number dependency in the low-frequency peak not captured by this inner scaling, in addition to noncaptured pressure gradient effects. The higher-Reynolds-number case shows higher normalized peak amplitudes at lower normalized frequencies than the lower-Reynolds-number case, and in both cases the peaks fail to collapse across the range of pressure gradient cases.

The low-frequency behavior proves more resistant to scaling efforts. The corresponding classical outer scaling replaces the viscous length and velocity scales with the boundary-layer thickness and edge velocity, respectively, and this scaling is shown in Fig. 18 with a 95% confidence interval of 3.58 dB. The low-frequency spectra do not collapse within the confidence bound under this scaling, which is not all together unsurprising given the clear pressure gradient history effects that were observed in the dimensional spectra in Fig. 14. Similar freestream Reynolds number and flow case dependencies are observed in the classical outer scaling as were in the low-frequency range of the classical inner.

While the outer region proves more difficult to collapse, it does display clear and well-behaved trends with downstream position and model angle of attack (Fig. 14), suggesting that it should scale at least reasonably well on some combination of parameters. A variety of scalings were attempted, systematically varying the pressure, length, and velocity scales in an attempt to achieve better collapse in the low frequencies.

First, it has been suggested that perhaps a better pressure scale for the outer region is the edge velocity dynamic pressure, $q_e = (1/2)\rho U_e^2$, owing to the fact that the wall shear stress τ_w is really an inner boundary-layer scaling [4]. Second, the behavior observed in the dimensional spectra seems to indicate that the amplitude of the low-frequency may vary in a similar manner to the integrated boundary-layer thicknesses δ^* and θ . Finally, a large variety of scaling velocities can be considered, including the edge velocity, shear velocity, broadband convection velocity, or one of many velocity defects. Of the many attempted scalings, the one that performed the best was based on the momentum thickness, friction velocity, and edge velocity dynamic pressure, shown in Fig. 19 with a 95% confidence band of 3.49 dB.

More than 95% of the spectra at frequencies $\omega\theta/u_\tau < 40$ are collapsed within the band, indicating that this scaling has statistical significance and the spectra may be considered scaled, despite not achieving the visual cleanliness of the classical inner scaling in Fig. 17. Most notably, the Reynolds number dependency in the peak

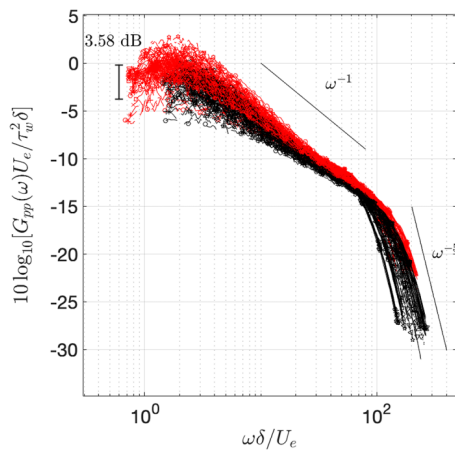


Fig. 18 Classical outer autospectral scaling applied to all measured spectra: black curves are $Re_c = 2M$, red are $Re_c = 3.5M$, and markers are found in Table 5.

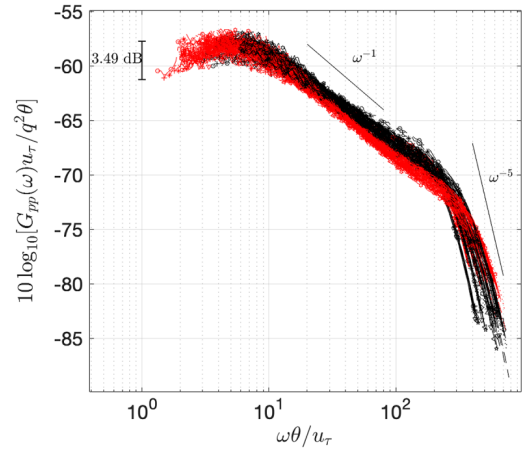


Fig. 19 Proposed outer autospectral scaling applied to all measured spectra: black curves are $Re_c = 2M$, red are $Re_c = 3.5M$, and markers are found in Table 5.

Table 5 Markers used for autospectral density scaling for Figs. 17–19

α	Marker
-10°	○
-8°	+
-6°	*
-4°	×
-2°	□
0°	●
2°	◇
4°	△
6°	▽
8°	◁
10°	△
12°	●

amplitude and frequency observed in the classical scalings vanish under this proposed scaling, lending it to an intriguing level of authenticity, despite not being an established scaling in the literature.

The mixed nature of the proposed scaling raises interesting possibilities about the nature of pressure gradient boundary-layer flows. The lack of successful collapse of the low-frequency spectra under purely outer variables combined with their successful collapse on a mixture of outer and inner variables appears to indicate that the relationship between turbulent scales and wall-distance may not be as straightforward as previously thought for these nonequilibrium pressure gradient flow cases. This is in keeping with the observations of Wei et al., who observed that viscous forces play an important role in turbulent dynamics far higher in the boundary layer than indicated by the traditional understanding [40].

G. Microphone-Based Shear Sensor

The universality of the high-frequency spectra under viscous scaling brings up an interesting possibility: Can this relationship be exploited to indirectly measure the skin friction in flows with non-equilibrium pressure gradient, flows in which measuring skin friction is canonically quite difficult? To do this, a power law fit was placed through the data for $\omega\nu/u_\tau^2 > 0.3$ in Fig. 17. This fit was found to be

$$\frac{G_{pp}(\omega)u_\tau^2}{\tau_w^2\nu} = 0.35\left(\frac{\omega\nu}{u_\tau^2}\right)^{-5} \quad (9)$$

A simple algorithm was then employed, which output the value of c_f that, for each spectra, best collapsed the high-frequency data with

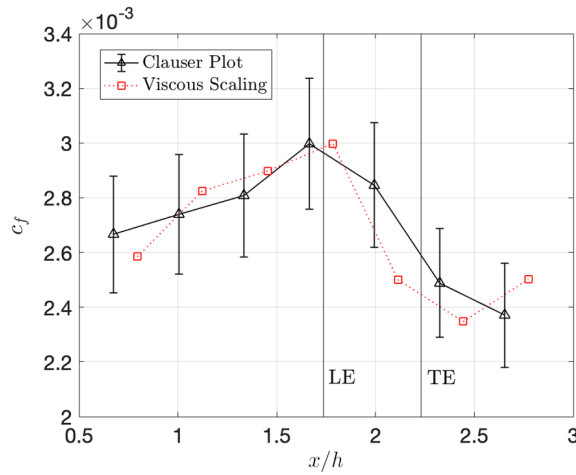


Fig. 20 Coefficient of friction as calculated from boundary-layer rake data using Clauser plot (black triangles) and using the universal high-frequency viscous scaling of microphone obtained pressure spectra (red squares). Data presented at $Re_c = 2M$ and $\alpha = -10^\circ$.

this fit. Figure 20 shows an example of the skin friction coefficient measured from the viscous scaling relation of the high-frequency pressure spectra against that measured using the Clauser plot method, including the uncertainty bars on the Clauser method, for the lower-Reynolds-number case ($Re_c = 2M$) at the highest shear stress condition, $\alpha = -10^\circ$. The match is imperfect, but inside the uncertainty bounds of the Clauser method. The universality of the high-frequency scaling of turbulent wall pressure spectra can potentially be exploited as a robust, reasonably accurate shear stress sensor in flows where that universality is a valid assumption, which appears, based on these results and the literature [19], to include smooth wall flows in mild pressure gradient of both favorable and adverse character, even when those pressure gradients vary and/or reverse sign.

H. Space-Time Correlation

The space-time correlation of the fluctuating pressure in the streamwise direction provides insight into the characteristics and behavior of the pressure-imparting turbulent structures as they are convected through the boundary layer. Figure 21 shows maps of the space-time correlation coefficient as a function of outer-normalized space and time for favorable, zero, and APG cases, taken at $x/h = 1.45$, $\alpha = -10^\circ$, 0° , 12° , respectively for the lower-Reynolds-number case.

In general, the space-time correlation of fluctuating pressure presents as an oval-shaped spot of highly correlated data, extending approximately $\delta/4$ in space and $\delta/2U_e$ in time. This oval is surrounded and extended by a long ridge of moderately correlated data. Increasing the pressure gradient (first from favorable to zero, then continuing zero to adverse) increases the strength of the small-separation correlation coefficients, darkening, widening, and lengthening the oval structure. Additionally, increasing pressure gradient

also increases the correlation strength and length in both space and time of the outer ridge. It is hypothesized that this effect is due to the stretching and compressing of turbulent structures experienced in pressure gradient boundary-layer flows. In APG, as the mean and convection velocities slow, the turbulent structures will pile up on each other, resulting in stronger and longer correlations. In favorable pressure gradient, as the mean and convection velocities increase, the structures become stretched. At first, it seems counterintuitive that a stretched structure will result in less correlation at large separations, but the correlation is a function of the entire turbulent field, not just a single structure, and that field is becoming sparse and losing kinetic energy in a favorable pressure gradient. These observations appear to run contrary to what is currently accepted in the literature; i.e., that coherence of the turbulence decays more rapidly in APG [35,41]; however, we do not believe that these results to be contrary, but rather indicative of different simultaneous physical effects. In APG, the midfrequency slope of the autospectrum steepens, indicating a more rapid decay of the turbulent energy and accounting for the rapid decay of coherence with frequency. Simultaneously, the convection velocity slows and the point of peak production moves further from the wall to regions with lesser temporal decay [40], increasing the temporal extent of the correlation. Assuming frozen turbulence, this increase in temporal extent corresponds to an equivalent increase in the spatial extent of the correlation.

I. Pressure Convection Velocity

By plotting the maxima of the space-time correlations of the fluctuating pressure as a function of separation in space and time, the convective ridge of the pressure imparting turbulence can be visualized and compared between cases, as shown in Fig. 22, the ratio of which (ξ/τ) represents the convection velocity of the pressure imparting turbulent eddies as they move downstream. Increasing the freestream Reynolds number steepens the convective ridge, implying that the turbulence is convecting faster, as would be expected. The pressure gradient effect on the convective ridge is fairly straightforward; in increasing APG, the slope becomes shallower, indicating a deceleration of the convection of pressure imparting eddies, the opposite being true in favorable pressure gradient. The greatest deviation in slope occurs at the point of maximum pressure coefficient, under the quarter chord at $x/h = 1.78$, and then returns to zero deviation at the outflow.

The relationship between the pressure gradient cases and the slope of the convective ridge implies that it may scale well on outer flow variables, as shown in Fig. 23; the slope of the ridge is close to universal when plotted as boundary-layer lengths as the spatial separation variable and $U_e\tau/\delta$ as the time separation variable. Further, this implies that the convection velocity of the pressure-imparting eddies is closely a function of those outer flow variables. A fit can be applied through these data shown in Fig. 23 of

$$\frac{\xi}{\delta} = \frac{4 U_e \tau}{5 \delta} \quad (10)$$

Thus, the broadband, large-scale convection velocity of the pressure-imparting turbulent eddies appears to be $\approx 0.8U_e$. It has

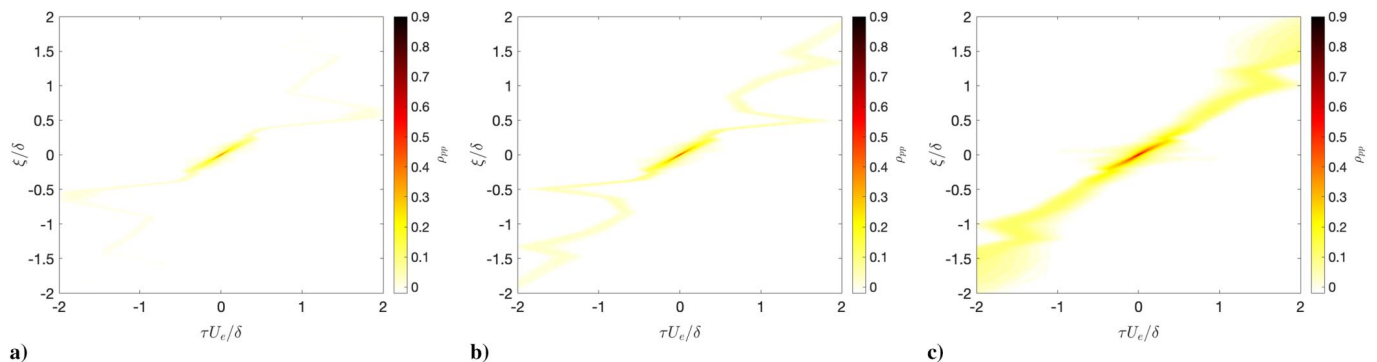


Fig. 21 Space-time correlation coefficient maps as a function of outer-variable-normalized space and time at $Re_c = 2M$ and $x/h = 1.45$: a) FPG ($\alpha = -10^\circ$), b) ZPG ($\alpha = 0^\circ$), and c) APG ($\alpha = 12^\circ$).

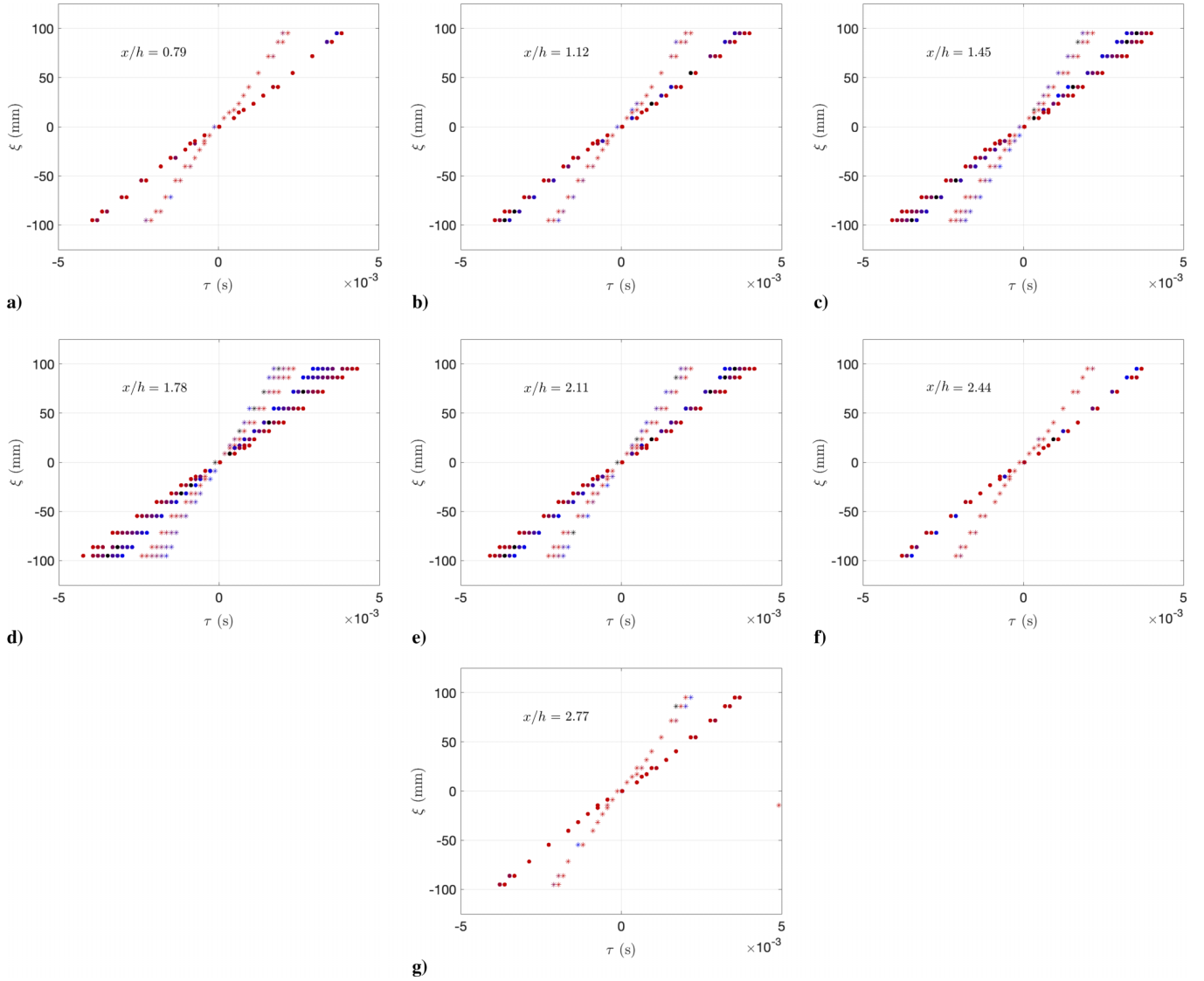


Fig. 22 Maxima of space-time correlation of fluctuating pressure as a function of separation in space and time. Blue is negative angles of attack, and red is positive. Dots are $Re_c = 2M$, and stars are $Re_c = 3.5M$.

been shown in previous literature [19] that this value ought to change with applied pressure gradient, shrinking in adverse and increasing in favorable, and the consistency of the implied convection velocity is taken to be a result of the mildness of the pressure gradients observed ($-0.8 < \beta < 0.7$). The outer bounds of the scaled convective ridge contain implied slopes between $0.75U_e$ and $0.85U_e$, which could

account for the small changes experienced under the different signs and magnitudes of pressure gradient.

However, while the $0.8U_e$ fit visually matches the overall trend in the data, it does not fully account for the pressure gradient effect on the pressure convection velocity. When the data points from Fig. 22 are plotted individually, as shown in Fig. 24 for the location of maximum pressure gradient, $x/h = 1.45$, the canonical pressure gradient effect is observed; i.e., the convection velocity increases with separation, and increases and decreases with favorable and APG, respectively.

With increasing separation, each curve of convection velocity appears to asymptote toward some value, which can be thought of as the broadband convection velocity of the flow. This can be calculated by fitting an asymptotic function of the form:

$$\frac{U_c}{U_e} = \frac{a(\xi/\delta) + b}{(\xi/\delta) + c} \quad (11)$$

where a , b , and c are empirically determined coefficients. This form produces a horizontal asymptote from which the broadband convection velocity is estimated.

Figure 25 shows the broadband convection velocity as a ratio of edge velocity at each station and angle of attack for the lower-Reynolds-number case. As expected, FPG increases this quantity while APG decreases it in the upstream region. Downstream, the trend follows closely to that of the local skin friction coefficient,

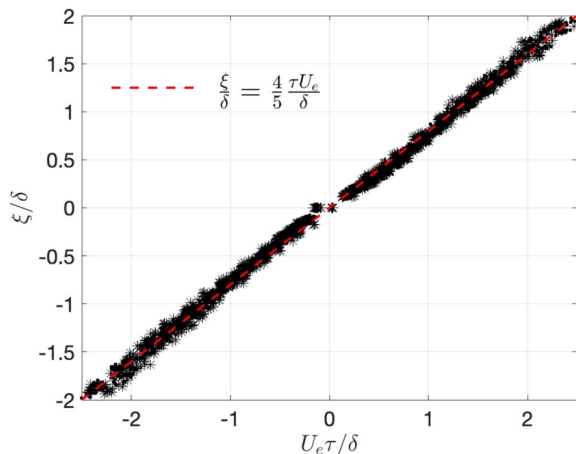


Fig. 23 Maxima of the space-time correlation of fluctuating pressure for all cases normalized on edge velocity and boundary-layer thickness.

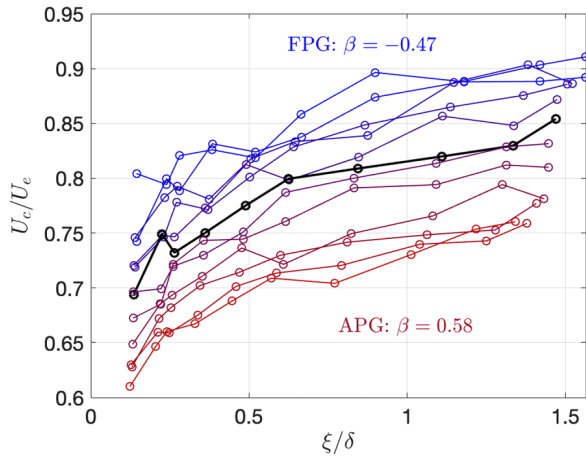


Fig. 24 Pressure convection velocity normalized on boundary layer edge velocity as a function of normalized streamwise separation for $Re_c = 2M$ at location of maximum pressure gradient, $x/h = 1.45$, colored in the default scheme by angle of attack.

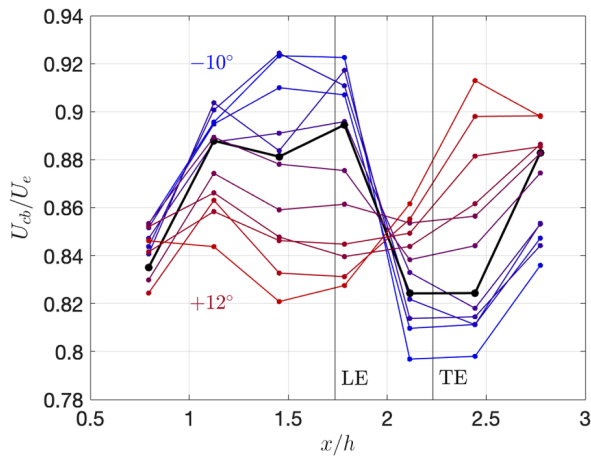


Fig. 25 Broadband convection velocity as a ratio of local edge velocity for all cases at $Re_c = 2M$.

reversing its trend with a crossover point at roughly the 1/2 chord, slightly downstream of the pressure gradient crossover, indicating the possibility of a very slight historical dependence.

J. Discussion of Historical and Nonequilibrium Effects

It is clear that the effect of this family of continually varying pressure gradients is nonlocal and contains downstream lags in

various observed behaviors. To quantify which effects can be denoted “history” effects, two assumptions will be made: First, in the absence of pressure gradient, this flow would show the trends of a canonical flat plate boundary layer; i.e., the growth of δ , δ^* , and θ would follow power law behavior, skin friction would be roughly constant in the streamwise direction and a function only of local Reynolds number, and the three regions of the pressure spectra would show the slopes and amplitudes associated with the canonical case. Second, if there were no history effects in the flow, the distributions of all variables displaced from their ZPG growth would qualitatively follow the distribution of either the mean pressure/velocity or the pressure gradient. If these two assumptions are valid, then history effects can be identified and quantified by the identification of features within the pressure gradient distribution that appear in other parameters at a different streamwise station, most notably crossover points.

If there is a crossover point in δ , it occurs farther downstream than the most downstream measurement. There are two possible explanations for this: δ varies with mean pressure and velocity, not pressure gradient, or the downstream lag in δ is extremely long, more than 25 boundary-layer thicknesses. Given the pressure gradient-independent growth of δ^+ (Fig. 12) we are inclined to believe the former; δ^* and θ experience a crossover point at approximately 1.11 and 1.20 m downstream of the crossover point of the pressure gradient, respectively, values which are seemingly Reynolds number independent. This begs the following question: What physics in the flow drives this specific downstream lag?

Consider the following: From the above results, we propose that a reduced-order model for the growth of a nonequilibrium boundary layer would be a function of three variables: one that describes the downstream development, one that describes the effect of pressure gradient, and one that describes the lag effects. The pressure gradient parameter has long been established as Clauser’s β . Based on the above results, and the same observation by Bobke et al. [21], it appears that $Re_\tau = \delta u_\tau / \nu$ governs the downstream development. What is needed is a third nondimensional parameter that governs the historical lag effect. Analysis shows that the classic boundary-layer variables (δ , δ^* , θ , H , c_f , etc.) form continuous, functional, saddle-point surfaces when viewed as 3D contours with a variety of variable combinations, e.g., $\theta(\beta, Re_\tau, H)$ or $c_f(\beta, Re_\tau, Re_\theta)$. While these 3D contours cannot be easily shown on paper, consider the 2D contours shown in Fig. 26, showing θ and c_f as functions of β and Re_τ . It can be seen that, with the addition of a third nondimensional variable, these form functional saddle-point surfaces for which empirical relations could be derived.

Based on the observations of the crossover point behavior, it seems that the third, history variable ought to be independent of both Reynolds number and pressure gradient magnitude—it could be a function of the shape of the β distribution, or a nondimensionalized mean pressure second derivative, or something else entirely. One likely choice is the defect shape factor of Mellor and Gibson [29].

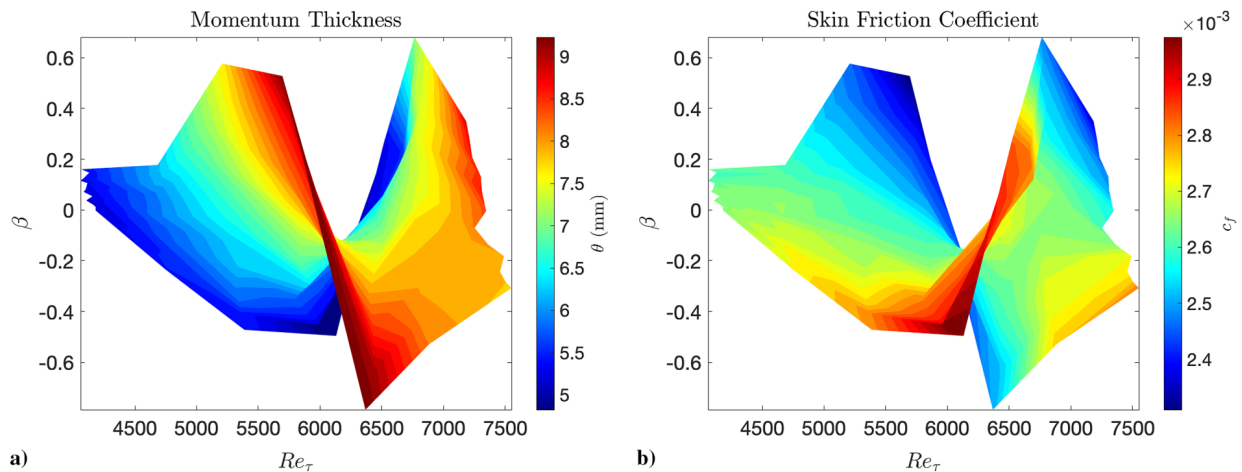


Fig. 26 Contour maps of momentum thickness (a) and skin friction coefficient (b) as 2D functions of Clauser parameter and friction Reynolds number.

Mellor and Gibson observed that, for a truly equilibrium boundary-layer flow, there was a direct and definable relationship between the Clauser parameter β and the defect shape factor G . Their equilibrium relationship, along with the data from the current work, is plotted in Fig. 27 using the standard color scheme and the marker styles found in Table 4.

Deviation from the equilibrium curve of Mellor and Gibson turns out to be correlated with the degree to which a given flow may be considered to be in equilibrium. At the inflow (+ markers) all data are clustered very near to the equilibrium curve. The deviation grows through the initial pressure gradient region (* and × markers) showing a suppression of the G parameter in APG (red markers) and an increase in favorable pressure gradient (blue markers). At the location of maximum mean pressure coefficient (Δ markers), the flow returns close to equilibrium. However, stepping downstream to the location of maximum secondary pressure gradient (\diamond markers), the flow becomes strongly nonequilibrium, in keeping with many of the observations made above, most notably the relationship between the wake strength parameter, Π , and β in Fig. 9b. In the same trend as the upstream flow, APG (blue markers) suppresses and favorable pressure gradient (red markers) increases G with respect to the expected equilibrium value. As the pressure gradient relaxes to the outflow (\square and \circ markers), the qualitative trend with model angle of attack returns to that of the equilibrium curve, but the magnitude of G remains displaced from equilibrium.

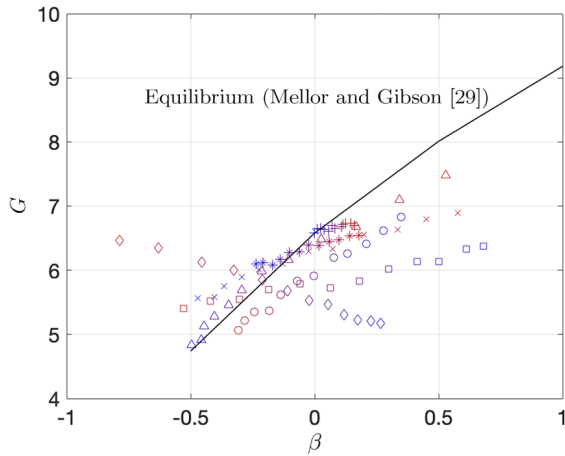


Fig. 27 Defect shape factor as a function of Clauser parameter, including equilibrium curve of Mellor and Gibson [29]. Standard color scheme, markers found in Table 4.

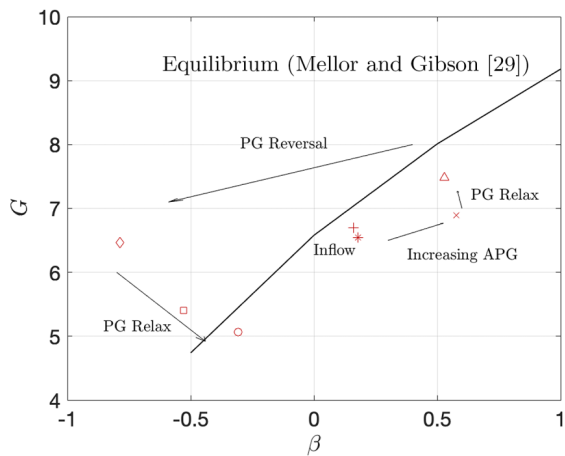


Fig. 28 Defect shape factor as a function of Clauser parameter, including equilibrium curve of Mellor and Gibson [29] for the $\alpha = 12^\circ$ case. Markers found in Table 4.

As expected based on many of the results presented here, the upstream region of the flow is nearly in equilibrium, despite the continually varying pressure gradient. In the downstream region, where the pressure gradient is reversed, however, the boundary layer enters a state that is strongly nonequilibrium, and this sustains far downstream, even as the pressure gradient relaxes. This is illustrated for the maximum initial APG case in Fig. 28.

IV. Conclusions

This investigation acquired a large, comprehensive data set of smooth wall TBL flows subjected to mild, continuously varying, bidirectional pressure gradients of both adverse and favorable character. The key issues examined were the effect of this family of pressure gradients on the development of the boundary layer and the effect of the pressure gradient through the boundary layer on the turbulent pressure fluctuations on the immersed surface. This was motivated by a need to generate and analyze a comprehensive database that more fully encompasses the near infinite space of non-equilibrium pressure gradient flows than previous studies, both to further our understanding of the dependent relationships within these flows and to provide a systematically divided data set for the development of appropriate turbulence models.

Perhaps the most important finding of this study is the observation of clear upstream history dependency in flows with pressure gradients, even mild, as evidenced by the systematic crossover points revealed when plotting the development of various parameters downstream through the family of pressure gradient cases together. The boundary-layer thickness, energy, turbulence statistics, and wall shear stress at a given point are all dependent on the downstream development of the boundary layer, the local freestream mean pressure and velocity, and the entire history of pressure gradients that the boundary layer has passed through upstream. This suggests that areas of a boundary-layer flow case cannot be isolated from what is happening upstream, which could potentially change the way that preliminary flow analysis is approached.

Similar history effects are observed in the autospectral density of the fluctuating wall pressure that vary in different regions of the spectra. The universality of the viscous scaling of the high-frequency region of the pressure autospectra is confirmed, independent of pressure gradient, and it is postulated that this relation may serve as a robust shear stress sensor in mild pressure gradient, smooth wall flows. The pressure gradient family has a strong impact on the slope of the midfrequency region, and this slope variation is found to be highly correlated with the local skin friction, possibly indicating a causal link between the skin friction and the dissipation rate of the large-scale turbulent structures. A new, mixed-variable scaling for the low-frequency region of the spectra has been identified after observing that none of the proposed outer variable scalings in the literature was able to collapse the spectra in this family of flows. No scalings were identified that could satisfactorily scale the midfrequency region, the variable slope making this almost certainly impossible, which indicates the lack of a universal overlap region for smooth wall flows in pressure gradient. The pressure–pressure correlation due to outer region flow structures and the associated convection velocities, however, show possible universal dependency on local, outer flow variables. The lack of successful scalings on local flow variables combined with the observed historical effects would seem to indicate that the spectral behavior ought to scale with the flow behavior upstream and/or a variable or variables that represent or capture those historical effects, but at this time the method for satisfactorily quantifying those effects remains elusive.

The friction Reynolds number, $Re_\tau = \delta^+ = \delta u_\tau / \nu$, grows independently of applied pressure gradient as a function only of turbulence origin and downstream development. This implies that the effect of pressure gradient is scale independent, affecting large and small turbulent scales to the same degree. This makes Re_τ a good candidate as the nondimensional parameter that governs the boundary-layer growth. Combined with the Clauser pressure gradient parameter, $\beta = (\delta^* / \tau_w)(dp/dx)$, and the Mellor and Gibson defect shape factor, $G = (1 - 1/H)/(u_\tau / U_e)$, quantifying the deviation

from equilibrium, it appears that a reduced-order model for non-equilibrium smooth wall boundary layers may exist.

These results indicate that our understanding of the complex relationship between streamwise mean pressure gradient and TBL flows is incomplete and that the impact of pressure gradient on wall-bounded flows is more dramatic and complex than previously thought. Given the wide variety of pressure gradients found in practical flow cases with complex curvature, an understanding of these effects is of critical importance.

Acknowledgments

The authors would like to thank Peter Chang and the Office of Naval Research for their support under grant numbers N00014-18-1-2455 and N00014-19-1-2109. The authors are extremely grateful for the contributions of Bill Oetjens, Julie Duetsch-Patel, Aldo Gargiulo, Surabhi Srivastava, Emily Sellards, Terelle Cadd, and Matt Szoke to wind tunnel testing. The authors also thank the Virginia Tech Aerospace and Ocean Engineering Machine Shop headed by James Lambert for their support in designing and manufacturing test hardware and instrumentation.

References

- [1] Lilley, G. M., and Hodgson, T. H., "On Surface Pressure Fluctuations in Turbulent Boundary Layers," NATO Rept. 276, 1960.
- [2] Corcos, G. M., "The Structure of the Turbulent Pressure Field in Boundary-Layer Flows," *Journal of Fluid Mechanics*, Vol. 18, No. 3, 1964, pp. 353–378.
<https://doi.org/10.1017/S002211206400026X>
- [3] Panton, R. L., and Linebarger, J. H., "Wall Pressure Spectra Calculations for Equilibrium Boundary Layers," *Journal of Fluid Mechanics*, Vol. 65, No. 2, 1974, pp. 261–287.
<https://doi.org/10.1017/S0022112074001388>
- [4] Bull, M. K., "Wall Pressure Fluctuations Beneath Turbulent Boundary Layers: Some Reflections on Forty Years of Research," *Journal of Sound and Vibration*, Vol. 190, No. 3, 1996, pp. 299–315.
<https://doi.org/10.1006/jsvi.1996.0066>
- [5] Chase, D. M., "Modeling the Wavenumber-Frequency Spectrum of Turbulent Boundary Layer Wall Pressure," *Journal of Sound and Vibration*, Vol. 70, No. 1, 1980, pp. 29–67.
[https://doi.org/10.1016/0022-460X\(80\)90553-2](https://doi.org/10.1016/0022-460X(80)90553-2)
- [6] Choi, H., and Moin, P., "On the Space-Time Characteristics of Wall Pressure Fluctuations," *Physics of Fluids*, Vol. 2, No. 8, 1990, pp. 1450–1460.
<https://doi.org/10.1063/1.857593>
- [7] Farabee, T., and Casarella, M., "Spectral Features of Wall Pressure Fluctuations Beneath Turbulent Boundary Layers," *Physics of Fluids*, Vol. 3, No. 10, 1991, pp. 2410–2420.
<https://doi.org/10.1063/1.858179>
- [8] Tsuji, Y., Fransson, J. H. M., Åfredsson, P. H., and Johansson, A. V., "Pressure Statistics and Their Scaling in High-Reynolds-Number Turbulent Boundary Layers," *Journal of Fluid Mechanics*, Vol. 585, Aug. 2007, pp. 1–40.
<https://doi.org/10.1017/S0022112007000676>
- [9] Buchmann, N. A., Küçükosman, Y. C., Ehrenfried, K., and Kähler, C. J., "Wall Pressure Signature in Compressible Boundary Layers," *Progress in Wall Turbulence: Understanding and Modeling*, Springer, Cham, Jan. 2014.
https://doi.org/10.1007/978-3-319-20388-1_8
- [10] Graham, W. R., "A Comparison of Models for the Wavenumber-Frequency Spectrum of Turbulent Boundary Layer Pressures," *Journal of Sound and Vibration*, Vol. 206, No. 4, 1997, pp. 541–565.
<https://doi.org/10.1006/jsvi.1997.1114>
- [11] Goody, M., "Empirical Spectral Model of Surface Pressure Fluctuations," *AIAA Journal*, Vol. 49, No. 9, 2004, pp. 1788–1794.
<https://doi.org/10.2514/1.9433>
- [12] Lee, Y.-T., Blake, W. K., and Farabee, T. M., "Modeling of Wall Pressure Fluctuations Based on Time Mean Flow Field," *Journal of Fluids Engineering*, Vol. 127, No. 2, 2005, pp. 233–240.
<https://doi.org/10.1115/1.1881698>
- [13] Grasso, G., Jaiswal, P., Wu, H., Moreau, S., and Roger, M., "Analytical Models of the Wall-Pressure Spectrum Under a Turbulent Boundary Layer," *Journal of Fluid Mechanics*, Vol. 877, Oct. 2019, pp. 1007–1062.
<https://doi.org/10.1017/jfm.2019.616>
- [14] Schofield, W. H., "Equilibrium Boundary Layers in Moderate to Strong Adverse Pressure Gradients," *Journal of Fluid Mechanics*, Vol. 113, Dec. 1981, pp. 91–122.
<https://doi.org/10.1017/S002211208100342X>
- [15] Nagano, Y., Tagawa, M., and Tsuji, T., "Effects of Adverse Pressure Gradients on Mean Flows and Turbulence Statistics in a Boundary Layer," *8th International Symposium on Turbulent Shear Flows*, Springer-Verlag, New York, Sept. 1991, pp. 7–21.
https://doi.org/10.1007/978-3-642-77674-8_2
- [16] Harun, Z., Monty, J. P., Mathis, R., and Marusic, I., "Pressure Gradient Effects on the Large-Scale Structure of Turbulent Boundary Layers," *Journal of Fluid Mechanics*, Vol. 715, Jan. 2013, pp. 477–498.
<https://doi.org/10.1017/jfm.2012.531>
- [17] Schatzman, D. M., and Thomas, F. O., "An Experimental Investigation of an Unsteady Adverse Pressure Gradient Turbulent Boundary Layer," *Journal of Fluid Mechanics*, Vol. 815, March 2017, pp. 592–642.
<https://doi.org/10.1017/jfm.2017.65>
- [18] Balantrapu, N. A., "The Space-Time Structure of an Axisymmetric Turbulent Boundary Layer Ingested by a Rotor," Ph.D. Dissertation, Virginia Polytechnic Inst. and State Univ., 2020.
- [19] Schloemer, H., "Effects of Pressure Gradients on Turbulent Boundary-Layer Wall-Pressure Fluctuations," U.S. Navy Underwater Sound Lab. Rept. 747, 1966. 10.1121/1.1943059
- [20] McGrath, B. E., and Simpson, R. L., "Some Features of Surface Pressure Fluctuations in Turbulent Boundary Layers with Zero and Favorable Pressure Gradient," NASA CR 4051, 1987.
- [21] Bobke, A., Örtü, R., Vinuesa, R., and Schlatter, P., "History Effects and Near-Equilibrium in Adverse-Pressure-Gradient Turbulent Boundary Layers," *Journal of Fluid Mechanics*, Vol. 820, June 2017, pp. 667–692.
<https://doi.org/10.1017/jfm.2017.236>
- [22] Hu, N., and Erbig, L., "Effect of Sensor Mounting and Flow History on Measured Wall Pressure Spectra," *AIAA Journal*, Vol. 58, No. 7, 2020, pp. 2964–2974.
<https://doi.org/10.2514/1.J057808>
- [23] Rozenburg, Y., Robert, G., and Moreau, S., "Wall-Pressure Spectral Model Including the Adverse Pressure Gradient Effects," *AIAA Journal*, Vol. 50, No. 10, 2012, pp. 2168–2179.
<https://doi.org/10.2514/1.J051500>
- [24] Catlett, M. R., Anderson, J. M., Forest, J. B., and Stewart, D. O., "Empirical Modeling of Pressure Spectra in Adverse Pressure Gradient Turbulent Boundary Layers," *AIAA Journal*, Vol. 54, No. 2, 2016, pp. 569–587.
<https://doi.org/10.2514/1.J054375>
- [25] Hu, N., "Empirical Spectral Model of Wall Pressure Fluctuations Including Adverse Pressure Gradient Effects," *AIAA Aviation Forum*, AIAA Paper 2017-3203, June 2017.
<https://doi.org/10.2514/6.2017-3203>
- [26] Lee, S., "Empirical Wall-Pressure Spectral Modeling for Zero and Adverse Pressure Gradient Flows," *AIAA Journal*, Vol. 56, No. 5, 2018, pp. 1818–1829.
<https://doi.org/10.2514/1.J056528>
- [27] Bradshaw, P., and Ferris, D. H., "The Response of a Retarded Equilibrium Turbulent Boundary Layer to the Sudden Removal of Pressure Gradient," National Physics Lab. Rept. 1145, 1965.
- [28] Clauser, F. H., "Turbulent Boundary Layers in Adverse Pressure Gradient," *Journal of the Aeronautical Sciences*, Vol. 21, No. 2, 1954, pp. 91–108.
<https://doi.org/10.2514/8.2938>
- [29] Mellor, G. L., and Gibson, D. M., "Equilibrium Turbulent Boundary Layers," *Journal of Fluid Mechanics*, Vol. 24, No. 2, 1966, pp. 225–253.
<https://doi.org/10.1017/S0022112066000612>
- [30] Devenport, W. J., Burdisso, R., Borgoltz, A., Ravetta, P., Barone, M., Brown, K., and Morton, M., "The Kevlar-Walled Anechoic Wind Tunnel," *Journal of Sound and Vibration*, Vol. 332, No. 17, 2013, pp. 3971–3991.
<https://doi.org/10.1016/j.jsv.2013.02.043>
- [31] Vishwanathan, V., Szoke, M., Duetsch-Patel, J. E., Fritsch, D. J., Gargiulo, A., Borgoltz, A., Lowe, K. T., Roy, C. J., and Devenport, W. J., "Aerodynamic Design and Validation of a Contraction Profile for Flow Field Improvement and Uncertainty Quantification," *AIAA Science and Technology Forum*, AIAA Paper 2020-2211, Jan. 2020.
<https://doi.org/10.2514/6.2020-2211>
- [32] Duetsch-Patel, J. E., Vishwanathan, V., Minionis, J., Totten, E., Gargiulo, A., Fritsch, D. J., Szoke, M., Bortoltz, A., Roy, C. J., Lowe, K. T., and Devenport, W. J., "Aerodynamic Design and Validation of Modular Test Section Walls for Hybrid Anechoic Wind Tunnels," *AIAA Science and Technology Forum*, AIAA Paper 2020-2214, Jan. 2020.
<https://doi.org/10.2514/6.2020-2214>

- [33] Spalding, D. B., "A Single Formula for the 'Law of the Wall,'" *Journal of Applied Mechanics*, Vol. 28, No. 3, 1961, pp. 455–458.
- [34] Gravante, S., Naguib, A., Waker, C., and Nagib, H., "Characterization of the Pressure Fluctuations Under a Fully Developed Turbulent Boundary Layer," *AIAA Journal*, Vol. 36, No. 10, 1998, pp. 1808–1816. <https://doi.org/10.2514/2.296>
- [35] Fritsch, D. J., Vishwanathan, V., Lowe, K. T., and Devenport, W. J., "The Effect of Grazing Flow on Pinhole Condenser Microphones," *AIAA Science and Technology Forum*, AIAA Paper 2021-0130, Jan. 2021. <https://doi.org/10.2514/6.2021-0130>
- [36] Dixit, A. D., and Ramesh, O. N., "Determination of Skin Friction in Strong Pressure-Gradient Equilibrium and Near-Equilibrium Turbulent Boundary Layers," *Experiments in Fluids*, Vol. 47, June 2009, pp. 1045–1058. <https://doi.org/10.1007/s00348-009-0698-2>
- [37] Coles, D., "The Law of the Wake in the Turbulent Boundary Layer," *Journal of Fluid Mechanics*, Vol. 1, No. 2, 1956, pp. 191–226. <https://doi.org/10.1017/S0022112056000135>
- [38] Durbin, P. A., and Reif, B. A. P., *Statistical Theory and Modeling for Turbulent Flows*, Wiley, New York, 2001, Chap. 4.
- [39] Meyers, T., Forest, J. B., and Devenport, W. J., "The Wall-Pressure Spectrum of High-Reynolds-Number Turbulent Boundary-Layer Flows over Rough Surfaces," *Journal of Fluid Mechanics*, Vol. 768, April 2015, pp. 261–293. <https://doi.org/10.1017/jfm.2014.743>
- [40] Wei, T., Fife, P., Klewicki, J., and McMurtry, P., "Properties of the Mean Momentum Balance in Turbulent Boundary Layer, Pipe, and Channel Flows," *Journal of Fluid Mechanics*, Vol. 522, Jan. 2005, pp. 303–327. <https://doi.org/10.1017/S0022112004001958>
- [41] Hu, N., "Coherence of Wall Pressure Fluctuations in Zero and Adverse Pressure Gradients," *Journal of Sound and Vibration*, Vol. 511, Oct. 2021, Paper 116316. <https://doi.org/10.1016/j.jsv.2021.116316>

C. Lee
Associate Editor

Chapter 4

Experimental and Computational Study of 2D Smooth Wall Turbulent Boundary Layers in Pressure Gradients

This chapter includes a paper presented in a NATO Special Session at the 2022 *AIAA Science and Technology Forum* that covers the collaborative efforts, methods, and results of a collaborative computational study of the flows discussed in Chapter 3. This paper is reprinted with permission of the American Institute of Aeronautics and Astronautics, Inc. [51].

Attributions

Daniel J. Fritsch is the primary contributor, first author, and organizer of the collaboration. All figures and text are his original work, except under methods sections from the collaborating organizations.

Vidya Vishwanathan and K. Todd Lowe participated in the generation of the experimental data.

Christopher J. Roy advised the computational setup, referencing, and collaboration organization.

William J. Devenport chaired the NATO session and advised the work.

The authors from DLR, Chalmers, MARIN/IST, and Sirehna provided computational results and participated in collaborative discussions and advancements.

The authors from the University of Melbourne provided computational results, participated in collaborative discussion and advancements, and designed and implemented the machine learning framework.



Experimental and Computational Study of 2D Smooth Wall Turbulent Boundary Layers in Pressure Gradient

Daniel J. Fritsch*, Vidya Vishwanathan*, Christopher J. Roy†, K. Todd Lowe†, and William J. Devenport‡
Virginia Tech, Blacksburg, VA, USA

Yasunari Nishi§, Tobias Knopp¶, Philip Ströer¶, and Andreas Krumbein¶
Deutsches Zentrum für Luft- und Raumfahrt (DLR), Göttingen, Germany

Richard D. Sandberg|| and Chitrarth Lav**
University of Melbourne, Melbourne, Victoria, Australia

Rickard E. Bensow††
Chalmers University of Technology, Göteborg, Sweden

Luís Eça‡‡
Universidade de Lisboa, Lisboa, Portugal

Serge L. Toxopeus§§ and Maarten Kerkvliet¶¶
Maritime Research Institute Netherlands (MARIN), Wageningen, The Netherlands

Myriam Slama*** and Luc Bordier***
Sirehna Naval Group, Bouguenais, France

This paper describes a collaborative experimental and computational study of smooth wall boundary layers in a systematic family of favorable and adverse pressure gradients. The objective is to advance turbulence modeling of these flows, in particular the effects of pressure gradients that can be classified as non-equilibrium. This collaboration is a component of the larger NATO AVT-349 Research Task Group. Experiments under this effort are conducted at Virginia Tech and computational efforts are presented from Virginia Tech, the German Aerospace Center (DLR), the University of Melbourne, Chalmers University of Technology, the Maritime Research Institute Netherlands (MARIN) in conjunction with the University of Lisbon *Instituto Superior Técnico* (IST) (MARIN/IST), and the Sirehna Naval Group. This paper describes some of the key elements of the experimental and computational approaches, the efforts made for cross-discipline collaboration, verification, and validation, and reports on some initial results and findings. The agreement between various RANS solutions and RANS turbulence models and between RANS solutions and experiment are generally good, but questions remain as to the efficacy of RANS modeling for non-equilibrium boundary layer flows and some potential directions for future investigations are suggested.

*Graduate Research Assistant, Crofton Dept. Aerospace & Ocean Engineering, AIAA Student Member

†Professor, Crofton Dept. Aerospace & Ocean Engineering, AIAA Associate Fellow

‡Crofton Professor of Engineering, Crofton Dept. Aerospace & Ocean Engineering, AIAA Associate Fellow

§Research Assistant, Institute of Aerodynamics and Flow Technology, C²A²S²E

¶Research Scientist, Institute of Aerodynamics and Flow Technology, C²A²S²E

||Professor, Dept. Mechanical Engineering, AIAA Senior Member

**Honorary Fellow, Dept. Mechanical Engineering

††Professor, Dept. Mechanics and Maritime Sciences

‡‡Professor, Mechanical Engineering Dept., Instituto Superior Técnico

§§Senior Researcher, Research and Development

¶¶Researcher, Research and Development

***Research Engineer, Modelling and Simulations in Hydrodynamics

I. Nomenclature

c_f	=	Skin friction coefficient, $= \tau_w / (1/2 \rho_{ref} V_{ref}^2)$
c_p	=	Pressure coefficient, $= (p - p_{ref}) / (1/2 \rho_{ref} V_{ref}^2)$
G	=	Defect shape factor, $= \frac{1-1/H}{u_\tau/U_e}$
H	=	Shape factor, $= \delta^* / \theta$
k	=	Turbulent kinetic energy
M	=	Mach number
p	=	Pressure
Re	=	Reynolds number
u	=	Streamwise velocity
U_e	=	Boundary layer edge velocity
u^+	=	Viscous normalized velocity, $= u / u_\tau$
u_τ	=	Friction velocity
V	=	Velocity
y^+	=	Viscous normalized wall normal coordinate, $= y u_\tau / \nu$
β	=	Clauser parameter, $= \frac{\delta^*}{\tau_w} \frac{dp}{dx}$
δ	=	Boundary layer thickness
δ^*	=	Displacement thickness
θ	=	Momentum thickness
ν	=	Kinematic viscosity
ρ	=	density
τ_w	=	Wall shear stress
ω	=	Specific turbulent dissipation rate

II. Introduction

MANY practically applicable boundary layer flows contain complex pressure gradient behaviors; gradients of both adverse (positive sign) and favorable (negative sign) character, continually varying pressure gradient magnitudes, and pressure gradient reversals. Pressure gradients can have dramatic effects on the development of the boundary layer and the performance of the system on which it grows, thickening the layer, increasing turbulence intensity, and potentially separating the flow [1, 2]. As such, the ability to accurately predict these flows is of paramount importance. Unfortunately, real-world pressure gradient flows often contain pressure gradient reversals or streamwise non-homogeneity that can introduce non-equilibrium (not self-similar or self-preserving) behavior into the boundary layer development [1, 3, 4]. Because of these poorly understood effects, successful modeling of these flows is a challenge with current Reynolds Average Navier-Stokes (RANS) simulations, the predominantly used technique due to the inability of current computational methods to efficiently simulate the full turbulent flow-field at practical Reynolds numbers.

RANS requires that the effect of turbulence within the flow-field be modelled, which is typically achieved through the Boussinesq eddy viscosity hypothesis [5]. The major weakness of the Boussinesq hypothesis for non-equilibrium pressure gradient flows is its dependence only on local conditions, for it has been observed that a primary effect of non-equilibrium pressure gradients is non-local, historically dependent behavior [6–9]. The ability of Boussinesq hypothesis turbulence models to predict the growth of boundary layers under non-equilibrium pressure gradients has never been rigorously tested and no turbulence models developed for such flows have been widely adopted. Improving the modeling of these flows is the subject of an ongoing international collaboration through the North Atlantic Treaty Organization (NATO) Science & Technology Organization (STO) Applied Vehicle Technology (AVT) 349 Research Task Group (RTG) on Non-Equilibrium Turbulent Boundary Layers in High Reynolds Number Flow at Incompressible Conditions.

A research initiative on turbulent boundary layer flows in pressure gradient was started ten years ago at DLR, in cooperation with the Institute of Fluid Mechanics and Aerodynamics at the University of the Federal Armed Forces in Munich headed by Professor Christian Kähler. Three different turbulent boundary layer experiments at adverse pressure gradient and at high Reynolds numbers have been performed since then. The aim was to study the behavior of the mean velocity profile and the Reynolds stresses in adverse pressure gradient (APG) and to use this knowledge for the improvement of RANS turbulence models. The first two experiments were for a moderately strong APG far from

separation at a moderately large Re_θ (up to 18000) for the first experiment [10] and at Re_θ up to more than 50000 for the second experiment [11]. The third experiment featured a strong APG with flow separation [12, 13]. A major finding of the experiments was that significant historical effects were observed in the outer layer, and these were found to affect the outer part of the inner layer and its mean velocity profile. Thus, one of the lessons learned from these experiments was that more research is needed on the role of historical effects and non-equilibrium in streamwise evolving flows, in particular for high Reynolds number flows, in keeping with the observations of [6–9].

Concerning RANS turbulence modelling, one major aim is to investigate the possible advantages of a differential Reynolds Stress Transport Model (RSTM) compared to models based on the eddy-viscosity hypothesis for non-equilibrium turbulent boundary layer flows. The SSG/LRR- ω model [14] is used in the present work. This model was found to be quite successful for a large number of aerodynamic flows [14–17]. Recent work at DLR was on the improvement of the SSG/LRR- ω model for turbulent boundary layers in adverse pressure gradient [12, 13], for flows with separation, reattachment and free shear flows [18, 19], and for reattachment [20]. From the perspective of RANS turbulence modelling, the issue of departure of the flow from equilibrium and historical effects poses many open questions, in particular for the redistribution tensor and for the length scale equation. For an overview of the challenges and needs for future efforts in RANS modelling, see also [21].

While second-moment Reynolds stress closure offer potential benefits over traditional Boussinesq hypothesis models, they come with not-insignificant cost increases. Another possible approach is to develop an expanded, non-linear first-moment closure for the Reynolds stresses in lieu of the Boussinesq approximation, such as the Quadratic Constitutive Relation (QCR) [22]. This can also be achieved through the use of Gene-Expression Programming (GEP) [23], a symbolic regression machine-learning algorithm, which embodies the closure for the Reynolds stress as a tangible mathematical equation. Such machine-learned turbulence models are being developed by the University of Melbourne for better prediction of non-equilibrium pressure gradient boundary layer flows. The sparseness of the available reference data, i.e., the experiments discussed in Section III, is suited to the CFD-in-a-loop approach of [24] described in more detail in Section IV.F.1.

This paper describes the preliminary findings of the collaborative work of NATO AVT-349 on the turbulence modeling of 2D boundary layers in non-equilibrium pressure gradients. The major goals of this work are to assess the current abilities of the state-of-the-art in RANS modeling to compute such flows across a wide variety of numerical algorithms and turbulence models and to communicate some of the developments being made to improve capabilities in this area. The validation flow case will be discussed in Section III and then the methods used to generate this collaborative data will be presented in Section IV. The results that have been generated thus far will be presented in V, discussed in Section VI, and finally some concluding remarks on the findings and the future direction of this collaboration will be offered in Section VII.

III. Flow Case

The flow case to be considered herein is based off of a series of experiments performed in the Virginia Tech Stability Wind Tunnel (VTSWT) in hard-wall (i.e., non-acoustic) configuration [25, 26]. The experiment involves the study of the low Mach number ($M < 0.2$), high Reynolds number ($Re_\theta > 10,000$) turbulent boundary layer flows developing on the port wall of the tunnel test section (1.85×1.85 m) while a 0.914 m chord NACA0012 airfoil model is installed in the test section center and swept to various angles of attack, as shown in Fig. 1. The presence of the airfoil displaces a continually varying, bi-directional (i.e., both adverse and favorable pressure gradients in a single flow case) pressure distribution onto the wall that is controllable by rotating the airfoil model. Experimental results from this flow case have been discussed at previous AIAA conferences [7–9]. Experimental data was collected at two free-stream conditions, a Reynolds number based on the inflow tunnel velocity and model chord length of 2 million and 3.5 million respectively, but for the sake of brevity this work will consider only data at $Re = 2M$.

This case generates a systematically divided family of bi-directional pressure gradient boundary layer flows with the pressure coefficient distributions shown in Fig. 2a, which have the corresponding pressure gradient distributions (presented as the non-dimensional Clauser parameter) in Fig. 2b. Each unique flow case generated by each model angle of attack generates an initial pressure gradient (adverse for $\alpha > 2^\circ$, favorable for $\alpha < 2^\circ$) that increases in magnitude until reaching a maximum around half a chord length forward of the streamwise location of the model leading edge. The pressure coefficient reaches a maximum magnitude at the streamwise location of the model quarter chord, before reversing its trend. Downstream of the model quarter chord, the flow experiences an equal and opposite pressure gradient from the initial behavior. This pressure gradient reversal is what makes this flow case of interest to modelers and computationalists; the rapid reversal of pressure gradient flavor introduces non-equilibrium behavior that is difficult

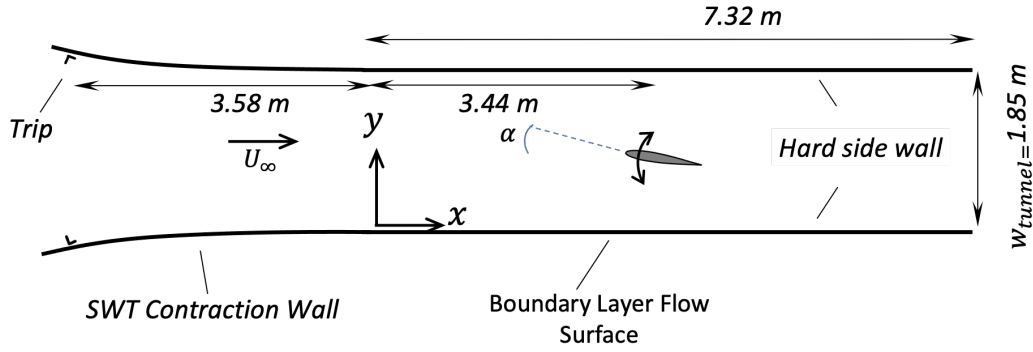


Fig. 1 Flow case system showing coordinate system origin, primary dimensions, and model and trip locations.

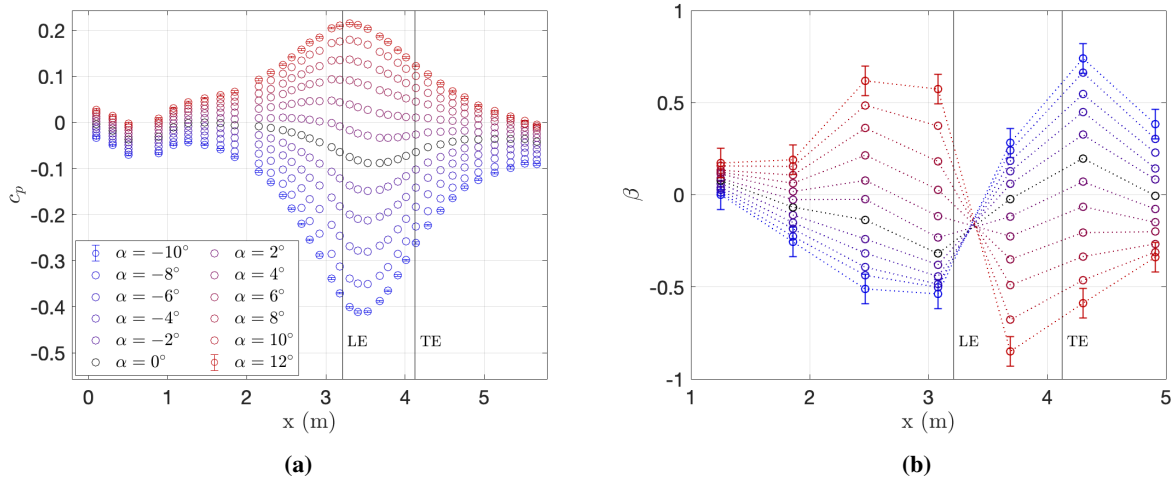


Fig. 2 Pressure coefficient (a) and pressure gradient parameter (b) distributions for flow cases at twelve angles of attack.

for RANS models to capture.

These bi-directional, continually varying pressure gradient flows show a strongly non-local dependence on upstream flow history, most easily recognized in the streamwise lagging of integrated boundary layer thicknesses, seen in Fig. 3. In the upstream region, δ^* grows in adverse pressure gradient and shrinks in favorable, as would be expected, but the behavior departs from this expectation as the boundary layers pass through the pressure gradient reversal. Downstream, the reversed pressure gradient begins to grow or shrink based on the sign of the secondary gradient, but the boundary layers do not collapse back to something universal, but rather "cross-over" each other downstream of the trailing edge and then continue on this trend, resulting in a displacement from the expected zero pressure gradient boundary layer growth that is flow-case dependent.

In addition to the force coefficients and boundary layer growth on the wall, the discussion herein will focus on three key locations within the flow: the most upstream measurement plane ($x = 1.25 \text{ m}$), the maximum initial pressure gradient ($x = 2.47 \text{ m}$) and the the maximum secondary pressure gradient ($x = 3.69 \text{ m}$), referred to as panels P3, P5, and P7 respectively. The boundary layer profiles are measured using a wall-normal rake of Pitot-static probes, and the resulting velocity profiles are used to estimate the skin friction in a Clauser plot method. Turbulent stresses are measured using planar time-resolved Particle Image Velocimetry (PIV). Experimental uncertainties were estimated

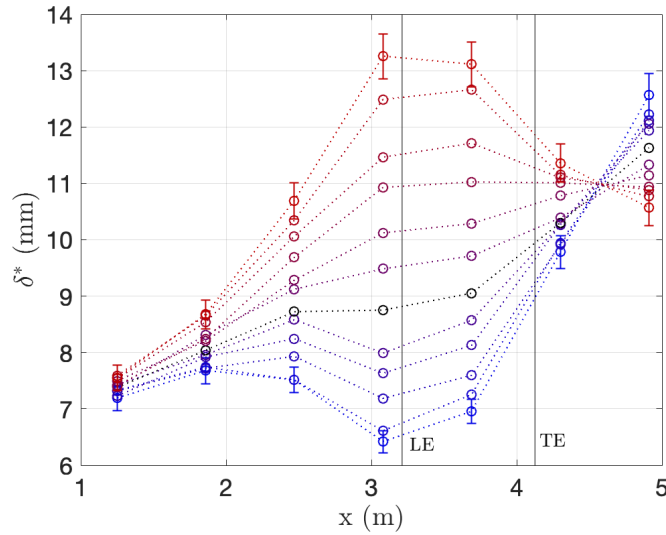


Fig. 3 Displacement thickness growth for flow cases at twelve angles of attack.

using the known instrumentation error and repeat sampling. More details on the experimental measurements and their uncertainties can be found in [7–9].

IV. Methods

A. Collaboration

This work was performed as part of the NATO AVT-349 collaboration. NATO AVT-349 is a group of 32 universities and government agencies from twelve NATO and NATO partner nations representing experimentalists, computationalists, and modelers working collaboratively to address the problem of turbulence modeling for low Mach number, high Reynolds number turbulent boundary layers in non-equilibrium conditions. Eleven flow cases are being assessed within AVT-349 considering various non-equilibrium conditions including surface roughness, pressure gradients, and three-dimensional curvature. This paper represents a sub-group of AVT-349 dealing with nominally two-dimensional boundary layers under the influence of non-equilibrium streamwise pressure gradients. The details of the flow case in question were presented in Section III.

Collaborating across time zones, languages, and professional disciplines presents unique challenges. Firstly, to ensure robust comparisons between experimental and computational data, a common referencing scheme was developed. A single reference point was chosen, a location where, in the experiment, a measurement of static pressure was being made. For this case, a pressure tap on the starboard (opposite the boundary layer wall) wall of the VTSWT along the tunnel center-line, located at $x = 1.47$, $y = 1.85$, $z = 0.00$ m was chosen. The reference point was placed on the starboard wall so as to ensure there would be a reference pressure measurement even when instrumentation was installed on the boundary layer wall. In addition to this reference static pressure, the VTSWT also records a reference stagnation pressure and stagnation temperature. Using compressible, isentropic flow relations, these three reference values are used to compute a reference Mach number, velocity, temperature, density, and dynamic pressure. This process is repeated in each CFD simulation, querying the same physical location for reference static and stagnation variables. All non-dimensional coefficients were then computed to these reference values, allowing a consistent and robust methodology for CFD-to-CFD and CFD-to-experiment comparisons.

Several other challenges had to be addressed to facilitate this collaboration, including open and accessible sharing of data (including specifying universal file formats and layouts), carefully defining all parameters (particularly the boundary layer edge/edge velocity and free-stream Reynolds number), and ensuring universal communication and understanding of coordinate systems/locations, geometry, reference and boundary conditions, and other methodologies.

B. Grid Development

In order to provide the most consistent results across different solvers, a common family of CFD grids was developed. Since the flow case in question is nominally two-dimensional and there are significant computational cost benefits, the grid family is 2D. At first, a constant-cross section grid was used with both walls being no-slip condition boundary layers; however, these grids failed to accurately capture the pressure gradient on the wall of interest. It was hypothesized that this is due to the lack of the other two boundary layers that will grow on the floor and ceiling of the VTSWT, generating a favorable pressure gradient that is missing in the 2D representation. Instead, the final grid family features one no-slip wall on which the boundary layer of interest grows and one slip wall, set at an angle of 0.46° to replicate the background FPG measured in the empty VTSWT. A representative diagram of the grid layout is shown in Fig. 4. The inflow plane is uniform, i.e., no inflow boundary layer is prescribed. The streamwise length of the domain upstream of the model was set such that the displacement thickness and velocity profile at the location of the most upstream experimental data, roughly two chord lengths upstream of the leading edge, was closely matched.

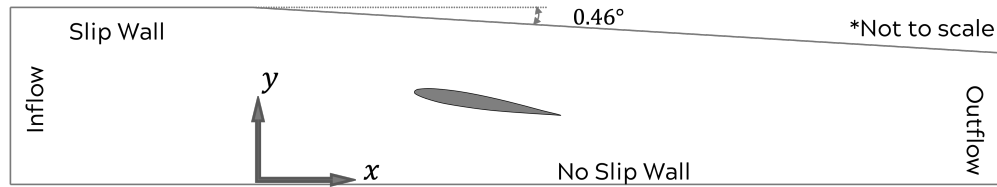


Fig. 4 Geometry layout of 2D CFD grids used for common collaborative grid family.

The topology is fully structured, with hyperbolically extruded boundary layers on the no-slip-wall and airfoil surface. The airfoil topology is a C-Grid type, extended approximately 0.1 m around the surface and a 1 m wake. The wake is then fanned to the outlet. The Elliptic Solver in Pointwise was utilized to smooth the connections between the Cartesian boundary layer grid and the airfoil C-Grid.

C. Grid Refinement

In compliance with the requirements set by the AVT-349 Grid Sharing Committee, a total of five grid levels were generated, ordered such that Grid Level 1 (GL1) is the finest and GL5 is the coarsest. Grid Levels 3 and 5 were obtained by coarsening GL1 by a factor of 2 in all directions, i.e., removing every other node. Grid Levels 2 and 4 were obtained using an open-source refinement script, refining Grid Levels 3 and 5 respectively by a factor of $\sqrt{2}$. The relevant grid metrics for all five grid levels are shown in Table 1.

Grid Level	# Cells	Average Cell Area (m^2)	RMS Cell Area (m^2)
GL1	792,432	4.98×10^{-5}	9.07×10^{-5}
GL2	396,355	9.94×10^{-5}	1.81×10^{-4}
GL3	198,108	1.99×10^{-4}	3.64×10^{-4}
GL4	99,108	3.98×10^{-4}	7.27×10^{-4}
GL5	49,527	7.96×10^{-4}	1.46×10^{-3}

Table 1 Grid metrics for systematically refined 2D grid family.

To assess the "systematicness" of this refinement, the arithmetic average and root-mean-square cell area were output for each grid level. If the refinement of the grid is systematic, the ratio of average to RMS area should be constant for all grid levels. The average and RMS cell areas are shown in Fig. 5.

Additionally, for a systematic grid refinement, it would be expected that Grid Levels 1, 3, and 5 would lie on top of each other, each successively refined grid bisecting each cell face of the previous grid level. This is demonstrated in Fig. 6.

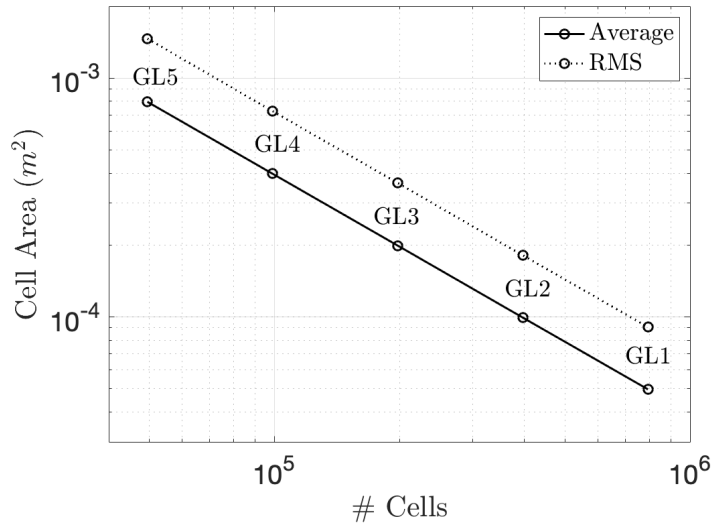


Fig. 5 Arithmetic average and root-mean-square cell areas for each grid level.

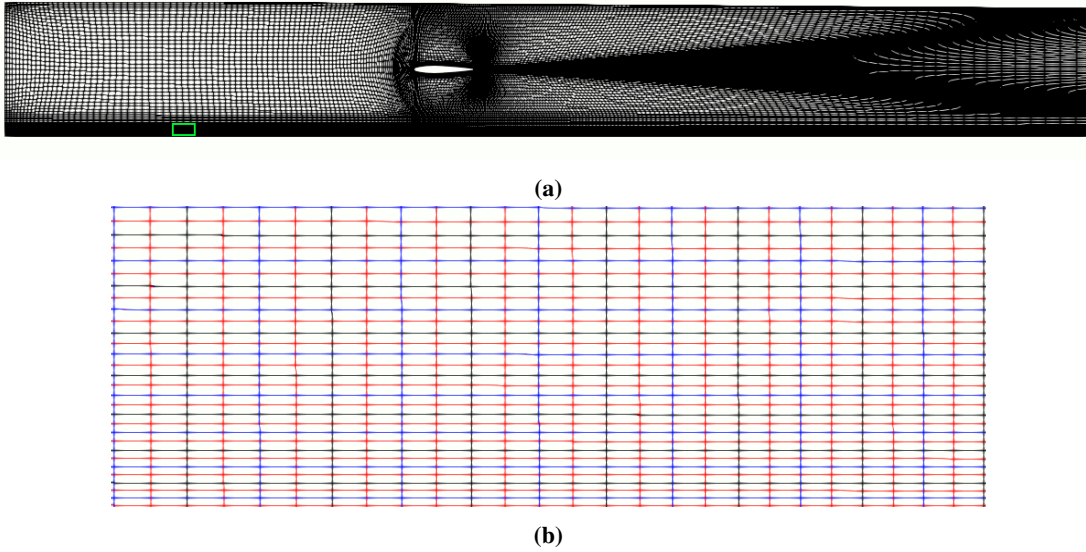


Fig. 6 Grid Levels 1 —, 3 —, and 5 —. Full grid for GL5 shown in (a), zoomed image corresponding to green box for all three levels shown in (b)

D. Virginia Tech Simulations

The Virginia Tech simulations were performed using the HPCMP CREATE™-AV Kestrel KCFD compressible finite-volume solver. Kestrel uses a fully implicit numerical scheme for both governing and turbulence equations that is second order accurate in both space and time. More details on the Kestrel solver can be found in [27].

The inflow is modeled as a uniform momentum source with constant stagnation properties, $p_0 = 94,922.4 \text{ Pa}$, $T_0 = 284.7 \text{ K}$ and the outflow is modeled as a momentum sink with constant static pressure $p = 94,272.0 \text{ Pa}$. All five grid levels were computed in Kestrel for the -10° and $+12^\circ$ cases using the Menter $k-\omega$ SST model [28] to assess the discretization error and grid convergence behavior. The observed order of accuracy was approximately 1.34, and it is theorized that this reduction from second order occurs due to the singularities that develop on the airfoil model leading and trailing edges. After observing the convergence behavior, GL3 was chosen as the main grid for further computations, based on the balance it presented between a rapid computation time and solution accuracy, as the differences between

Grid Levels 1, 2, and 3 were considered negligible (see Appendix VIII.A for more details). Roache’s Grid Convergence Index [29] was used to estimate the discretization error on Grid Level 3, resulting in the approximate uncertainties presented in Table 2.

Parameter	c_p	c_f	U_e	δ^*
RGCI Uncertainty	$+8.8 \times 10^{-4}$	$\pm 1.7 \times 10^{-5}$	-0.039 m/s	$+0.21 \text{ mm}$

Table 2 Estimates of uncertainties due to discretization error for Kestrel simulations.

The Kestrel simulations consistently saw 4 – 5 orders of magnitude residual convergence before stalling. In order to estimate the iterative error associated with this, one solution was converged without flux limiting to 8 orders of magnitude in all equation residuals. This solution was used to estimate the iterative error in the main solutions, which is approximately 0.36% in integrated parameters. More details of the grid convergence study can be found in Appendix VIII.A.

Kestrel solutions are presented using the following turbulence models: Spalart-Allmaras (SA) [30], Menter Baseline $k-\omega$ (BSL) [28], and Menter $k-\omega$ Shear Stress Transport (SST) [28]. The formulation of the models has been modified from the original to achieve optimal performance [27].

E. DLR Simulations

DLR performed the numerical simulations of this test-case using the DLR TAU-code, which is a compressible finite-volume flow solver for hybrid unstructured grids developed at the German Aerospace Center (DLR), see e.g. [31] for an overview. The DLR-TAU code is based on cell-vertex type finite-volume discretization and uses the dual-grid approach. The inviscid fluxes of the mean flow are computed by a second-order central differencing with artificial matrix-valued dissipation. Here a skew symmetric Kok scheme is applied. For the turbulence equations, a second-order central scheme is used for one-equation turbulence models, whereas the first order Roe upwind scheme is applied for two-equation turbulence models and for the differential Reynolds stress models. For a temporal discretization, an implicit backward Euler scheme solved with the lower-upper symmetric Gauss-Seidel (LU-SGS) scheme is used. In addition, due to the low Mach number of this test case, a low-Mach number preconditioning is applied in order to obtain accurate results using the compressible flow solver.

Regarding the RANS turbulence modeling, the negative Spalart-Allmaras (SA) model (SA-neg) [32], the $k-\omega$ SST model [33], and the SSG/LRR- ω Reynolds stress model [14] are used in the present work. The $k-\omega$ SST model used in the present work corresponds to what is called Menter SST Two-Equation Model from 2003 (SST-2003) on the NASA Turbulence Modeling Resource web-site (NASA-TMR). The scalar velocity gradient parameter Ω is defined by the strain invariant rather than magnitude of vorticity in this version. The SSG/LRR- ω Reynolds stress model used in the present work corresponds to what is called “SSG/LRR-omega Full Reynolds Stress Model with Simple Diffusion (SSG/LRR-RSM-w2012-SD)”. The diffusion term is modeled via a simple diffusion rather than a generalized gradient diffusion model.

After a mesh convergence study, the mesh level 3 was chosen for all simulations. The boundary conditions used in the numerical simulations are as follows. At the inlet of the computational domain, a so-called “reservoir-pressure inflow” boundary condition is applied, where the total pressure and total density are prescribed. At the outlet, a so-called “exit-pressure outflow” boundary condition is used, where the static reference pressure is prescribed by default. Optionally, the TAU allows users to prescribe the reference pressure at a desired position in the computational domain, by modifying the exit pressure during the iteration. This functionality, referred to as “Match measured pressure”, is used to obtain the freestream velocity $U_{\text{inf}} = 33.5 \text{ m/s}$ at $x = 0$, which leads to $Re = 2 \times 10^6$ at this position. A non-slip wall boundary is used on the bottom wall, and a slip-wall boundary is used on the top wall. The surface of the airfoil is treated as a non-slip wall. Additionally, DLR provided the results without activating “Match measured pressure”. For these results, the reference pressure is prescribed at the outlet boundary, which leads to $Re = 1.88 \times 10^6$ upstream.

F. University of Melbourne Simulations

The contributions from the University of Melbourne predominantly focus on Machine-Learnt turbulence models that have been trained on the flow case described in Section III.

1. Closure Development Methodology

The most commonly used stress-strain relationship in RANS modeling is the Boussinesq approximation:

$$\overline{u'_i u'_j} = \frac{2}{3} k \delta_{ij} - 2\nu_t S_{ij}, \quad (1)$$

where $S_{ij} = 0.5(\partial U_i / \partial x_j + \partial U_j / \partial x_i)$ is the mean strain-rate tensor. The modification of this relationship is accomplished using the generalized eddy viscosity hypothesis [34]:

$$\overline{u'_i u'_j} = \frac{2}{3} k \delta_{ij} - 2\nu_t S_{ij} + 2k a_{ij}^x, \quad (2)$$

where

$$a_{ij}^x = g_1 V_{ij}^1 + g_2 V_{ij}^2 + g_3 V_{ij}^3 \quad (3)$$

and

$$V_{ij}^1 = \frac{S_{ij}}{\omega} \quad (4)$$

$$V_{ij}^2 = \frac{S_{ik} \Omega_{kj} - \Omega_{ik} S_{kj}}{\omega^2} \quad (5)$$

$$V_{ij}^3 = \frac{S_{ik} S_{kj} - 1/3 S_{nm} S_{nm}}{\omega^2}. \quad (6)$$

Here $\Omega_{ij} = 0.5(\partial U_i / \partial x_j - \partial U_j / \partial x_i)$ is the mean rotation-rate tensor while the coefficients g_i are obtained through GEP as functions of random constants and scalar invariants $I_1 = S_{mn} S_{nm} / \omega^2$ and $I_2 = \Omega_{mn} \Omega_{nm} / \omega^2$. As briefly touched upon in the introduction, the sparseness of the reference data suits the CFD-in-a-loop approach, where a RANS solver is interfaced with GEP to produce the stress closure. The OpenFOAM integration with GEP follows the approach adopted in the heat-flux modeling setup of a previous study [35]. Defining a cost-function to minimise the error between the RANS and the experiment, GEP produces a set of candidate closures which are then evaluated by running the RANS with these candidates. The closures that perform suitably in the evaluation, i.e. have a lower error between the RANS and experiment, are promoted in a survival-of-the-fittest style tournament. The candidates undergo mutation and reproduction to generate a new set of candidate closures and the process continues iteratively for several generations until the best performing model emerges. In this study, the aim is to improve the boundary-layer prediction and so the wall-scaled velocity profiles are considered as the appropriate cost-function, i.e. the aim is to obtain a Reynolds stress closure which improves the u^+ prediction compared to the Boussinesq approximation.

2. Reduced domain

Since the computational cost associated with the model development is directly proportional to the cost of the RANS calculations, a subset of the spatial domain is used such that the domain mimics the 2D boundary layers developing under the different pressure gradient regimes. Thus, a 2D reduced domain that spans 0.1016 to 5.664 m in the x direction and 0 to 0.1778 m in the y direction is considered. The extents depend directly on the availability of the experimental data: in x the static pressure measurements at the wall and in y the velocity profiles. Following this, a grid convergence test is performed, the details of which are provided in Table 3.

Caption	$N_x \times N_y$	Processors
C0	200×50	1
C1	400×100	1
C2	800×200	4
C3	$1,600 \times 400$	4

Table 3 Details of grids of the reduced domain tested. Each subsequent grid starts the calculation from the converged solution of the previous RANS grid level.

In these calculations the steady-state incompressible solver `simpleFoam` is used with a reference density of 1.1077 kg/m^3 and kinematic viscosity of $1.637 \times 10^{-5} \text{ m}^2 \text{ s}^{-1}$. The grid orthogonality allowed the use of a centered second-order

scheme for the gradient estimation while the divergence terms were discretized with a second-order upwind-biased scheme. The inflow ($x = 0.1016$ m) is prescribed with profiles of the velocity, k and ω , which have been obtained by running a precursor RANS of the full setup, i.e. the airfoil grid and extracting the profiles at $x = 0.1016$ m. The outflow ($x = 5.664$ m) is prescribed as zero gradient for all quantities, the wall ($y = 0$ m) prescribed with zero velocity, zero k and the `omegaWallFunction`. The pressure is specified to zero gradient on the inflow, wall and outflow while the static pressure values from the experiment values are prescribed at $y = 0.1778$ m. This setup decouples the pressure from the velocity field and can produce significant computational cost savings. For reference, on 1 processor the coarsest grid C0 takes about 10 seconds for 500 iterations as opposed to the coarsest airfoil domain grid L5 taking about 530 seconds for 500 iterations.

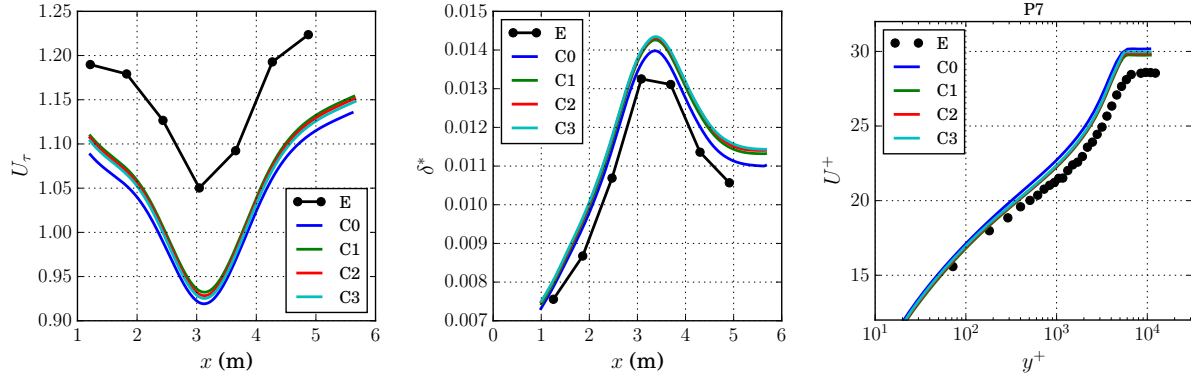


Fig. 7 Grid convergence test on the reduced domain, comparing the baseline RANS on the wall-friction velocity (u_τ), the displacement thickness (δ^*) and the wall-scaled velocity (u^+) for location P7.

Select results of the grid convergence performed for the 12° angle of attack case are presented in Fig. 7, where from the different quantities it is clear grid level C1 is a suitable choice to conduct the model development exercise. It must be pointed out that the purpose of the present study is to evaluate whether a closure can be obtained to produce improvement over the baseline RANS with the availability of the limited data. As such, the goal is not to find the “best” model, which would require a detailed study of various parameters governing the GEP algorithm as well as including additional reference data sets. As such, only the 12° angle of attack case is considered for demonstration. The converged solution on level C1 is used as the initialization for each candidate model’s evaluation in the RANS. The GEP algorithm is run for 100 generations with 1000 candidate models generated, competing in tournaments of size 12 with 10 mating operations per generation. This means that there are 120 RANS evaluations per generation, which takes about 40 hours to finish for the 100 generations. The final expression for the Reynolds stress closure is given by:

$$\begin{aligned} a_{ij}^x = & V_{ij}^1 (2.0I_1^4 - 0.02I_1^3 + 3.482I_1^2 - 2.0I_1 + I_2 - 0.02) \\ & + V_{ij}^2 (I_1^2 + I_1I_2 + 1.741I_1 + 1.0) \\ & + V_{ij}^3 (3I_1^2 + 2.0I_1 - 1.0) \end{aligned} \quad (7)$$

The performance of the above closure is presented in Fig. 8, where a marked improvement is observed in u_τ and u^+ . This is reassuring since the model was developed by minimizing the error between the experimental u^+ and the candidate model’s u^+ . However, the prediction of δ^* worsens with the new closure, which can be attributed to an enhanced deviation of the streamlines, thereby increasing the flux out of the $y = 0.1778$ m plane by 30%.

Nevertheless, the results in Fig. 8 show that re-developing turbulence stress closures is a good option to improve the prediction of the boundary layer flows under pressure gradients.

3. Airfoil section domain

The assessment of the model in Eq. 7 was conducted in a reduced domain that decoupled the pressure from the velocity field since the pressure distribution was known and fixed. In most cases, this is not known *a priori* and so, in this section, the model developed on the extreme APG case (12° angle of attack) is tested on the airfoil section domain

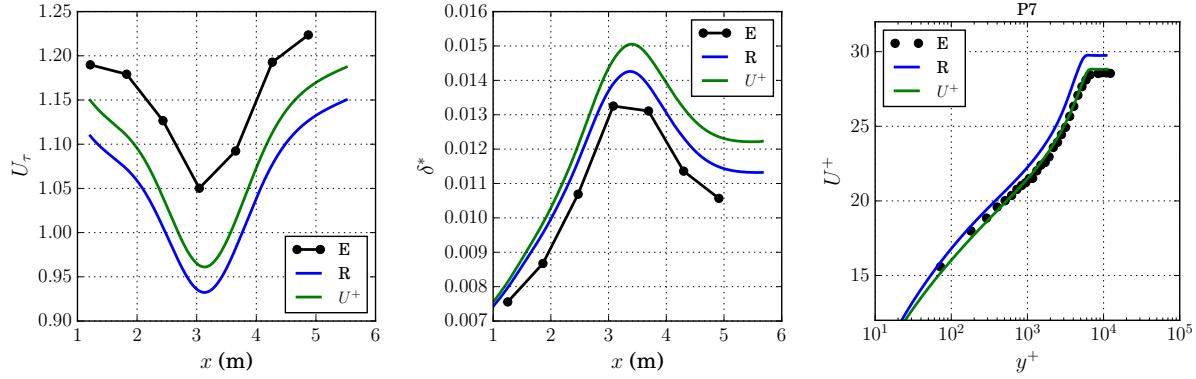


Fig. 8 Comparison of the baseline RANS to the new Reynolds stress-closure (using u^+ as the cost-function) on the wall-friction velocity (u_τ), the displacement thickness (δ^*) and the wall-scaled velocity (u^+) for location P7.

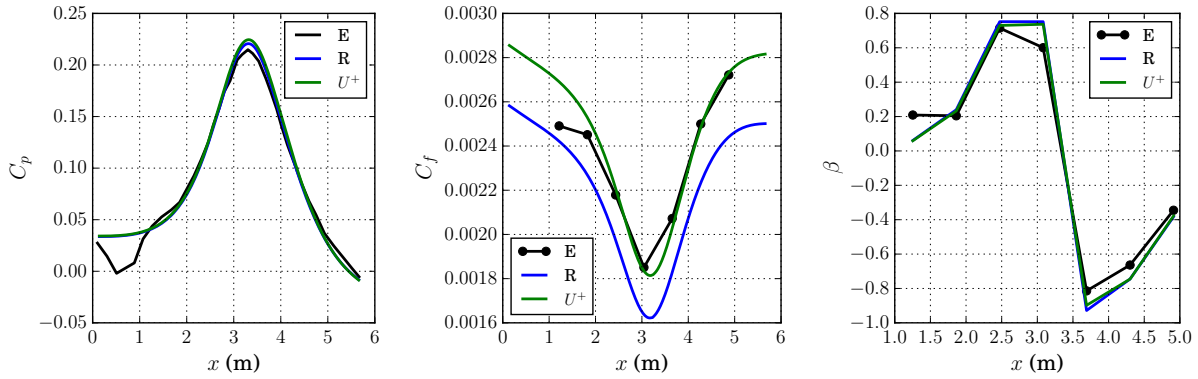


Fig. 9 Comparison of the streamwise evolution of c_p , c_f and β between the baseline RANS (legend R) and the machine-learned model using u^+ as the cost-function.

grids provided by VT. A grid convergence was first conducted on the different resolutions made available, where it was decided that Grid Level 4 was sufficiently fine enough to provide a solution with acceptable numerical uncertainty (see Appendix VIII.B for convergence details). The domain inlet provided a volumetric flow rate of $0.61975 \text{ m}^3/\text{s}$ for a bulk inflow velocity of 33.5 m/s . The inflow turbulence kinetic energy and specific dissipation rate were specified with a turbulence intensity of 0.02% and a mixing length of 0.005 m respectively. The large non-orthogonality in the grids required a cell-limited second-order scheme for the gradient estimates while the divergence terms used a cell-limited version of the second-order upwind-biased scheme. The cell-limiter bounds the values of the quantities such that they do not fall outside the values of the immediately surrounding cells. Additionally, 3 non-orthogonal corrector loops for the pressure solution were employed to compensate for the grid non-orthogonality and larger relative tolerance levels were utilised. The converged RANS solution was used as the initialization for the machine-learned model's calculation. Figure 9 plots the streamwise variation of c_p , c_f and β where the two calculations show a good agreement in the c_p distribution with the experiment. The use of the new stress closure shows an improvement in the c_f profile, which was also observed in the reduced domain calculations through u_τ . The displacement thickness (not shown here) is over-predicted similar to the reduced domain calculations. As a consequence, the estimation of β remains the same with the new stress closure since the increase in τ_w is compensated by a comparable increase in δ^* , thereby maintaining a similar ratio between the baseline and machine-learned RANS.

The locally-normalized velocity profiles at three measurement locations are presented in Fig. 10, where the baseline RANS and the GEP model agree well with the experimental data. The figure also plots the wall-scaled velocity profiles, where the addition of the new turbulence closure leads to an improvement in the smaller y^+ values. The shape of the curves show a minor difference (considering location P7) compared with the profiles in the reduced domain computation.

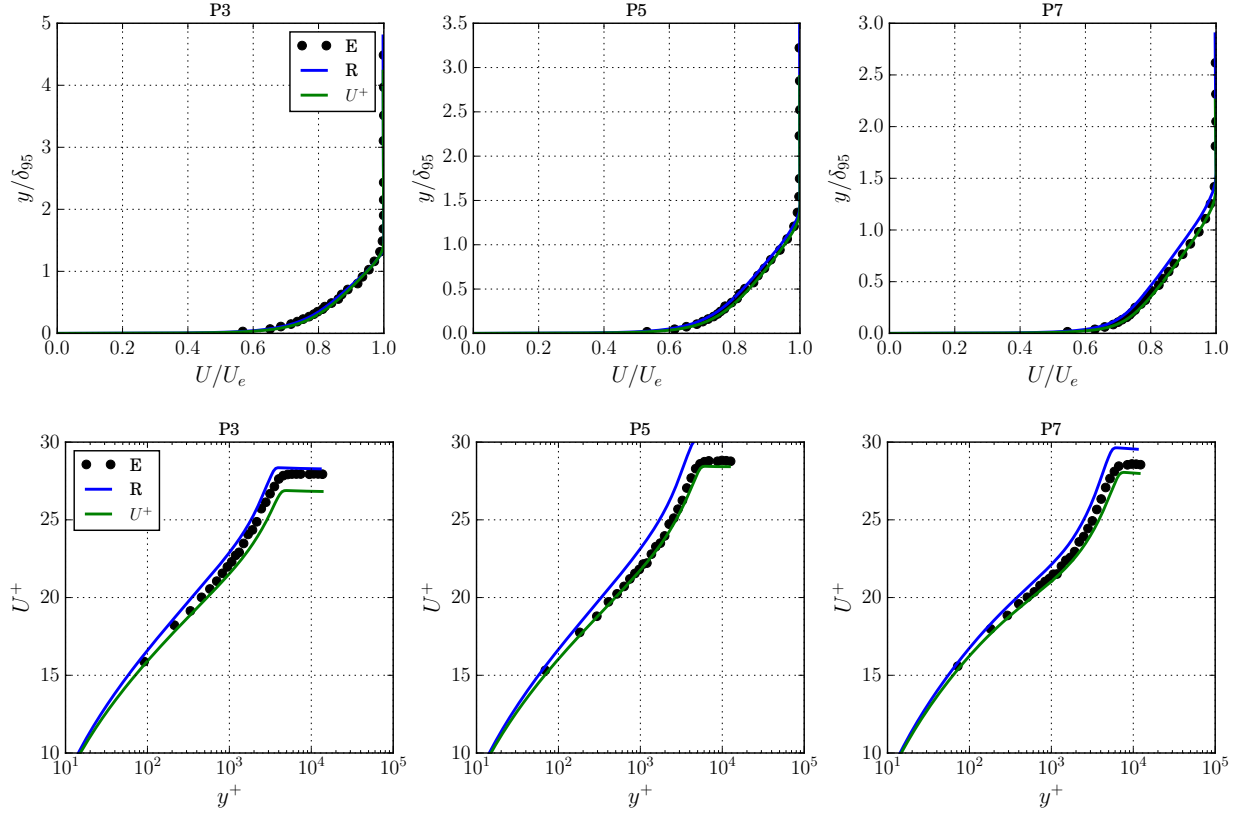


Fig. 10 Comparison of the wall-normal profiles of u/U_e and u^+ between the baseline RANS (legend R) and the machine-learned model using u^+ as the cost-function.

Finally, the wall-scaled Reynolds stress profiles are presented in Fig. 11. The red datapoint in the figure corresponds to a wall-normal location of 6 mm, the data under which the experimental measurements are known to damp the magnitudes. Even so, for $y^+ < 10^3$, both calculations show an overprediction in the magnitudes where the wall-normal location is larger than 6 mm. However, the GEP model matches the experimental data better than the baseline RANS for $y^+ > 10^3$. These results demonstrate that the turbulence closure developed on the reduced domain translates its improvements when applied to the full CFD domain, thus serving as an attractive choice when developing turbulence closures cost-effectively. Further investigations are warranted in developing a more robust closure that improves the integral quantities as well as the wall-scaled quantities. This can be realised by potentially using additional quantities as part of the cost-function, such as δ^* or involving more features into the expression in Eq. 2.

G. Chalmers University of Technology Simulations

The submitted results from Chalmers University of Technology were run with OpenFOAM v2006. OpenFOAM is a set of open source C++ libraries, primarily used for CFD. The solver used for this work was `simpleFoam`, as provided with the installation. The standard SIMPLEC algorithm was used with under relaxation. The spatial discretization is performed using a cell centered co-located finite volume (FV) method with arbitrary cell-shapes.

All simulations were run with the second order upwind scheme `linearUpwind` for the convective momentum term, pure upwind for advection of turbulent quantities, and second order for all other terms. Simulations were run for 5000 iterations, but convergence was for most meshed achieved much earlier; an example plot of the residuals is provided in Figure 12.

For turbulence modelling, the as distributed $k - \omega$ -SST model was used. According to the documentation, it follows the implementation in [36] with updated coefficients from [33] but still using the consistent production term from the first paper.

The following boundary conditions were applied:

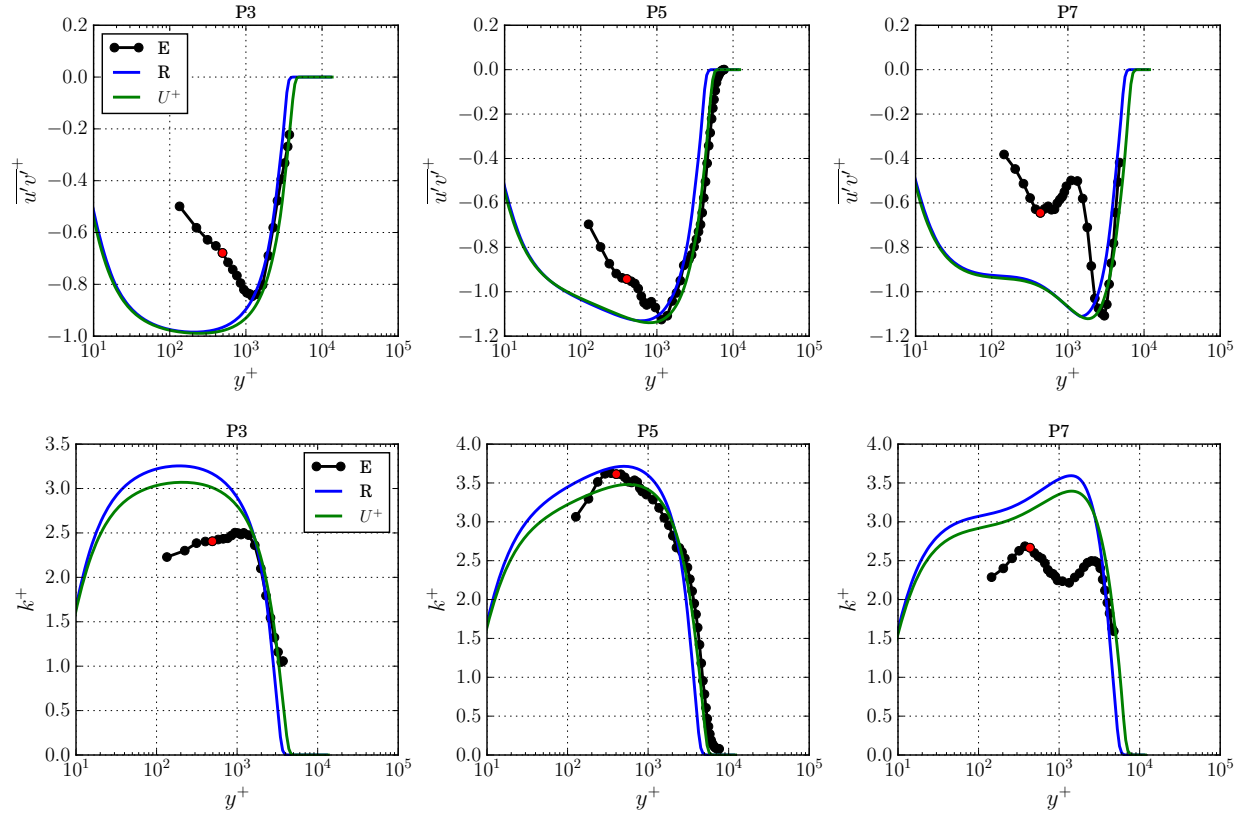


Fig. 11 Comparison of the wall-normal profiles of $\overline{u'v'}^+$ and k^+ between the baseline RANS (legend R) and the machine-learned model using u^+ as the cost-function. Red data point represents point below which data is known to be attenuated.

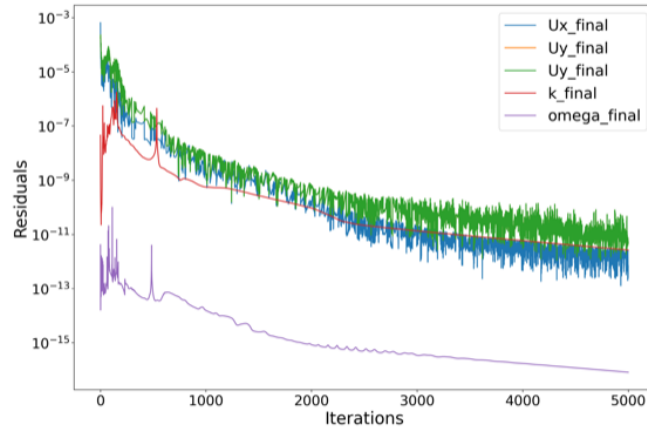


Fig. 12 Example L2 norms of steady residuals from Chalmers OpenFOAM simulations.

- The bottom wall and the airfoil were set as a hydraulically smooth no slip surface. For omega the general `omegaWallFunction` was used and for k the `kLowReWallFunction`. As the meshes are wall resolved ($y^+ < 1$), these boundary conditions should then act as no slip.
- On the outflow boundary, the `inletOutlet` conditions is used, which corresponds to a fixed pressure and

Neumann condition for other variables.

- Fixed velocity is set on the inflow boundary, with $U = (33.5, 0, 0)$. Turbulence inflow was set assuming 0.02% turbulence intensity and a turbulent viscosity ratio of 10, in this case then $k_{inflow} = 6.7335e - 5$ and $\omega_{inflow} = 0.44$.

H. MARIN/IST Simulations

1. ReFRESH Flow Solver

ReFRESH is a CFD solver based on a finite volume discretization of the continuity and momentum equations written in strong conservation form. The solver uses a fully-located arrangement and a face-based approach that enables the use of cells with an arbitrary number of faces. Picard linearization is applied and segregated or coupled approaches are available with mass conservation ensured using a SIMPLE-like algorithm [37] and a pressure-weighted interpolation technique to avoid spurious oscillations [38]. A volume of fluid technique is used for multiphase flows and several alternative mathematical formulations can be used to solve turbulent flow. Thorough code verification is performed for all releases of ReFRESH [39].

In the present simulations, a single-phase, incompressible fluid is adopted and time-averaging is applied to the continuity and momentum equations to obtain the Reynolds-averaged Navier-Stokes (RANS) equations for a statistically steady flow. Two eddy-viscosity turbulence models are used:

- 1) One-equation Spalart & Allmaras model [30];
- 2) Two-equation, Shear-Stress Transport (SST), $k - \omega$ model [33].

2. Numerical settings

Simulations were performed with the segregated approach, which means that momentum equations, pressure-correction equation derived from mass conservation and turbulence quantities transport equations are solved sequentially. All transport equations are discretized with second-order schemes and limiters are included in the schemes applied to the convective terms. Linear systems of equations are solved with the generalized minimal residuals (GMRES) method with the exception of the pressure correction equation that is solved with a conjugate gradient (CG) method. Jacobi preconditioning is used for all systems.

Iterative error is controlled by the maximum of normalized residuals, which are equivalent to dimensionless dependent variables changes in a simple Jacobi iteration. Iterative convergence criteria requires that the maximum normalized residuals of momentum and continuity (pressure correction) equations are smaller than 10^{-10} .

Calculations were also performed with a first-order upwind scheme applied to the convective terms of the turbulence quantities transport equations. These simulations were used to generate the initial condition for the simulations performed with second-order upwind applied to the turbulence quantities transport equations.

3. Problem Settings

The proposed test case is two-dimensional and the domain is almost rectangular as described in Section IV.B. In the two proposed settings, the NACA 0012 airfoil is placed at angles of attack of $\alpha = -10^\circ$ and $\alpha = 12^\circ$. The Reynolds number based on the reference velocity U_∞ , chord of the airfoil c and kinematic viscosity of the fluid ν of

$$Re = \frac{U_\infty c}{\nu} = 2 \times 10^6 .$$

4. Boundary conditions

Boundary conditions are required at five boundaries: inlet, outlet, bottom, top and surface of the airfoil.

Inlet boundary Specified conditions are imposed to all flow quantities except the pressure that is obtained from linear extrapolation from the interior of the domain. For both settings, the specified values are:

$$u_x = u_\infty, u_y = 0, I = 0.01 \text{ and } \nu_t = 0.02\nu .$$

u_x is the horizontal velocity component, u_y is the vertical velocity component, I is the turbulence intensity and ν_t is the eddy-viscosity. The dependent variables of the turbulence models, $\tilde{\nu}$, k and ω , are derived from I and ν_t .

Outlet boundary Pressure is specified as a constant at the outlet boundary and derivatives of all remaining dependent variables with respect to x are set equal to zero.

Top boundary Free slip conditions are applied at the top boundary. This implies that the velocity component normal to the boundary is set equal to zero. The derivatives of all remaining dependent variables with respect to the normal direction to the boundary are set equal to zero.

Bottom boundary and airfoil surface No-slip and impermeability conditions are applied at the bottom boundary and airfoil surface. As a consequence velocity components, turbulence kinetic energy and undamped eddy-viscosity are set equal to zero. ω is specified at the near-wall cell centre using the analytical solution. Pressure derivative in the normal direction to the wall is set equal to zero.

5. Iterative convergence

Calculations were performed in the five grids provided by Virginia Tech for each test condition ($\alpha = -10^\circ$ and $\alpha = 12^\circ$). The solution strategy was identical for the two turbulence models:

- Determine the flow field in the five available grids using first-order upwind in the convective terms of the turbulence quantities transport equations.
 - 1) Calculate the solution in the coarsest grid (Grid 5) copying the inlet conditions to the complete domain to obtain the initial condition.
 - 2) Solve grids 4 to 1 interpolating the starting condition from the previous grid refinement level.
- Solve all grids using second-order upwind in the convective terms of the turbulence quantities transport equations using as initial condition the flow fields obtained with the previous simulations.

Figures 13 and 14 present the L_∞ and L_2 norms of the normalized residuals and changes between consecutive iterations of the simulations performed in GL1 with the second-order schemes with limiters also applied to the turbulence quantities transport equations.

Iterative convergence criteria is satisfied by all transport equations, except the k equation in the $k - \omega$ SST simulations. The stagnation of the k equation iterative convergence occurs at a region where the eddy-viscosity is negligible and is a consequence of the techniques used to prevent negative turbulence quantities.

It must also be stated that there was no attempt to optimize under-relaxation coefficients to enhance the efficiency of the iterative convergence.

6. Numerical uncertainty estimation

All simulations were performed with 14 digits precision and so the contribution of the round-off error to the numerical error is negligible. The present iterative convergence criteria ensures that the numerical error is dominated by the discretization error. In such conditions, the discretization error can be estimated with power series expansions [40] to obtain the numerical uncertainty of any local or functional quantity of interest.

The MARIN/IST submission data was obtained in the finest grid (Grid 1). Numerical uncertainties were estimated for all the quantities of interest using the solutions obtained in the five grids.

I. Sirehna Naval Group Simulations

All submissions provided by Naval Group were computed with STAR-CCM+. STAR-CCM+ is a generic multi-purpose commercial flow solver originally developed and distributed by CD-Adapco, and now part of Siemens PLM Software engineering suite. This is a finite volume based solver running with unstructured meshes composed of arbitrary shaped cells (hexahedra dominant or polyhedra). It provides a range of models for turbulence, as well as many other capabilities relevant to marine applications such as multiphase flows and mesh motions. Steady-state Reynolds-Averaged Navier-Stokes (RANS) approaches and unsteady Large-Eddy Simulation (LES) and Detached-Eddy Simulation (DES) are available. Steady or unsteady flows can be resolved by means of a coupled solver or a segregated solver using predictor / corrector algorithm to couple pressure and velocity (SIMPLE-like algorithm). It uses co-located variables with a Rhie-Chow type pressure-velocity coupling.

In the context of this project, Naval Group used the steady state, incompressible, segregated flow solver with a $k - \omega$ SST turbulence model. The turbulence model version is referenced as the original publication of 1994 [28]. However, the documentation specifies a modification from the original model which uses the modulus of the vorticity

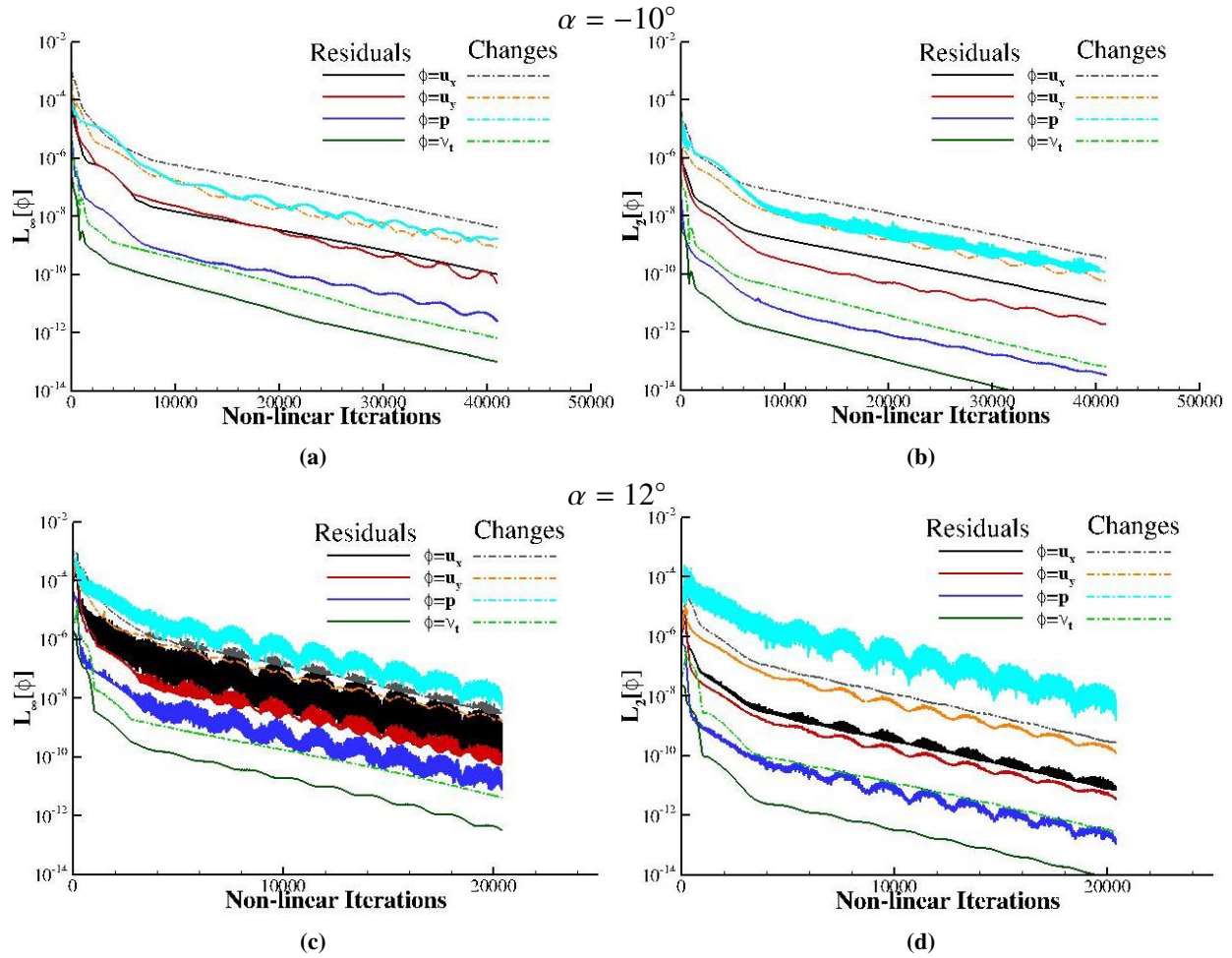


Fig. 13 Iterative convergence of the MARIN/IST calculations performed with the Spalart-Allmaras one-equation eddy-viscosity model.

tensor by switching to the use of the modulus of the strain tensor for the computation of the eddy viscosity. This slight modification is said to extend the applicability of the model beyond aerodynamic applications. Furthermore, a Durbin realizability constraint is used by default instead of the original Menter proposal. This realizability constraint has been switched off in these computations, after observing no particular effect on the results for this exercise. A specific model is used for managing wall functions (All y^+ wall treatment), but as the y^+ induced by the grid provided in the project is much lower than 1, this specific model does not apply any wall function and the viscous sub-layer could be resolved.

The numerical discretization methodology used implies a second order upwind scheme for segregated flow solver and turbulence terms.

The boundary conditions employed are matching the instruction requirements. The top wall is considered as a slip wall and the bottom wall and NACA0012 surface are considered as smooth no-slip walls. The upstream boundary is considered as a velocity inlet and the downstream boundary as a pressure outlet with a uniform pressure fixed as the reference pressure indicated in the instructions.

The convergence is monitored given the L_2 norm of the STAR-CCM+ residuals, which were made non-dimensional given the value at the first iteration. Examples of convergence plots are given in Fig. 15.

Computations were made with Grid Levels 5, 4 and 3. The results using GL3 are retained for this publication.

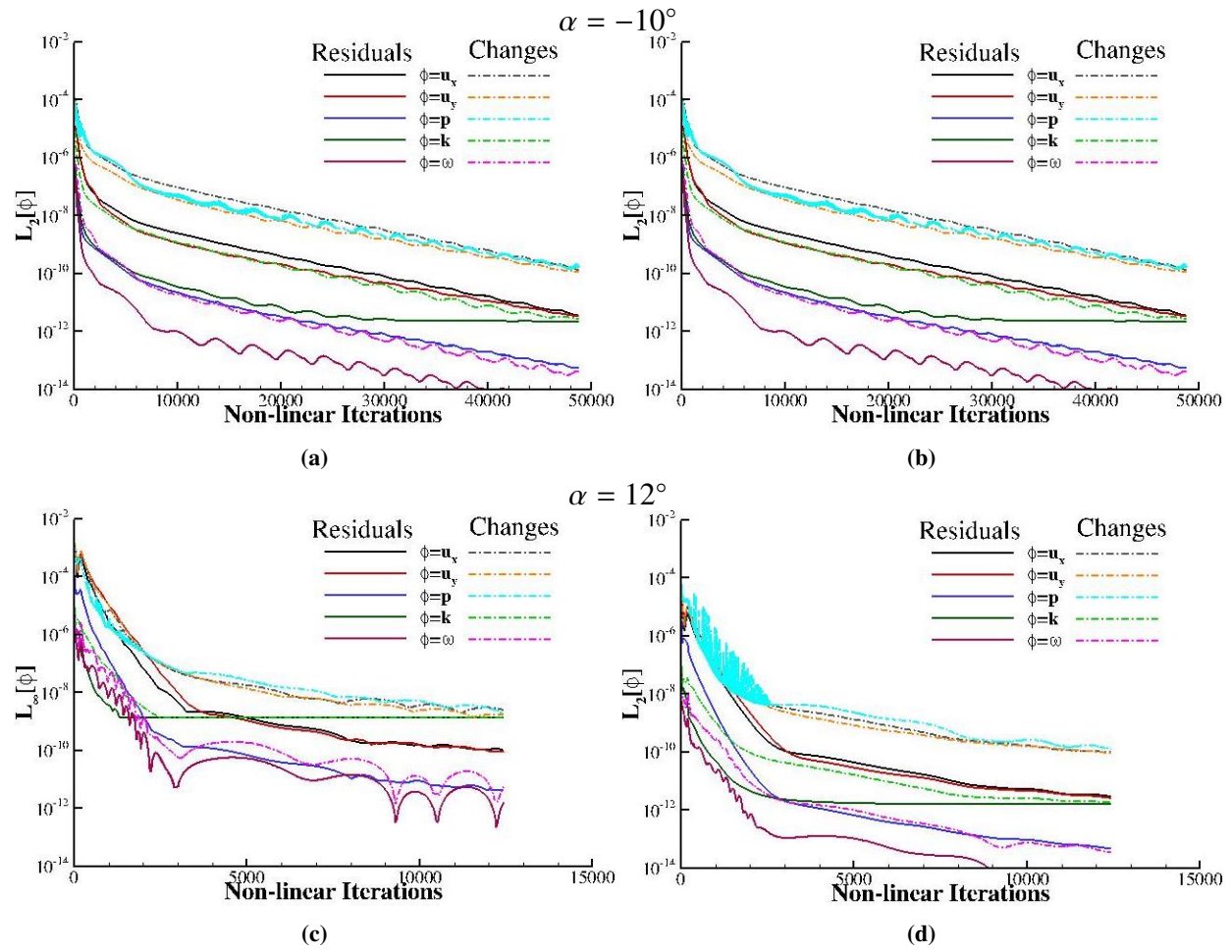


Fig. 14 Iterative convergence of the MARIN/IST calculations performed with the $k - \omega$ SST two-equation eddy-viscosity model.

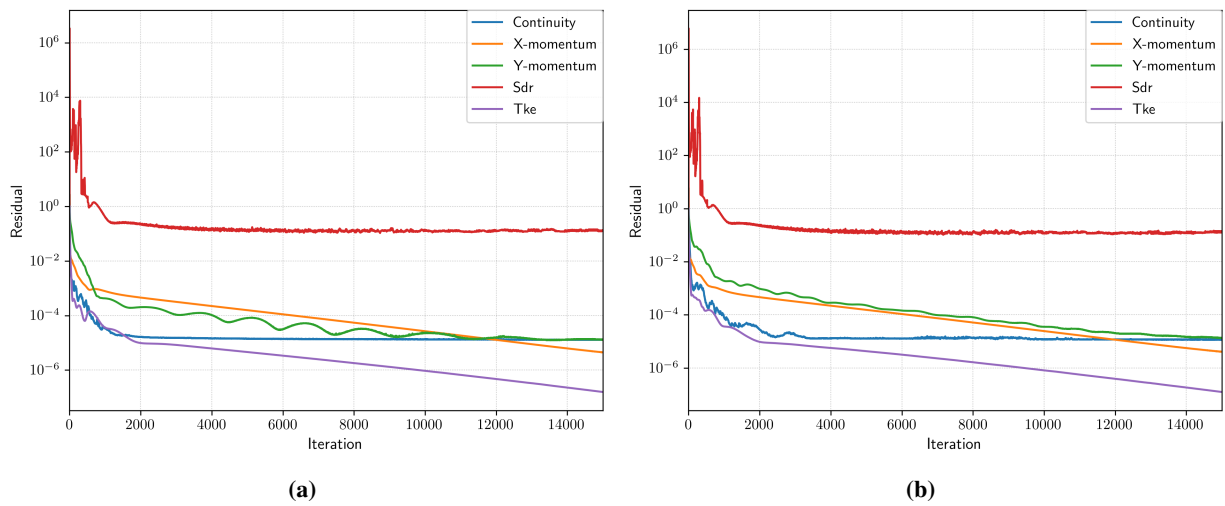


Fig. 15 Sirehna STAR-CCM+ L_2 norm residuals for -10° (a) and 12° (b) cases.

V. Results

Results were obtained using the solvers and methods described in Section IV for two flow cases, with the airfoil model positioned at $+12^\circ$ and -10° .

A. Solution Comparisons

The first comparison assessed was between the various CFD solvers represented within the collaborative group, all using the common grid family and the Menter $k-\omega$ SST turbulence model [28].

1. $\alpha = +12^\circ$

Figure 16 shows the pressure (normal) (Fig. 16a) and skin friction (shear) (Fig. 16b) force coefficients as a function of downstream boundary layer development for the $\alpha = +12^\circ$ case. With the model at a positive angle of attack, the mean pressure coefficient initially grows downstream, an adverse pressure gradient, before reaching a maximum beneath the model quarter chord and returning towards zero, a favorable pressure gradient. The skin friction shows an opposing trend, decreasing when the pressure gradient is adverse and *vice versa*. The maximum displacement of the force coefficients caused by the presence of the airfoil is around 0.2 for pressure and 1×10^{-3} for skin friction.

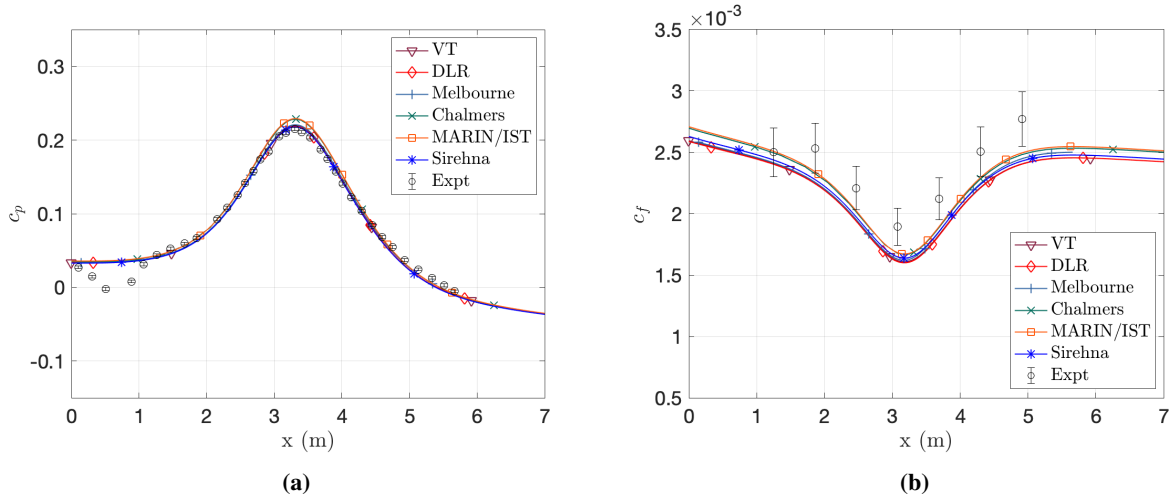


Fig. 16 Pressure (a) and skin friction (b) coefficients as computed for the 12° case using all solvers with Menter SST.

In general, the agreement with experimental results for the pressure coefficient (Fig. 16a) is quite good, with the notable exception of a dip in experimental c_p between $x = 0$ and $x = 1$ m. This is attributed to 3D effects at the end of the VTSWT contraction that are not captured in a 2D domain. The solver-to-solver agreement is also excellent, except at the peak pressure point where the Chalmers and MARIN/IST data over-predict the peak pressure compared to both experiment and the other computational solutions. This is attributed to the fact that the two outliers, Chalmers (OpenFOAM) and MARIN/IST (ReFRESCO) are both incompressible solutions. The computations from Sirehna Naval Group (STAR-CCM+) are also incompressible, but match better with the compressible solutions, owing to a difference in adjustment to the non-dimensional force coefficient referencing scheme for incompressible solutions, i.e., the method of calculating V_{ref} and ρ_{ref} .

Similar observations are made between different computational solutions in the skin friction development. However, none of the CFD solutions show as good agreement with experiment for the skin friction as they did for the mean pressure, consistently under-predicting by around $\delta(c_f) \approx -2 \times 10^{-4}$. The computational solutions do almost cross into the experimental error bars at most streamwise locations.

Figure 17 shows the growth of the boundary layer through this bi-directional pressure gradient. It was observed early on that the traditional 99% edge velocity boundary layer thickness showed great discrepancies between different solvers and experiments and, as such, it was decided to use a definition that the boundary layer thickness, δ , is the point at which 95% of the edge velocity is recovered. This definition proves more robust.

The 95% edge velocity (δ) (Fig. 17a), displacement (δ^*) (Fig. 17b), and momentum (θ) (Fig. 17c) thicknesses all grow at a consistent rate that is disrupted by the presence of the airfoil between $x = 2$ and $x = 5$ m. In the initial, adverse, pressure gradient, δ , δ^* , and θ all experience an increase in growth rate that reaches a peak boundary layer thickness around the model quarter chord. Downstream of this point, in the secondary, favorable, pressure gradient region, the boundary layer is compressed, shrinking back towards where it might have been had the model not been present.

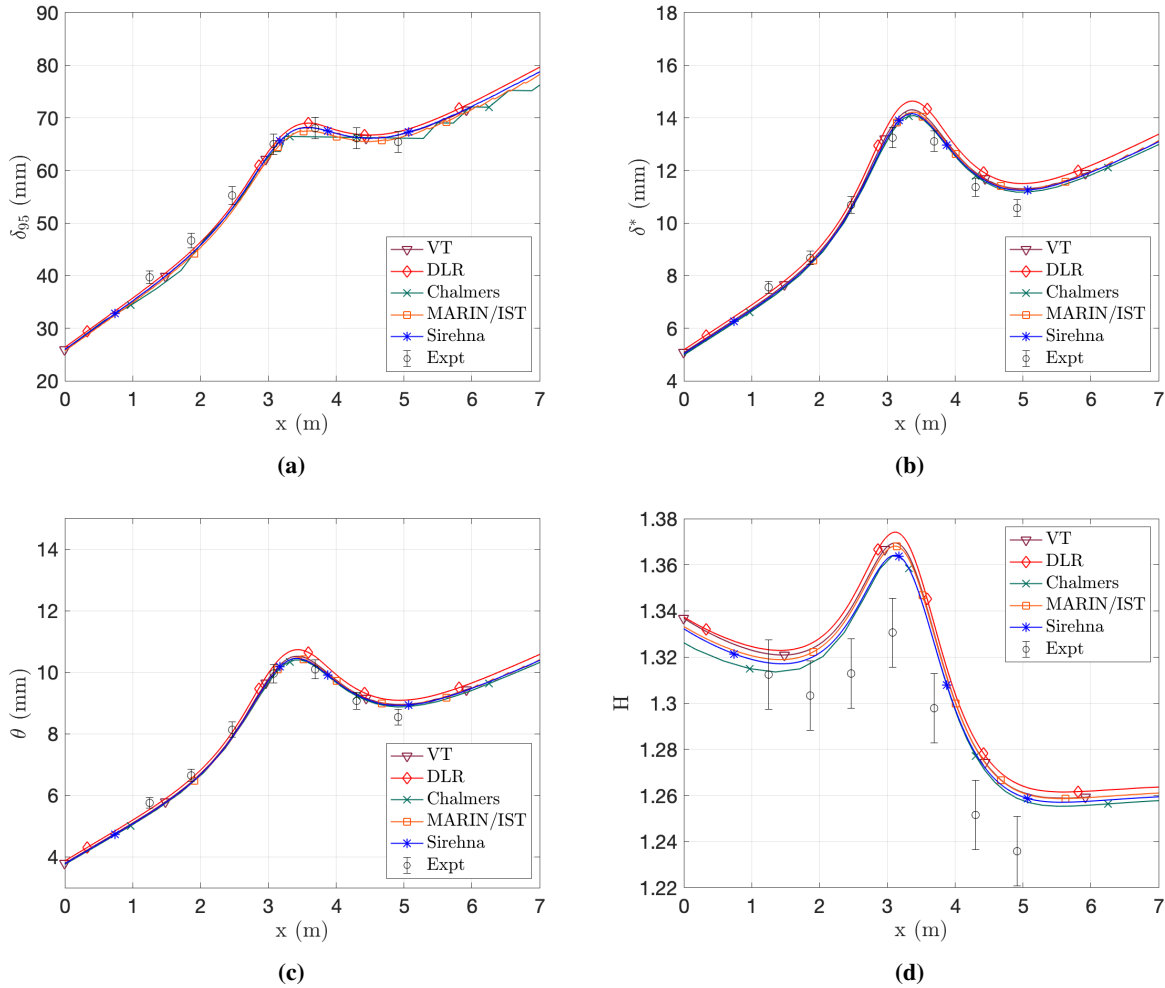


Fig. 17 95% edge velocity (a), displacement (b), and momentum (c) thicknesses and shape factor (d) as computed for the 12° case using all solvers with Menter SST.

The solver-to-solver agreement for δ , δ^* , and θ are quite good. The lone outlier is the DLR-TAU solution, which over-predicts δ^* and θ by around 5%. The TAU code outputs the boundary layer parameters directly, whereas the parameters were computed in post-processing for the other codes. In theory, the computations should be identical, but this is most likely cause for this discrepancy. The CFD-to-experiment agreement is also good for the boundary layer growth. In the secondary, favorable, gradient region the experiment shows a more aggressive compression than the CFD computes.

The shape factor, H , (Fig. 17d) shows more variation both between solvers and between the CFD and experiment results. All solvers over-predict H by $\approx 3\%$, though the incompressible solutions (Chalmers, MARIN/IST, and Sirehna) appear to do so less. This would appear to indicate that the agreement observed in Fig. 17b and Fig. 17c is less good than it appears to the naked eye.

There are two primary ways by which the degree of "non-equilibrium" of these flow cases might be assessed. The first is to observe the streamwise evolution of the Clauser parameter β (Fig. 18a). Clauser [1] postulated that a boundary layer flow would depart from equilibrium if β were not constant. β is continually varying for this flow case, as shown in

Fig. 18a, increasing upstream of the model to a maximum around 1, then rapidly (in space) reversing to an equal and opposite pressure gradient downstream. The solver-to-solver agreement for the Clauser parameter is quite good, as is the agreement with experiment. This is not altogether surprising given the way in which β is defined; it might be expected that errors in either computation or experiment would cancel out.

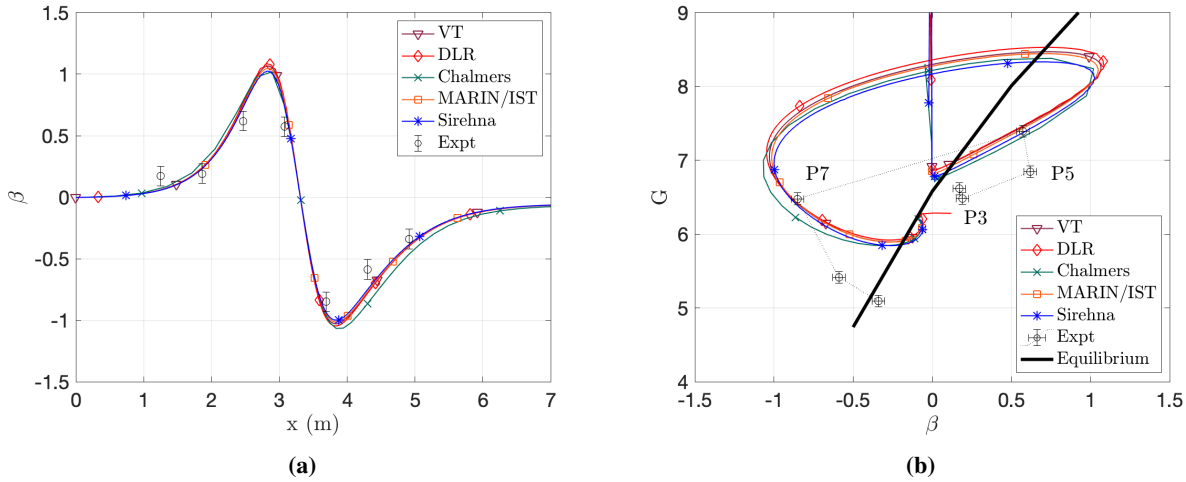


Fig. 18 Clauser parameter (a) and defect shape factor as a function of Clauser parameter (b) as computed for the 12° case using all solvers with Menter SST.

The second measure of non-equilibrium is given in the discussion of Mellor & Gibson [4], who postulated that there is a universal relationship between β and the defect shape factor, G , for an equilibrium boundary layer. This relation is plotted in Fig. 18b along with the data from experiment and computation. The data for this bi-directional pressure gradient flow case circles around the equilibrium curve of Mellor & Gibson, first one way then the other as the pressure gradient flavor reverses. The maximum deviation from the equilibrium curve occurs at P7 ($x = 3.69$ m, $\beta \approx -0.7$), just downstream of the pressure gradient cross-over. It has been observed previously in this case that this is the location where the boundary layer shows the greatest historical and non-self-similar behavior [7–9].

The solver-to-solver agreement for the G - β relationship is good, but the agreement between CFD and experiment is less so. The CFD predicts near perfect agreement with the equilibrium curve at both the inflow and outflow of the test section, where the experiment retains some deviation there. It is unclear if this is due to experimental error, lack of historical and 3D effects that would be present in the experiment but not replicated in the computation, or modeling error.

Figure 19 shows viscous normalized velocity (Fig. 19a-c), turbulent kinetic energy (TKE) (Fig. 19d-f), and Reynolds shear stress (Fig. 19g-i) profiles at the three primary assessment locations, as discussed in Section III.

Solver-to-solver agreement of the velocity profiles (Fig. 19a-c) is quite good through the entire boundary layer. The CFD and experiment match well in the logarithmic region, but the CFD over-predicts the magnitude of u^+ in the wake, most likely due to the under-prediction of skin friction. At P7 (Fig. 19c), the experimental data shows a suppression of u^+ in a region between the log layer and the wake, between $y^+ = 300$ and $y^+ = 1000$, which appears to be, at least qualitatively, somewhat captured in the CFD solutions. It is assumed from the experimental data that the development of this region is a consequence of the departure from equilibrium that occurs as the pressure gradient rapidly reverses signs, and, as such, it is somewhat surprising that the CFD appears to capture this effect. In the higher portions of the logarithmic region, particularly at P3, the CFD results seem to predict a slope value for the Law of the Wall that is slightly steeper than the classical $1/0.41$. Such steepening of the logarithmic slope has previously been observed in numerical solutions at high Reynolds number [41].

The experimental results for turbulent stresses are obtained from planar Particle Image Velocimetry [9]. Within ≈ 6 mm of the wall (y/δ of ≈ 0.167 , 0.120 , and 0.0923), the resolution of the images became too coarse to properly resolve the v' component, resulting in an under-measurement of TKE and $\overline{u'v'}$ stress. This cut-off is computed and marked in a red line on the turbulence figures.

The solver-to-solver agreement for the TKE (Fig. 19d-f) and $\overline{u'v'}$ Reynolds shear stress (Fig. 19g-i) is decent, but not as good as observed in mean variables above. The CFD-to-experiment agreement is lacking for the turbulence profiles,

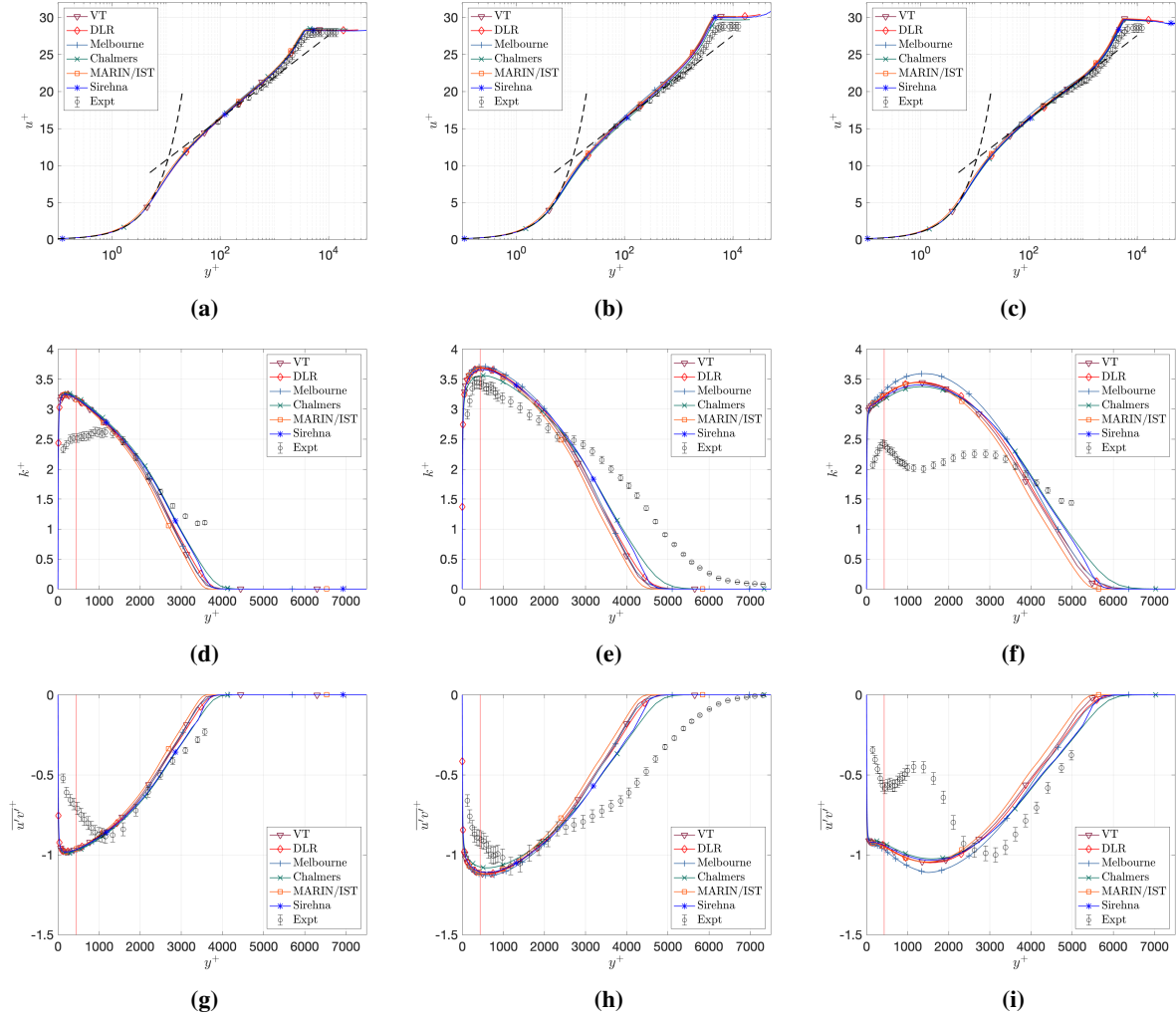


Fig. 19 Velocity (a-c), TKE (d-f), and Reynolds shear stress (g-i) profiles at the three primary assessment locations P3, P5, and P7 (left, middle, right columns respectively) as computed for the 12° case using all solvers with Menter SST. Linear sublayer and Law of the Wall with $\kappa = 0.41$ and $B = 5.1$ marked with black dashes.

particularly in the more downstream, stronger pressure gradient locations. At P5, CFD and experiment agree well on the peak stresses, but the CFD shows a steeper reduction into the free-stream than the PIV results. At P7, the PIV shows an interesting, double-peak stress profile that is not well captured in the CFD. This is believed to be a consequence of the out-of-equilibrium behavior that arises due to the rapid pressure gradient reversal, and it appears, based on these results, that the SST model is not fully replicating this behavior.

2. $\alpha = -10^\circ$

The second flow case, with the model positioned at $\alpha = -10^\circ$, is in many ways the opposite case. As shown in Fig. 20a, the mean pressure coefficient initially decreases in a favorable gradient before reversing to adverse in the downstream region. Again, the skin friction (Fig. 20b) shows the opposite trend to the pressure. The negative angle of attack case, however, shows a greater overall deviation due to the presence of the model. Where the $+12^\circ$ case showed a maximum deviation of 0.2 in the pressure coefficient, the -10° case shows a maximum pressure magnitude of double that, 0.4. This effectively illustrates the difference between the suction and pressure side of the airfoil flow, in that the pressure drop around the suction side will be greater than the pressure increase on the opposing surface.

The various flow solvers again show excellent agreement between themselves and with the experiment for the

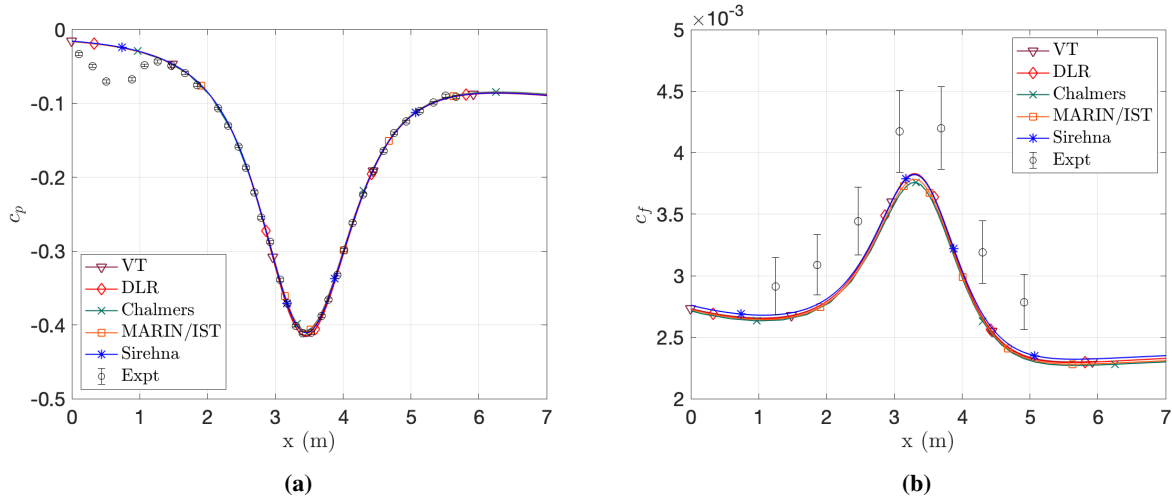


Fig. 20 Pressure (a) and skin friction (b) coefficients as computed for the -10° case using all solvers with Menter SST.

pressure coefficient evolution. The discrepancy between compressible and incompressible solvers that persisted in the $+12^\circ$ case do not appear here, nor in the skin friction coefficient (Fig. 20b). The CFD again under-predicts the skin friction as compared to the experimental data. The improvement in agreement between compressible and incompressible approaches is believed to be due to the Mach number at the reference location, on the top (starboard in experiment) wall. In the $+12^\circ$ case, the reference point is in the accelerating, suction-side region of the flow and will thus experience a higher Mach number than the free-stream value, increasing the deviation between compressible and incompressible estimates of ρ_{ref} and V_{ref} . In the -10° case, however, the reference point is now in the decelerating, pressure-side region of the flow, where the Mach number will be lowered from the free-stream value, bringing the compressible and incompressible estimates closer together.

The boundary layer thicknesses (Fig. 21a-c) show to opposite trend through the pressure gradient region to the $+12^\circ$ case, compressing in the upstream, favorable, pressure gradient and expanding in the downstream, adverse, pressure gradient. Similar observations can be made about the comparisons between CFD solvers and between CFD and experiment in both cases, including the slight over-prediction of the DLR-TAU code.

The shape factor, H , (Fig. 21d) again shows a greater spread of results between solvers than might be expected based on the results of δ^* and θ separately. In the -10° case, the agreement between CFD and experiment for H is improved, but still shows greater discrepancy than either δ^* or θ taken separately. In the $+12^\circ$ case, after moving through both pressure gradient regions, H settled to a constant value around 1.26, but in the -10° case $H = 1.34$ when the secondary pressure gradient relaxes, then begins to drop at a rate similar to that observed upstream of the pressure gradient region.

The β distribution for the -10° case, shown in Fig. 22a, shows a somewhat surprising suppression of magnitude at the upstream peak, only around -0.6 compared to the unity observed in the 12° case before reaching ≈ 1 in the second peak. For this case, the Chalmers (OpenFOAM) solution over-predicts the peak β magnitudes at both the initial and secondary points. Given the good agreement in each of the variables that feed into the β calculation (δ^* , skin friction, and pressure), it seems most likely this discrepancy is spurious.

The relationship between G and β for the -10° case flows in the opposite direction as the 12° case (Fig. 22b). Again, the maximum deviation from the equilibrium curve of Mellor & Gibson occurs at P7, the downstream, secondary pressure gradient peak. The solver-to-solver agreement for the -10° case is improved over the 12° case, with the exception of the Chalmers OpenFOAM solution, the discrepancies of which appear to come predominantly from the mismatch in β .

Figure 23 shows the velocity (Fig. 23a-c), TKE (Fig. 23d-f), and $\overline{u'v'}$ Reynolds stress (Fig. 23g-i) profiles for the -10° case. The velocity profiles show equally good solver-to-solver agreement and improved CFD-to-experiment agreement at P3 and P5. At P7, the agreement with experiment degrades, the CFD over-predicting u^+ in the wake region.

The solver-to-solver agreement in the turbulence profiles (Fig. 23d-i) are comparable to the 12° case. Agreement with experiment is generally improved, particularly in the outer region at P7. Compared with the 12° case, the turbulence profiles at all stations are thinner at the peak and decay faster into the free-stream. These trends (widening in the 12°

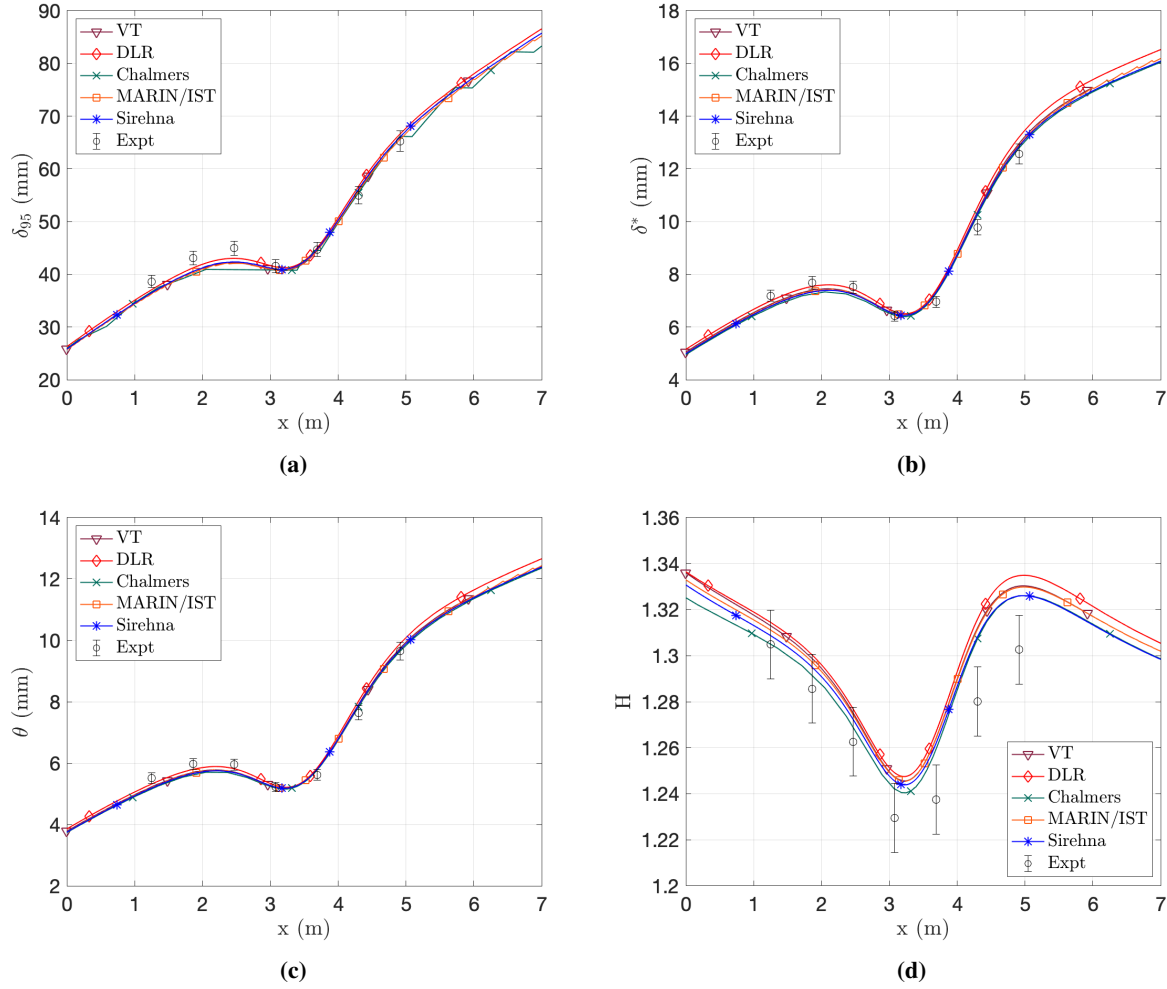


Fig. 21 95% edge velocity (a), displacement (b), and momentum (c) thicknesses and shape factor (d) as computed for the -10° case using all solvers with Menter SST.

case and compressing in the -10° case) persist through the secondary gradient region at P7, rather than reversing, indicating a historical dependency of the turbulence to the upstream pressure gradient.

B. Turbulence Model

In addition to the solutions using Menter SST [28], computations were also made using a variety of other models, including Spalart-Allmaras (SA) [30], Menter baseline $k-\omega$ (BSL) [28], DLR SSG/LLR- ω [14], and the machine-learned model (GEP) discussed in Section IV.F. SA, SST, and BSL computations were made by the Virginia Tech team in CREATE-AV Kestrel, the SSG/LLR- ω results from DLR in TAU, and the GEP results from the University of Melbourne in OpenFOAM.

Figure 24 shows the force coefficients for the 12° case. The model-to-model and CFD-to-experiment agreements for the pressure coefficient distribution (Fig. 24a) are quite good. Greater variation is observed in the skin friction coefficient (Fig. 24b). The variation between most of the models is reasonably small and under-predicts c_f as observed in the solver comparisons. The machine-learned GEP model, however, matches the skin friction distribution well.

The turbulence model comparison for the boundary layer growth in the 12° case is shown in Fig. 25. The δ_{95} growth (Fig. 25a) is sensitive to turbulence model choice, the Menter baseline $k-\omega$ predicting the thickest boundary layer, the SA model predicting the next largest. The SST and SSG/LLR- ω models show good agreement with each other, and the thinnest boundary layer thickness.

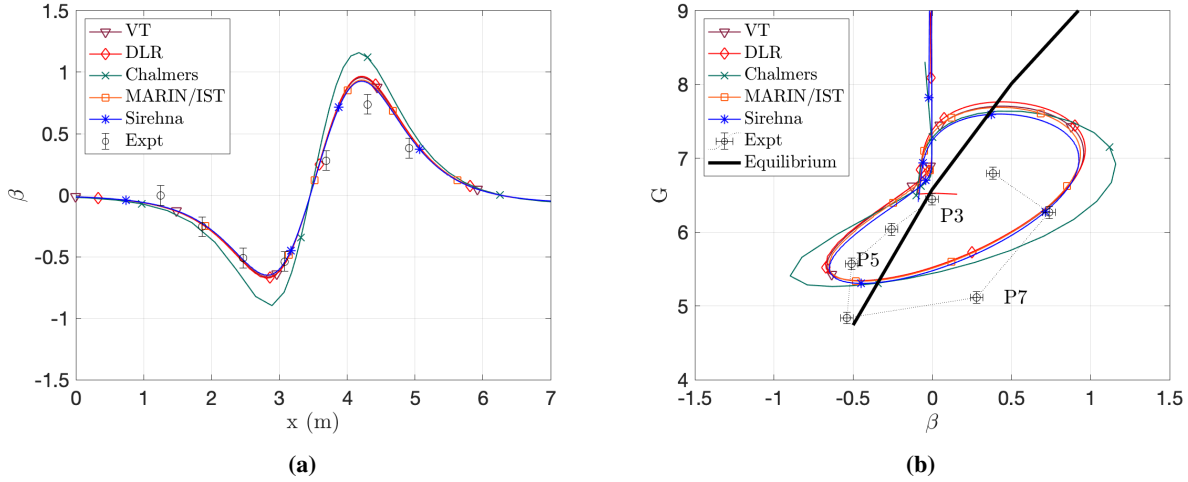


Fig. 22 Clauser parameter (a) and defect shape factor as a function of Clauser parameter (b) as computed for the -10° case using all solvers with Menter SST.

The agreement between turbulence models is better for the integrated boundary layer thicknesses, δ^* (Fig. 25b) and θ (Fig. 25c). In the downstream region of the θ distribution, the SA, BSL, and SSG/LRR- ω models all over-predict compared with the SST results.

Similar to what was observed in the solver comparisons, the variations observed in the shape factor distribution (Fig. 25d) are greater than might be expected based on the distributions of δ^* and θ taken separately. Here, the SST model predicts the highest values of H , followed, in order, by SSG/LRR- ω , SA, then BSL.

The distribution of the Clauser parameter (Fig. 26a) shows good agreement between the various turbulence models. Greater variation is observed in the relationship between β and the defect shape factor, G (Fig. 26b). All models predict the same general trend, moving away from equilibrium in regions of strongest pressure gradient, particularly the secondary gradient, but discrepancies arise in the exact path taken.

Figure 27 shows the viscous normalized velocity (Fig. 27a-c), turbulent kinetic energy (Fig. 27d-f), and $\overline{u'v'}$ Reynolds shear stress (Fig. 27g-i) profiles compared between the tested turbulence models. The SA model predicts different buffer layer behavior than the higher order models, u^+ rising more rapidly in the junction between the linear sublayer and log region. The agreement between the standard models in the logarithmic and wake regions is good, but over-predict compared to the experimental data, as was observed in the solver comparison. The GEP model, however, matches the experiment in the wake at all three stations.

Greater variation is observed in the turbulence profiles. Around the peak of TKE (Fig. 27d-f) at P3 and P5, the GEP model shows a lower peak Reynolds stress. At all three stations, the GEP model shows higher TKE in the outer region. These both serve to bring the GEP results closer in line with the experimentally measured profiles. In the plots of $\overline{u'v'}$ stress, the agreement between turbulence models at the peak is good, but the GEP model again predicts higher stresses in the outer region at all three stations.

VI. Discussion

A. Variations in CFD Solvers

In general, the solution agreement between the six computations and five CFD solvers represented here was quite good and overall better than the authors expected before generating the data. The agreement in mean and integrated variables showed variations that were negligible to the naked eye, with the exception of a small variation in the initially adverse pressure gradient case ($\alpha = 12^\circ$) between solutions generated using compressible vs. incompressible algorithms. Given the moderate Mach number of this flow case (≈ 0.1), either algorithm could be considered appropriate, making this a good case for direct comparison between compressible and incompressible solutions. The difference is predominantly observed in the force coefficients (Fig. 16), while the integrated boundary layer parameters (Fig. 17) and velocity profiles (Fig. 19) show little discernible variation between compressible and incompressible solutions. This suggests that the

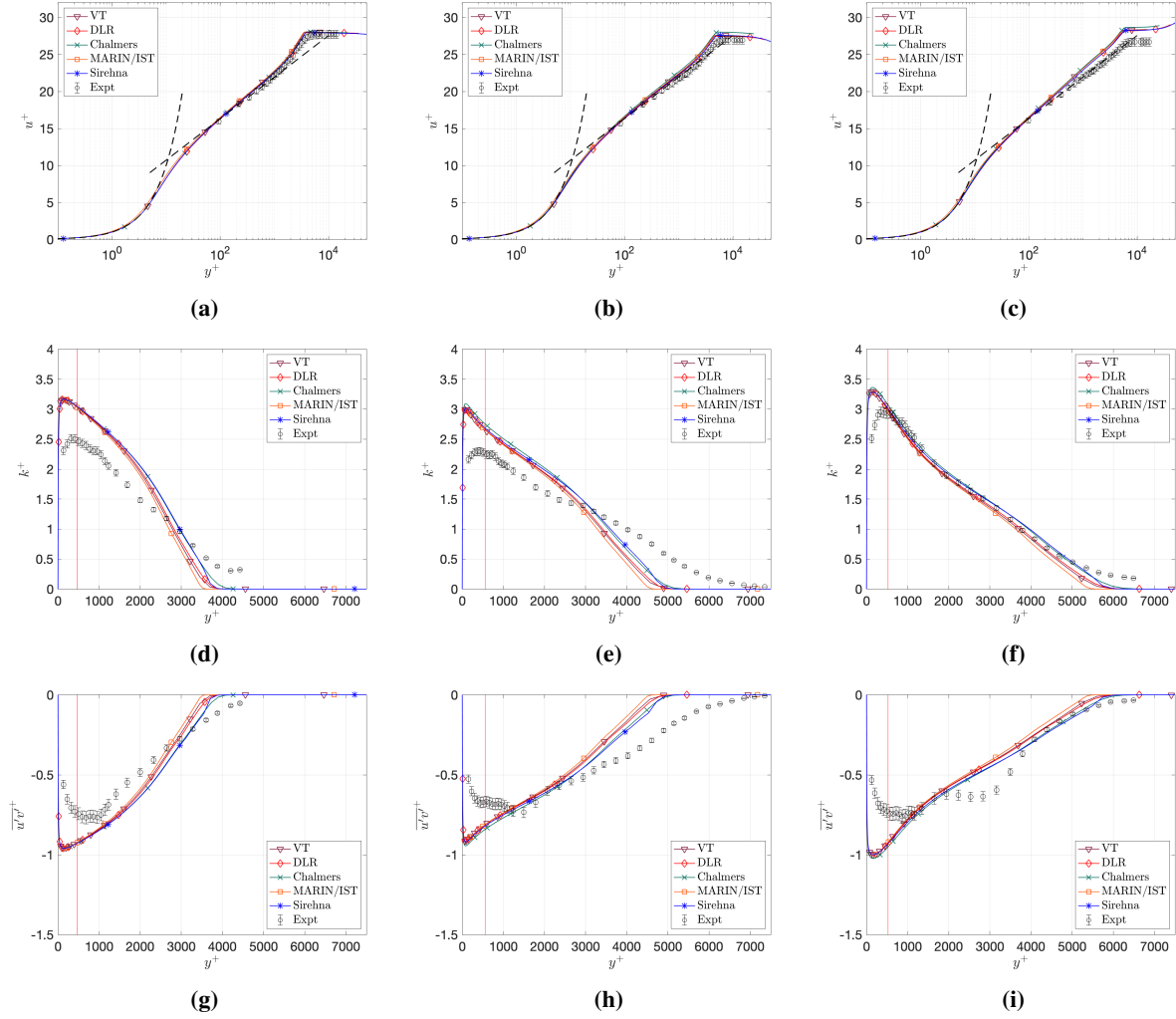


Fig. 23 Velocity (a-c), TKE (d-f), and Reynolds shear stress (g-i) profiles at the three primary assessment locations, P3, P5, and P7 (left, middle, right columns respectively) as computed for the -10° case using all solvers with Menter SST. Linear sublayer and Law of the Wall with $\kappa = 0.41$ and $B = 5.1$ marked with black dashes.

variation may arise primarily from the universal referencing scheme for the non-dimensional force coefficients, which, by definition, uses the compressible isentropic flow relations. The equivalent reference calculations using incompressible assumptions will produce a bias error in pressure and skin friction coefficient between two solutions with the same pressure and τ_w that is proportional to the difference between the compressible dynamic pressure and the incompressible gauge stagnation pressure. At Mach 0.1, this would be a difference of around 0.5%, which, for a static pressure of ≈ 94 kPa would result in a difference in peak c_p of 0.02 for the 12° case. The observed bias between the incompressible and compressible solutions at that point was ≈ 0.01 .

The largest variations between solvers are observed in the shape factor (Fig. 17 and Fig. 21) and turbulence profiles (Fig. 19 and Fig. 23). Variation in the turbulence profiles ought to result in variation in the parameters that are driven by the turbulence, like the skin friction and/or integrated boundary layer parameters, variation that, at first glance, does not appear to exist. However, when combined with the observation that H has greater variation than seems indicated by either δ^* or θ alone, this suggests that perhaps the agreement in the integrated parameters is not as good as it appears based on visual observation alone.

A more rigorous method than visual observation is needed in order to draw any meaningful conclusions from these comparisons. By knowing the estimated numerical uncertainty associated with each presented solution, we could define a 95% confidence band that represents the expected collapse within numerical uncertainty. This uncertainty

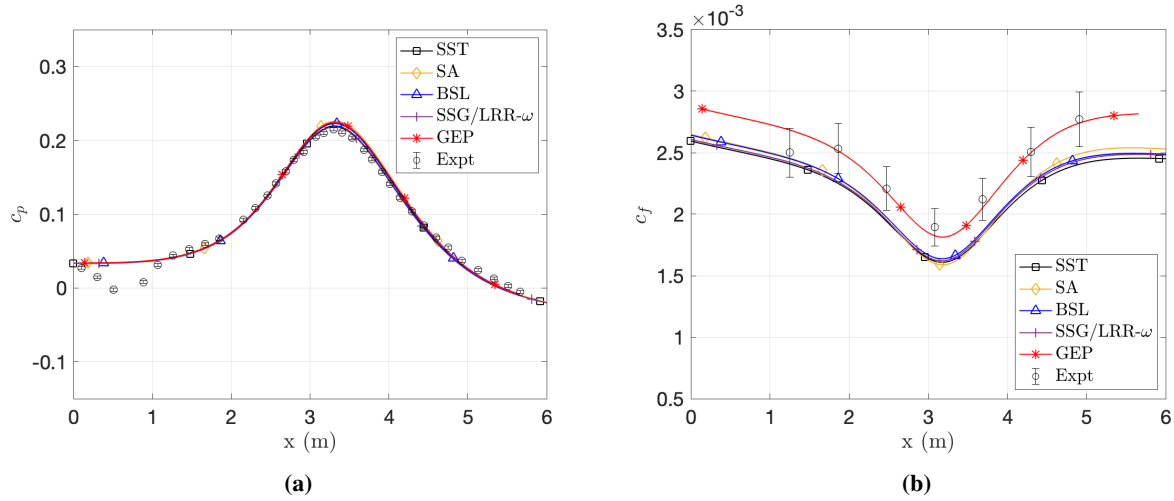


Fig. 24 Pressure (a) and skin friction (b) coefficients as computed for the 12° case using various turbulence models.

band effectively represents a single standard deviation based on an assumed Gaussian distribution around the computed solutions with the largest computed numerical error. Using the uncertainty estimates of the Virginia Tech Kestrel solutions, as an example, this would result in a band of 0.37 mm for δ^* , 0.26 mm for θ , and 3.67×10^{-5} for the skin friction coefficient. By comparison, the observed spreads at the peak of the 12° case are 0.56 mm in δ^* , 0.33 mm in θ , and 7.0×10^{-5} in c_f , all outside their respectively computed uncertainty bands. In other words, statistically significant variations between data can be lost in a visual observation of a plot, and it is critical to take great care in drawing conclusions from visual, qualitative observation of data alone.

B. Variations in Turbulence Model

The authors were surprised by the general quality of agreement between the assessed turbulence models. Before discussing this agreement, however, it must be noted that not all models were tested in the same solver. The SST, SA, and BSL results presented were all computed by the Virginia Tech in CREATE-AV Kestrel, but the SSG/LRR- ω results were computed in the DLR-TAU code, and the machine learnt Gene Expression Programming (GEP) results were computed by the University of Melbourne team in OpenFOAM. The solver comparison appears to indicate that variations between these solvers ought to be reasonably small, but this discrepancy is a weakness of the current assessment that must be taken into account.

The agreement between the three baseline turbulence models, Spalart-Allmaras (SA), Menter Baseline k - ω (BSL), and Menter Shear Stress Transport (SST) is quite good. There is no discernible variation in the c_p distribution (Fig. 24a), confirming that turbulence model choice will have little effect on the free-stream aerodynamics. The skin friction variation (Fig. 24b) is $\approx 5.1 \times 10^{-5}$, smaller than the observed spread between different solvers using the same turbulence model for the same case.

However, greater variation is observed between these models for the boundary layer parameters. A surprisingly large variation was observed in the distribution of δ_{95} (Fig. 25a). Compared with the SST model, both SA and BSL models predict a larger δ_{95} . Further observation revealed that this discrepancy comes not from disagreement on the value of free-stream stagnation pressure, but from the y -position at which it occurs. Agreement in the integrated parameters (Fig. 25b-c) was better, a 0.22 mm spread in the three baseline turbulence models for the peak δ^* . Given that the integrated parameters will be more heavily dependent on the inner layer behavior, these two observations suggest that the various Boussinesq-hypothesis turbulence models will agree well in the sub- and log-layers but differ most strongly in the wake. Very similar to the observations of solver-to-solver behavior, there is a much wider variety in shape factor (Fig. 25d) than would be expected from observing the δ^* and θ distributions alone. Thus, a similar conclusion can be drawn; there is statistically significant variations between the solutions for the boundary layer growth that are not readily apparent from visual observation of that growth.

This variation in shape factor likely contributes to the range of observed behavior in the equilibrium plot of G vs. β

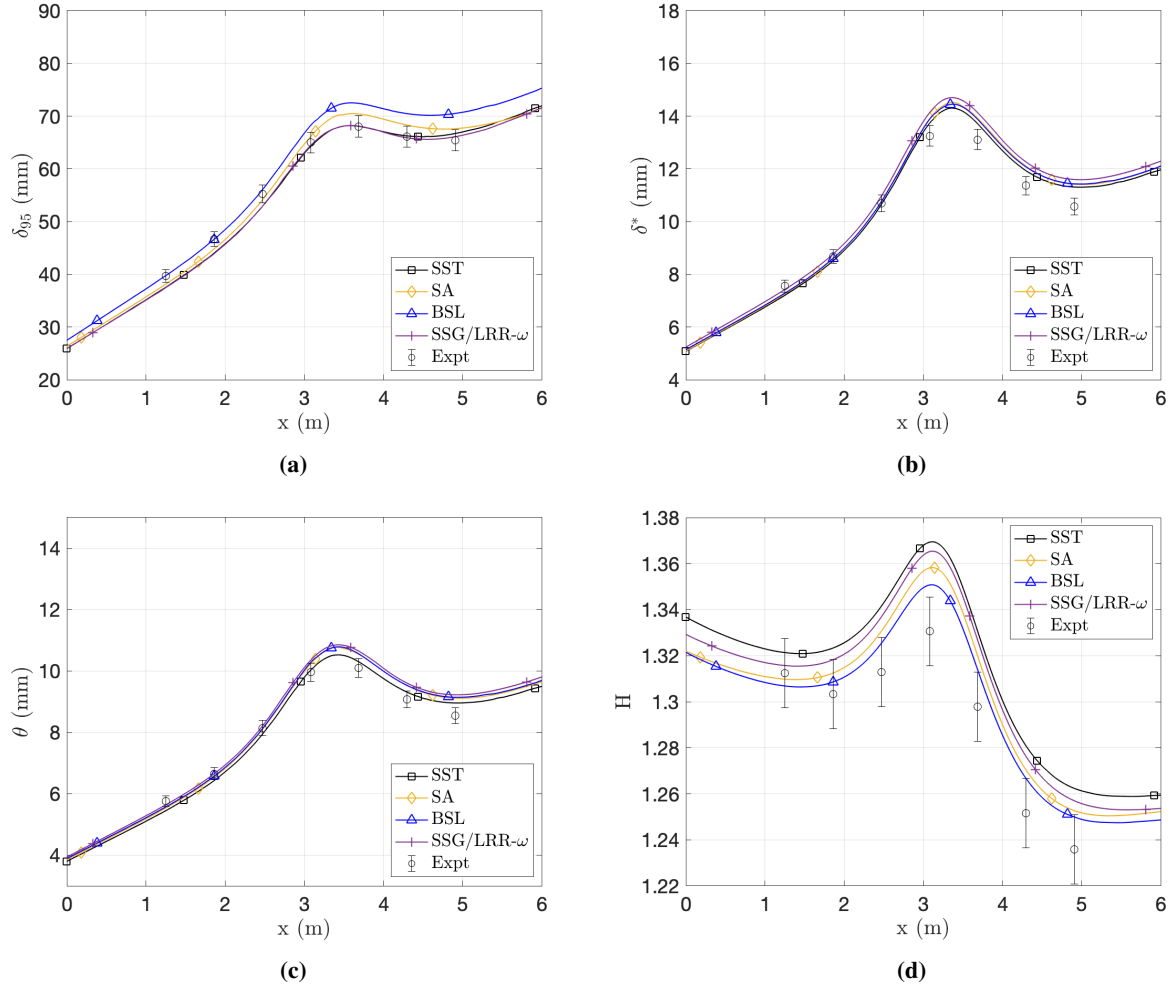


Fig. 25 95% edge velocity (a), displacement (b), and momentum (c) thicknesses and shape factor (d) as computed for the 12° case using various turbulence models.

in Fig. 26b. The three Boussinesq-hypothesis models show similar peaks at the maximum deviation points, but different paths to get there through the flow domain. This could potentially have implications for the ability of various turbulence models to account for non-equilibrium pressure gradient effects, but more information is needed, including more refined experimental data and greater assurances of the accuracy of the CFD in matching those experimental data as will be discussed in the next section.

As suggested by the observations of δ_{95} and the integrated boundary layer thicknesses, the three baseline models show excellent agreement in the sub- and log-layers, but a greater variation in the wake behavior (Fig. 27a-c). In the buffer layer, the one-equation SA model shows a different behavior to the two-equation models, u^+ rising more rapidly at first before moving into the log-region. If this has a meaningful impact on the development of the integrated parameters, it would be difficult to separate it from the impact of the difference in wake prediction.

The SST and BSL Menter models show good agreement for the prediction of the peak turbulent kinetic energy (Fig. 27d-f), both in the location from the wall and magnitude. However, they differ more strongly in the outer region, the BSL model predicting higher TKE and a slower decay to free-stream than SST. This may explain the fact that the BSL model predicts higher δ_{95} , δ^* , and c_f than the SST model. The main mathematical difference between these models is their treatment of the dissipation of turbulence far-from-the-wall, where the BSL model will retain a $k-\omega$ modeling approach while the SST model changes to a $k-\epsilon$ approach. The impact of this is fairly straightforward and illustrated by these results; the $k-\omega$ model will exhibit less turbulent dissipation far from the wall than the $k-\epsilon$ model, resulting in higher TKE, slower spatial decay into the free-stream, and, as a consequence, higher skin friction and a

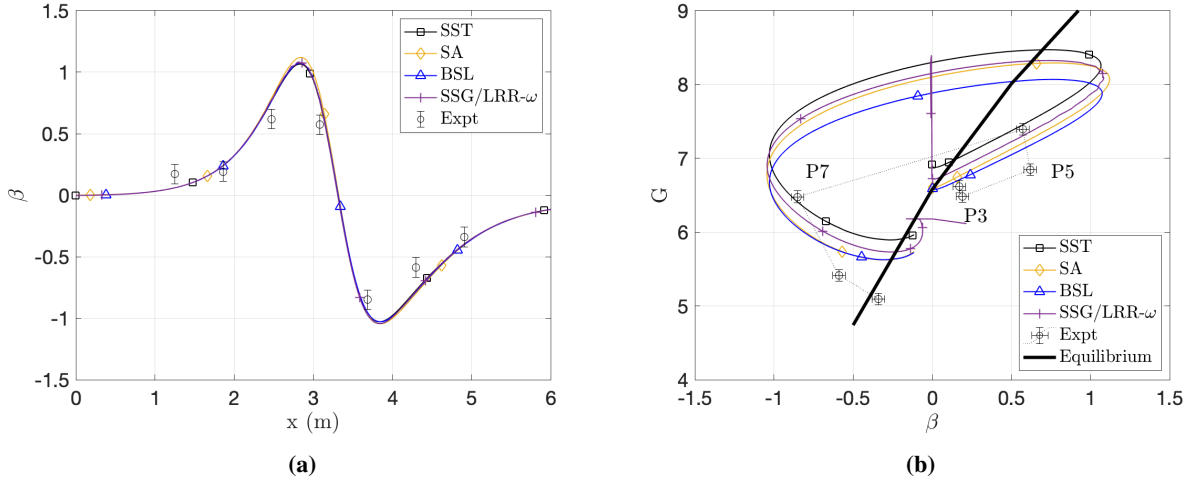


Fig. 26 Clauser parameter (a) and defect shape factor as a function of Clauser parameter (b) as computed for the 12° case using various turbulence models.

thicker boundary layer. A similar observation is made in the $\overline{u'v'}$ Reynolds shear stress profiles in Fig. 27g-i. All three models have decent agreement on the location and magnitude of the peak stress and the BSL model exhibits higher stress and slower decay than the SST model. The SA model lies in between them in the range of $2000 < y^+ < 4000$, but then shows an even slower decay into the free-stream than the BSL model.

Few, if any, meaningful differences are observed between the three Boussinesq-hypothesis models and the second-moment-closure DLR SSG/LRR- ω Reynolds stress transport model in the mean force coefficients (Fig. 24). The c_f distribution computed using the SSG/LRR- ω model lies almost perfectly in the middle of the spread of the Boussinesq models. In the δ_{95} distribution (Fig. 25a), the SSG/LRR- ω model agrees well with the Menter SST, predicting lower than the SA and Menter BSL models. The SSG/LRR- ω model does predict higher values of the integrated parameters (Fig. 25b-c), but it is unclear if this is a result of the turbulence model or the solver, as the DLR-TAU code over-predicted the integrated parameters when compared with Kestrel results. In the shape factor distribution (Fig. 25d), the SSG/LRR- ω model again lies in between the spread of the Boussinesq models.

In the mean velocity profiles (Fig. 27a-c), the SSG/LRR- ω model agrees most strongly with the two-equation Menter models in the inner region and the BSL model in the wake. The agreement with the BSL model in the wake is somewhat surprising, since the distribution of δ_{95} agrees more strongly with the SST model. This may be explained by the fact that the SSG/LRR- ω model agrees better with SST for the skin friction distribution, implying that, while the viscous normalized profile may agree best with the BSL model, the true boundary layer edge agrees better with the SST model.

Unsurprisingly, the greatest difference between the first- and second-moment closure models is observed in the turbulence profiles (Fig. 27d-i). All models show decent agreement for the location and magnitude of the peak TKE and shear stress at P3 and P5, but the SSG/LRR- ω model predicts a slower decay to the free-stream, particularly at $y^+ > 3500$. At P7, the SSG/LRR- ω model shows even greater variation from the Boussinesq models, predicting a higher peak magnitude that is farther from the wall.

Overall, the second-moment closure model shows less difference from the various first-moment closure models than might be expected. It is assumed that this is due to the two-dimensionality of the computational case and that greater variations will be observed in a 3D grid. It would appear that there is little appreciable benefit of the second-moment closure over the more efficient one- and two-equation models, at least for a 2D computation. Whether there is a more pronounced benefit in a 3D computation will be the subject of future work.

By contrast, the machine-learned GEP model shows a marked improvement in agreement with the experimental data. However, it must be noted that this model was trained using these data, and thus a good agreement would be expected. The authors believe that this illustrates the potential of machine learning to improve the standard of turbulence modeling, but this model will require more rigorous and varied testing before any meaningful conclusions about its performance and potential benefits can be drawn.

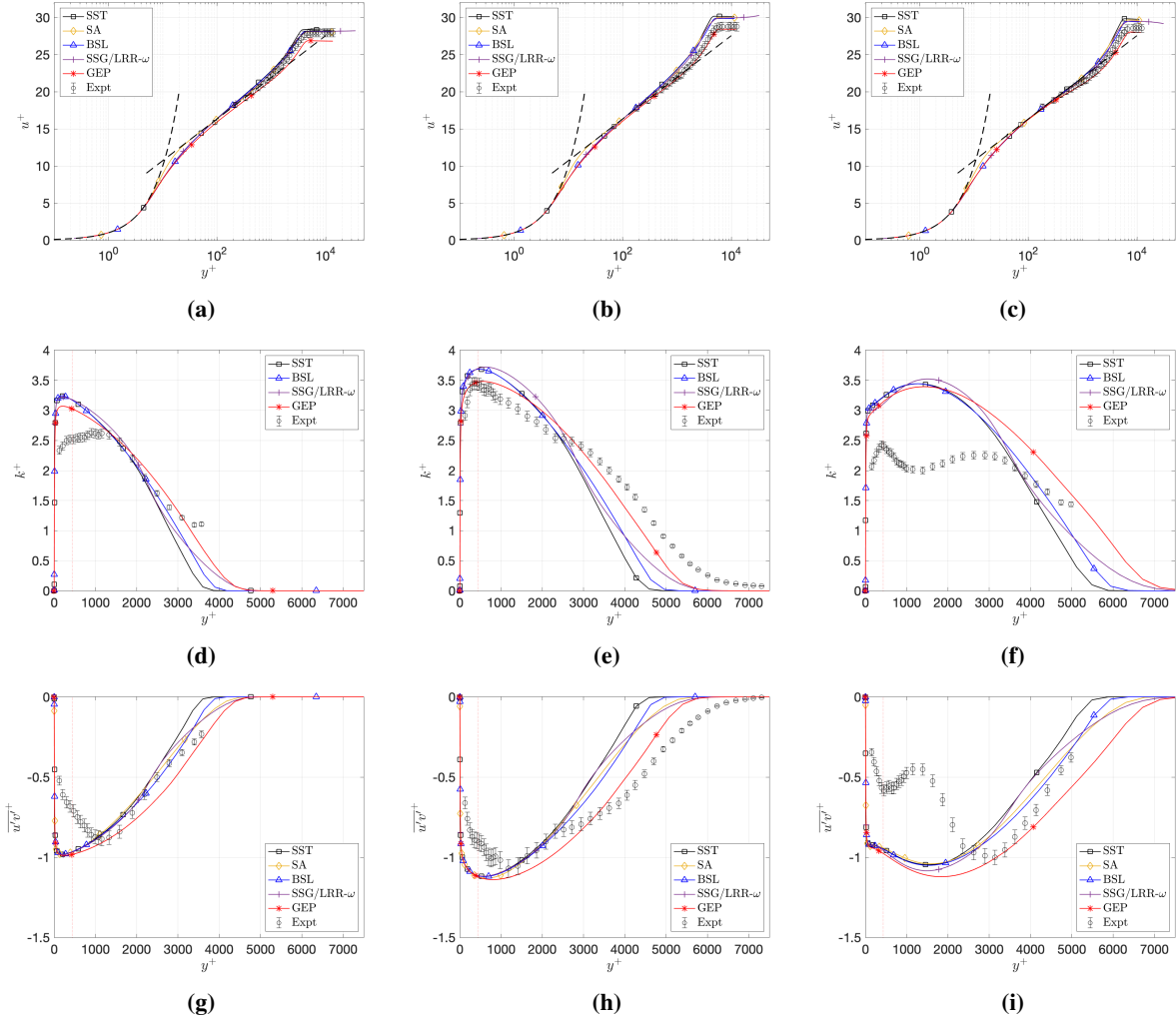


Fig. 27 Velocity (a-c), TKE (d-f), and Reynolds shear stress (g-i) profiles at the three primary assessment locations P3, P5, and P7 (left, middle, right columns respectively) as computed for the 12° case using various turbulence models. Linear sublayer and Law of the Wall with $\kappa = 0.41$ and $B = 5.1$ marked with black dashes.

C. Agreement with Experiment

It is critical to note that any comparison to experimental data in this case should be made with great care. First, the computational domain is not a perfect replication of the physical case. The grids used here are two-dimensional and contain neither the contraction nor diffuser geometry of the VTSWT. The top wall is also a slip-wall, which has no physical meaning in a viscous flow. Additionally, the airfoil is modelled with a sharp trailing edge and is assumed to be fully turbulent, where the experimental model is tripped at 5% chord and has some finite trailing edge thickness, however small. Additionally, while preliminary estimates of numerical uncertainty have been made, they have not been fully incorporated into a quantitative comparison with experimental data at this time.

Perhaps most critically, the airfoil grid resolution used here is coarse by the standards of airfoil simulations [42]. In the finest grid, there are 384 points on the airfoil surface with leading and trailing edge streamwise spacings of $\approx 1 \times 10^{-5}$ chord lengths. This lack of refinement lead to oscillations in the pressure and skin friction coefficients at the leading and trailing edges that create errors in the lift and drag on the model, which will create similar errors in the wall pressure and skin friction coefficients. A second grid family was developed and solved in ReFRESCO by the MARIN/IST team that used around three times the number of points on the airfoil surface, and it was observed that this refinement eliminated the majority of oscillatory behavior on the foil surface and reduced the drag coefficient by around 7%. Preliminary observation showed only small differences in the boundary layer behavior at a given level of grid

refinement, but the grid convergence behavior was changed significantly, increasing the observed order of accuracy, in the second grid family, suggesting these grids will have different discretization error and numerical uncertainty behavior. Sufficient time was not available to repeat the comparisons presented herein with the new grid family, so a true accounting of the impact of airfoil resolution is not available at this time, but such a study will be part of the future work of this collaboration.

That being said, the overall agreement with experiment presented here is decent for most mean and integrated parameters. Some of this agreement is self-fulfilling, e.g., the inflow length was set to match the experimental inflow boundary layer and the top wall angle was set to match the experimentally measured pressure gradient, but the CFD appears to correctly predict the qualitative trends observed in the boundary layer development, despite the complexity of the pressure gradient-induced flow physics. This flow case has a large historical dependence on upstream flow history [7–9], a dependence that it was unclear *a priori* would be captured by Boussinesq-hypothesis RANS modeling. One of the major findings of this work, then, is that, at least in a qualitative sense, RANS modeling has the capability to account for the non-local, historical effects of continually varying pressure gradient. This may imply something meaningful about the physics of these effects; that they originate in the mean flow and the parameters that are inputs to the turbulence models, namely the mean strain rate, and then filter into the turbulent fluctuations rather than the other way around. However, we believe that such conclusions must wait for forthcoming analysis on the effects of three-dimensionality and airfoil grid refinement.

The greatest disagreement between CFD and experiment were observed in the turbulence profiles and skin friction distributions. It is worth noting that these are also the parameters with the greatest experimental uncertainty, and any conclusions made on these comparisons can only be made after a more detailed analysis of the experimental case, including improved resolution of PIV measurements and the inclusion of redundant skin friction estimates.

In the outer portion of the logarithmic region of the velocity profiles, it was observed that the RANS results had a slightly steeper slope than the experiment and the Law of the Wall using classical coefficients ($\kappa = 0.41$, $B = 5.1$). This is a known phenomenon of RANS results at high Reynolds number [41], however, it is unclear if this is present in the true physics or is an error associated with the Boussinesq-hypothesis turbulence models. In either case, this may well explain the discrepancies observed between RANS and experiment in the skin friction coefficient; the experiment c_f values were obtained using a Clauser chart method assuming the classical coefficient of the Law of the Wall. If the κ value is lower in the true physics, then this would lead to a biased over-prediction of the experimental skin friction coefficient. If it is a feature only of the RANS models, it will drive the RANS results for the skin friction down, creating a bias under-prediction in the RANS results.

VII. Conclusion

We have presented some promising preliminary results of a collaborative effort to study the turbulence modeling of low Mach number, high Reynolds number 2D boundary layer flows subjected to continually varying pressure gradients of both favorable and adverse character, as part of the greater NATO AVT-349 collaboration. 2D RANS solutions have been presented from six computations in five CFD solvers for two pressure gradient cases using five different turbulence models, including one- and two-equation Boussinesq-hypothesis models, a second-moment closure Reynolds Stress Transport model, and a machine-learned model.

All else (grid, turbulence model, reference conditions, free-stream conditions) held constant, the various solvers showed qualitatively good agreement to the naked eye, though this agreement does show statistically significant variation that shows more readily in certain parameters. Similarly, the various turbulence models show decent agreement for integrated parameters and larger discrepancies arise in turbulence profiles. Second moment closure appears to offer little benefit in these cases, but this is possibly due to the two-dimensionality. Machine learning appears to offer potential benefits, but this was a training case and further assessment is needed.

Many lessons have been learned through this work, some related to the physics, some related to the modeling, and many related to the art of collaboration and verification and validation activities across a large number of groups. The choice of grid is critically important. In order to perform a true comparison between two solvers, the same grid family with a similar level of numerical uncertainty must be used; otherwise, the possibility of grid-born solution differences cannot be ruled out, particularly for internal and wind tunnel flows, as presented here, where inflow length and inclusion or lack thereof of contraction and/or diffuser geometry may differ and can generate significant solution differences. Additionally, this case includes an airfoil geometry, though it is not the focus of the analysis, and the global solution appears to be strongly dependent on the refinement of the airfoil grid, independent of the overall grid resolution.

When performing a large collaboration such as this one, particularly on topics related to validation of models and

software, making and adhering to common definitions is important. For this work, a common referencing scheme was defined in order to ensure faithful comparison of non-dimensionalized variables between various computations and experimental data. Unfortunately, this scheme was defined using compressible isentropic flow relations, which had to be adapted for incompressible RANS solutions, leading to potentially avoidable discrepancies in the data.

Several questions remain to be answered: the effect of two- vs. three-dimensional simulations and inclusion of wind tunnel geometry, particularly on the relative performance of second-moment closure models, the effect of airfoil grid resolution, the universality of machine-learned models, and the validity of the comparison of these solutions with experimental data. This collaboration continues into the next year and will be undertaking further computations and analyses to answer some of these questions. This work, in combination with future, rigorous analyses of solver and model performance on these non-equilibrium pressure gradient flows has the potential to quantify the efficacy of the current state-of-the-art in turbulence modeling for flow cases in non-equilibrium pressure gradient, as well as to provide a future direction for the development of more appropriate models.

VIII. Appendix

A. VT Grid Convergence

Figure 28 shows the c_p , c_f , and δ^* distributions for the $+12^\circ$ angle of attack case using Menter SST in Kestrel for all five systematically refined grid levels. For all outputs, GL5 shows a reasonably large discrepancy from the other Grid Levels but the remaining solutions show only slight change with increasing grid refinement. The difference between solutions on Grid Levels 1, 2, and 3 is practically negligible, which is why GL3 was chosen as the main grid for presented solutions from the Virginia Tech team.

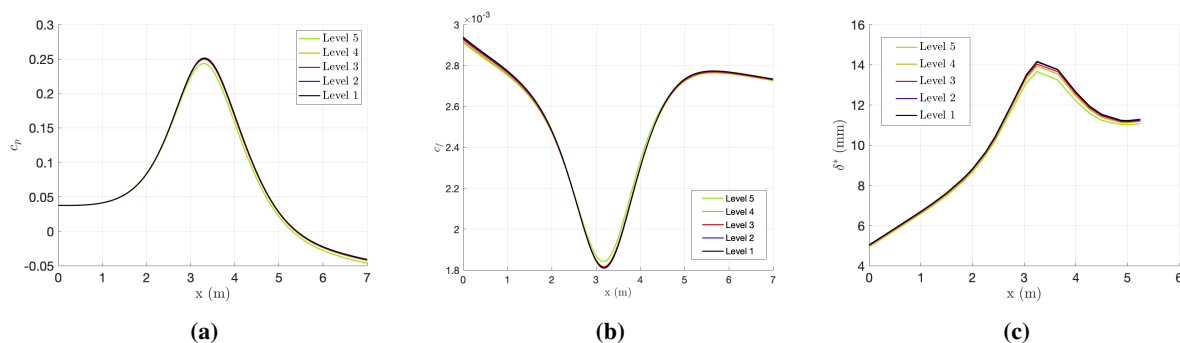


Fig. 28 Comparison of main outputs, c_p , c_f , and δ^* across systematically refined grid family from VT Kestrel simulations.

Figure 29 shows an example iterative convergence plot for the Kestrel simulations. The solution experiences residual stall for most equations between 3 and 4 orders of magnitude reduction from the first iteration. This was consistent between solutions and was accounted for as described in Section IV.D.

B. UofM Airfoil Section Domain Grid Convergence

Figures 30 and 31 show the results of the different grid resolutions for the 12° angle of attack case. The differences between the grids GL4, GL3 and GL2 appear negligible, thereby allowing the use of GL4 for the subsequent model evaluation.

Acknowledgments

The authors would like to thank Drs. Paul Croaker and David Pook and Oksana Tkachenko of the Australia Defense Science and Technology Group (DSTG) for their contributions to this collaboration. We would also like to thank the NATO S&T Organization and AVT-349 for hosting this collaboration.

The authors from Virginia Tech would like to thank Dr. Peter Chang and the U.S. Office of Naval Research (ONR) for their support of experimental work through grant numbers N00014-18-1-2455 and N00014-19-1-2109. We would also

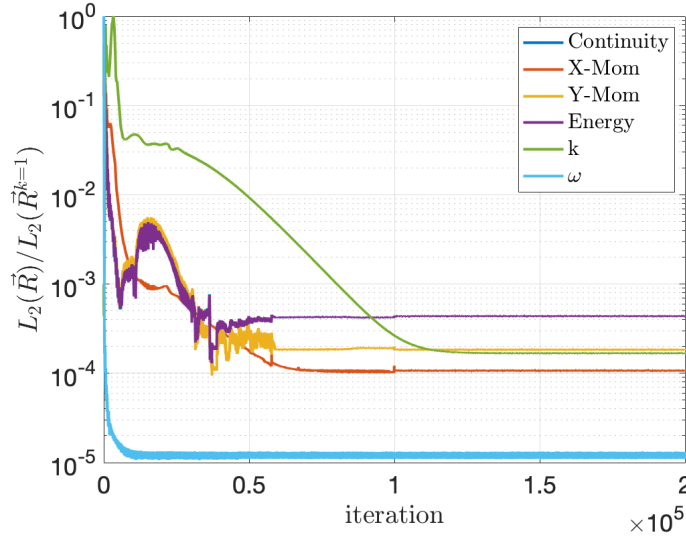


Fig. 29 Residual convergence for VT Kestrel simulation of $\alpha = -10^\circ$, Menter SST on GL3.

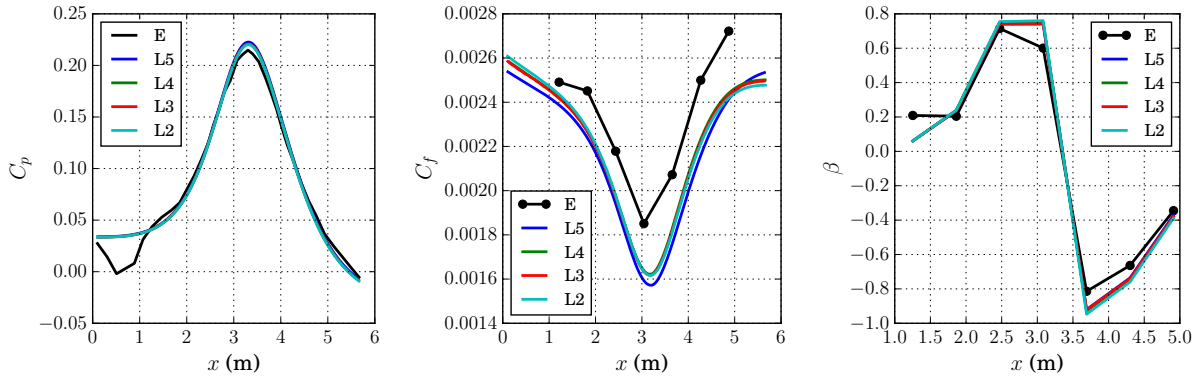


Fig. 30 Grid convergence of the streamwise evolution of C_p , C_f and β

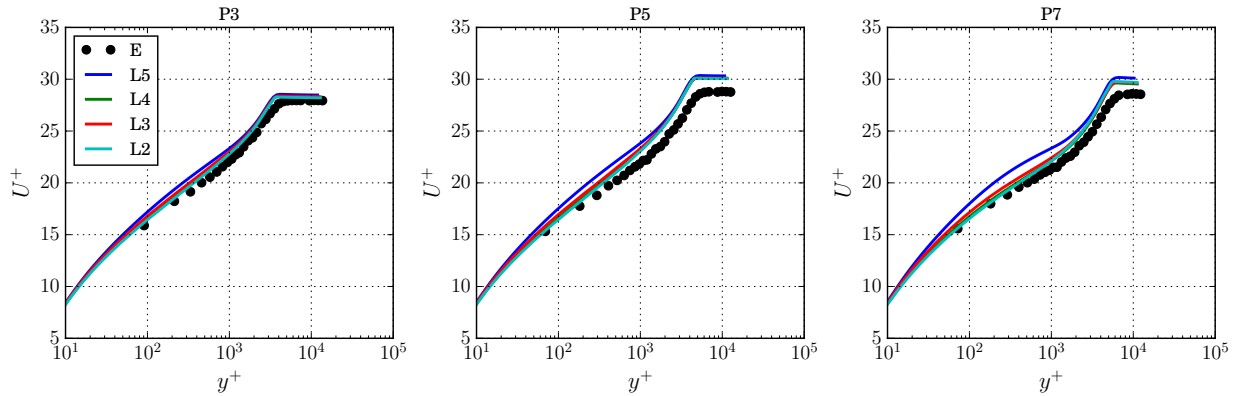


Fig. 31 Grid convergence of the wall-normal profiles of U^+ .

like to thank the U.S. Department of Defense High Performance Computing Modernization Program (HPCMP) and the Naval Air Warfare Center - Aircraft Division Applied Aerodynamics and Store Separation Branch for computational

resources.

The authors from the University of Melbourne acknowledge support from the Australian Research Council and the U.S. Office of Naval Research under NICOP Grant N62909-20-1-2046 with program monitors Dr. Ki-Han Kim (ONR) and Dr. Sun-Eun Kim (ONR Global, Tokyo).

References

- [1] Clauser, F. H., “Turbulent Boundary Layers in Adverse Pressure Gradient,” *Journal of the Aeronautical Sciences*, Vol. 21, No. 2, 1954, pp. 91–108.
- [2] Nagano, Y., Tagawa, M., and Tsuji, T., “Effects of Adverse Pressure Gradients on Mean Flows and Turbulence Statistics in a Boundary Layer,” *8th International Symposium on Turbulent Shear Flows*, Springer-Verlag, New York, USA, Munich, Germany, 9–11 September, 1991.
- [3] Devenport, W. J., and Lowe, K. T., “Equilibrium and Non-Equilibrium Turbulent Boundary Layers,” *Progress in Aerospace Sciences*, Vol. Submitted for Publication, 2021.
- [4] Mellor, G. L., and Gibson, D. M., “Equilibrium turbulent boundary layers,” *Journal of Fluid Mechanics*, Vol. 24, No. 2, 1966, pp. 225–253.
- [5] Boussinesq, J., “Essai sur la théorie des eaux courantes,” *Mémoires présentés par divers savants à l’Académie des Sciences*, Vol. 23, No. 1, 1987, pp. 1–680.
- [6] Bobke, A., Örtü, R., Vinuesa, R., and Schlatter, P., “History effects and near-equilibrium in adverse-pressure-gradient turbulent boundary layers,” *Journal of Fluid Mechanics*, Vol. 820, 2017, pp. 667–692.
- [7] Fritsch, D. J., Vishwanathan, V., Duetsch-Patel, J. E., Gargiulo, A., Lowe, K. T., and Devenport, W. J., “The Pressure Signature of Smooth Wall Turbulent Boundary Layers in Pressure Gradient Family,” *AIAA Aviation Forum*, Reno, NV, USA, 15–19 June 2020.
- [8] Fritsch, D. J., Vishwanathan, V., Lowe, K. T., and Devenport, W. J., “The Space-Time Correlation of Pressure Under High Reynolds Number Smooth Wall Turbulent Boundary Layers in Pressure Gradient Family,” *AIAA Science and Technology Forum*, Nashville, TN, USA, 11–21 January 2021.
- [9] Vishwanathan, V., Fritsch, D. J., Lowe, K. T., and Devenport, W. J., “Analysis of Coherent Structures Over a Smooth Wall Turbulent Boundary Layer in Pressure Gradient Using Spectral Proper Orthogonal Decomposition,” *AIAA Aviation Forum*, 2–6 August, 2021.
- [10] Knopp, T., Schanz, D., Schröder, A., Dumitra, M., Hain, R., and Kähler, C. J., “Experimental investigation of the log-law for an adverse pressure gradient turbulent boundary layer flow at Re_θ up to 10000,” *Flow, Turbulence and Combustion*, Vol. 92, 2014, pp. 451–471.
- [11] Knopp, T., Reuther, N., Novara, M., Schanz, D., Schüle, E., Schröder, A., and Kähler, C. J., “Experimental analysis of the log law at adverse pressure gradient,” *J. Fluid Mech.*, Vol. 918, 2021, p. A17. <https://doi.org/10.1017/jfm.2021.331>.
- [12] Knopp, T., Novara, M., Schanz, D., Geisler, R., Philipp, F., Schröder, A., Willert, C., and Krumbein, A., “Modification of the SSG/LRR-omega RSM for turbulent boundary layers at adverse pressure gradient with separation using the new DLR VicToria experiment,” *New Results in Numerical and Experimental Fluid Mechanics. Contributions to the 21th STAB/DGLR Symposium Darmstadt, Germany 2018*, edited by A. Dillmann, G. Heller, E. Krämer, C. Wagner, C. Tropea, and S. Jakirlic, Springer, 2018.
- [13] Knopp, T., “Modification of RANS turbulence models for pressure induced separation on smooth surfaces using the DLR VicToria experiment,” *AVT 44th Panel Business Meeting Week, 7–9. Okt. 2019, Trondheim, Norway*, 2019.
- [14] Eisfeld, B., Rumsey, C., and Togiti, V., “Verification and Validation of a Second-Moment-Closure Model,” *AIAA Journal*, Vol. 54, 2016, pp. 1524–1541.
- [15] Eisfeld, B., and Brodersen, O., “Advanced Turbulence Modelling and Stress Analysis for the DLR-F6 Configuration,” *AIAA Paper 2005-4727*, 2005.
- [16] Cecora, R. D., Radespiel, R., Eisfeld, B., and Probst, A., “Differential Reynolds-Stress Modeling for Aeronautics,” *AIAA Journal*, Vol. 53, 2015, pp. 739–755.

- [17] Sporschill, G., Billard, F., Mallet, M., and Manceau, R., "Reynolds stress RANS models for industrial aeronautical applications," *WCCM-ECCOMAS Congress - 14th World Congress in Computational Mechanics and ECCOMAS Congress, Jan 2021, Paris / Virtual, France*, 2021.
- [18] Eisfeld, B., "Steps towards a Reynolds Stress Model for the Prediction of Separated Flows," *AVT 44th Panel Business Meeting Week, 7.-9. Okt. 2019, Trondheim, Norway*, 2019.
- [19] Eisfeld, B., "Characteristics of Incompressible Free Shear Flows and Implications for Turbulence Modeling," *AIAA Journal*, Vol. 59, 2021, pp. 180–195.
- [20] Eisfeld, B., and Rumsey, C. L., "Length-Scale Correction for Reynolds-Stress Modeling," *AIAA Journal*, Vol. 58, 2020, pp. 1518–1528.
- [21] Bush, R. H., Chyczewski, T. S., Duraisamy, K., Eisfeld, B., Rumsey, C. L., and Smith, B. R., "Recommendations for Future Efforts in RANS Modeling and Simulation," 2019. AIAA Paper 2019-0317.
- [22] Spalart, P. R., and Allmaras, S. R., "Strategies for Turbulence Modelling and Simulation," *International Journal of Heat and Fluid Flow*, Vol. 21, No. 3, 2000, pp. 252–263.
- [23] Weatheritt, J., and Sandberg, R. D., "A novel evolutionary algorithm applied to algebraic modifications of the RANS stress-strain relationship," *Journal of Computational Physics*, Vol. 325, 2016, pp. 22–37. <https://doi.org/10.1016/j.jcp.2016.08.015>.
- [24] Zhao, Y., Akolekar, H. D., Weatheritt, J., Michelassi, V., and Sandberg, R. D., "RANS turbulence model development using CFD-driven machine learning," *Journal of Computational Physics*, Vol. 411, 2020, p. 109413.
- [25] Devenport, W. J., Burdisso, R., Borgoltz, A., Ravetta, P., Barone, M., Brown, K., and Morton, M., "The Kevlar-walled Anechoic Wind Tunnel," *Journal of Sound and Vibration*, Vol. 332, No. 17, 2013, pp. 3971,3991.
- [26] Duetsch-Patel, J. E., Viswanathan, V., Minionis, J., Totten, E., Gargiulo, A., Fritsch, D. J., Szoke, M., Bortoltz, A., Roy, C. J., Lowe, K. T., and Devenport, W. J., "Aerodynamic Design and Validation of Modular Test Section Walls for Hybrid Anechoic Wind Tunnels," *AIAA Science and Technology Forum*, Orlando, FL, USA, 6-10 January, 2020.
- [27] McDaniel, D. R., and Tuckey, T. R., "HPCMP CREATE™-AV Kestrel New and Emerging Capabilities," *AIAA Science and Technology Forum*, Orlando, FL, USA, 6-10 January 2020.
- [28] Menter, F. R., "Two-equation eddy-viscosity turbulence models for engineering applications," *AIAA Journal*, Vol. 32, 1994, pp. 1598–1605.
- [29] Roache, P. J., Ghia, K., and White, F., "Editorial Policy Statement on the Control of Numerical Accuracy," *ASME Journal of Fluids Engineering*, Vol. 108, No. 1, 1986, p. 2.
- [30] Spalart, P., and Allmaras, S., "A one-equation turbulence model for aerodynamic flows," American Institute of Aeronautics and Astronautics, 1992. <https://doi.org/10.2514/6.1992-439>.
- [31] Schwamborn, D., Gerhold, T., and Heinrich, R., "The DLR TAU-Code: Recent Applications in Research and Industry," *European Conference on Computational Fluid Dynamics, ECCOMAS CFD 2006*, edited by P. Wesseling, E. Onate, and J. Periaux, TU Delft, The Netherlands, 2006.
- [32] Allmaras, S. R., Johnson, F. T., and Spalart, P. R., "Modifications and Clarifications for the Implementation of the Spalart-Allmaras Turbulence Model," 2012. ICCFD7-1902, 7th International Conference on Computational Fluid Dynamics, Big Island, Hawaii, 9-13 July 2012.
- [33] Menter, F., Kuntz, M., and Langtry, R. B., "Ten years of industrial experience with the SST turbulence model," *Heat and Mass Transfer*, Vol. 4, 2003.
- [34] Pope, S. B., "A more general effective-viscosity hypothesis," *Journal of Fluid Mechanics*, Vol. 72, No. 2, 1975, pp. 331–340.
- [35] Lav, C., Haghiri, A., and Sandberg, R. D., "RANS predictions of trailing-edge slot flows using heat-flux closures developed with CFD-driven machine learning," *Journal of the Global Power and Propulsion Society*, , No. May, 2021, pp. 1–13.
- [36] Menter, F. R., and Esch, T., "Elements of Industrial Heat Transfer Prediction," *16th Brazilian Congress of Mechanical Engineering (COBEM)*, 2001.

- [37] Klaij, C. M., and Vuik, C., “SIMPLE-type preconditioners for cell-centered, collocated finite volume discretization of incompressible Reynolds-averaged Navier-Stokes equations,” *International Journal for Numerical Methods in Fluids*, Vol. 71, No. 7, 2013, p. 830–849.
- [38] Miller, T. F., and Schmidt, F. W., “Use of a pressure weighted interpolation method for the solution of the incompressible Navier-Stokes equations on a nonstaggered grid system,” *Journal of Numerical Heat Transfer*, Vol. 14, 1988, pp. 213–233.
- [39] Eça, L., Klaij, C. M., Vaz, G., Hoekstra, M., and Pereira, F. S., “On Code Verification of RANS Solvers,” *Journal of Computational Physics*, Vol. 310, 2016, pp. 418–439.
- [40] Eça, L., and Hoekstra, M., “A Procedure for the Estimation of the Numerical Uncertainty of CFD Calculations Based on Grid Refinement Studies,” *Journal of Computational Physics*, Vol. 261, 2014, pp. 104–130.
- [41] Eça, L., and Hoekstra, M., “Near-wall profiles of mean flow and turbulence quantities predicted by eddy-viscosity turbulence models,” *Numerical Methods in Fluids*, Vol. 63, No. 8, 2010, pp. 953–988.
- [42] Roy, C. J., Rumsey, C. L., and Tinoco, E. N., “Summary of Data from the Sixth AIAA CFD Drag Prediction Workshop: Case 1 Code Verification,” *Journal of Aircraft*, Vol. 55, No. 4, 2018.

Chapter 5

Turbulence and pressure fluctuations in rough wall boundary layers in pressure gradients

This chapter presents a manuscript accepted for publication in *Experiments in Fluids* as part of a Topical Collection on rough wall flows. This chapter presents the experimental findings of the study of rough wall flows under the influence of non-equilibrium pressure gradients along with preliminary computational results.

Attributions

Daniel J. Fritsch is the primary contributor and first author. All text and figures are his original work.

Vidya Vishwanathan aided in the experimental setup and gathering and post-processing of experimental data.

Christopher J. Roy advised the computational work.

K. Todd Lowe and William J. Devenport secured funding for this work and advised the experimental design and execution.

Turbulence and pressure fluctuations in rough wall boundary layers in pressure gradients

Daniel J. Fritsch^{1*}, Vidya Vishwanathan¹, Christopher J. Roy¹, K. Todd Lowe¹ and William J. Devenport^{1*}

¹Crofton Dept. Aerospace and Ocean Engineering, Virginia Tech,
225 Stanger St, Blacksburg, 24060, VA, USA.

*Corresponding author(s). E-mail(s): dannyf96@vt.edu;
devenport@vt.edu;

Abstract

Experimental and steady RANS data were generated for high Reynolds number rough wall flows beneath a systematically constructed family of bi-directional, continually varying pressure gradient distributions. These flows demonstrate outer-scale Reynolds number independence and qualitatively similar pressure gradient dependence, but reduced history dependence, compared to an equivalent smooth wall flow. The spectrum of fluctuating wall pressure beneath these flows is largely simplified compared to equivalent smooth wall behavior, collapsing on an outer-variable scaling and exhibiting an overlap region independent of pressure gradient and pressure gradient history. The universality of the high frequency behavior suggests a corresponding universality in the near wall dissipative behavior, contrary to current modeling philosophies for rough wall flows. Corresponding RANS data reveal fundamental issues with the classical roughness boundary condition definition; RANS data fail to replicate the correct Reynolds number dependencies of rough wall flows. These results suggest that, while a full understanding of rough wall flow physics is still lacking, such flows exhibit simple, universal relations that are exploitable for advancing our physical understanding and predictive modeling capability.

Keywords: Boundary Layers, Roughness, Pressure Fluctuations, CFD

1 Introduction

Aero/hydrodynamic flows, both internal and external, are often complicated by the presence of surface roughness. Such roughness comes from many places: manufacturing, both intentional and unintentional, corrosion, rust, accumulation of debris, ice, surface damage, and many others. The presence of roughness complicates the boundary layer flow developing above its canopy; intensifying and altering the nature of the turbulence generated within. The large portion of practical fluid dynamics problems that involve rough wall flows motivates the development of robust and useful *a priori* predictive tools for such flows, predictive tools that can only be developed after gaining an understanding of the physics involved in rough wall bounded turbulence that is currently lacking.

The primary effect of roughness on the overlying boundary layer is to increase the thickness of the wake region, resulting in a thicker overall boundary layer, and increase the kinetic energy of the turbulence within [1–3]. The increase in turbulent kinetic energy (TKE) is correlated with an increase in local skin friction over an equivalent smooth wall flow. This shows itself most clearly in the reduction of the viscous normalized velocity profile in the logarithmic region, denoted Δu^+ , where u is the local streamwise velocity and the superscript $+$ denotes normalization on viscous scales (the shear velocity u_τ and the kinematic viscosity, ν). For a fully rough flow, the roughness function is directly correlated with the roughness Reynolds number, $k^+ = k_s u_\tau / \nu$, where k_s is the sandgrain roughness height [4, 5].

It has been proposed that the effect of the roughness is contained within the near-wall region, inside the roughness layer, and that the boundary layer above the canopy will exhibit self-similarity, a concept generally referred to as outer region Reynolds number similarity or Townsend’s Hypothesis [6]. There has been a fair amount of evidence gathered in support of Townsend’s Hypothesis [3, 7, 8], but it appears clear that there is a requirement for large separation between the boundary layer thickness, δ , and the geometric roughness height, k_g ; at least $\delta/k_g > 40$ [3] and possibly even greater [8]. However, Mehdi *et al.* (2013) provided evidence that the effect of the roughness elements is felt higher in the boundary layer, above the roughness canopy, and that the lack of outer region similarity explains much of the lack of understanding within the field [9].

“Roughness” can refer to an infinite number of boundary layer flow surfaces with varying combinations of size, shape, and distribution. Within this infinite dimensional space, it is critical to have some mean or means of characterizing and categorizing various rough wall flows. Nikuradse (1950) characterized rough pipe flows of varying graded-sand-type roughness by their sandgrain height, k_s , and found that the corresponding Reynolds number, k^+ , categorized the flow into three distinct regimes: hydraulically smooth ($k^+ \leq 5$), transitionally rough ($5 < k^+ < 25$), and fully rough ($k^+ \geq 25$) [4]. In the fully rough regime, the character of the flow was fully described knowing the value of k^+ .

However, k_s is not known *a priori* for most rough wall flows. It can be found *posteriori* for a fully rough flow by measuring the roughness function,

Δu^+ , and using the correlations of Nikuradse (1950) [4] or Schlichting (1979) [10] to estimate an equivalent sandgrain roughness height. *A priori* knowledge of the equivalent sandgrain height would require knowledge of the relationship between the geometry of the roughness (its height, shape, and density or distributed pattern) and the corresponding effect on the boundary layer flow. Several correlations of this type have been proposed [5, 11–14], but none have proven to be universally applicable, only describing the roughness within a small niche of that infinite dimensional space. The inability to know k_s from roughness geometry *a priori* presents a challenge to the advancement of our understanding of rough wall flows, particularly to the modeling and simulation of such flows.

Of particular interest is the spectrum of fluctuating pressure that the turbulence in the rough wall boundary layer imparts onto the surface. The wall pressure spectrum is known to be an integrated effect of the turbulence structure throughout the boundary layer [15] and, as such, an understanding of the behavior of the wall pressure spectrum reveals fundamental insights into the workings of that turbulence structure. Compared to smooth wall boundary layer flows, the pressure spectrum on rough walls exhibits a heightened peak amplitude, representative of the increased turbulence intensity in the overlying boundary layer, and an accelerated inertial (mid-frequency) dissipation [16–20]. It is known that the root-mean-square amplitude and spectral behavior is affected by the roughness height and configuration, but the exact nature of this relationship remains unknown.

Meyers *et al.* (2015) proposed that the high frequency roll-off of the spectrum is universal under viscous scaling [19], much as the smooth wall spectrum is known to be [15]. Their method of computing the proper scale, however, was self-fulfilling until Joseph (2017) provided a robust *a priori* relationship for the universal scaling parameters that collapsed a wide variety of rough wall flows [20]. This scaling separates the friction velocity, u_τ (and by extension the wall shear stress, τ_w), into two components: a shear component, u_ν , and a form-drag component, u_p . The shear component collapses the rough wall high frequency spectra onto the same universal curve as what is observed in smooth wall flows.

A streamwise gradient in the mean surface pressure, achieved through curvature of said surface or a corresponding gradient in the boundary layer edge velocity, affects the growth of the boundary layer and the evolution of its turbulence. Adverse pressure gradients (APG) of increasing surface pressure thicken the boundary layer and intensify its turbulence, pushing the boundary layer toward separation, while favorable pressure gradients (FPG) of decreasing surface pressure do the opposite in smooth wall flows, pushing the boundary layer back towards laminar flow [21, 22]. In rough wall flows, however, FPG does not push the flow to relaminarization; the turbulent stresses will reduce compared to an equivalent zero pressure gradient (ZPG) rough wall flow, but cannot be completely eliminated, in part due to the acceleration of the flow at the roughness canopy, which intensifies the velocity scales of the wake and causes

the surface to effectively become "rougher" [23–25]. While rough, FPG flows are characterized by an upward shift in the logarithmic velocity profile, this is countered by an increase in local shear velocity, u_τ , and a corresponding increase in k^+ , leaving the roughness function/Reynolds number relationship intact [23, 24].

Pressure gradients are most easily classified by the Clauser parameter:

$$\beta = \frac{\delta^*}{\tau_w} \frac{dp}{dx} \quad (1)$$

where δ^* is the displacement thickness and dp/dx is the gradient of the mean surface pressure, p , in the streamwise (x) direction. For flows of constant β , the outer-region boundary layer development can be considered in equilibrium, meaning it will exhibit self-similar behavior, though that self-similar behavior will differ from zero pressure gradient (ZPG) boundary layers as a function of β . Flows with non-constant β are not as well understood, as they exhibit non-equilibrium (non-self-similar) and flow-history dependent effects [25–27].

The effect of pressure gradient on the fluctuating surface pressure is complex, affecting different regions of the autospectra in different ways [27, 28]. However, the high frequency content has been found to be universal on a viscous scaling, regardless of applied pressure gradient or pressure gradient history [27]. The primary impact of pressure gradient on the pressure autospectra beneath smooth wall boundary layers is a change in the mid-frequency slope, steepening in APG and flattening in FPG [27].

Relatively little is known about the development of boundary layers over rough walls while simultaneously in pressure gradient. A handful of studies have investigated the velocity statistics in rough wall boundary layers in constant APG [5, 29–31] and a few others in FPG [32–34], but none have considered systematically divided pressure gradient cases of both adverse and favorable character, and very little has been investigated on the effect of combined roughness and pressure gradient effects on the fluctuating surface pressure field [35].

The gaps in our understanding of the physics of rough wall flows leads to difficulties in successful predictive modeling. Modeling rough wall flows with computational fluid dynamics (CFD) is notoriously difficult [36], and it appears that this difficulty arises from a failure to understand the relationship between the roughness and the turbulence quantities of interest. It is obviously impractical to model the exact geometry of a rough surface in a steady CFD computation; instead, the effect of roughness is typically modeled as a change to the nature of the no-slip-wall boundary condition (BC). The most widely adapted of these modified boundary conditions is that of Wilcox (1988 [37], update 2006 [38]) to the k - ω models. In a typical no-slip-wall condition for a k - ω simulation, the turbulent kinetic energy, k , is set to zero at the wall, in correspondence with the lack of motion enforced by the no-slip-condition, and the specific dissipation rate, $\omega = \epsilon/C_\mu k$ (where ϵ is the dissipation rate and C_μ is a constant), theoretically then goes to infinity. In practicality, ω is typically fixed at a very large number to avoid numerical issues with division by zero.

The Wilcox correction reduces this value of ω as a function of k^+ , which has the effect of reducing the dissipation rate in the near wall region and driving a corresponding increase in overall TKE. The Wilcox correction matches well with experimental data for low roughness Reynolds numbers, $k^+ < 100$, but rapidly rolls off the fully rough asymptote for higher Reynolds numbers [39]. Updated roughness boundary conditions have been proposed [39–42], but all have problematic issues with numerical behavior and/or predictive accuracy in one or more roughness regimes. The exact relationship between a roughness condition and a corresponding numerical model and from said model to an accurate representation of the overlying boundary layer flow is not straightforward and remains an unsolved problem.

This work is a product of an ongoing project at Virginia Tech in collaboration with the North Atlantic Treaty Organization (NATO) Applied Vehicles Technology (AVT) 349 Research Task Group (RTG) on Non-Equilibrium Boundary Layers at Incompressible Conditions. The test case to be described in Section 2.1.1 has been thoroughly evaluated for a smooth wall condition [27, 43–45], which has revealed that boundary layers subjected to continually varying pressure gradients exhibit non-equilibrium and history dependent behaviors as complex functions of Reynolds number, pressure gradient sign, pressure gradient magnitude, and upstream flow history. This work will build on those aforementioned with the addition of surface roughness. The methods employed will be detailed in the following section, the obtained experimental and computational results will be presented and discussed in Sections 3–5, and some concluding remarks will be given in Section 6.

2 Methods

2.1 Experiments

2.1.1 Flow Case Setup

The experiment was performed in the hard-wall configuration of the hybrid-anechoic test section of the Virginia Tech Stability Wind Tunnel (VTSWT). Details of the tunnel and this specific configuration are documented by [46, 47]. The VTSWT features a $1.85 \times 1.85 \times 7.32 \text{ m}$ test section downstream of a 9:1 ratio contraction and turbulence screens, in a closed-circuit loop with a 4.3 m diameter fan driven by a 0.45 MW motor. The facility can produce test section free-stream speeds up to 80 m/s ($Re = 5 \times 10^6 / \text{m}$) at low turbulence intensities, 0.012% at 30 m/s and 0.020% at 60 m/s .

This experiment involves the study of a rough wall flow produced on the port-side wall of the test section while a 0.914 m chord NACA0012 airfoil model is mounted vertically in the test-section center. The model functions to produce bi-directional, continually varying pressure gradient distributions on the rough wall, enabling the simultaneous study of roughness and pressure gradient effects. The continual variation and bi-directionality of the pressure gradient

distributions means that these pressure gradient flows, particularly those further downstream in the test section, will exhibit non-equilibrium behavior, as observed in the equivalent smooth wall flow studied by [27].

A diagram of the test-section configuration for this experiment is given in Fig. 1. The coordinate system is defined such that $x = 0$ at the junction between contraction and test section and is positive downstream, $y = 0$ at the surface of the port wall and is positive away from the wall into the test section, and $z = 0$ at the centerline of the port wall, equally 0.925m from the floor and ceiling and is positive up via the right hand rule. The boundary layer flow is tripped 3.58m upstream of the rough surface origin by a zig-zag type trip installed on the contraction walls that is 3.18mm high, 20.39mm wide, and has a 27.6° zig-zag pattern. Results are obtained at twenty-four conditions; two Reynolds numbers of 2×10^6 and 3.5×10^6 based on the inflow velocity and model chord length and twelve angles of attack ranging from -10° to $+12^\circ$ at 2° intervals. Primary boundary layer measurements are obtained at seven streamwise locations, marked on Fig. 1.

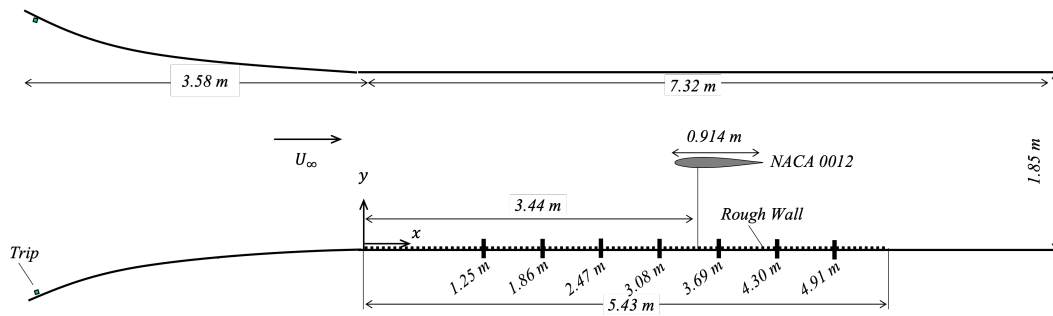


Fig. 1: Top-down view of test-section with installed NACA0012 model showing coordinate system, major dimensions, and measurement locations.

2.1.2 Rough Surface

The rough surface was designed collaboratively with Johns Hopkins University and with the U.S. Naval Academy. The surface consists of ordered, staggered circular cylinder elements of constant 2mm height and 3.14mm diameter. The surface covers the full span of the port-side wall of the VTSWT from the coordinate origin at $x = 0\text{m}$ to $x = 5.43\text{m}$, downstream of the primary airfoil influence, as shown in Fig. 1. A diagram of the surface layout is shown in Fig. 2.

The rough surface is constructed as a series of periodic, $2\text{ft} \times 2\text{ft}$ modular panels, consistent with the design of Duetsch-Patel *et al.* (2020) [47]. Each base panel is $2\text{ft} \times 2\text{ft} \times 1/8\text{in}$ rolled aluminum. The roughness pattern is applied via a CNC milled HDPE mold of the designed surface filled with epoxy resin. The mold is vacuum sealed to the panel for 24 hours before removal. To facilitate ease of manufacturing, each cylindrical mold is tapered 1° .

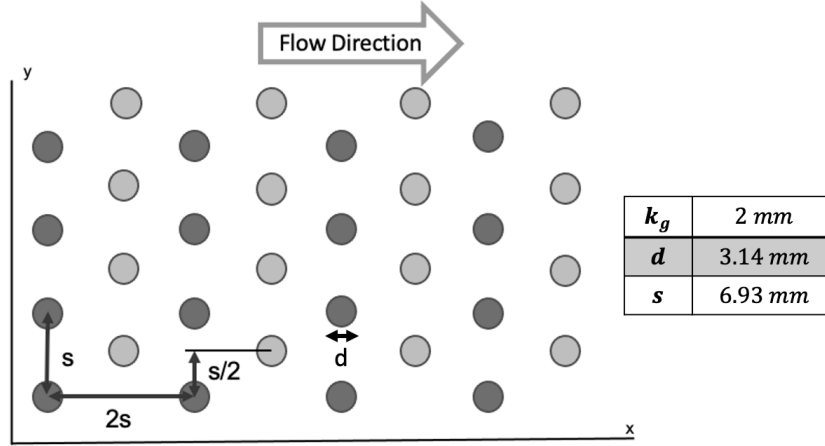


Fig. 2: Rough surface layout. Element shading is for ease of visualization only, all elements are identical.

2.1.3 Experimental Measurements and Processing

Measurements of mean static pressure are made on both side walls of the test section and the surface of the airfoil model utilizing 1mm diameter taps attached via Tygon tubing to pressure transducers. The wall taps are sampled by a 4 in. H2O DTC Initium ESP 32-HD transducer, and the model taps to a 2.5 psi Esterline 9816. Mean pressures were averaged over twenty-five records, where each individual record is the average of samples acquired at 600Hz for 0.94s. Mean static pressures were converted to pressure coefficients via the relation:

$$c_p = \frac{p - p_{ref}}{\frac{1}{2}\rho V_{ref}^2} \quad (2)$$

where c_p is the pressure coefficient, p is the local static pressure, p_{ref} is a reference static pressure, ρ is the fluid density, and V_{ref} is a reference velocity. Normally, p_{ref} is taken as the free-stream static pressure and V_{ref} as the free-stream velocity; however, to facilitate a more effective comparison to CFD results, in this case p_{ref} is a measured quantity on the starboard (opposite the roughness) wall centerline at $x = 1.67m$, $y = 1.85m$, $z = 0.0m$. The rest of the reference values are then computed from this reference condition using compressible, isentropic flow relations from the measured p_{ref} , an inferred free-stream stagnation pressure p_0 , and a measured stagnation temperature T_0 , measured by an Omega Thermistor Type 44004 thermocouple placed at approximately $x = 7.5m$, $y = 0m$, $z = 0.7m$.

Measurements of the velocity profile in the boundary layer were obtained using a 30 probe Pitot-static rake. Each probe has a 0.56mm inner diameter and protrudes 100mm forward of a 114mm chord NACA0012 aerodynamic fairing. The probe array spans from the top of the roughness canopy to approximately 180mm above the surface in a pseudo-logarithmic distribution (primarily logarithmic with linear spacing of the first five probes from the

wall). Each probe is connected via Tygon tubing to a 20 in. H2O DTC ESP 32-HD pressure transducer and is sampled in the same fashion as the mean static pressures. These measured local stagnation pressures are then converted to velocities using the compressible isentropic relations using a simultaneous measurement of the local static pressure at the streamwise location of the probe leading edges. The obtained velocity profiles were used to estimate the roughness function, Δu^+ , and the corresponding shear velocity, u_τ , in the method of Perry & Joubert (1963) [29]. This method is effectively a modified Clauser method; a constant-slope logarithmic region is identified in a modified outer normalized velocity profile, u/U_e vs. yU_e/ν , where U_e is the boundary layer edge velocity, and the slope of this log region is enforced as being equal to $\frac{1}{\kappa} \sqrt{\frac{c_f}{2}}$, i.e., enforcing that the log region has constant slope $1/\kappa$ under viscous normalization. This relies on the assumption that these rough wall pressure gradient flows have such a logarithmic region and that the slope of the various log regions is independent of the applied pressure gradients. Based on the work of Dixit & Ramesh (2009), the value of κ can be considered constant for flows of acceleration parameter magnitude $K = (\nu/U_e)(dU_e/dx) < 1 \times 10^{-7}$ [48]. The pressure gradients observed herein are mild, and the maximum magnitude of K observed is 3.04×10^{-8} , indicating that a constant κ can be assumed. Nevertheless, there is not-insignificant uncertainty in this method, particularly in identifying which points are part of the log region. The sensitivity of skin friction and roughness function to the identification of the log region was quantified and incorporated in the associated uncertainty. Upon estimation of the skin friction and roughness function, the equivalent sandgrain roughness was computed from the relation $\Delta u^+ = \frac{1}{\kappa} \ln[k^+] - 3.5$. It was found that the equivalent sandgrain roughness was $1.65k_g = 3.30mm$ and effectively pressure gradient and Reynolds number independent. More details on the determination of the sandgrain roughness can be found in Vishwanathan *et al.* (2022) [49].

Fluctuating pressure was measured using an array of seven Hottinger-Brüel & Kjaer (HBK) Type 4138 – A-015 1/8th in. pressure field condenser microphones, arranged as shown in Fig. 3. Data were acquired at $65,536Hz$ for $32s$, high-pass filtered at $0.7Hz$, and anti-alias low-pass filtered at $25.6kHz$ using an HBK 24-bit Pulse LAN-XI data acquisition system. Before each test, the sensitivity of each sensor was determined using an HBK Type 4228 pistonphone calibrator.

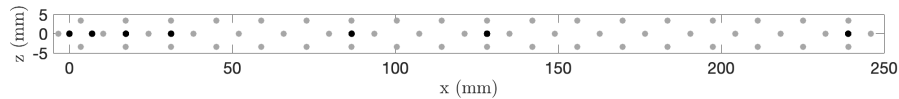


Fig. 3: Microphone array layout for streamwise orientation. Gray marks show locations of roughness elements.

Each condenser microphone was equipped with a $1/2\text{mm}$ diameter pinhole cap to reduce the spatial averaging of small-scale turbulence, which is known to generate errors in the measured spectra. The pinhole attenuates high frequency data above a cut-off frequency determined as a function of the viscous normalized pinhole diameter, $d^+ = du_\tau/\nu$ [50]. The pinhole cap also creates a cavity between itself and the microphone diaphragm, which acts as a Helmholtz resonator, altering the dynamic response of the sensor, which is flat up to 140kHz when uncovered. Under the pinhole cap, the response contains a resonant peak of around 12dB at approximately 15kHz , which can be corrected by assuming the Helmholtz resonance is a second-order dynamic system measured *a priori* via the transfer function between a capped and flat-response microphone subjected to pure white noise in an anechoic environment. This calibration is known to be a function of grazing flow [51, 52], pushing to 14dB at approximately 16kHz in the higher Reynolds number case to be presented, which is corrected *posteriori* using an optimization algorithm that minimizes discontinuities in the mid- and high frequency autospectral slopes. Auto- and cross-spectral densities were computed using the Welch algorithm with an 8,192-record-length Hanning window with 50% overlap, which was then 20th octave binned, giving the one-sided spectral density, G , in units $\text{Pa}^2/\text{frequency}$, i.e., $G(f)$ (Pa^2/Hz) in time and $G(\omega)$ ($\text{Pa}^2\text{s}/\text{rad}$) in radians, related by a scalar factor of $2\pi\text{rad}$.

Experimental uncertainties were computed in a three-step process. First, the fundamental uncertainty of each instrument is known from the manufacturer's documentation. Second, repeat measurements were made using primary instruments (static pressure taps, boundary layer rake, and microphones), the root-mean-square deviations of which can be used to improve the primary estimate of each instrument's uncertainty. These can be carried through to derived parameters. Finally, corrections can be made for the uncertainty in model angle of attack, processing algorithms (primarily the Welch algorithm), and instrument calibrations, based on observations of the measurement statistics across repeat measurements. Estimates for the measured uncertainties are given in Table 1.

p, ρ, ν, U_∞	u	δ, δ^*	θ	τ_w, β	G_{ppLow}	G_{ppMid}	G_{ppHigh}
$\pm 0.1\%$	$\pm 0.9\%$	$\pm 3.0\%$	$\pm 4.0\%$	$\pm 8.0\%$	$\pm 2.5\text{ dB}$	$\pm 1.5\text{ dB}$	$\pm 1.75\text{ dB}$

Table 1: Estimates of uncertainty in measured quantities. dB relative to $p_{ref} = 20\mu\text{Pa}$.

2.2 Computations

The flow case was simulated as a 2D steady RANS simulation in CREATE-AV Kestrel KCFD, an unstructured finite volume CFD solver. The test-section domain consists of a no-slip wall boundary condition fully resolved below

$y^+ = 1$, a sharp-trailing edge NACA0012 airfoil profile in a quasi-C-grid topology, and a slip-wall boundary condition opposite the boundary layer wall, set at a 0.46° converging angle to match the favorable pressure gradient generated by the four walls of boundary layer growth in the VTSWT. Upstream of the test section domain is a constant $1.85m$ square cross-section with a smooth, no-slip-wall, the length of which is set to match the inflow displacement thickness in the smooth wall case. The test-section rough wall boundary condition is an adaptation of the Wilcox (2006) [38] roughness function, which prescribes a wall specific dissipation rate as a function of the equivalent sand-grain roughness height, k_s . Solutions were converged on five systematically refined grid levels to estimate the discretization error associated with the presented solutions. More details on the grid development and smooth wall results are found in [45].

3 Measured Boundary Layer Development

The experimentally measured mean pressure coefficient, skin friction coefficient, and normalized pressure gradient in the form of the Clauser parameter are shown in Fig. 4a, b, and c respectively. The tested Reynolds numbers are distinguished by line style, solid for $Re = 2M$ and dotted for $Re = 3.5M$, and the airfoil model angle of attack is distinguished both by color, ranging from blue at $\alpha = -10^\circ$ to red at $\alpha = 12^\circ$, and by the marker styles shown in Table 2. This line and marker styling will be used for the remainder of the figures in this section, and the $\alpha = 0^\circ$ case is black and bold in each figure.

$\alpha = -10^\circ$	-8°	-6°	-4°	-2°	0°	2°	4°	6°	8°	10°	12°
\triangle	\square	$+$	$*$	\triangleleft	\circ	\diamond	\star	\triangleright	\times	\star	∇

Table 2: Marker styles.

The pressure coefficient distribution for each case is roughly Gaussian, increasing for positive angles of attack and decreasing for negative to a maximum/minimum occurring near the x-location of the model center of rotation (quarter chord), then reversing trend downstream. This behavior is closely Reynolds number independent, as was observed in the equivalent smooth wall flow [27].

The corresponding pressure gradient (Fig. 4c), represented by the Clauser parameter, β , is roughly sinusoidal for each case, reaching a maximum magnitude just upstream of the x-location of the airfoil model leading edge before reversing trend, exhibiting a clean cross-over at the model quarter chord and reaching a secondary maximum magnitude just downstream of the model. Each angle of attack case features both adverse and favorable pressure gradients; one in the upstream region and one in the downstream region. This pressure gradient reversal is known to produce out-of-equilibrium, non-self similar behavior [27].

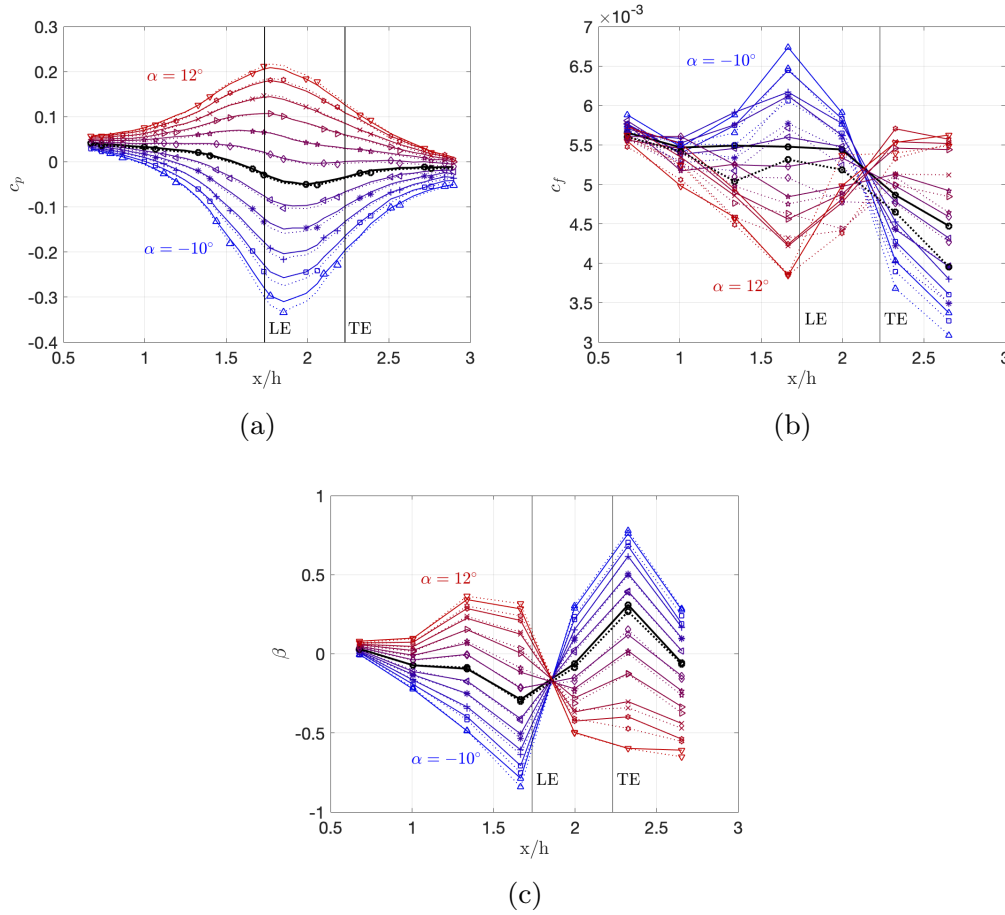
Turbulence and pressure fluctuations in rough wall boundary layers in pressure gradients

Fig. 4: Measured mean pressure coefficient (a), skin friction coefficient (b), and Clauser parameter (c) distributions.

The skin friction coefficient (Fig. 4b) distribution is more complicated. In general, c_f increases in FPG and decreases in APG, but this relation lags behind the pressure gradient reversal in the downstream region. This is indicative of a history dependence of the skin friction and was also observed in the equivalent smooth wall flow [27]. There is, however, no apparent Reynolds number dependence in these data, which is unique to the rough wall case and indicates that these flows are of sufficient k^+ to have achieved Reynolds number similarity [6].

Figure 5a-g shows the viscous normalized velocity profiles at each of the seven boundary layer measurement stations, alongside the logarithmic Law of the Wall with constants $\kappa = 0.41$ and $B = 5.0$. As is typically observed in rough wall flows, the logarithmic regions of the velocity profiles is displaced downwards by some $\Delta u^+ \propto k^+$. Under this normalization, the velocity profile exhibits both pressure gradient and Reynolds number dependence, whereas the logarithmic region was universal in the equivalent smooth wall flow following the classical Law of the Wall [27]. The higher Reynolds number case exhibits a consistently higher Δu^+ , consistent with its heightened k^+ . In the upstream

region (Fig. 5a-d), the effect of pressure gradient is to increase u^+ in APG and decrease in FPG. This trend is reversed in the downstream region (Fig. 5d-g), but it lags downstream in a similar manner to the skin friction coefficient in Fig. 4b.

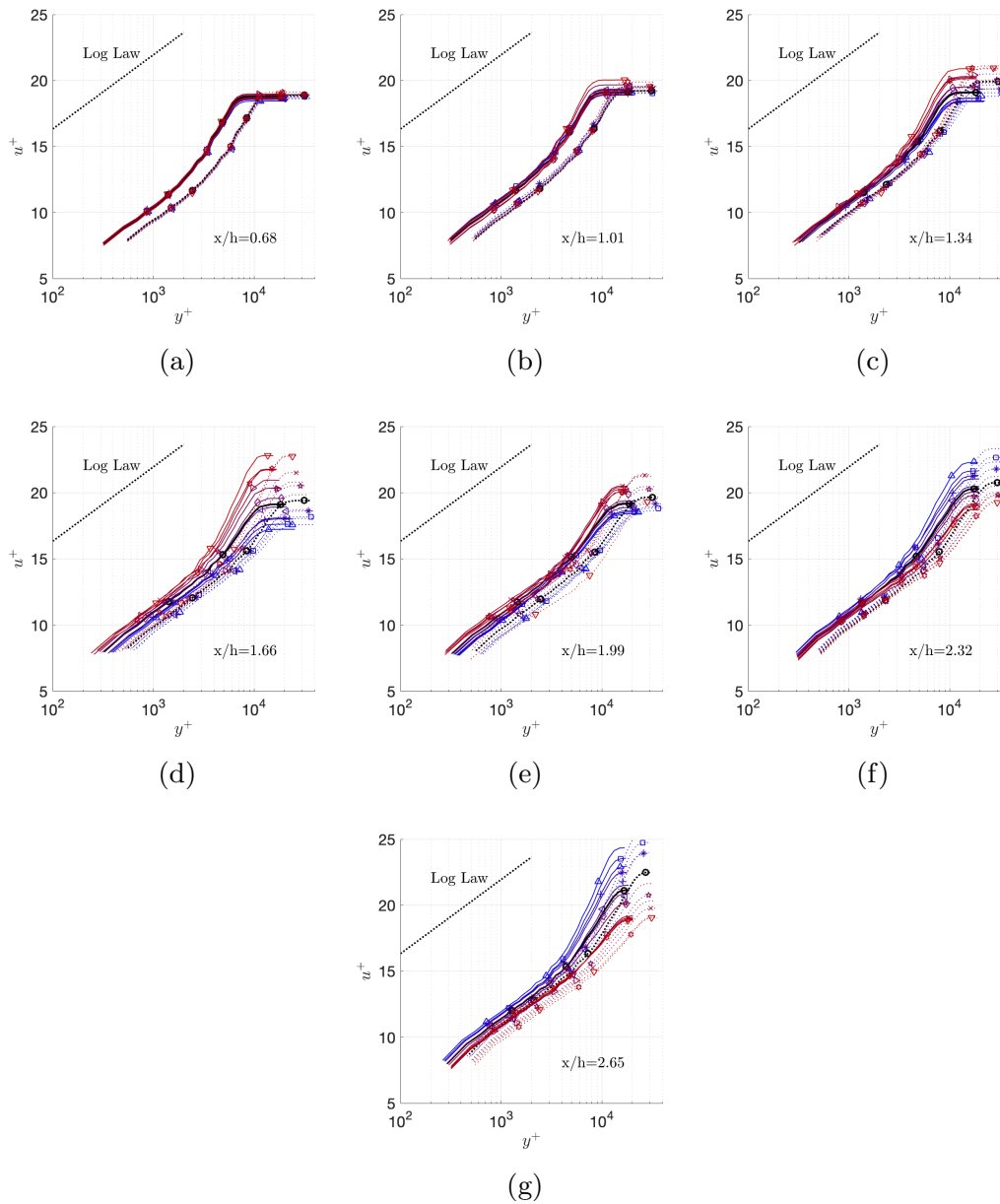


Fig. 5: Measured mean velocity profiles under viscous normalization at each measurement location.

If Townsend's Hypothesis [6] holds true, then we could expect that these velocity profiles ought to collapse instead on an outer scaling, u/U_e vs. y/δ as shown in Fig. 6. This hypothesis is confirmed, both with (Fig. 6b) and without

(Fig. 6a) pressure gradient effects. The outer normalization does not account for the effect of pressure gradient as shown in Fig. 6b, but the effects of pressure gradient and pressure gradient history can be shown to be independent of the Reynolds number. As demonstrated in Fig. 6c, the change in u/U_e between Reynolds number cases at equivalent β is zero.

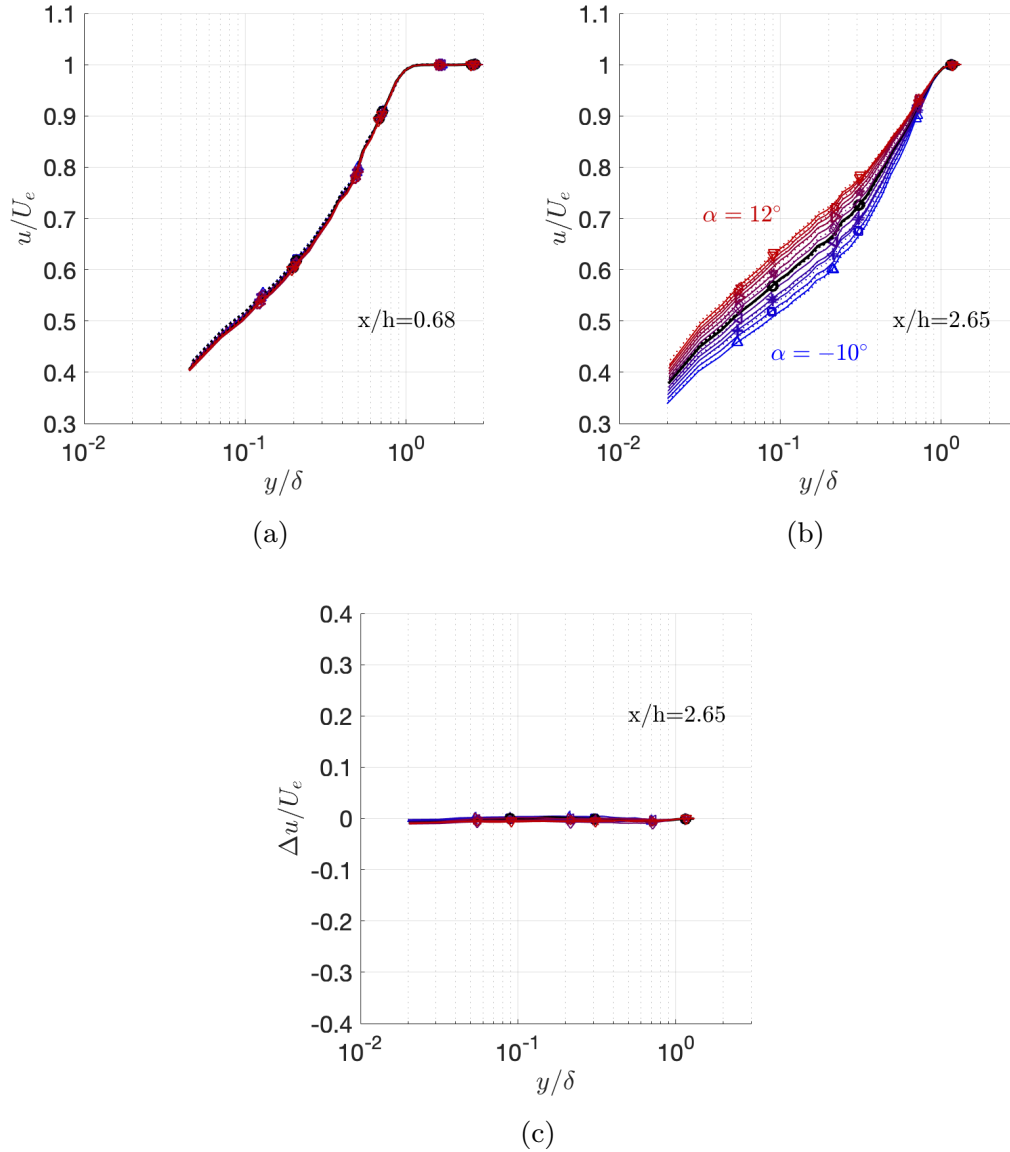


Fig. 6: Measured mean velocity profiles under outer normalization for inflow (a) and outflow (b) measurement planes and change in outer normalized velocity between Reynolds number cases at outflow plane (c).

The corresponding boundary layer thicknesses, δ , δ^* , and θ are shown in Fig. 7a-c respectively. The 99% edge velocity boundary layer thickness (Fig. 7a) at the first measurement plane is larger than the equivalent smooth wall case,

but only by around a 10% increase [27]. The integrated thicknesses (Fig. 7b,c), by contrast, show around a 2x increase from their equivalent smooth wall values at the inflow plane. The rough wall boundary layer also grows more rapidly downstream than the smooth, more than doubling in thickness across this rough wall test case between the most upstream and downstream measurement planes, while increasing by just 75% in the equivalent smooth wall case with the measurement locations held constant.

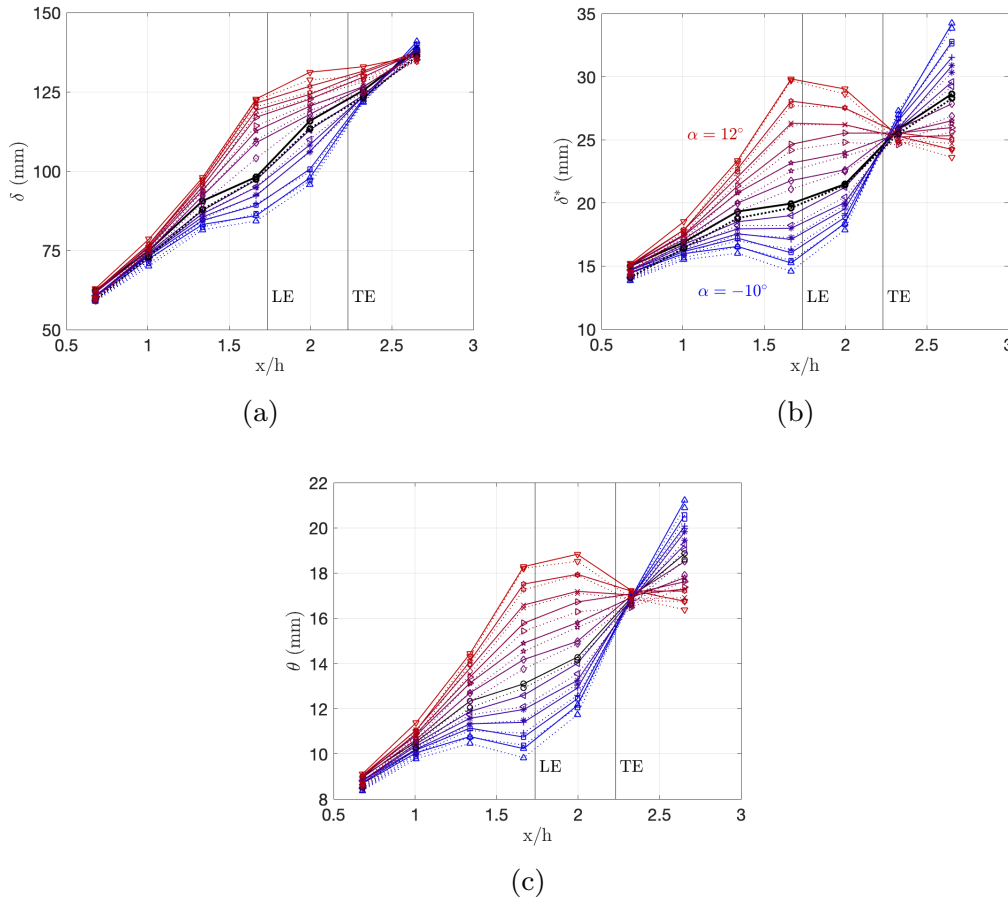


Fig. 7: Measured boundary layer 99% edge velocity (a), displacement (b), and momentum (c) thicknesses.

Over smooth walls, the boundary layer thickness decreases with free-stream Reynolds number [27], but in this case, we observe a complete independence of the 99% edge velocity and integrated boundary layer thicknesses with Reynolds number. This is to be expected after the same observation was made on the outer-normalized velocity profiles.

The pressure gradient effect on the boundary layer thickness in the upstream region is straightforward, increasing in APG and decreasing in FPG. Similar to the skin friction, however, the reversal of the trend lags behind the

pressure gradient, achieving a cross-over point now downstream of the model. The history lag is reduced in the rough wall flow compared to the smooth, the former crossing over just upstream of the second-to-last measurement point, while the latter exhibited this behavior between the second-to-last and final measurement stations. The shifting of the cross-over point closer to that of the pressure gradient itself indicates a reduction in history dependence for the rough wall flow. This is quantified in Table 3, along with the range of δ^* values observed at $x/h = 2.32$. In the smooth wall flow at this location, δ^* was largest for the higher angles of attack, but in the rough wall case this is reversed. We hypothesize that the reduction of history effects in the rough wall case is due to intensification of inner region dynamics; the presence of roughness increases the relative importance of the inner motions to the overall boundary layer dynamics, and the equivalent smooth wall case has demonstrated that the inner region is subject to significantly less history dependence than the outer layer [27]. If the pressure gradient and pressure gradient history effects on the inner motions are similar in the rough wall, then the dynamics of the rough wall boundary layer would be more heavily dependent on history-independent motions than equivalent smooth wall flows, and thus experience a reduced overall history dependence.

	Smooth	Rough
δ^* @ $x/h = 2.32, \alpha = -10^\circ$	7.6mm	27.3mm
δ^* @ $x/h = 2.32, \alpha = 12^\circ$	8.7mm	24.6mm
Cross-over Location in δ^*	2.42 ± 0.1	2.28 ± 0.1

Table 3: Select quantities from rough and smooth walls for $Re = 2M$ quantifying history effects.

4 Surface Pressure Statistics

Figure 8 shows the measured autospectral density of wall pressure at each measurement station, colored and marked with the same scheme as the previous section. As is typical for turbulent boundary layers, the spectrum presents as three regions; at low frequencies, spectral amplitude increases with frequency before reaching a peak at 90dB at 150Hz in the lower Reynolds number case and 96dB at 250Hz for the higher Reynolds number case. As observed in smooth wall boundary layers, the effect of increasing Reynolds number is to push the spectrum to higher amplitudes and frequencies. Beyond the peak, the spectral amplitude rolls off, first at one rate and then steepening further into the high frequency region. It has been repeatedly observed [15, 19, 20, 27] that the slope of the highest frequency region is universally f^{-5} and this is repeated in these new data, seemingly independent of pressure gradient and Reynolds number.

In the equivalent smooth wall case, the predominant effect of pressure gradient on the spectra was on the slope of the mid-frequency region, steepening

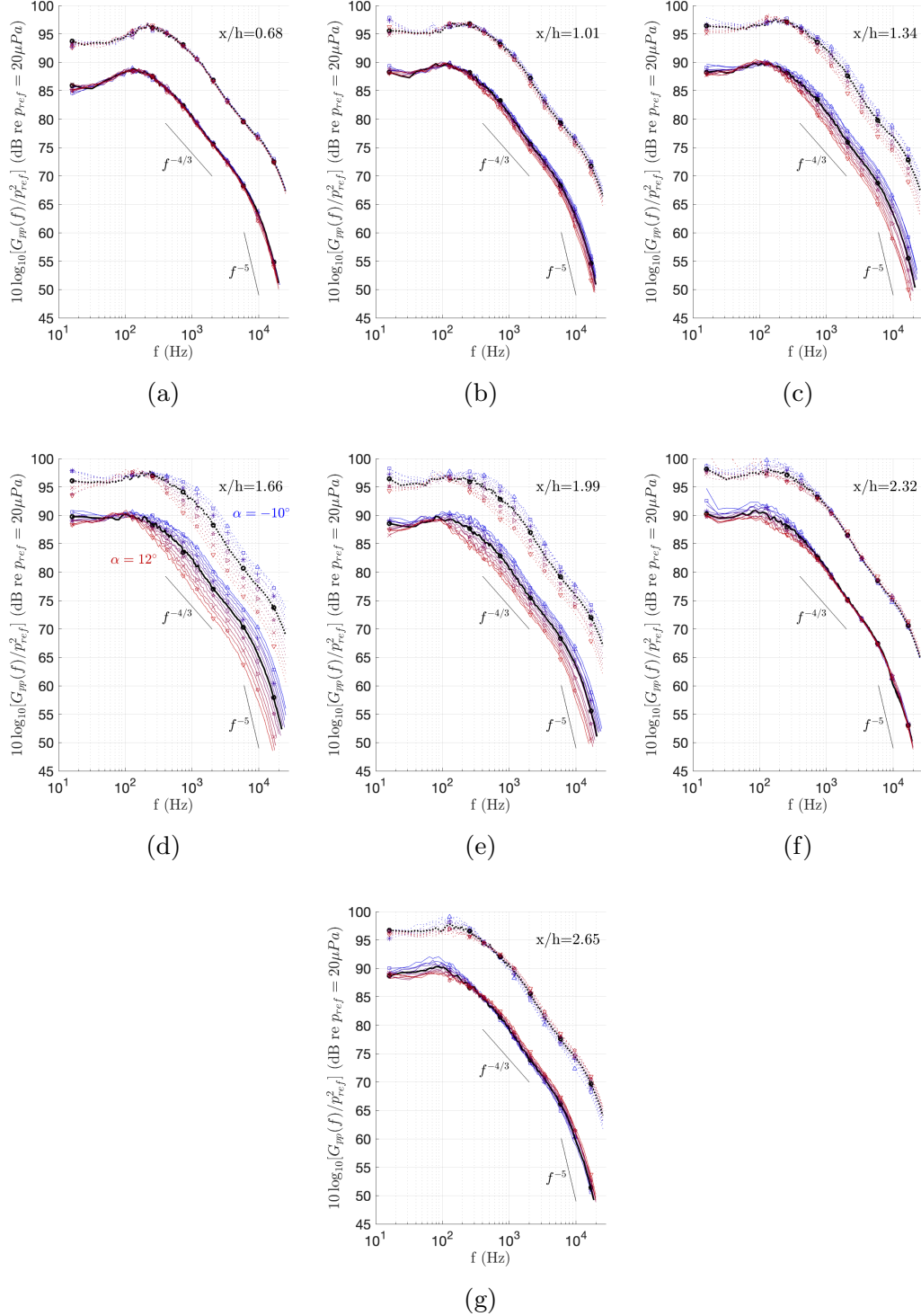


Fig. 8: Measured autospectral densities of fluctuating wall pressure.

in APG and shallowing in FPG [27]. In the rough wall flow, however, the mid-frequency region appears to have parallel slopes at all stations and angles of attack. It has previously been postulated [19] that the slope of this region is

approximately $f^{-4/3}$, which is closely matched by these new data. The pressure gradient also appears to have only small, if any, statistically meaningful effect on the low frequency region of the spectrum, with the majority of the pressure gradient effect seemingly captured in the peak frequency, shifting higher in FPG and lower in AGP.

The lack of pressure gradient dependence on the mid-frequency slope offers insight into the physical meaning of the mid-frequency behavior. Joseph (2017) observed that a fluctuating pressure sensor mounted flush with the roughness tops, rather than the surface below, measured a smooth wall pressure spectrum [20]. This implies that the roughness effects on the spectrum are produced by the region contained within the canopy. Additionally, Meyers *et al.* (2015) [19] and Joseph (2017) [20] observed that the slope of the mid-frequency region was dependent on element height and density. One possible interpretation of these findings is that the mid-frequency slope and the energy transfer it represents are directly dependent on the wall-normal position at which the bulk of the pressure fluctuations are being produced, hence the steepening of the slope in rough wall flows, where that source position is pushed from the wall with k_s . This would explain the variation observed by Meyers *et al.* and Joseph, as the mid-frequency slope would then be a function of k_s for a rough wall flow, as well as explaining the constant slopes observed in Fig. 8, as these rough wall flows exhibit constant k_s . Further, this also explains the trends observed in the equivalent smooth wall flow [27], where FPG compresses the boundary layer, driving the source point towards the wall and shallowing the mid-frequency slope, and APG expands the boundary layer, pulling the source point away from the wall and steepening the mid-frequency slope. The same pressure gradient effects are not observed in the rough wall, since the effect of increasing k_s dominates.

Downstream of the peak mean pressure coefficient (Fig. 8e-g), the mid-frequency region appears to split into two sub-regions. The higher of these two frequency regions maintains the parallel slopes observed previously, but the lower frequency region begins to show a pressure gradient dependent slope. This is most clearly observed in Fig. 8f, at $x/h = 2.32$, where the spectra are collapsed above $1kHz$ for the low Reynolds number case but retain an angle of attack dependence between the peak of the spectra and that point. This suggests these flows may collapse on just two scalings, which was not possible in the equivalent smooth wall flow [27], but was postulated to be valid for rough wall flows by Meyers *et al.* [19], since the pressure gradient effect can effectively be divided into just two regimes: the low frequency behavior, where there is no collapse in Fig. 8f, and the mid- and high frequency regions combined, which do collapse.

In the smooth wall case, the high frequency returned to the same curve for all angles of attack at the most downstream location [27], but in the rough wall case, this is achieved one station further upstream (Fig. 8f) and, at the most downstream station (Fig. 8g), the trends observed upstream begin to reverse. This has two major implications: just as was observed in the growth

of the boundary layer in Fig. 7, the history dependence of the flow is reduced between equivalent smooth and rough wall flows and the effect of the reversing pressure gradient is not just to bring the flow back to its pre-pressure-gradient state, but to continue to impact the spectral development beyond the point at which collapse is achieved and bring about a character that is displaced from an equivalent “baseline” ZPG case, even beyond the point at which the pressure gradient has returned to zero.

Meyers *et al.* (2015) proposed that the high frequency region of rough wall pressure spectra were universal on a newly defined scaling based on a modified shear velocity, u_ν [19]. They postulated that u_ν represented the portion of u_τ driven by the viscous sublayer developing between the roughness elements, while $u_p = u_\tau - u_\nu$ represented the local shear stress due to roughness element profile drag, thus, $u_\nu = u_\tau$ in a smooth wall flow. u_ν is calculated by enforcing a collapse of the high frequency spectra in the same manner as is observed under viscous scaling for smooth wall flows. The result is a full collapse within a statistically significant 95% confidence band of 3.01dB, as shown in Fig. 9a. Figure 9b shows the same data, now plotted alongside the equivalent smooth wall viscous scaled data.

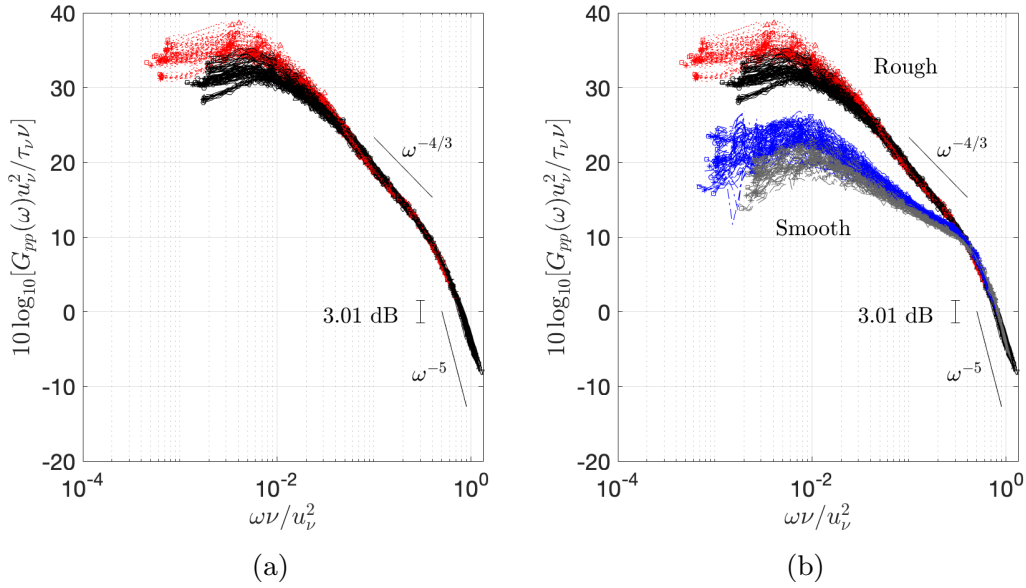


Fig. 9: Pressure spectra under viscous scaling of Meyers *et al.* (2015) [19]. Comparison with smooth wall data of Fritsch *et al.* [27] (2022) shown in (b). — Rough, $Re = 2M$, ... Rough, $Re = 3.5M$, - - - Smooth, $Re = 2M$, -.- Smooth, $Re = 3.5M$.

Given that u_ν is determined *posteriori* under the assumption that such a scale must exist, physical interpretation of this parameter requires observations of its behavior outside of the pressure spectra scaling. Figure 10a shows

the distribution of the calculated u_ν values, expressed as a ratio of the edge velocity (proportional to the square root of the associated skin friction coefficient). The general trend of this relation closely follows that of the overall skin friction coefficient – increasing in FPG, decreasing in APG, and reversing trend with a downstream lag relative to the mean pressure gradient. There are two marked differences, however; the ratio u_ν/U_e is not Reynolds number independent, decreasing with increasing free-stream Reynolds number. Additionally, the cross-over point has shifted upstream, in Fig. 4b it is located at approximately $x/h = 2.25$, but is located around $x/h = 2.0$ in Fig. 10a. If we take u_ν to be the characteristic scale of the inner motion, which seems valid given its successful collapse of the high frequency pressure spectra, then this would indicate that the inner scales respond more rapidly to applied pressure gradient than the outer, which was also the conclusion of Fritsch *et al.* (2022) [27].

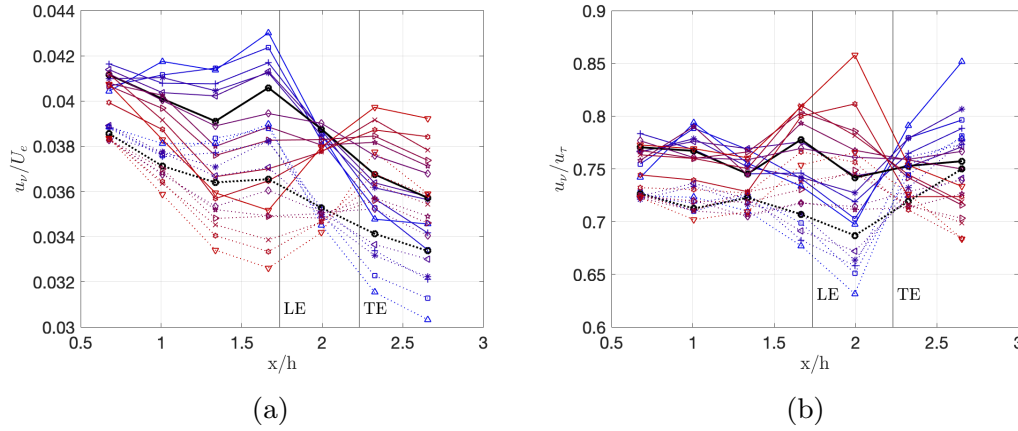


Fig. 10: Viscous scale u_ν of Meyers *et al.* (2015) [19] presented as ratios of U_e (a) and u_τ (b).

When viewed as scaled by the friction velocity, u_ν/u_τ , the functional dependency changes. u_ν/u_τ appears to be roughly constant, within a generous uncertainty, except for the fifth measurement station at $x/h \approx 2$. Here, there is a large angle of attack dependence too large to be purely associated with uncertainty. We propose two hypotheses to explain this discrepancy: first, Fritsch *et al.* (2022) observed that this measurement station, associated with the maximum magnitude of the secondary pressure gradient, exhibited the farthest out-of-equilibrium behavior because of the rapid reversal of the pressure gradient sign [45]. However, the previous observation that $c_{f\nu}$ responds more rapidly to the pressure gradient than c_f could explain the deviations here, since the difference in history dependence would reveal itself most strongly in $u_\nu/u_\tau \propto c_{f\nu}/c_f$ at this station.

Based on these observations, we propose an update to the theories of Meyers *et al.* (2015) [19] and Joseph (2017) [20]. u_ν represents the local contribution

to shear that is driven by the viscous dissipation of fluid kinetic energy to heat. The collapse observed in Fig. 9b suggests this process is not a function of Reynolds number, pressure gradient, roughness, or flow history, which implies it can be described as a function of just two variables: the local viscosity, ν , and the modified shear velocity, u_ν . Figure 10b, along with the observations of Joseph [20], implies that u_ν may be a function only of k^+ . This implies that the increase in shear in the rough wall case, $u_p = u_\tau - u_\nu$, is not associated with dissipation, as the near wall dissipation is dominated by viscous effects which are driven primarily by the fluid properties. In a smooth wall boundary layer, the sublayer acts a momentum sink [53], taking momentum out of the flow by dissipating the smallest turbulent motions to heat, adhering the fluid near the wall to the wall (no slip condition), and thus creating drag. If this process is universal, then the increase in drag on the rough wall must come from some other mechanism. We propose that mechanism is the roughness elements acting as a momentum source in the sublayer, generating turbulent motions on the scale of the roughness height that then lift into the boundary layer. This increase in turbulent production drives an increase in the local drag. The intensity of these turbulent motions at the roughness canopy will increase with Reynolds number, decreasing the relative contribution of the viscous scale to the full u_τ as demonstrated in Fig. 10b.

In the equivalent smooth wall flow, the low frequency region of the spectrum proved nearly impossible to satisfactorily scale [27]. In the rough wall case, the scaling of the low frequency region turns out to be more straightforward, collapsing on a standard outer-flow-variable scaling, using the local edge velocity, momentum thickness, and dynamic pressure, $q = \frac{1}{2}\rho U_e^2$, as shown in Fig. 11. This scaling, in fact, appears to collapse the entire spectrum within a reasonable tolerance, something that was shown to be impossible for smooth wall flows in pressure gradients. The autospectrum of the fluctuating pressure beneath rough walls appears to be driven by simpler physics than an equivalent smooth wall case, even in pressure gradient, and dependent primarily on the outer flow variables, which are themselves functions primarily of the roughness height, k_s , independent of Reynolds number, and responding to the applied pressure gradient more rapidly than over smooth walls.

In addition to the point spectrum, two-point space-time correlation statistics can reveal much of the physics of the turbulent flow. Figure 12 shows the convection velocity distributions at the location of maximum initial pressure gradient magnitude, $x/h = 1.34$, found by locating the maxima of the space-time correlation and, assuming Taylor's hypothesis of frozen turbulence, computing the associated pressure convection velocity as $U_c = \xi/\tau$, where ξ is the spatial separation between two synchronized measurements and τ is the time delay at which the correlation is at its maximum. The effect of pressure gradient on the convection velocity is straightforward and in agreement with what is generally accepted in the literature; APG decreases the convection velocity relative to the edge velocity while FPG increases it.

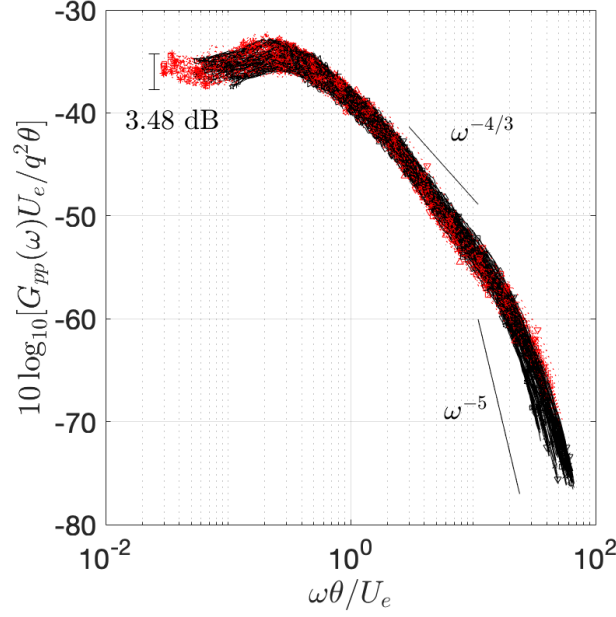


Fig. 11: Pressure spectra under outer scaling. Linestyles found in Fig. 9

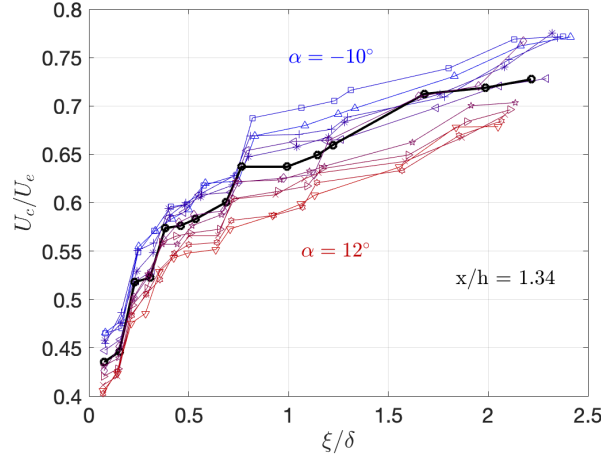


Fig. 12: Local pressure convection velocity distributions for each model angle measured at $x/h = 1.34$.

The local convection velocity increases with increasing separation, asymptoting towards some value typically referred to as the broadband convection velocity. It is generally accepted [15] that, in ZPG over smooth walls, this asymptotic broadband value is $\approx 0.8U_e < U_{cbb} < 0.85U_e$. In the equivalent smooth wall case, the ZPG cases asymptoted to approximately $0.85U_e$, with a spread of $0.8U_e < U_{cbb} < 0.92U_e$ under adverse and favorable pressure gradient [27]. Here, the convection velocities are suppressed over the rough wall flow, appearing to asymptote towards only $\approx 0.75U_e$ in ZPG.

Figure 13 shows the broadband convection velocity values obtained at each station and angle of attack. This distribution shows higher uncertainty than in the smooth wall case [27]; this is attributed to the roughness elements breaking up the large turbulent structures and decreasing their correlation at large separations, lowering the peak correlation amplitude and raising the uncertainty in identifying said peak. At the inflow, in \approx ZPG, the value of U_{cbb} is indeed close to $0.75U_e$, which spreads in the range $0.66U_e < U_{cbb} < 0.79U_e$ in the initial adverse and favorable pressure gradient cases. The trend then roughly reverses in the downstream region, with a small lag in the cross-over point, similar to what was observed in the smooth wall case [27]. Interestingly, as the flow progresses downstream, the broadband convection velocity at 0° angle of attack lowers, reaching $\approx 0.68U_e$ by the most downstream measurement plane. This reduction is attributed to the accumulated drag over the continuous roughness surface, i.e., whatever physics at play are reducing U_{cbb} in the rough wall flow continue reducing the convection velocity as the flow continues over the roughness. The behavior of the convection velocities offers insight into the physical mechanisms by which the history effects of rough wall flows are reduced; as the speed at which information is convection downstream is reduced, the distance at which history effects lag will naturally reduce as well.

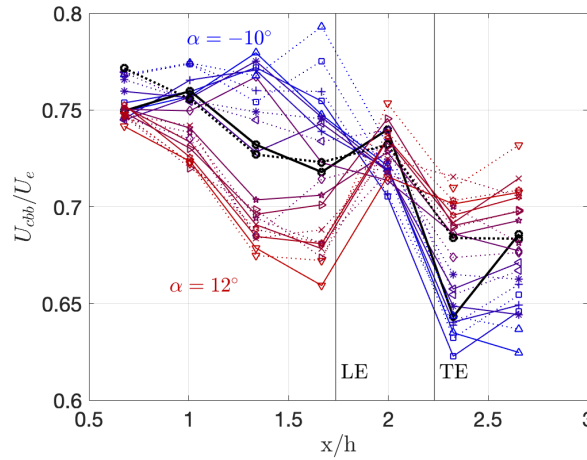


Fig. 13: Measured broadband pressure convection velocity distributions.

5 Modeling Considerations

For the equivalent smooth wall case, it was found that steady 2D RANS qualitatively captured the local and history pressure gradient effects generated in these flows [45]. Given that the majority of the field solution is the same for a rough wall case, it might be expected that similar results would be found when

simulating these rough wall flows; however, the validity of the current state-of-the-art in rough wall boundary condition modeling should not be taken for granted.

Figure 14 shows the measured and predicted displacement thickness growth for both Reynolds numbers with the model set at $\alpha = 12^\circ$. These results are obtained using the Menter Baseline $k-\omega$ model [54] with the KCFD $k-\omega$ roughness boundary condition, adapted from the Wilcox (2006) [38] boundary condition, with $k_s = 1.65k_g = 3.30\text{mm}$. In the lower Reynolds number case, the CFD consistently underpredicts the displacement thickness, but does capture the qualitative pressure gradient and pressure gradient history effects. In the higher Reynolds number case, there is no Reynolds number similarity observed in the computational results, the CFD overpredicting compared to experiment by a significant margin ($\approx 90\%$). While the CFD captures the pressure gradient effects, it fails to accurately capture the roughness effect, the observed Reynolds number similarity, or a canonical Reynolds number effect.

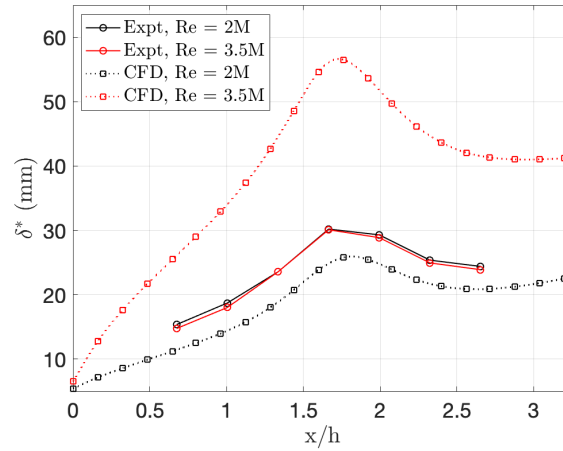


Fig. 14: Displacement thickness growth measured and predicted, $\alpha = 12^\circ$.

By reversing the logic in the discussion of Fig. 5 & 7 in Section 3, it would be expected that the CFD results will not show outer-layer Reynolds number similarity, as shown in Fig. 15. Similar to what is shown in Fig. 14, while the experimental velocity profiles show Reynolds number similarity on outer scales, the CFD results do not.

More concerning than the model's performance in predicting a given case is its failure to correctly capture the correct trends with increasing free-stream and roughness Reynolds numbers. To generate a comparison point, we attempted to increase the prescribed wall k_s for the lower Reynolds number case to find the value that would match the measured data, and found that no such value of k_s existed; increasing k_s beyond $1.65k_g$ did not change the converged solution. A full sweep of k_s values was attempted at both experimentally tested Reynolds numbers and the results for the computed roughness

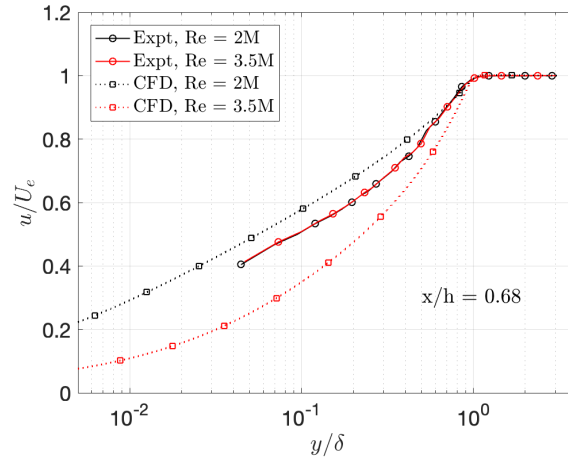


Fig. 15: Outer normalized velocity profiles as measured and predicted, $x/h = 0.68$, $\alpha = 12^\circ$.

function trend with k^+ is shown in Fig. 16 beside the curve of Nikuradse (1950), generally accepted to be accurate for all fully rough flows [4].

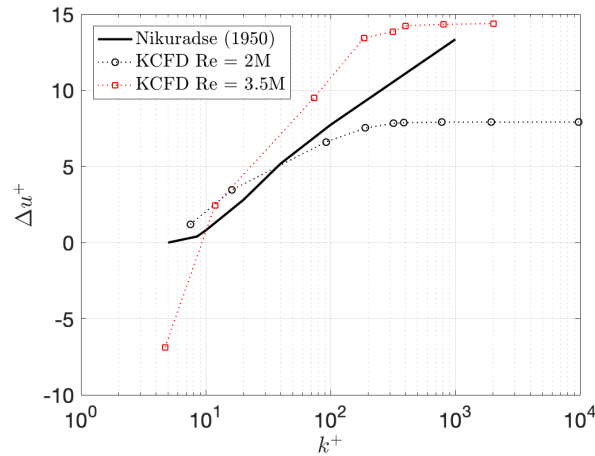


Fig. 16: Roughness function as a function of roughness Reynolds number as computed against the curve of Nikuradse (1950) [4].

The computed results do not match Nikuradse's data; at higher Reynolds numbers, the computed data reaches a horizontal asymptote, a point beyond which increasing k^+ fails to have an impact on the converged CFD solution, which is non-physical based on the logarithmic increase observed by Nikuradse [4] and confirmed by many other studies [8]. The magnitude of this asymptote, and the slope of the relation before it, are variable with free-stream Reynolds number, which is also non-physical. These results are not ground breaking; this trend was also observed by Aupoix (2014) [39].

Roughness boundary conditions for wall-resolved k - ω models, like that used in KCFD, prescribe wall-bounded values of the specific dissipation rate, ω_{wall} , to account for roughness effects, as opposed to directly enforcing the Nikuradse correlation as some wall-function models do. Wall-functions are known to better replicate the Nikuradse curve, but have many issues of their own, particularly in pressure gradient, and are not the focus of this work. In a classic, smooth wall k - ω simulation, the no-slip-condition is enforced as $V_{wall} = 0$, $k_{wall} = 0$, which follows directly from the physical interpretation of the no-slip-wall. Recalling that ω is defined $\omega = \epsilon/C_\mu k$, the k wall boundary condition implies that $\omega_{wall} = \infty$. Given that computers don't well handle Inf values, ω_{wall} is typically set as some very large number. As described by Wilcox (2006), then, an efficient method for simulating roughness effects is to lower the value of ω_{wall} , thus driving up the turbulent motion near the wall due to the decrease in near-wall-dissipation, which is correlated with a depression in the log-law intercept, effectively simulating a roughness function, Δu^+ [38]. He defines:

$$\omega_{wall} = SR \frac{u_\tau^2}{\nu} \quad (3)$$

where the coefficient SR is a function of roughness Reynolds number, k^+ . The KCFD boundary condition functions similarly. Wilcox showed that reducing ω_{wall} was correlated with increasing Δu^+ , but only considered a narrow range of k^+ values, and it has been previously observed that the original Wilcox formulation breaks down at high k^+ , much as the KCFD function does [39, 42].

This begs the question, can some function $SR(k^+)$ be defined such that the behavior observed by Nikuradse is properly modeled? It turns out that no such solution can exist, as demonstrated by data obtained in KCFD shown in Fig. 17. Expressed as a function directly of SR , the roughness function asymptotes to constant value (right to left in Fig. 17) and retains a free-stream Reynolds number dependence.

It is clear from these results and the comprehensive review of Aupoix (2014) [39] that the Wilcox ω_{wall} rough wall boundary condition correction fails to accurately replicate the physics of high k^+ rough wall flows, not due to the chosen form of $SR(k^+)$, but due to a more fundamental issue in the BC itself. Reduction of ω_{wall} does not produce a Reynolds-number-similar roughness effect, nor does it generate a trending $\Delta u^+(k^+)$ that matches experimental data above $k^+ > 100$. We believe that the observations made on this novel rough wall in pressure gradient case offer a physical explanation for why this relation cannot work and a path forward.

The Wilcox formulation of reducing ω_{wall} while holding k_{wall} constant essentially represents a reduction of $\epsilon_{wall}(k^+)$ (ignoring, for the moment, the fact that $\omega_{wall} \equiv \infty$ if $k_{wall} = 0$). However, observations of the spectral behavior of the fluctuating wall pressure and the behavior of the parameter u_ν appears to indicate quite strongly that near-wall dissipative effects are not impacted by roughness and the canonical roughness effects are driven instead by turbulent production, more analogous to an increase in k at constant ϵ . A lack of physical meaning could be ignored for a model that produces effective

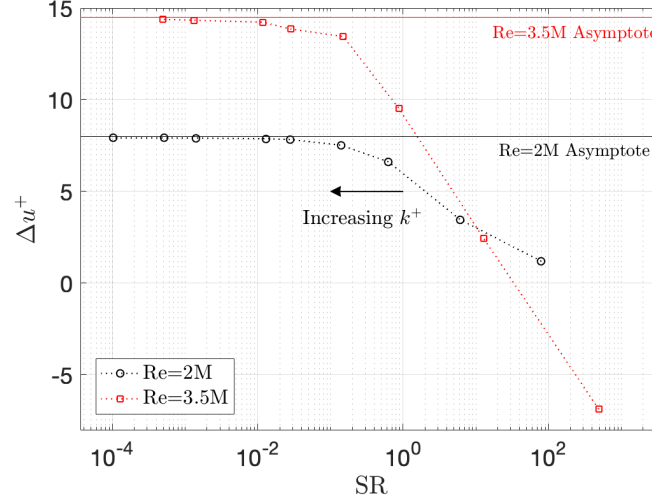


Fig. 17: Roughness function as a direct function of wall BC parameter SR for both measured Reynolds numbers.

and industrially useful results, but Fig. 16 & 17 demonstrate that this is not the case.

Our observations of turbulent behavior over rough walls suggests that the primary effect of roughness is to serve as a source of turbulent kinetic energy and momentum in the near-wall region. We believe a more physically meaningful roughness correction for k - ω models would therefore be based on an increase in k_{wall} and a reduction in ω_{wall} that serves to incorporate the increase in k_{wall} while holding ϵ_{wall} constant, similar to the model proposed by Aupoix (2014) [39].

6 Conclusions

Detailed experimental measurements have been made of the mean pressure and velocity and fluctuating pressure over high k^+ rough wall flows in a systematic family of bi-directional, continually varying pressure gradient distributions. These data are consistent with outer-layer Reynolds number similarity, in keeping with Townsend's Hypothesis [6] independent of applied pressure gradient or pressure gradient history effects. The general effect of pressure gradient on the mean and integrated boundary layer parameters is the same over a rough wall flow as for an equivalent smooth wall flow, but, the history dependent, downstream lagging observed in flows of pressure gradient reversal respond more rapidly over rough walls than smooth, owing, we believe, to the increased dominance of small scale, near wall motions, which are known to respond more rapidly to pressure gradient.

The autospectrum of fluctuating pressure beneath rough wall boundary layers exhibits a simplified dependence on pressure gradient and pressure gradient history compared with an equivalent smooth wall flow, fully collapsing on an outer variable scaling and containing constant, pressure-gradient-independent

mid-frequency slope. Collapsing the high frequency of the spectra under the scaling of Meyers *et al.* (2015) [19] suggests that high frequency spectral behavior is a universal function of the near-wall viscous dissipation, exhibiting pressure gradient, Reynolds number, and k^+ independence. The universality of the near-wall dissipation between smooth and rough walls implies that the increase in local skin friction over a rough surface is due to an increase in turbulent production near the wall, a region that serves only as a sink of turbulent momentum in a smooth wall flow.

The pressure convection velocity over rough walls flows is suppressed from the canonical smooth wall values, and this suppression increases with downstream development over constant roughness height and distribution. This appears to indicate a progressive history dependence of the turbulence behavior on development length, and we hypothesize this is due to the roughness elements breaking up larger turbulent structures and thus reducing or eliminating large-separation correlations.

We attempted to replicate these flows in a steady RANS environment, which revealed many underlying issues with the current state-of-the-art in k - ω roughness modeling for high k^+ flows. The Wilcox style reduced-wall-specific-dissipation model of the roughness effect fails to accurately predict rough wall flows outside of a narrow band of k^+ inputs. With increasing k_s at constant U_∞ , the model asymptotes at moderate Reynolds number to a constant Δu^+ that is independent of increasing k_s . At constant k_s and increasing U_∞ , the roughness function rises above the curve of Nikuradse [4] to non-physical values. The result is a dimensional space that fails to replicate the correct roughness Reynolds number dependence and free-stream Reynolds number independence that is repeatedly observed in the literature.

We have shown evidence that this is not associated with the specific definition of the wall boundary condition, but with the underlying definition itself. The Wilcox (2006) [38] style ω_{wall} correction effectively represents a reduction of near wall dissipation with constant near wall kinetic energy, the opposite of what the experimental results suggest is occurring in this flow region. A physically accurate rough wall boundary condition must account for an increase in near-wall turbulent kinetic energy without reducing the associated dissipation rate.

These results show quite strongly that our understanding of the physics of rough wall flows is still not entirely complete. However, it appears that rough wall flows exhibit certain physical simplifications that are not present in equivalent smooth wall flows, which ought to be exploitable for the advancement of our understanding and modeling capabilities of these flows. Future works should explore the Reynolds number independence of the outer scales and turbulent motions to postulate reduced order models for the k_s dependencies, as well as further the state-of-the-art roughness boundary condition modeling.

Acknowledgments

The authors would like to thank Dr. Peter Chang and the Office of Naval Research for their support under grant numbers N00014-18-1-2455 and N00014-19-1-2109. We are extremely grateful for the contributions of Bill Oetjens, Mason Fitzsimmons, Sasha Mintz, Jarrod Banks, and Humza Butt to wind tunnel testing. We also thank the Virginia Tech Aerospace and Ocean Engineering Machine Shop headed by Mr. James Lambert for their support in designing and manufacturing test hardware and instrumentation. Finally, we thank the Department of Defense High Performance Computing Modernization Program (HPCMP), the Naval Air Warfare Center Aircraft Division (NAWCAD), and the Computational Research and Engineering Acquisition Tools and Environments (CREATE) team for computational resources.

Authors' Contributions

D.J.F. and V.V. performed the experiments, processed the data, and made the figures. D.J.F. performed the computations. C.J.R. supervised and advised the computational work. K.T.L. and W.J.D. supervised the research and oversaw the experiments. All authors contributed to the writing of the paper.

Compliance with Ethical Standards

Conflict of Interest

The authors declare they have no conflicts of interest.

References

- [1] Raupach, M.R.: Conditional statistics of reynolds stress in rough-wall and smooth-wall turbulent boundary layers. *Journal of Fluid Mechanics* **108**, 363–382 (1981). <https://doi.org/10.1017/S0022112081002164>
- [2] Krogstad, P.A., Antonia, R.A., Browne, L.W.: Comparison between rough- and smooth-wall turbulent boundary layers. *Journal of Fluid Mechanics* **245**, 599–617 (1992). <https://doi.org/10.1017/S0022112092000594>
- [3] Jimenez, J.: Turbulent flows over rough walls. *Annual Review of Fluid Mechanics* **36**, 173–196 (2004). <https://doi.org/10.1146/annurev.fluid.36.050802.122103>
- [4] Nikuradse, J.: Laws of flow in rough pipes. NACA Technical Report (TM 1292) (1950)

Turbulence and pressure fluctuations in rough wall boundary layers in pressure gradients

- [5] Dvorak, F.A.: Calculation of turbulent boundary layers on rough surfaces in pressure gradient. *AIAA Journal* **7**(9), 1752–1759 (1969). <https://doi.org/10.2514/3.5386>
- [6] Townsend, A.A.: *The Structure of Turbulent Shear Flow*. Cambridge University Press, Cambridge, UK (1976)
- [7] Flack, K.A., Schultz, M.P., Shapiro, T.A.: Support for townsend’s reynolds number similarity hypothesis on rough walls. *Physics of Fluids* **17**, 035102 (2005). <https://doi.org/10.1063/1.1843135>
- [8] Flack, K.A., Schultz, M.P.: Roughness effects on wall-bounded turbulence. *Physics of Fluids* **26**, 26–43 (2014). <https://doi.org/10.1063/1.4896280>
- [9] Mehdi, F., Klewicki, J.C., White, C.M.: Mean force structure and its scaling in rough-wall turbulent boundary layers. *Journal of Fluid Mechanics* **731**, 682–712 (2013). <https://doi.org/10.1017/jfm.2013.385>
- [10] Schlichting, H.: *Boundary Layer Theory*. McGraw-Hill, USA (1979)
- [11] Betterman, D.: Contribution a l’etude de la convection force turbulente le long de plaques rogneuses. *International Journal of Heat and Mass Transfer* **9**, 153–164 (1966)
- [12] Simpson, R.L.: A generalized correlation of roughness density effects on the turbulent boundary layer. *AIAA Journal* **11**(2), 242–244 (1973). <https://doi.org/10.2514/3.6736>
- [13] Donne, M., Meyer, L.: Turbulent convective heat transfer from rough surfaces with two-dimensional rectangular ribs. *International Journal of Heat and Mass Transfer* **20**, 583–620 (1977). [https://doi.org/10.1016/0017-9310\(77\)90047-3](https://doi.org/10.1016/0017-9310(77)90047-3)
- [14] Sigal, A., Danberg, J.E.: New correlation of roughness density effect on the turbulent boundary layer. *AIAA Journal* **28**(3), 554–556 (2012). <https://doi.org/10.2514/3.10427>
- [15] Bull, M.K.: Wall pressure fluctuations beneath turbulent boundary layers: Some reflections on forty years of research. *Journal of Sound and Vibration* **190**(3), 299–315 (1996). <https://doi.org/10.1006/jsvi.1996.0066>
- [16] Blake, W.K.: Turbulent boundary-layer wall-pressure fluctuations on smooth and rough walls. *Journal of Fluid Mechanics* **44**(4), 637–660 (1970). <https://doi.org/10.1017/S0022112070002069>
- [17] Aupperle, F.A., Lambert, R.F.: Effects of roughness on measured wall-pressure fluctuations beneath a turbulent boundary layer. *Journal of the*

- Acoustical Society of America **47**, 359–370 (1970). <https://doi.org/10.1121/1.1911506>
- [18] Forest, J.B.: The wall pressure spectrum of high reynolds number rough-wall turbulent boundary layers. Master’s thesis, Virginia Polytechnic Institute and State University (2012)
- [19] Meyers, T., Forest, J.B., Devenport, W.J.: The wall-pressure spectrum of high-reynolds-number turbulent boundary-layer flows over rough surfaces. *Journal of Fluid Mechanics* **768**, 261–293 (2015). <https://doi.org/10.1017/jfm.2014.743>
- [20] Joseph, L.A.: Pressure fluctuations in a high-reynolds-number turbulent boundary layer over rough surfaces of different configurations. PhD thesis, Virginia Polytechnic Institute and State University (2017)
- [21] Clauser, F.H.: Turbulent boundary layers in adverse pressure gradient. *Journal of the Aeronautical Sciences* **21**(2), 91–108 (1954). <https://doi.org/10.2514/8.2938>
- [22] Nagano, Y., Tagawa, M., Tsuji, T.: Effects of adverse pressure gradients on mean flows and turbulence statistics in a boundary layer. In: 8th International Symposium on Turbulent Shear Flows. Springer, Munich, Germany (9-11 September, 1991). https://doi.org/10.1007/978-3-642-77674-8_2
- [23] Yuan, J., Piomelli, U.: Numerical simulations of sink-flow boundary layers over rough surfaces. *Physics of Fluids* **26**(1), 015113 (2014). <https://doi.org/10.1063/1.4862672>
- [24] Yuan, J., Piomelli, U.: Numerical simulation of a spatially developing accelerating boundary layer over roughness. *Journal of Fluid Mechanics* **780**, 192–214 (2015). <https://doi.org/10.1017/jfm.2015.437>
- [25] Devenport, W.J., Lowe, K.T.: Equilibrium and non-equilibrium turbulent boundary layers. *Progress in Aerospace Sciences* **131**, 100807 (2022). <https://doi.org/10.1016/j.paerosci.2022.100807>
- [26] Bobke, A., Örtü, R., Vinuesa, R., Schlatter, P.: History effects and near-equilibrium in adverse-pressure-gradient turbulent boundary layers. *Journal of Fluid Mechanics* **820**, 667–692 (2017). <https://doi.org/10.1017/jfm.2017.236>
- [27] Fritsch, D.J., Vishwanathan, V., Lowe, K.T., Devenport, W.J.: Fluctuating pressure beneath smooth wall boundary layers in non-equilibrium pressure gradients. *AIAA Journal* **60**(8), 4725–4743 (2022). <https://doi.org/10.2514/1.J061431>

Turbulence and pressure fluctuations in rough wall boundary layers in pressure gradients

- [28] Schloemer, H.: Effects of pressure gradients on turbulent boundary-layer wall-pressure fluctuations. US Navy Underwater Sound Laboratory Report (747) (1966). <https://doi.org/10.1121/1.1943059>
- [29] Perry, A.E., Joubert, P.N.: Rough-wall boundary layers in adverse pressure gradients. *Journal of Fluid Mechanics* **17**(2), 193–211 (1963). <https://doi.org/10.1017/S0022112063001245>
- [30] Tay, G.F.K.: Influence of adverse pressure gradient on rough-wall turbulent flows. *International Journal of Heat and Fluid Flow* **30**(2), 249–265 (2009). <https://doi.org/10.1016/j.ijheatfluidflow.2009.01.001>
- [31] Brzek, B., Chao, D., Turan, O., Castillo, L.: Characterizing developing adverse pressure gradient flows subject to surface roughness. *Experiments in Fluids* **48**(4), 663–77 (2010). <https://doi.org/10.1007/s00348-009-0759-6>
- [32] Coleman, H.W., Moffat, R.J., Kays, W.M.: The accelerated fully rough turbulent boundary layer. *Journal of Fluid Mechanics* **82**(3), 507–528 (1977). <https://doi.org/10.1017/S0022112077000810>
- [33] Cal, R.B., Brzek, B., Johansson, T.G., Castillo, L.: The rough favourable pressure gradient turbulent boundary layer. *Journal of Fluid Mechanics* **641**, 129–155 (2009). <https://doi.org/10.1017/S0022112009991352>
- [34] Min, D.H., Christensen, K.T.: Combined roughness and favorable-pressure-gradient effects in a turbulent boundary layer. In: 40th AIAA Fluid Dynamics Conference. American Institute of Aeronautics and Astronautics, Chicago, IL, USA (28 June - 1 July 2010)
- [35] Burton, T.E.: Wall pressure fluctuations at smooth and rough surfaces under turbulent boundary layers with favorable and adverse pressure gradients. ONR Report (AD-772 548) (1973)
- [36] Song, S., Demirel, Y.K., Atlar, M., Dai, S., Turan, O.: Validation of the cfd approach for modelling roughness effect on ship resistance. *Ocean Engineering* **200** (2020). <https://doi.org/10.1016/j.oceaneng.2020.107029>
- [37] Wilcox, D.C.: Reassessment of the scale-determining equation for advanced turbulence models. *AIAA Journal* **46**, 2823–2838 (1988). <https://doi.org/10.2514/3.10041>
- [38] Wilcox, D.C.: *Turbulence Modeling for CFD*, 3rd edn. DCW Industries, La Cañada, CA, USA (2006)
- [39] Aupoix, B.: Wall roughness modeling with k-w sst model. In: 10th International Symposium on Engineering Turbulence Modelling and

Measurements, Marbella, Spain (Sep 2014)

- [40] Hellsten, A., Laine, S.: Extension of the k-w shear-stress transport turbulence model for rough-wall flows. *AIAA Journal* **36**, 1728–1729 (1998). <https://doi.org/10.2514/2.7543>
- [41] Aupoix, B., Spalart, P.R.: Extensions of the spalart-allmaras turbulence model to account for wall roughness. *International Journal of Heat and Fluid Flows* **24** (2003). [https://doi.org/10.1016/S0142-727X\(03\)00043-2](https://doi.org/10.1016/S0142-727X(03)00043-2)
- [42] Knopp, T., Eisfeld, B., Calvo, J.B.: A new extension for k-w turbulence models to account for wall roughness. *International Journal of Heat and Fluid Flow* **30**, 54–65 (2009). <https://doi.org/10.1016/j.ijheatfluidflow.2008.09.009>
- [43] Fritsch, D.J., Vishwanathan, V., Duetsch-Patel, J.E., Gargiulo, A., Lowe, K.T., Devenport, W.J.: The pressure signature of smooth wall turbulent boundary layers in pressure gradient family. In: *AIAA Aviation Forum*, Reno, NV, USA (15-19 June 2020). <https://doi.org/10.2514/6.2020-3066>
- [44] Vishwanathan, V., Fritsch, D.J., Lowe, K.T., Devenport, W.J.: Analysis of coherent structures over a smooth wall turbulent boundary layer in pressure gradient using spectral proper orthogonal decomposition. In: *AIAA Aviation Forum, Virtual Event* (2-6 August, 2021). <https://doi.org/10.2514/6.2021-2893>
- [45] Fritsch, D.J., Vishwanathan, V., Roy, C.J., Lowe, K.T., Devenport, W.J., Nishi, Y., Knopp, T., Ströer, P., Krumbein, A., Sandberg, R.D., Lav, C., Bensow, R.E., Eça, L., Toxopeus, S.L., Kerkvliet, M., Slama, M., Bordier, L.: Experimental and computational study of 2d smooth wall turbulent boundary layers in pressure gradient. In: *AIAA Science and Technology Forum*, San Diego, CA, USA (3-7 January 2022). <https://doi.org/10.2514/6.2022-0696>
- [46] Devenport, W.J., Burdisso, R., Borgoltz, A., Ravetta, P., Barone, M., Brown, K., Morton, M.: The kevlar-walled anechoic wind tunnel. *Journal of Sound and Vibration* **332**(17), 3971–3991 (2013). <https://doi.org/10.1016/j.jsv.2013.02.043>
- [47] Duetsch-Patel, J.E., Viswanathan, V., Minionis, J., Totten, E., Gargiulo, A., Fritsch, D.J., Szoke, M., Bortoltz, A., Roy, C.J., Lowe, K.T., Devenport, W.J.: Aerodynamic design and validation of modular test section walls for hybrid anechoic wind tunnels. In: *AIAA Science and Technology Forum*, Orlando, FL, USA (6-10 January, 2020). <https://doi.org/10.2514/6.2020-2214>
- [48] Dixit, A.D., Ramesh, O.N.: Determination of skin friction in strong

- pressure-gradient equilibrium and near-equilibrium turbulent boundary layers. *Experiments in Fluids* **47** (2009). <https://doi.org/10.1007/s00348-009-0698-2>
- [49] Vishwanathan, V., Fritsch, D.J., Lowe, K.T., Devenport, W.J.: History effects and wall similarity of non-equilibrium turbulent boundary layers in varying pressure gradient over rough and smooth surfaces. In: 12th International Symposium on Turbulence and Shear Flow Phenomena (TSFP12), Osaka, Japan (19-22 July, 2022)
 - [50] Gravante, S., Naguib, A., Waker, C., Nagib, H.: Characterization of the pressure fluctuations under a fully developed turbulent boundary layer. *AIAA Journal* **36**(10), 1808–1816 (1998). <https://doi.org/10.2514/2.296>
 - [51] Balantrapu, N.A., Repasky, R.J., Joseph, L.A., Devenport, W.J.: The dynamic response of a pinhole microphone under flows of varying shear stress. In: AIAA Aviation Forum, Atlanta, GA, USA (25-19 June, 2018). <https://doi.org/10.2514/6.2018-3933>
 - [52] Fritsch, D.J., Vishwanathan, V., Lowe, K.T., Devenport, W.J.: The effect of grazing flow on pinhole condenser microphones. In: AIAA Science and Technology Forum, Nashville, TN, USA (11-21 January 2021). <https://doi.org/10.2514/6.2021-0130>
 - [53] Wei, T., Fife, P., Klewicki, J., McMurtry, P.: Properties of the mean momentum balance in turbulent boundary layer, pipe, and channel flows. *Journal of Fluid Mechanics* **522**, 303–327 (2005). <https://doi.org/10.1017/S0022112004001958>
 - [54] Menter, F.R.: Two-equation eddy-viscosity turbulence models for engineering applications. *AIAA Journal* **32**, 1598–1605 (1994). <https://doi.org/10.2514/3.12149>

Chapter 6

Modeling the Surface Pressure Spectrum Beneath Turbulent Boundary Layers in Pressure Gradients

This chapter presents a manuscript currently under review in *AIAA Journal* that gives a comprehensive overview of the current state-of-the-art in pressure spectrum modeling and proposes two new models: a machine-learned empirical model and an update to the protocol of Grasso *et al.* (2019) that purposefully incorporates RANS data. This work is collaborative through NATO AVT-349.

Attributions

Daniel J. Fritsch is the primary contributor, first author, and organizer of the collaboration. All figures and text are his original work, except under Section VII.

Vidya Vishwanthan, K. Todd Lowe, and William J. Devenport supported and advised the gathering of experimental data.

Christopher J. Roy advised the generation of computational data.

The Authors from DSTG assisted in the development of the new analytical modeling protocols and performed the Reynolds Stress Transport Modeling.

The Authors from the University of Melbourne performed the machine learning work.

Modeling the Surface Pressure Spectrum Beneath Turbulent Boundary Layers in Pressure Gradients*

Daniel J. Fritsch[†], Vidya Vishwanathan[†], Christopher J. Roy[‡], K. Todd Lowe[‡], and William J. Devenport[§]
Virginia Tech, Blacksburg, VA, USA

Paul Croaker[¶], Graeme Lane[¶], Oksana Tkachenko^{**}, and David Pook[¶]
Defence Science and Technology Group (DSTG), Melbourne, Victoria, Australia

Shubham Shubham^{††} and Richard D. Sandberg^{‡‡}
University of Melbourne, Melbourne, Victoria, Australia

A wide variety of models and methods for the prediction of the surface pressure spectrum beneath turbulent boundary layers are presented and assessed. A thorough review is made of the current state-of-the-art in empirical and analytical pressure spectrum models, and predictions of zero, adverse, favorable, and non-equilibrium pressure gradient boundary layers are examined using steady RANS prediction of a subset of a pressure gradient boundary layer benchmark flow case. The existing empirical models show either an inability to adapt to pressure gradient conditions or an over-sensitivity to model inputs, producing non-physical results under certain flow conditions. New empirical models are created using a Gene Expression Programming machine learning algorithm, based on either both experimental and RANS inputs. The various input options for analytical TNO modeling are presented and assessed, and recommendations for best practices are made. The developed models show improvement in both accuracy and robustness over existing models.

I. Nomenclature

c_f = Skin friction coefficient

c_p = Pressure coefficient

G = Defect shape factor, $= (1 - 1/H)/(u_\tau/U_e)$

G_{pp} = One-sided autospectral density of wall pressure ((f) Pa^2/Hz , (ω) Pa^2s/rad)

*This paper was originally presented at the 2022 AIAA/CEAS Aeroacoustics Conference - AIAA 2022-2843

[†]Graduate Research Assistant, Crofton Dept. Aerospace & Ocean Engineering, AIAA Student Member, Correspondence: dannyf96@vt.edu

[‡]Professor, Crofton Dept. Aerospace & Ocean Engineering, AIAA Associate Fellow

[§]Crofton Professor of Engineering, Crofton Dept. Aerospace & Ocean Engineering, AIAA Associate Fellow, Correspondence: devenport@vt.edu

[¶]Defence Scientist, Hydroacoustics Group, Maritime Division

^{||}Senior Research Associate, Mechanical and Automotive Engineering, RMIT University

^{**}Research Assistant, School of Mechanical and Manufacturing Engineering, U. New South Wales

^{††}Graduate Research Assistant, Dept. Mechanical Engineering

^{‡‡}Professor, Dept. Mechanical Engineering, AIAA Senior Member, Correspondence: richard.sandberg@unimelb.edu.au

H	=	Shape factor, $= \delta^* / \theta$
K	=	Wavenumber magnitude
K_i	=	i^{th} wavenumber component
K_c	=	Defect acoustic wavenumber, Eq. 2
K_e	=	Characteristic wavenumber of the integral length scale, Eq. 24
k	=	Turbulent kinetic energy
M	=	Mach number
p	=	Pressure
q	=	Dynamic pressure
Re	=	Reynolds number (subscript ℓ denotes length scale)
R_T	=	Spectral time scale ratio, $= (u_\tau \delta / \nu) \sqrt{c_f / 2}$
U_c	=	Convection velocity
U_e	=	Boundary layer edge velocity
u_τ	=	Shear velocity
x	=	Streamwise coordinate
y	=	Wall-normal coordinate
β_ℓ	=	Clauser parameter with length scale ℓ (no subscript indicates original Clauser parameter based on δ^*), $= (\ell / \tau_w)(dp/dx)$
Δ_{RC}	=	Rotta-Clauser length scale, $= \delta^* \sqrt{2/c_f}$
Δ_{ZS}	=	Zagarola & Smits parameter, $= \delta / \delta^*$
δ	=	99% edge velocity boundary layer thickness
δ^*	=	Displacement thickness
θ	=	Momentum thickness
Λ	=	Integral length scale
ν	=	Kinematic viscosity
ξ_ℓ	=	Catlett pressure gradient parameter with length scale ℓ , $= (\ell / q)(dp/dx)$
Π	=	Cole's wake strength parameter
ρ	=	Density
τ_w	=	Wall shear stress
ν	=	Wilson spectrum tuning parameter
ϕ	=	Wavenumber-frequency spectral density
ω	=	Frequency, specific turbulence dissipation rate
$\bar{\omega}$	=	Dimensionless Frequency ($\omega \delta^* / U_e$)

II. Introduction

ACCURATE prediction of aero/hydrodynamic noise resulting from turbulent boundary layer flows is a challenge, primarily due to the difficulty associated with predicting the spectrum of the fluctuating pressure at the wall, on which the observed far-field noise directly depends for cases of trailing edge and boundary layer self-noise [1, 2]. The surface pressure spectrum is known to be a function of the entire boundary layer beneath which it is immersed [3], meaning that an accurate and rigorous prediction of the spectrum would require accurate prediction of the boundary layer characteristics, something that is difficult to achieve in and of itself.

This becomes even more challenging for complex, non-canonical boundary layer flows; flows with curvature, pressure gradient, and roughness. Flows with streamwise pressure gradient are known to impact the surface pressure spectrum in ways that are not straightforward; the pressure gradient having differing effects on different regions of the spectrum that are a combined function of the pressure gradient sign, magnitude, and upstream history, and the exact nature of these relationships is still being explored [4–7]. Furthermore, even if the effects of pressure gradient boundary layers on the surface spectrum were perfectly understood, the behavior of that boundary layer would still need to be known, meaning there must be some accurate method of predicting the flow itself.

From a design and analysis perspective, this means Computational Fluid Dynamics (CFD). The majority of CFD solutions used in government and industry solve the Reynolds Averaged Navier-Stokes (RANS) equations, which contain no time-resolved behavior on the scale of the turbulence. The effect of turbulence is instead modeled, with varying degrees of fidelity and accuracy depending on which model is used.

The efficacy of practical prediction methods for turbulent boundary layer noise thus depends on two things: our understanding of how the boundary layer behavior drives the fluctuating surface pressure, and our ability to predict that boundary layer behavior with RANS. A variety of empirical models [8–18] exist in the literature that relate the spectrum of fluctuating wall pressure to simple, mean coefficients and parameters. These models are easy to employ with RANS data, but are not necessarily valid for a wide variety of flow cases [5, 19]. Analytical modeling protocols also exist [20–25], but these models are more complex to employ, require a greater fidelity of input data, and leave too many unknowns when working from RANS data.

An alternative to increasing modeling fidelity is the employment of machine learning strategies [26]. One such method is Gene Expression Programming (GEP), which has been shown to enable the development of improved turbulence [27] and pressure spectrum models [28]. Crucially, the models are driven by robust, real-world data, and can thus incorporate a wide variety of flow conditions and spectral characteristics.

This paper presents a comprehensive review and assessment of the current state-of-the-art in wall pressure spectrum modeling and proposes two new modeling ideas that improve upon that state-of-the-art. RANS data have been generated to provide a database of non-equilibrium pressure gradient boundary layer flows, as part of the NATO Applied Vehicle Technology (AVT) 349 Research Task Group (RTG) on Non-Equilibrium Boundary Layers at Incompressible Conditions,

and these data have been employed with a wide variety of spectral models in an attempt to predict the pressure fluctuations at zero, adverse, favorable, and mixed pressure gradient conditions. A Gene Expression Programming (GEP) machine learning formulation was employed to develop new empirical models for pressure fluctuations beneath pressure gradient boundary layers that show marked improvement in robustness and accuracy over the existing empirical models in the literature. The sensitivities of modeling requirements of an analytical TNO formulation based on the updates of Grasso *et al.* [25] have been assessed and quantified, and recommendations have been made for sub-modeling choices for successful prediction of model inputs from RANS and Reynolds-Stress-Transport-Modeling (RSTM) data, including a proposed length scale model and empirical formulation for wavenumber anisotropy. Section III describes the methods used in this study, the results of which are provided in Sections IV and V, and finally conclusions will be drawn in Section VI.

III. Flow Case

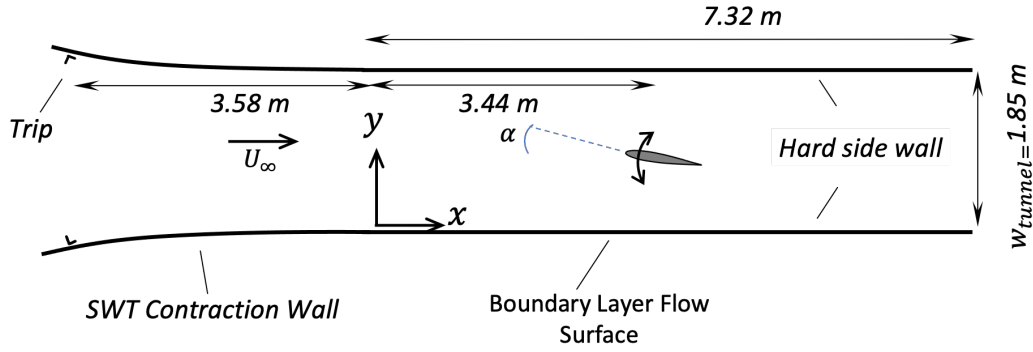
A. Experiment

The flow case considered here is a high Reynolds number ($Re_\theta > 10,000$), low Mach number ($M < 0.1$) wind tunnel experiment performed in the Virginia Tech Stability Wind Tunnel (VTSWT), in which a flat plate boundary layer is observed on the test-section side wall while a NACA0012 airfoil is present in the test-section center as shown in Fig. 1a. The presence of the airfoil model displaces a continually varying, bi-directional (both adverse and favorable) pressure gradient onto the boundary layer wall, distributions of which are shown in Fig. 1b. This flow case has been previously reported as a fundamental boundary layer in pressure gradient test case [5–7, 29] and as a CFD validation case [30]. The data from this case have also been made available as a public-domain data repository [31].

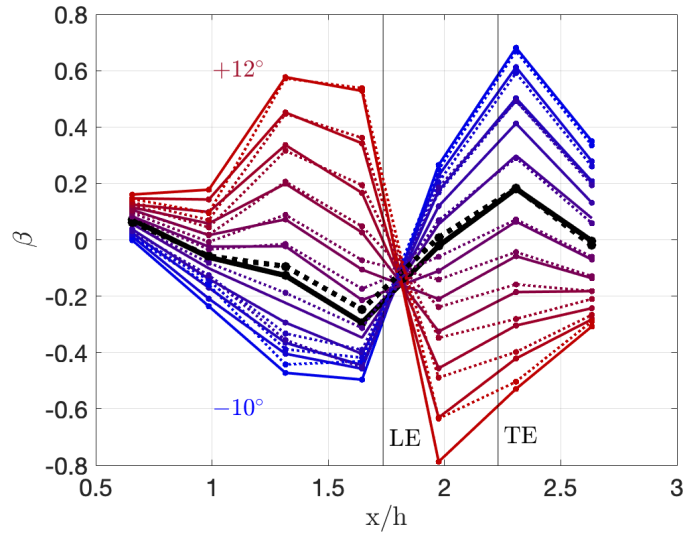
This flow case was chosen as the basis for this work for a few reasons. First, the bi-directional nature of the pressure gradient distributions closely replicates the pressure distribution over many practical surfaces, while the flat boundary layer wall enables experimental measurement of boundary layer parameters with greater ease than a typical application model study. The boundary layer in this case has been more thoroughly documented than the majority of test cases, making it a better candidate for the assessment and development of models that rely on the boundary layer characteristics for inputs. Secondly, the data for this case are readily available through the NATO AVT-349 collaboration and a public-domain repository [31], enabling collaborative modeling efforts.

The conditions used herein are a Reynolds number based on the chord length of the airfoil model ($0.914m$) and the free-stream tunnel velocity ($\approx 33m/s$) of 2×10^6 . This results in an inflow displacement thickness of $\delta^* \approx 6mm$ and $Re_\theta \approx 12,000$.

Experimental data are available for the mean static pressure distribution, Pitot-static wall-normal velocity distributions at seven streamwise locations, fluctuating surface pressure at seven streamwise locations from an array of six sensors



(a)



(b)

Fig. 1 Flow case system showing coordinate system origin, primary dimensions, and model and trip locations (a), and corresponding distributions of Clauser pressure gradient parameter (b). Taken with permission from Fritsch *et al.* (2022) [7]. Black curves are taken with the model at 0° , blue at negative angles, and red at positive. Solid curves are taken at a chord-based Reynolds number $Re_c = 2 \times 10^6$, dotted at $Re_c = 3.5 \times 10^6$.

arranged both span- and streamwise, and time-resolved Particle Image Velocimetry (PIV) at four streamwise locations. Additionally, the wind tunnel geometry is known exactly from spatially resolved laser scans.

B. Numerical Simulations

The flow case is simulated numerically on a systematically refined 2D grid family using the CREATE-AV Kestrel compressible, finite-volume, steady RANS solver [32]. The bulk of the results to be presented were obtained using the Menter $k-\omega$ Shear Stress Transport (SST) model [33]. The grids used are two-dimensional, quasi-constant-area

cross-section, fully-structured meshes with a sharp-trailing-edge representation of the NACA0012 geometry. A symmetric, constant cross-section 2D representation of the wind tunnel does not accurately replicate the pressure gradient distributions on the wall of interest due to the lack of the floor and ceiling boundary layers, the juncture flows around the airfoil model, and the blockage they represent. To account for this, the top wall is set as a slip wall boundary condition and angled at 0.46° to simulated the favorable pressure gradient (FPG) that arises due to the boundary layer growth on the walls, floor, and ceiling of the real tunnel, as seen in Fig. 2. The specified angle was determined by converging simulations without the airfoil model and with the airfoil model at select angles of attack with varying angles for the top wall and comparing the resulting dimensional, dp/dx , and non-dimensional, β , pressure gradient distributions.

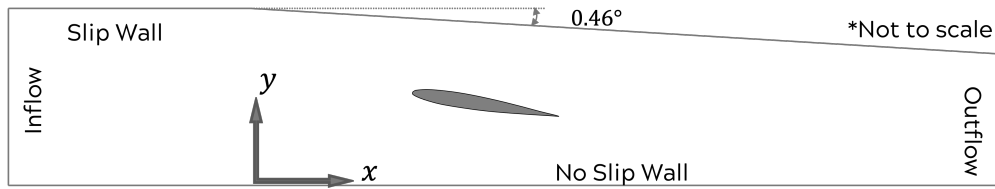


Fig. 2 Representative diagram of CFD grid domain. Taken with permission from Fritsch *et al.* (2022) [30].

In addition to the eddy-viscosity SST model, results were also obtained using the RSM-BSL Reynolds Stress Transport Model (RSTM) in ANSYS/Fluent [34]. RSTM offers a distinct advantage for flow simulation for the purposes of pressure spectrum modeling as it produces direct estimates for all Reynolds stress components rather than employing the linear Boussinesq eddy-viscosity hypothesis.

These simulations have previously been evaluated for their numerical consistency and ability to replicate the experimentally observed flow behavior [30].

IV. Empirical Modeling

A. Review of Existing Models

A variety of empirical models for the turbulent wall pressure spectrum have been proposed, starting with the 1980 wavenumber-frequency spectrum model of Chase [8], which was updated in 1987 [9]. The Chase models have the advantage of capturing the full wavenumber-frequency domain of the fluctuating pressure field, offering more physical insight, but fail to capture the high frequency viscous roll-off of the frequency spectrum. The Chase model also has the advantage of being semi-analytical; the form of the model having been derived from conservation of momentum with only the tuning parameters set via empirical methods. The spectrum of fluctuating pressure at a surface is given in terms of the streamwise and spanwise wavenumbers and the angular frequency according to:

$$\phi_{pp}(K_1, K_3, \omega) = \frac{\rho^2 u_\tau^3}{K_+^2 + (b\delta)^{-2}} [C_M (\frac{K}{|K_c|})^2 K_1^2 + [c_2 (\frac{|K_c|}{K})^2 + 1 - c_2 - c_3] C_T K^2 [\frac{K_+^2 + (b\delta)^{-2}}{K^2 + (b\delta)^{-2}}]] \quad (1)$$

where b , c_2 , c_3 , C_M , and C_T are the empirically tuned parameters, K_c is the defect acoustic wavenumber:

$$K_c = \sqrt{|\frac{\omega^2}{c^2} - K^2|} \quad (2)$$

where c is the speed of sound, and

$$K_+^2 = \frac{(\omega - U_c K_1)^2}{u_\tau^2 h^2} + K^2 \quad (3)$$

where h is another empirically tuned parameter.

Howe [10] further simplified the Chase wavenumber-frequency spectral model, making assumptions about the convective relationship between the wavenumber and frequency domains, thus analytically integrating to a generic form for the autospectral density:

$$\frac{G_{pp}(\omega) U_e}{\tau_w^2 \delta^*} = \frac{2(\omega \delta^* / U_e)^2}{[(\omega \delta^* / U_e)^2 + 0.0144]^{3/2}} \quad (4)$$

This model can be calculated readily using minimal information about the boundary layer as input, but it does not capture any of the high frequency portion of the pressure spectrum.

Perhaps the most well-known empirical frequency spectrum model is that of Goody [11], which empirically fits the canonical shape of the frequency spectrum as a function of the ratio of time scales, R_T . The Goody model is essentially an expansion of Howe's model, adding a new term in the denominator which captures the high frequency roll-off. The Goody model is known to give good agreement with experimentally measured spectra for flat plate zero pressure gradient (ZPG) boundary layers, but fails to adapt to non-canonical conditions.

Several Goody-style models have been proposed that attempt to adapt the structure of Goody's model to non-canonical flows. Rozenberg *et al.* [12], Kamruzzaman *et al.* [13], Catlett *et al.* [14], Lee [17], and Hu [18] proposed models in the Goody framework to capture the effects of adverse pressure gradient (APG), and Joseph [35] proposed a Goody-style model for rough surfaces. The Goody model structure is formulated as such:

$$G_{pp} SS = \frac{a(\omega FS)^b}{[i(\omega FS)^c + d]^e + [(f R_T^g)(\omega FS)]^h} \quad (5)$$

where SS and FS are non-dimensional spectral and frequency scalings respectively and a - h are the model coefficients.

The values of these scalings and coefficients for the aforementioned models are given in Tables 1-4.

A brief overview of these models as applied to the flow case considered herein is found in [5].

Model	a	b	c
Howe [10]	2.0	2.0	2.0
Goody [11]	3.0	2.0	0.75
Rozenberg <i>et al.</i> [12]	$[2.82\Delta_{ZS}^2(6.13\Delta_{ZS}^{-0.75} + d)^e][4.2(\frac{\Pi}{\Delta_{ZS}}) + 1]$	2.0	0.75
Kamruzzaman <i>et al.</i> [13]	$0.45[1.75(\Pi^2\beta^2)^m + 15]$, $m = 0.5(\frac{H}{1.31})^{0.3}$	2.0	1.637
Catlett <i>et al.</i> [14]	$3.0 + \exp[7.98(\xi_{\Delta RC} Re_{\Delta RC})^{0.131} - 10.7]$	2.0	$0.912 + 20.9(\xi_{\delta} Re_{\delta}^{0.05})^{2.76}$
Lee [17]	$\max[a_{Rozenberg}, (0.25\beta_{\theta} - 0.52)a_{Rozenberg}]$	2.0	0.75
Hu [18]	$(81.004d + 2.154) \times 10^{-7}$	1.0	$1.5h^{1.6}$

Table 1 *a-c* parameters for empirical Goody-style empirical models corresponding to Eq. 5.

Model	d	e	f
Howe [10]	0.0144	1.5	0.0
Goody [11]	0.5	3.7	1.1
Rozenberg <i>et al.</i> [12]	$4.76(\frac{1.4}{\Delta_{ZS}})^{0.75}[0.375e - 1]$	$3.7 + 1.5\beta_{\theta}$	8.8
Kamruzzaman <i>et al.</i> [13]	0.27	2.47	$1.15^{-2/7}$
Catlett <i>et al.</i> [14]	$0.397 + 0.328(\xi_{\Delta RC} Re_{\Delta RC}^{0.35})^{0.310}$	$3.872 - 19.3(\xi_{\delta} Re_{\delta}^{0.05})^{0.628}$	$2.19 - 2.57(\xi_{\delta} Re_{\delta}^{0.05})^{0.224}$
Lee [17]	$\max[1.0, d_{Rozenberg}]$	$3.7 + 1.5\beta_{\theta}$	8.8
Hu [18]	$10^{-5.8 \times 10^{-5} Re_{\theta} H - 0.35}$	$1.3/h^{0.6}$	$7.645(\sqrt{2/c_f})^g$

Table 2 *d-f* parameters for empirical Goody-style empirical models corresponding to Eq. 5.

Model	g	h	i
Howe [10]	0.0	0.0	1.0
Goody [11]	-0.57	7.0	1.0
Rozenberg <i>et al.</i> [12]	-0.57	$\min[3.0, (\frac{19}{\sqrt{R_T}})] + 7.0$	4.76
Kamruzzaman <i>et al.</i> [13]	-2/7	7.0	1.0
Catlett <i>et al.</i> [14]	$-0.5424 + 38.1(\xi_{\delta} H^{-0.5})^{2.11}$	$7.31 + 0.797(\xi_{\Delta RC} Re_{\Delta RC}^{0.35})^{0.0724}$	1.0
Lee [17]	-0.57	$\min[3.0, (0.139 + 3.104\beta_{\theta})] + 7.0$	4.76
Hu [18]	-0.411	$1.169 \ln(H) + 0.642$	1.0

Table 3 *g-i* parameters for empirical Goody-style empirical models corresponding to Eq. 5.

Model	SS	FS
Howe [10]	$U_e/\tau_w^2\delta^*$	δ^*/U_e
Goody [11]	$U_e/\tau_w^2\delta$	δ/U_e
Rozenberg <i>et al.</i> [12]	$U_e/\tau_w^2\delta^*$	δ^*/U_e
Kamruzzaman <i>et al.</i> [13]	$U_e/\tau_w^2\delta^*$	δ^*/U_e
Catlett <i>et al.</i> [14]	$U_e/\tau_w^2\delta$	δ/U_e
Lee [17]	$U_e/\tau_w^2\delta^*$	δ^*/U_e
Hu [18]	$u_{\tau}/(q^2\theta)$	θ/U_e

Table 4 Scalings for empirical Goody-style empirical models corresponding to Eq. 5.

B. Assessment of Existing Models at Pressure Gradient Conditions

The database of flows described in Section III.A contains over 150 unique pressure gradient cases, in the dimensional space $11,000 < Re_\theta < 20,000$ and $-0.8 < \beta < 0.8$. For the sake of brevity, we will isolate four key cases for which the various spectral models will be assessed: approximately ZPG ($\alpha = 12^\circ, x = 1.25m$), APG ($\alpha = 12^\circ, x = 2.47m$), FPG ($\alpha = -10^\circ, x = 2.47m$), and an out-of-equilibrium APG-FPG cross ($\alpha = 12^\circ, x = 3.69m$). For each of these four cases, RANS data were generated at a free-stream model chord Reynolds number of 2×10^6 using CREATE-AV Kestrel with the Menter $k-\omega$ SST model [33]. Details on the sensitivity of the computed data to the choice of solver and turbulence model are described by Fritsch *et al.* (2022) [30]. The model input parameters for all of the aforementioned empirical models were computed from these data and are shown in Table 5.

	ZPG	APG	FPG	APG-FPG
c_f	2.50×10^{-3}	2.20×10^{-3}	2.62×10^{-3}	2.25×10^{-3}
H	1.32	1.34	1.28	1.33
q (Pa)	572	522	659	481
Re_δ	9.67×10^4	1.28×10^5	1.21×10^5	1.56×10^5
$Re_{\Delta RC}$	4.20×10^5	6.31×10^5	4.43×10^5	7.70×10^5
Re_θ	11,200	15,600	12,600	19,400
R_T	120	140	159	175
U_c (m/s)	25.2	24.0	27.0	23.1
U_e (m/s)	31.4	30.0	33.8	28.8
u_τ (m/s)	1.11	0.996	1.23	0.966
β	0.0604	0.763	-0.538	-0.964
β_δ	0.395	4.66	-4.06	-5.84
β_θ	0.0457	0.569	-0.422	-0.725
δ (m)	0.0470	0.0650	0.0550	0.0830
δ^* (m)	7.20×10^{-3}	0.0106	7.28×10^{-3}	0.0137
Δ_{RC} (m)	0.204	0.321	0.201	0.410
Δ_{ZS}	6.53	6.11	7.55	6.06
θ (m)	5.45×10^{-3}	7.94×10^{-3}	5.71×10^{-3}	0.0103
ξ_δ	9.81×10^{-4}	0.0102	-0.0107	-0.0131
$\xi_{\Delta RC}$	4.30×10^{-3}	0.0505	-0.0390	-0.646
Π	0.508	0.841	0.118	-0.185
ρ (kg/m ³)	1.16	1.16	1.16	1.16
τ_w (Pa)	1.42	1.15	1.73	1.08

Table 5 Empirical model input parameters as computed from RANS data.

Figure 3 shows the corresponding computed spectra alongside the experimentally measured spectra for each case. In the ZPG case (Fig. 3a), the overall spread of the various models is quite large, $\approx 8dB$ at $\omega\delta^*/U_e = 1$ ($< 5dB$ if the models of Chase and Howe are excluded), and a variety of mid-frequency slopes and high frequency roll-off locations are observed. Unsurprisingly, the standard Goody model (red triangles) [11] shows the best agreement with experiment at

ZPG conditions, and consistently matches well with experimental data in the non-ZPG cases as well. The Goody model does not adapt well to the spectral changes in non-ZPG conditions, maintaining a fixed peak location and amplitude and mid-frequency slope, but the mildness of the pressure gradient effect means the standard Goody model is never far off.

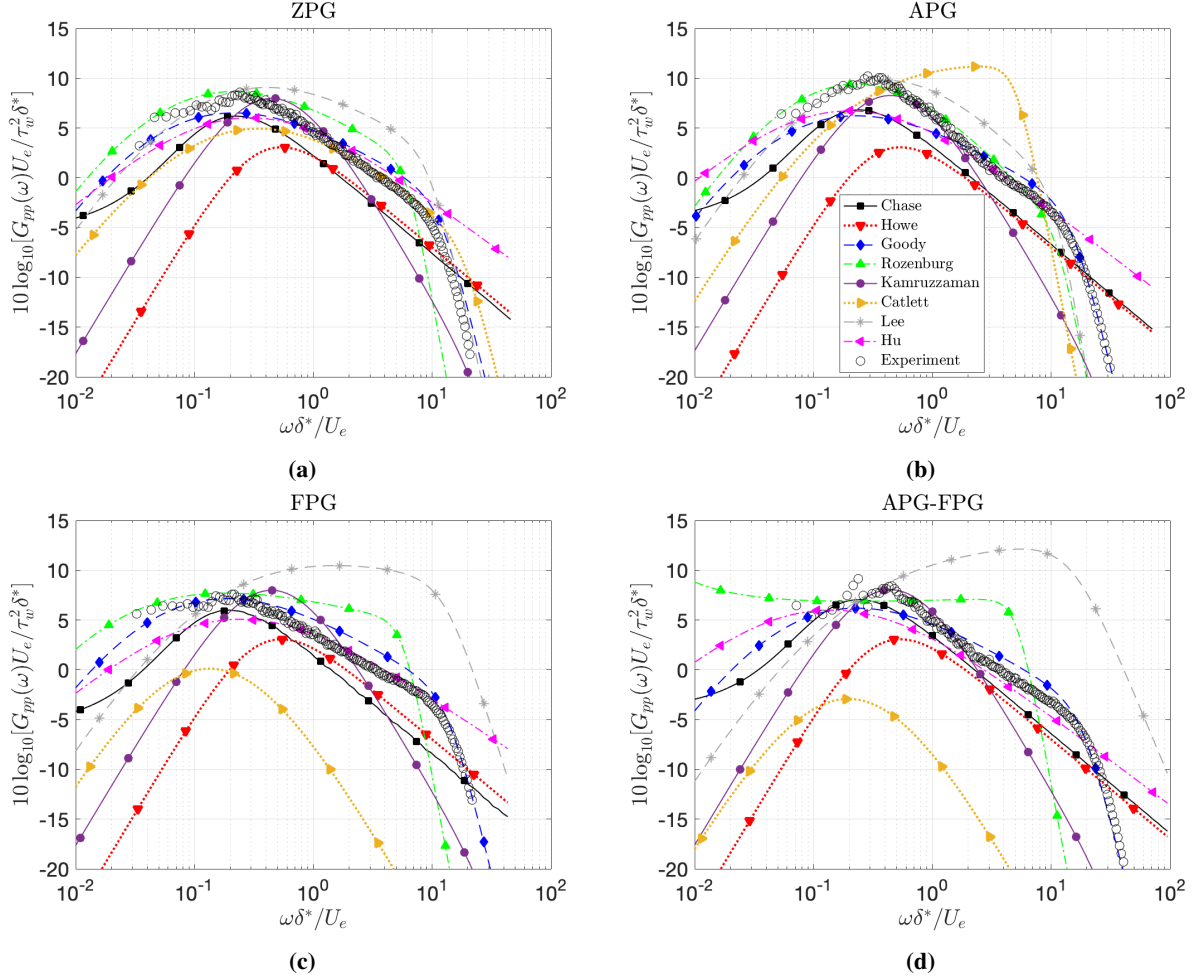


Fig. 3 Measured and empirically modeled surface pressure spectra at ZPG (a), APG (b), FPG (c), and APG-FPG (d) conditions.

The Chase [9] model predicts the peak spectral amplitude and frequency fairly well, but exhibits several problems, the lack of a high frequency roll-off being the most obvious. The roll-off slope of the Chase model is fixed at ω^{-1} , meaning it does not adapt well to the changes observed in the measured spectra under non-ZPG conditions. The Howe [10] model shows similar issues and, additionally, under-predicts the behavior in the low frequency region.

The APG-tuned models show a much wider range of behaviors across varying flow conditions. In ZPG (Fig. 3a), all of these models show reasonably consistent behavior, with the Rozenberg *et al.* [12] and Hu [18] models matching the Goody and measured spectra most closely. In APG (Fig. 3b), the Rozenberg *et al.* model most accurately accounts for the change in measured spectra, with the Lee [17] model a close second-best. The Hu model performs well in the higher

frequencies, but under-predicts the spectral amplitude at low frequencies.

None of the APG-tuned models perform well in FPG conditions (Fig. 3c), with the Catlett *et al.* [14] and Lee [17] models showing particularly non-physical behavior. The Kamruzzaman *et al.* ([13] and Hu [18] models best retain their physicality at FPG conditions, but their agreement is reduced from the ZPG and APG cases.

The out-of-equilibrium case (Fig. 3d) shows similar results; with the exception of the Kamruzzaman *et al.* [13] and Hu [18] models, neither of which shows good agreement, none of the APG-tuned models predict a physically meaningful spectrum under these conditions. The non-physicality of the Catlett *et al.* [14] and Lee [17] models is exacerbated compared to the straight FPG case.

Table 6 shows the root-mean-square of the decibel error of each model at each condition. The original Goody [11] model shows the smallest errors for all cases, even under the influence of pressure gradient and pressure gradient history. This is not due, however, to the fundamental accuracy of the Goody model under these conditions, but rather the fact that the Goody model retains its shape due to the stiffness of the model, being dependent only on the time scale ratio when expressed in normalized coordinates. The APG-tuned Goody-style models appear to be over-defined, particularly in the FPG and out-of-equilibrium cases that lie far outside their respective tuning envelopes.

	ZPG	APG	FPG	APG-FPG
Chase	2.88	3.08	3.21	2.32
Howe	5.13	5.12	4.82	3.90
Goody	1.49	1.80	1.34	1.28
Rozenberg	5.43	4.51	6.61	13.0
Kamruzzaman	4.16	5.32	5.08	6.50
Catlett	9.93	8.53	17.7	21.8
Lee	3.74	4.73	8.46	11.5
Hu	3.09	2.99	1.92	2.45

Table 6 Root-mean-square decibel error of empirical model spectra ($\text{R.M.S.}[\mathbf{10 \log_{10}(G_{pptrue}) - 10 \log_{10}(G_{ppmodel})}]$).

In the APG case, the Rozenberg *et al.* [12], Lee [17], and Hu [18] models manage to better capture the shape of the spectrum, but show larger errors than the standard Goody model. The improvement in spectral shape is unsurprising, since these models were developed specifically to out-perform the Goody model in APG. The enlarged error appears to come mainly from the high frequency roll-off, where the standard Goody model matches better, despite the APG tuned models matching better in the low frequencies, illustrating two points: the heavy contribution of the high frequency content to the R.M.S. pre-multiplied pressure levels and the accuracy of Goody’s original R_T formulation of this high frequency behavior. In FPG and AGP-FPG cross, the standard Goody model shows the lowest error of all the tested models, and several of the APG tuned models show extremely large errors where they break down. The Hu model manages to remain fairly robust in these conditions, though not as much so as the standard Goody.

In order to better understand the behavior of the Goody-style model of Eq. 5, the coefficients were fit to the measured data with the hope that understanding how the coefficients are changing in these cases would shed light onto the behavior of the model and its relationship to the underlying physics. At first, all eight coefficients were included in the fitting, but it quickly became clear that this model was over-defined, failing to produce neither well-fit spectra nor physically meaningful trends in the output coefficients. Instead, just four coefficients were isolated for fitting, much in the method of Goody's original paper [11]. The a , c , f , and i coefficients, one from each bulk term plus the scaling factor i in the method of Rozenberg *et al.* [12] and Lee [17], were fit while holding the others constant at the original Goody values, which produced better fit spectra and more meaningful variations in the tuned parameters. These choices were made based on the original Goody work as well as a sensitivity study of the nine coefficients, shown in Fig. 4.

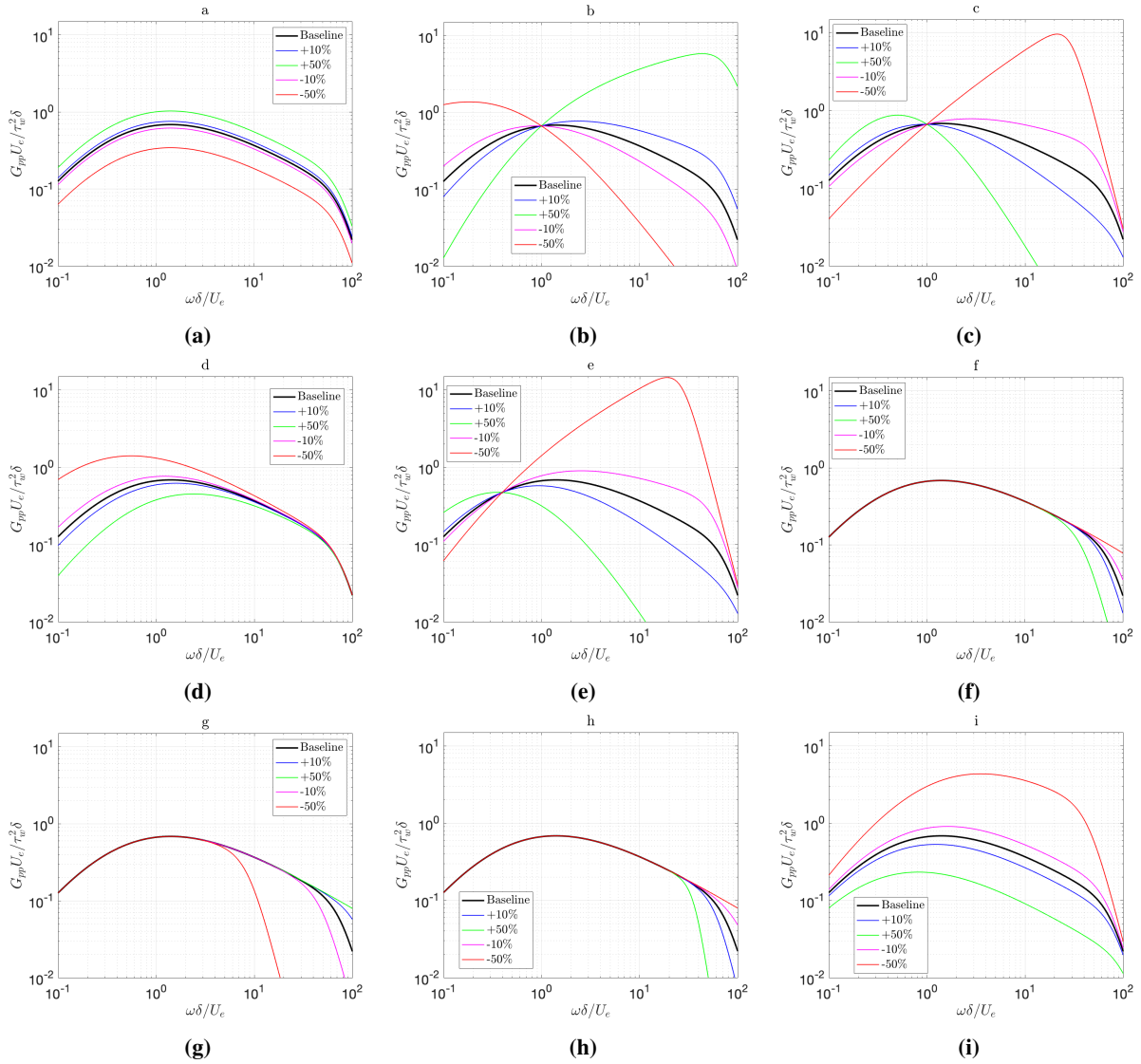


Fig. 4 Sensitivity studies of nine Goody-style model parameters (Eq. 5).

Firstly, the b and h coefficients are not tuned because, as shown by Goody [11], the combination of these two coefficients drives the high frequency slope such that this slope is equal to $b - h = -5$. This is a critical and universal feature of the spectra and so it will not be changed. Second, the c and e coefficients can be seen to have virtually the same impact on the model spectrum and, thus, for the sake of simplicity only one will be tuned. We choose to tune the c coefficient as this is what was done in the original work by Goody. Third, the f and g coefficients are of the same term in Eq. 5, but have opposing effects. The fitting algorithm struggled to reach convergence when considering both coefficients, and so the g coefficient is left constant and only f is tuned. Similarly, both the c and d coefficients affect the mid-frequency slope, but in different ways. Including both c and d in the fitting also resulted in over-definition. The pivoting behavior of the c coefficient more close replicates the observed effects of pressure gradient on the spectrum than that of the d coefficient, and so only the c coefficient is tuned.

The fitting was performed using a numerical optimization algorithm using the root-mean-square of the error as the objective function, and produced the tuned coefficients shown in Table 7. Additionally, the uncertainties in the tuned coefficients were quantified by finding the displacement of each coefficient that resulted in a 10% increase in the R.M.S. error objective function. Under this formulation, a smaller uncertainty implies a greater sensitivity of the model to that coefficient. Fig. 5 shows the tuned spectra against the tuning experimental data, as well as the associated R.M.S. dB error. Tuning the model enables a non-negligible reduction in the spectral error, achieving as low as 0.664 dB in the APG-FPG case, but none of the tuned cases are perfect.

	Goody	ZPG	APG	FPG	APG-FPG
a	3.0	2.94 ± 0.20	3.67 ± 0.12	2.11 ± 0.045	2.63 ± 0.075
c	0.75	0.806 ± 0.0060	0.836 ± 0.0043	0.777 ± 0.0020	0.799 ± 0.0033
f	1.1	1.29 ± 0.025	1.29 ± 0.040	1.00 ± 0.030	1.03 ± 0.022
i	1.0	0.868 ± 0.013	0.746 ± 0.0085	0.900 ± 0.0060	0.900 ± 0.063

Table 7 Select Goody model parameters, original [11] and tuned to measured data.

Based on sensitivity analyses of the Goody model form, we would expect the bulk of the pressure gradient effect to be driven by the c coefficient, which strongly impacts the mid-frequency spectral slope. All of the c coefficients are larger than the baseline 0.75 from Goody [11], which is attributed to the fact that these flows show a steeper ZPG slope (≈ 0.8) compared with Goody's original model of 0.7. These cases show a β distribution of $\approx \pm 0.8$ and a corresponding spread in the c coefficient of $\approx \pm 4\%$, which demonstrates the key issue with this particular style of empirical modeling; effectively capturing the effect of large changes in the flow requires very small changes to the model coefficients. A successful, all-encompassing Goody-style model would need to correlate a wide range of values of β , Re , etc. to very subtle changes in the model coefficients. As an example, consider the Hu [18] model. The c equation for this model (Table 1) is proportional to the natural log of the shape factor, $\ln[H]$. The spread of values for $\ln[H]$ as predicted by RANS modeling for these flows is $\approx \pm 8\%$, twice as large as the effective change in c for the associated spectra. This

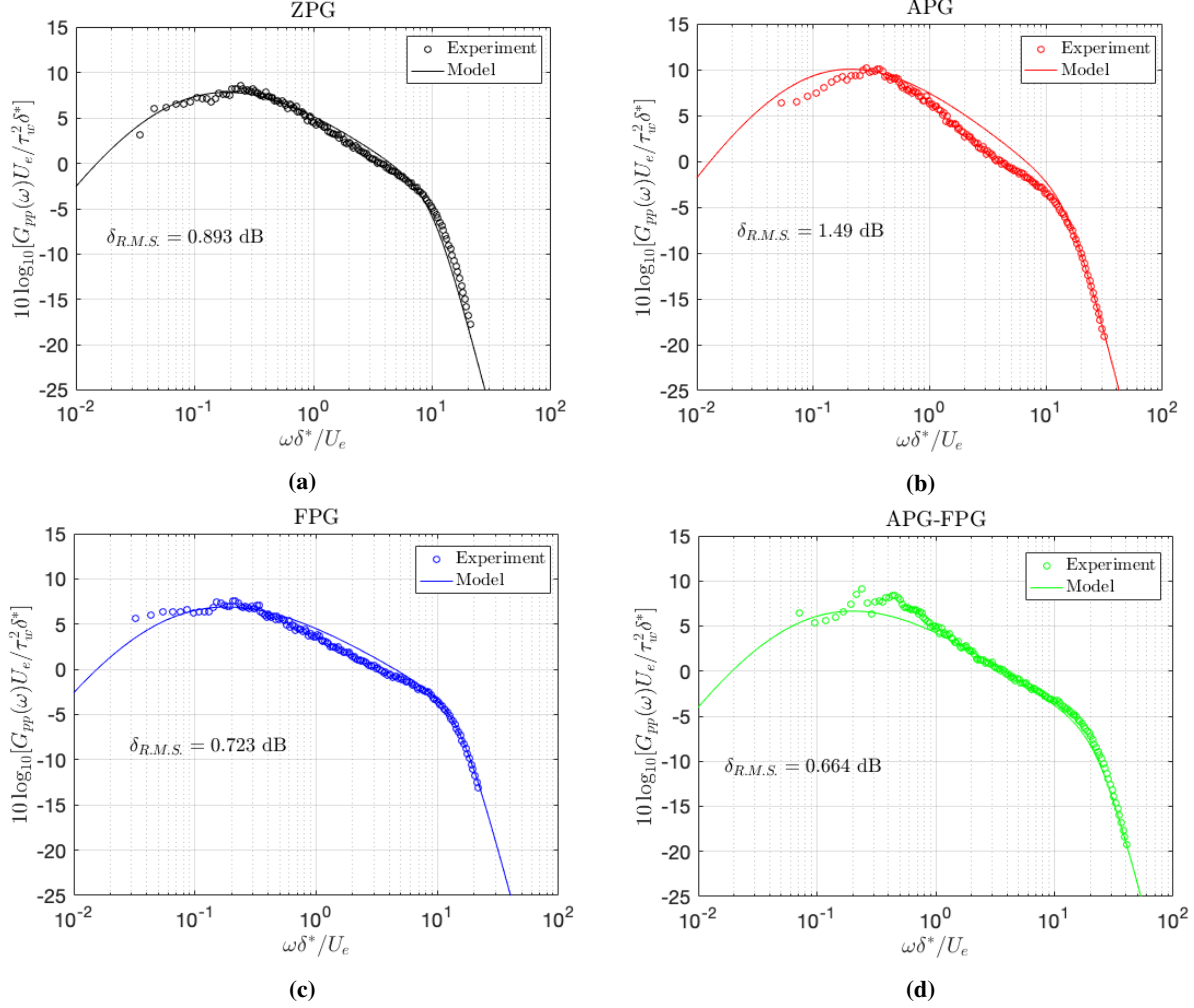


Fig. 5 Tuned Goody model parameters and experimental data used for tuning at ZGP (a), APG (b), FPG (c), and APG-FPG (d) conditions.

problem only becomes compounded when considering the infinite dimensional space of flows that could be considered across all relevant flow cases.

The lack of a universally applicable Goody-style model does not mean that such empirical models are not useful. They are easy to code, require only knowledge of scalar parameters (as opposed to the profile data required for analytical modeling as described in Section V), and fast to compute. However, successful implementation of such models should rely on a toolbox of stiff, mildly sensitive models with coefficient models that only change a few percent across a wide range of flows, rather than a single, flexible model with coefficient model equations that allow for large percent changes in input coefficients.

C. Development of New Empirical Modeling with GEP

1. GEP Overview and Methodology

Gene Expression Programming (GEP) [36] is an evolutionary algorithm within the broader class of Genetic Programming; the underlying principle is to iterate and evolve a population of individuals based on the criteria of survival of the fittest. It is a non-deterministic approach where random changes are introduced in the population, an effective method for symbolic regression, where one can obtain a mathematical functional form with given input data. This transparency makes it easier to understand the effect of each parameter on the resulting model. Symbolic models also tend to predict more robustly when extrapolated to parameters outside the training range. This is one of the significant advantages and a defining feature of this methodology over neural network models, which tend to suffer from over-fitting and under-fitting in the absence of sufficient data. This ultimately leads to poorer performance when predictions are made outside the training range of parameters.

The GEP method improves its solution, f^{new} , based on a cost function defined as:

$$fitness = 1 - \frac{1}{n} \sum_{i=1}^n \frac{||f^{new} - f||}{||f||} \quad (6)$$

The lower the value of the fitness, the closer the predicted value of the novel functional form is to the input data.

GEP takes its terminology from biological processes; a candidate solution is referred to as an individual, or chromosome, which is composed of one or more genes. A gene consists of mathematical operators and terminal functions, e.g., variables and constants, formally divided into head and tail parts. The head consists of all permissible objects while the tail only consists of symbols from the terminal set. The purpose of the tail is to make sure the resulting gene is well defined mathematically when converted to a mathematical expression. An example of a gene consisting of a head and a tail, separated by a vertical line, is:

$$+ \log -4x + |7yxyxyx \quad (7)$$

This would result in the mathematical expression:

$$f^{new} = \log(4 - x)(y + 7) \quad (8)$$

A GEP individual can have multiple genes of different lengths, and each of the genes can evolve separately as independent objects, which helps in finding short functional forms for complex solutions, speeds convergence, and helps in improving the diversity of the individuals. The independent evolution improves the performance in cases where multiple parameter effects are present. These individual genes are linked with mathematical operators which can either be prescribed beforehand or can be randomly evolved, for example:

$$+x - y|4yxyx < + > - + y + |7xyxy \quad (9)$$

which consists of two genes and is linked by the + operation. The corresponding equation is:

$$(x + (y - 4)) + (y + (7 + x) - y) \quad (10)$$

A population of N individuals is randomly created at the initial generation from the list of specified symbols. Fitness is determined for all individuals created before the next step, in which a tournament selection is used to replace the individuals with weaker fitness. The individual with the highest fitness wins the tournament, and this is repeated N-1 times to fill the same number of spaces. The final space is therefore always filled with the fittest individuals to ensure the best solution does not get removed if not selected for a tournament.

The genetic operators are used to bring more diversity to the population so that fitter solutions can more easily be obtained; the least fit variants are then filtered out in the tournament selection step. The most common genetic operators are mutation and recombination: mutations require only one individual while recombination requires two individuals. A full description of this algorithm is shown in the flowchart in Fig. 6 and can be further explored in detail [27].

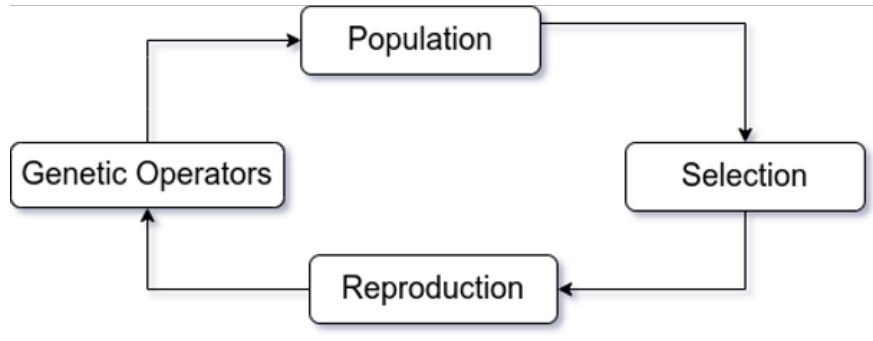


Fig. 6 Flowchart showing the GEP algorithm.

2. Modifications to Existing GEP Algorithm

The empirical wall pressure spectrum modeling used in the current study takes advantage of the multiple genes framework in the individual populations. The equation described here is representative of typical empirical models with 3 individual functions combined in this manner:

$$G_{pp}(\omega)SS = \frac{f_1(\omega FS)}{f_2(\omega FS) + f_3(\omega FS)} \quad (11)$$

Each individual function controls a certain region in the frequency space of the pressure spectrum. In the general

algorithm of GEP, the three genes are connected as follows:

$$f_1 < O1 > f_2 < O2 > f_3 \quad (12)$$

where $O1$ and $O2$ are random operators.

Using the traditional framework, it would not be possible to create a form of the model described in 11. The specific form requires the last two genes to be added and then divided as a whole, thus, the previous algorithm was not able to encapsulate multiple genes together in a bracket. To overcome this difficulty, linking functions for the 3 genes were introduced to maintain the basic structure of the functional form shown in Eqn.11. For our modeling purposes, these 3 functions will be treated as 3 genes in an individual which will be evolved separately based on the algorithm described above.

3. Assessment of GEP Model Sensitivities

Gene expression programming has been utilized to develop new empirical models for surface pressure spectra. The existing empirical models (see Section IV.B) do not predict the surface spectrum with accuracy across all cases, with predictions for higher-value adverse pressure gradient cases being particularly unsatisfactory, implying that the underlying physics for the changing parameters have not been appropriately captured and the models may benefit from corrections. The available experimental reference data (Section III.A) have been divided into test and training sets, and new models are trained using GEP as described in Section IV.C.1 using the data described in Sections III.A & III.B. The accuracy of the machine-learned empirical models is ascertained by their performance on test data at four conditions: zero pressure gradient, adverse pressure gradient, favorable pressure gradient, and under a non-equilibrium adverse-then-favorable pressure gradient. For training purposes, the required model inputs from either the experimental data or from RANS calculations have been used to evolve separate semi-empirical expressions.

Figure 7 shows the empirical model prediction given by Hu [18] using boundary layer parameters from both experiment and RANS as inputs. The RANS-based predictions show a considerable error with respect to the experiment, while the predictions using parameters obtained from experiments fare better; however, the error margins can be improved for both cases. The performance has been tested for both adverse and favorable pressure gradient conditions; in the case of a favorable pressure gradient, the results based on RANS boundary layer inputs are less different when compared to the results obtained with experimental boundary layer inputs, as compared to the APG case, but an overall error in spectral shape remains. This clearly shows the need for new empirical models that perform better at a wide range of conditions. It is also evident that when the input parameters themselves are not accurate, the pressure spectrum prediction accuracy also deteriorates, particularly for APG cases, for which the RANS closure errors are greater. Hence, in this work, we also attempt to develop a model that can absorb the inherent RANS modeling errors to predict the

pressure spectra. This new model will not be universal, as it will depend on the turbulence model used to provide the input parameters, however, it is of interest to evaluate whether a model can be developed that provides accurate surface pressure predictions based on RANS outputs, as access to the true boundary layer parameters will, in practice, be limited.

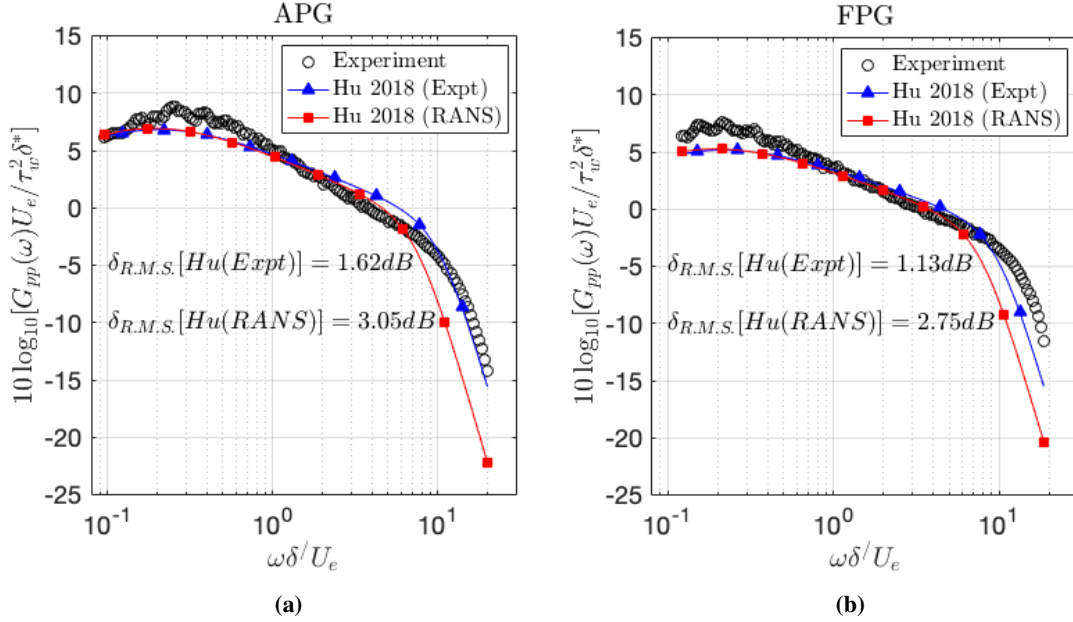


Fig. 7 GEP model prediction at APG (a) and FPG (b) conditions compared with experimental data and existing empirical model of Hu (2018) [18].

Machine learnt models are sensitive to the type, fidelity, and amount of data used in the model training. The modeling in the present work is performed on 4 different subsets of the data to understand the sensitivities of selection of training data on the final performance of the machine learnt model. The 4 different training datasets are:

- Full data - using all angles of attack (C1) - 11,424 data points
- Data only from every other angle of attack (C2) - 5,712 data points
- Data only from positive angles of attack (C3) - 5,712 data points
- Data only from negative angles of attack (C4) - 5,712 data points

Figure 8 shows a comparison of the predicted spectra at two different conditions, APG and FPG, using GEP models obtained from the different data subsets, and with experimental boundary layer data as inputs. It is evident that the empirical model performs well when all available data are utilized (C1). The model also performs quite well for the C3-dataset across the two cases shown here. Although the model based on the C2-dataset has the lowest error for the APG cases, the maximum error is lowest for models trained on the C3-dataset across the two cases shown in the figure.. Going forward, we employ dataset (C3) for training and analyze the performance of the obtained model based on this dataset only. For the three cases using only a subset of the full data (C2-C4), the models are tested on data not used for

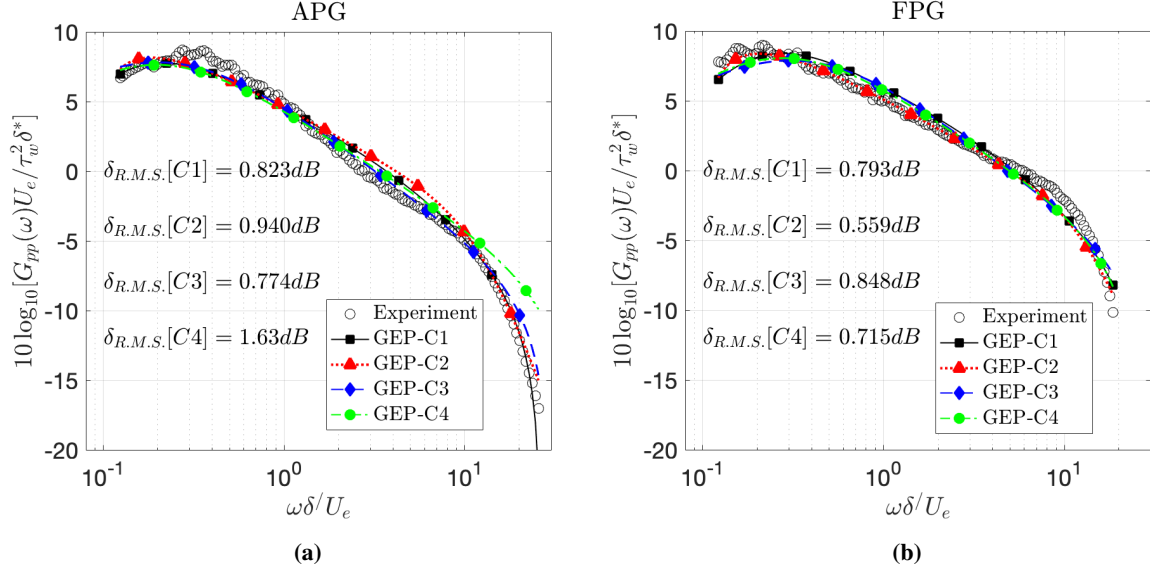


Fig. 8 Sensitivity of Performance of GEP model on different experimental data training sets at APG (a) and FPG (b) conditions.

training. In addition, all the models are tested on the extreme adverse and favorable pressure gradient cases.

4. GEP Produced Models and Results

The final expression shows distinct behaviour in the different regions of the spectrum, similar to previously developed models. The final model form is:

$$G_{pp}(\omega) = \frac{f_1 + f_2(\omega)}{f_3(\omega) + f_4(\omega)} \quad (13)$$

where, each function f_1 , f_2 , f_3 , and f_4 controls a specific part of the spectrum.

The GEP expression obtained using input parameters from the experiments is as follows:

$$\begin{aligned} f_1 &= -\delta(c_p G + c_p - G + 0.793) \\ f_2(\omega) &= -\delta(c_p - 1.067)(c_p - 0.48)\bar{\omega}^{(1.516)} \\ f_3(\omega) &= (-0.163G + H)\bar{\omega}^{(-0.976)} \\ f_4(\omega) &= R_T^{0.26571}(2.977c_p + 5.929G)\bar{\omega}^{(0.827)} \end{aligned} \quad (14)$$

The functional form of each sub-function is shown in Fig. 9 to aid in analyzing the role of each function. The solid black line is the experimental (target) spectrum and the black dashed and dash-dotted lines represent the two halves of the spectrum. The two lines clearly show that the shape and amplitude of the spectra is dominated by the

frequency-dependent part f_2 , and that f_1 only contributes at lower frequencies. The red lines are used to show the influence of the two functions in the denominator. f_3 is dominant from the low to mid-frequency range while f_4 seems to be activated in the high frequency region, causing the sharp change in gradient. The individual functions can be further analyzed by looking at their composition in terms of boundary layer parameters.

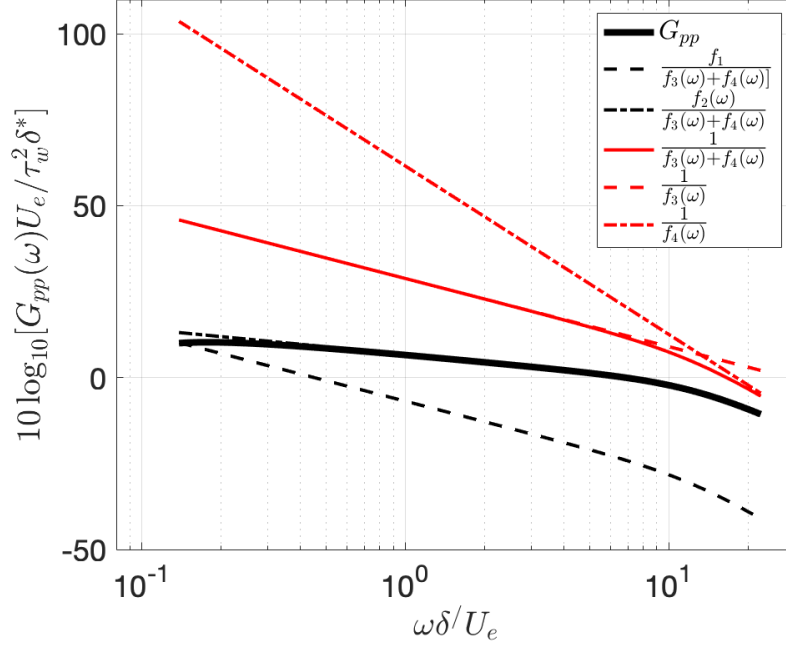


Fig. 9 Contribution of each GEP model sub-function.

The GEP expression obtained using boundary layer parameters from RANS is as follows:

$$\begin{aligned}
 f_1 &= \delta(c_p - 0.657)(c_p + 3.666) \\
 f_2(\omega) &= \delta(c_p - 0.657)\left(\frac{c_p}{G} - 1\right)(H - 0.59)\bar{\omega}^{(0.957)} \\
 f_3(\omega) &= (0.258c_p - 0.17)\left(\frac{c_p}{G} + \frac{\Delta_{ZS}}{G^2}\right)\bar{\omega}^{(-1.436)} \\
 f_4(\omega) &= -2.104R_T^{0.276}\Delta_{ZS}\bar{\omega}^{(0.784)}
 \end{aligned} \tag{15}$$

Figures 10a and 10b show the performance of the GEP model at training and non-training conditions and the associated overall error. The error is lower than the Hu (2018) model when testing the model at training conditions, and lower when testing outside of the training conditions for the particular case plotted. The predictive performance in non-training conditions is very encouraging, given that only APG data were used for training while the mode is tested for an FPG case. Overall, the model performs well and, as such, its performance is investigated thoroughly for additional

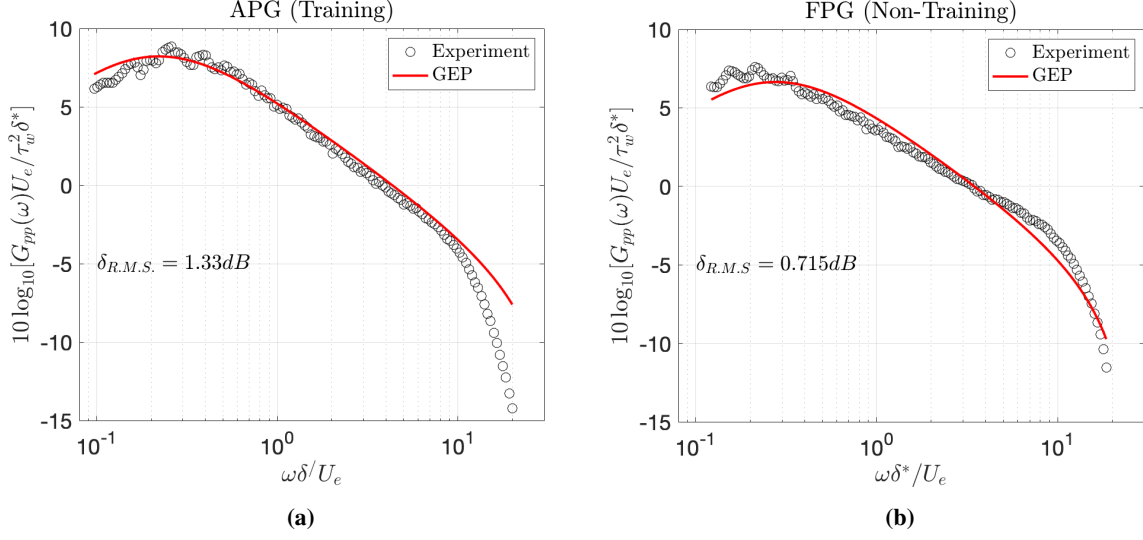


Fig. 10 Validation of GEP model at training (a) and non-training (b) conditions.

test conditions in the next section, along with an assessment of the sensitivity to the source of the input parameters.

The empirical models are tested at 4 different conditions: ZPG, APG, FPG, and APG-FPG using the two GEP models developed separately using boundary layer inputs either from experiments or RANS. Figures 11 and 12 show the results for the GEP models developed using experimental and RANS data, respectively. There are 5 different lines in each sub-figure to compare the results of the new models with experiments and with predictions using the Hu model [18]; $Hu(Expt)$, $Hu(RANS)$, $GEP(Expt)$, and $GEP(RANS)$ refer to whether the input parameters used for the GEP or Hu model predictions were obtained from RANS or experiments. The error is also compared and listed in the sub-figures for each case.

Based on the qualitative observation as well as measured error, it is evident that the GEP models improve the accuracy of prediction considerably at all the different pressure gradient conditions compared to the Hu model. The $\delta[GEP(Expt)]$ is the most important error while analyzing Figure 11 and $\delta[GEP(RANS)]$ is the most important for Figure 12, since these specific spectra and their corresponding errors represent the models tested on inputs from the same source as the training data, i.e., RANS-RANS or experiment-experiment. Thus, it is not a surprise that this error is the lowest. One more encouraging result that is shown here is that $\delta[GEP(RANS)]$ for Figure 11 and $\delta[GEP(Expt)]$ for Figure 12, where testing and training is done with inputs from opposite sources, also show reasonably small errors. Overall, the model trained on experimental data and using data from experiments for testing produces the best results, as shown in Figure 11.

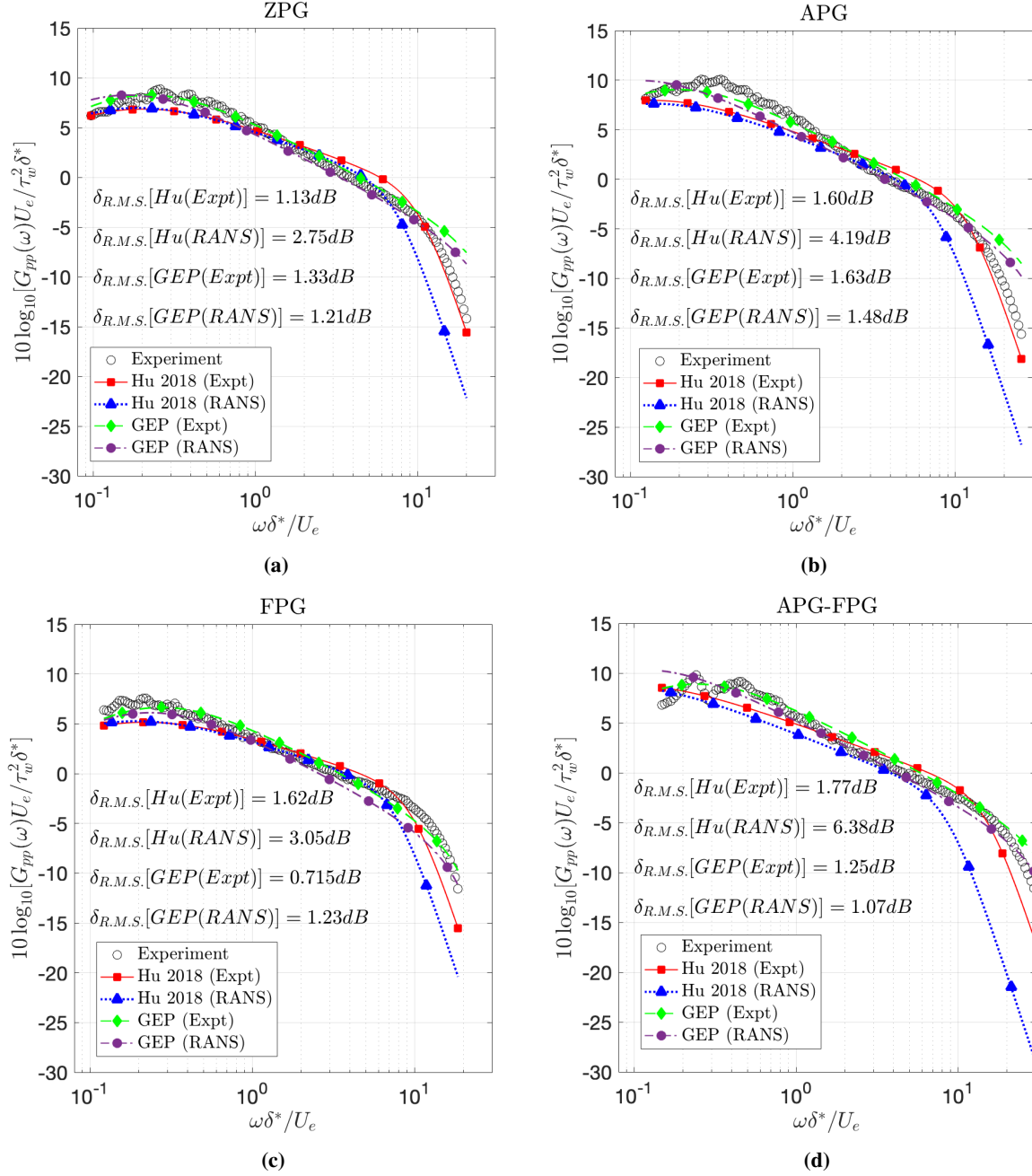


Fig. 11 Performance of experiment-based GEP model at ZPG (a), APG (b), FPG (c), and APG-FPG (d) conditions.

V. Analytical TNO Modeling

A. Overview

While empirical models can be applied quickly and easily and are often useful, they lack a foundation in fundamental physics and typically fail when applied outside of the range of flow characteristics used to tune the models. The fundamental foundation for incompressible turbulent pressure fluctuations is the Pressure Poisson Equation (PPE):

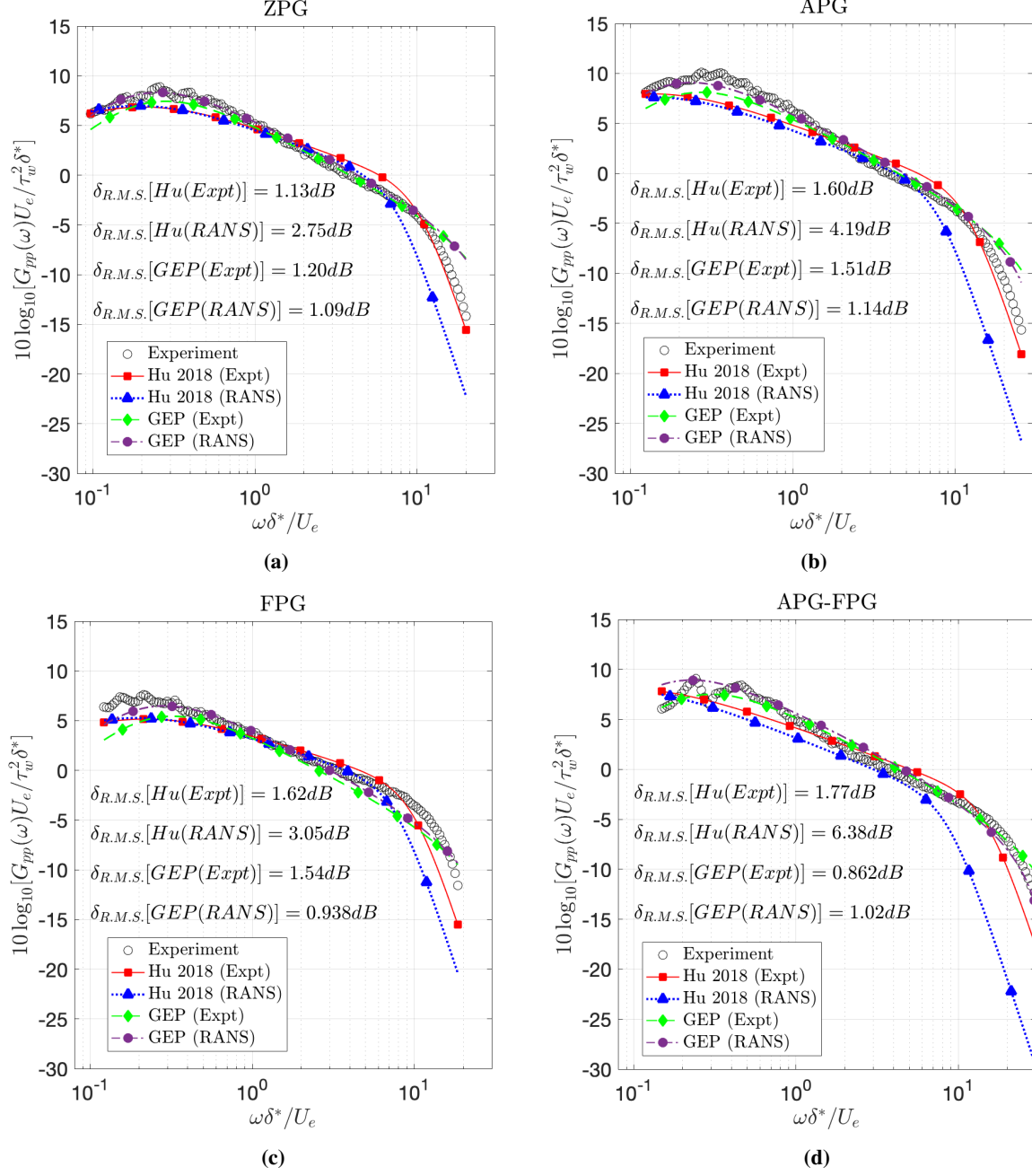


Fig. 12 Performance of RANS-based GEP model at ZPG (a), AGP (b), FPG (c), and APG-FPG (d) conditions.

$$\frac{1}{\rho} \nabla^2 p' = -2 \frac{\partial u'_j}{\partial x_i} \frac{\partial U_i}{\partial x_j} - \frac{\partial^2}{\partial x_i \partial x_j} (u'_i u'_j - \overline{u'_i u'_j}) \quad (16)$$

Making use of certain assumptions, most notably the boundary layer assumptions and that the source of pressure fluctuations exists as a homogeneous wall-parallel plane, the PPE can be solved at the wall and Fourier transformed using a tailored Green's function, yielding an equation for the wall pressure spectrum.

The most widely known of these analytical models is the TNO-Blake model [20, 21], but updates, alterations, and modifications to this scheme have been proposed as well [22, 24, 25, 37]. A good summary of the current state-of-the-art in analytical wall pressure spectrum modeling is given by Grasso *et al.* [25]. Grasso *et al.*, along with most of the other PPE modelers, splits the solution to the PPE into two parts, the rapid, turbulence-mean shear (TM) term and the slow, turbulence-turbulence (TT) term, the first and second terms of Eq. 16 respectively. The TM term is fairly straightforward to solve and transform using a tailored Green's function, resulting in a solution for the wavenumber spectrum:

$$\phi_{pp}^{TM}(K) = 4\rho^2 \int_0^\infty \int_0^\infty \frac{K_1^2}{K_1^2 + K_3^2} \exp[-(x_2 + x'_2)\sqrt{K_1^2 + K_3^2}] \frac{\partial U_1(x_2)}{\partial x_2} \frac{\partial U_1(x'_2)}{\partial x'_2} \phi_{22} dx_2 dx'_2 \quad (17)$$

Here, subscripts 1, 2, and 3 represent the streamwise, wall-normal, and spanwise coordinates respectively.

The TT term is more difficult to solve; there is no agreed-upon solution in the literature. Grasso *et al.* proposes solving this term by assuming homogeneous, isotropic flow in the boundary layer, an obviously invalid physical assumption, but one that can yield a solution:

$$\phi_{pp}^{TT}(K) = \frac{\rho^2 L^2}{128\pi} (K_1^2 + K_3^2) (28 + L^2 (K_1^2 + K_3^2)) \exp\left[-\frac{L^2 (K_1^2 + K_3^2)}{8}\right] \int_0^\infty \int_0^\infty \frac{4}{9} k(x_2) k(x'_2) \exp[-(x_2 + x'_2)\sqrt{K_1^2 + K_3^2}] \mathcal{F}_2^2 dx_2 dx'_2 \quad (18)$$

Here, \mathcal{F}_2 is the wall-normal velocity correlation function, which is difficult to know in-and-of itself, though Grasso *et al.* recommend simply assuming a Gaussian or exponential distribution under the assumption of homogeneous turbulence.

We employ the TT term using the Gaussian distribution:

$$\mathcal{F}_2 = \exp\left[-\frac{(x_2 - x'_2)^2}{L^2}\right] \quad (19)$$

The wavenumber spectrum can be transformed to the frequency spectrum assuming a constant convection speed of the pressure-imparting eddies:

$$G_{pp}(\omega) = \frac{\int_{-\infty}^{+\infty} \phi_{pp}(K_c, K_3) dK_3}{U_c} \quad (20)$$

The simplest interpretation of this convection speed is the broadband pressure convection velocity, the asymptotic value of convection velocity that is approached with increasing correlation separation, where a local U_c is defined by the peak location of the correlation function. This is known to be a function of pressure gradient, and Fritsch *et al.* (2022) observed a canonical pressure gradient relationship for these flow cases, reducing in APG and increasing in FPG from a ZPG value of $\approx 0.85U_e$, independent of history effects [7]. Based on the results of Fritsch *et al.*, we define:

$$U_c = \begin{cases} 0.85U_e & \beta \approx 0 \\ 0.8U_e & \beta > 0 \\ 0.9U_e & \beta < 0 \end{cases} \quad (21)$$

This simple formulation works well within the confines of the flow cases considered herein, in which the pressure gradient magnitudes are mild, but extension to higher magnitudes of β will require a more sophisticated model. Experimental results suggest that, in the limit of $\beta \rightarrow \infty$, $U_c \rightarrow 0.6U_e$ [19].

The predominant issue with the current state of analytical models is that they rely on successful prediction of the wall-normal velocity spectrum, ϕ_{22} . In a practical setting, this would need to be predicted from RANS, which will give no time or frequency dependent information on sufficiently small scales, meaning this term must be modeled. A few models for the velocity spectrum do exist, including those of von Kármán [38] and Liepmann *et al.* [39]. A generalized form of the spectrum is given by Wilson (1997) [40]:

$$\phi_{22}(K, x_2, x'_2) = \frac{\sqrt{u_2^2(x_2)u_2^2(x'_2)}(K_1^2 + K_3^2)\zeta^{\nu+2}}{K_e^4\Gamma(\nu)\pi 2^{\nu+1}(1 + (K_1^2 + K_3^2)/K_e^2)^{\nu+2}}\mathcal{K}_{\nu+2}(\zeta) \quad (22)$$

$$\zeta = |x_2 - x'_2|K_e\sqrt{1 + (K_1^2 + K_3^2)/K_e^2} \quad (23)$$

$$K_e = \frac{1}{L} = \frac{\sqrt{\pi}}{\Lambda} \frac{\Gamma(\nu + 0.5)}{\Gamma(\nu)} \quad (24)$$

where Γ is the Gamma function and \mathcal{K} is the Bessel-K function. The tuning parameter, ν , changes the spectrum to match various empirical models; $\nu = 1/3$ results in the original von Kármán spectrum [38], $\nu = 1/2$ results in the Liepmann spectrum [39], and, according to Grasso *et al.*, $\nu = 7/6$ results in a spectrum that matches well with the observations of Rapid Distortion Theory.

This and other empirical formulations for the turbulent velocity spectrum suffer from similar potential issues as the empirical pressure spectrum models, lacking a fundamental basis and failing to respond to non-canonical conditions, particularly given the fact that the velocity spectrum models are typically built around the assumption of isotropic flow. Some authors have proposed accounting for this by applying an anisotropy factor as a function of wall-normal distance [22], but these models are also empirical in nature.

Analytically formulated pressure spectrum models have the potential to solve many of the problems associated with empirical models, at the expense of greater computational cost. The formulation of Grasso *et al.* (2019) [25] provides a thorough framework through which to predict the surface pressure spectrum from the analytical basis of the pressure

Poisson equation and the TNO model. However, successful implementation of this model requires three inputs that are notoriously difficult to predict, particularly when working with RANS flow data: the wall-normal Reynolds stress, the integral length scale, and the wall-normal velocity wavenumber spectrum. This section will explore a number of options for how these may be computed within the limitations of RANS data as input, and the corresponding effects on the modeled pressure spectrum.

B. Source Sensitivities

1. Reynolds Stresses

RANS models typically compute the effect of the turbulent stresses via the Boussinesq eddy-viscosity hypothesis:

$$\tau_{ij} = -\overline{\rho u'_i u'_j} = 2\mu_T S_{ij} - \frac{2}{3}\rho k \delta_{ij} \quad (25)$$

where S_{ij} is the mean strain rate tensor:

$$S_{ij} = \frac{1}{2} \left(\frac{\partial U_i}{\partial x_j} + \frac{\partial U_j}{\partial x_i} - \frac{2}{3} \frac{\partial U_k}{\partial x_k} \delta_{ij} \right) \quad (26)$$

and δ_{ij} is the Kronecker delta function. Operating within this framework, there are three primary means of estimating the wall-normal Reynolds stress, $\overline{u_2'^2}$.

The Boussinesq Approximation Rearranging Eqs. 25 and 26, it can be seen that:

$$\overline{u_2'^2} = \frac{2}{3}k - \frac{2}{3} \frac{\mu_T}{\rho} \frac{\partial U_2}{\partial x_2} \quad (27)$$

Assume Isotropic Flow Assuming the flow is isotropic, i.e., that the Reynolds stresses are the same in all coordinate directions, implies:

$$\overline{u_2'^2} = \frac{2}{3}k \quad (28)$$

For a ZPG flow, this is exactly equal to the Boussinesq approximation, where $\partial U_2 / \partial x_2 = 0$.

Apply an Anisotropy Factor In a boundary layer flow, the turbulent stresses will not be isotropic, but the Boussinesq approximation is known to be a poor model for that anisotropy. Instead, an empirical anisotropy model could be applied such that:

$$\overline{u_2'^2} = \frac{2}{3}k f_{aniso} \quad (29)$$

where f_{aniso} is some model of the wall-normal component anisotropy as a function of x_2 . For this study, f_{aniso} was defined using the model of Kamruzzaman *et al.* (2010) [41]:

$$f_{aniso22} = Re_{\lambda}^{-0.09} \quad (30)$$

$$Re_{\lambda} = \frac{\sqrt{\frac{2}{3}} k \lambda}{\nu} \quad (31)$$

$$\lambda = \left[\frac{15\nu(\frac{2}{3}k)}{2\epsilon} \right]^{1/2} \quad (32)$$

In addition to the above models, there is a fourth option: simulate the flow using a Reynolds Stress Transport model (RSTM), which will contain the anisotropic nature of the turbulent stresses directly. While more computationally expensive than a traditional RANS simulation, RSTM provides a distinct advantage in the application to pressure spectrum modeling with its inclusion of anisotropic normal stresses.

Figure 13a displays these various Reynolds stress distributions for the ZPG case and Fig. 13b shows the corresponding modeled pressure spectra, with all else held constant, using an empirical isotropic length scale (Eq. 38) and the von Kármán velocity spectrum model.

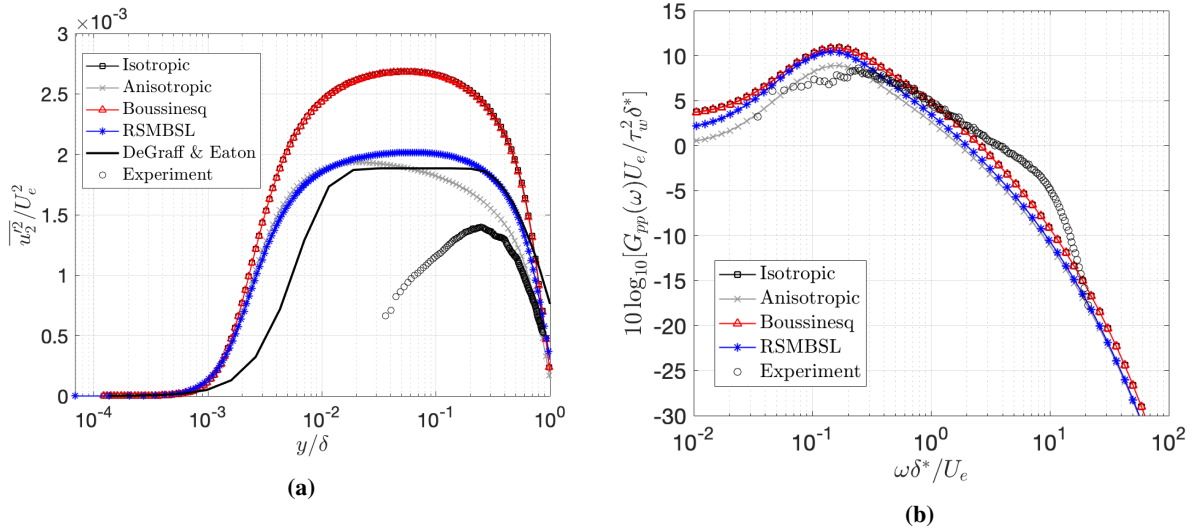


Fig. 13 Reynolds stress distributions (a) and corresponding TNO model spectra (b).

As might be expected, the Boussinesq hypothesis and isotropic distributions are virtually indistinguishable, and model a higher stress than the anisotropic models, the experimental data, and the data of DeGraff & Eaton [42]. This implies that the stress modeled by Eq. 25 is dominated by k , the μ_T term being comparatively negligible. The

Kamruzzaman *et al.* [41] anisotropy factor matches well with the RSTM results in the inner region, but the RSTM predicts the peak Reynolds stress lasting further into the boundary layer, which matches more closely with both the DeGraff & Eaton profile and the experimental data. The experimental data falls below that of DeGraff & Eaton in the inner region due to spatial resolution limitations near the wall in PIV techniques [29].

Figure 13b shows the corresponding model pressure spectra. The effect of changing Reynolds stress is contained primarily in the low and mid-frequency ranges, unsurprising given that the discrepancies in stress models are contained primarily in outer part of the boundary layer. The anisotropy factor stress model produces a pressure spectrum that is consistently lower than the other models, including the RSTM model, which actually matches closer with the isotropic and Boussinesq hypothesis models at the pressure spectrum peak. In general, then, the Reynolds stress magnitude is correlated with the pressure spectrum amplitude, i.e., higher Reynolds stresses produce stronger pressure fluctuations. This behavior is further correlated between varying boundary layer regions to spectral regions in a straightforward manner: Reynolds stress behavior closer to the wall affects the high frequency portion of the pressure spectrum and stress behavior in the outer region affects the low frequency portion of the spectrum. This is most clearly seen by observing the RSTM data compared to the anisotropic RANS (blue stars vs. gray x markers); these models produce virtually identical Reynolds stresses near the wall and corresponding identical mid- and high frequency modeled pressure spectra. In the outer region, the anisotropic RANS predicts a lower Reynolds stress, which corresponds to lower modeled pressure spectrum amplitude in the low frequency region, the split occurring around $y/\delta \approx 0.01$ and $\omega\delta^*/U_e \approx 10$. The similarity in predicted pressure spectra between the isotropic RANS and RSTM seems surprising, given the large discrepancy in predicted peak stress magnitude. We hypothesize that the peak region has a disproportionately small effect compared to the very-near-wall and wake regions, where there is significantly less difference between RANS and RSTM.

2. Velocity Spectrum

The wall-normal velocity spectrum is difficult to model, as it is a function of the turbulence itself in ways that are not captured with RANS models. A variety of empirical velocity spectrum models exist in the literature, but not all of them have structures that allow them to be easily implemented into the TNO formulation. Following the recommendation of Grasso *et al.* (2019) [25], we employ the Wilson (1997) generalized wall-normal velocity spectrum [40] as shown in Eqs. 22-24. The strength of this model is the tuning parameter, ν , which allows the spectrum to take various shapes. Setting $\nu = 1/3$ returns the original von Kármán spectrum [38], $\nu = 1/2$ returns the spectrum of Liepmann *et al.* [39], and, according to the analysis of Grasso *et al.* [25], $\nu = 7/6$ returns a velocity spectrum that matches closely with a spectrum derived from Rapid Distortion Theory (RDT). In addition to the tuning parameter, there is also the question of wavenumber anisotropy. Grasso *et al.* recommends dealing with this as such:

$$\phi_{22} = \alpha \phi_{22}^{iso}(\alpha K_1, K_3, y, y') \quad (33)$$

where α is an anisotropy factor and ϕ_{22}^{iso} is the isotropic velocity spectrum in Eq. 22. Grasso *et al.* do not specify a formulation for the anisotropy factor, α , but do present experimental measurements of the wavenumber anisotropy, based on measured correlations in the streamwise and transverse directions. By applying a fit to these experimental measurements, we model this wavenumber anisotropy as:

$$\alpha = \begin{cases} 2.4 \exp[-1.5 \frac{y}{\delta}] + 0.355, & \frac{y}{\delta} \leq 0.875 \\ 1.0, & \frac{y}{\delta} > 0.875 \end{cases} \quad (34)$$

Figure 14 shows the velocity spectrum models at $y/\delta = 0.55$ integrated across all K_3 and the corresponding pressure spectra, holding all else constant using an isotropic Reynolds stress ($\overline{u'^2} = 2/3k$) and empirical length scale (Eq. 38). The von Kármán ($\nu = 1/3$) spectrum exhibits a classic $-5/3$ slope roll-off, consistent with the experimental data, and the predominant effect of increasing ν is a steepening of this slope. This translates into a suppression of pressure spectrum level, as the spectral density of fluctuating velocity drops off. The effect of the wavenumber anisotropy is quite clear, raising the low frequency levels and lowering the high frequency levels in both velocity and pressure spectra. The anisotropic models match the experimental data more closely in the velocity spectrum, but less so in the pressure spectrum; however, it is important to note that this statement is made with the caveat that all else is held constant.

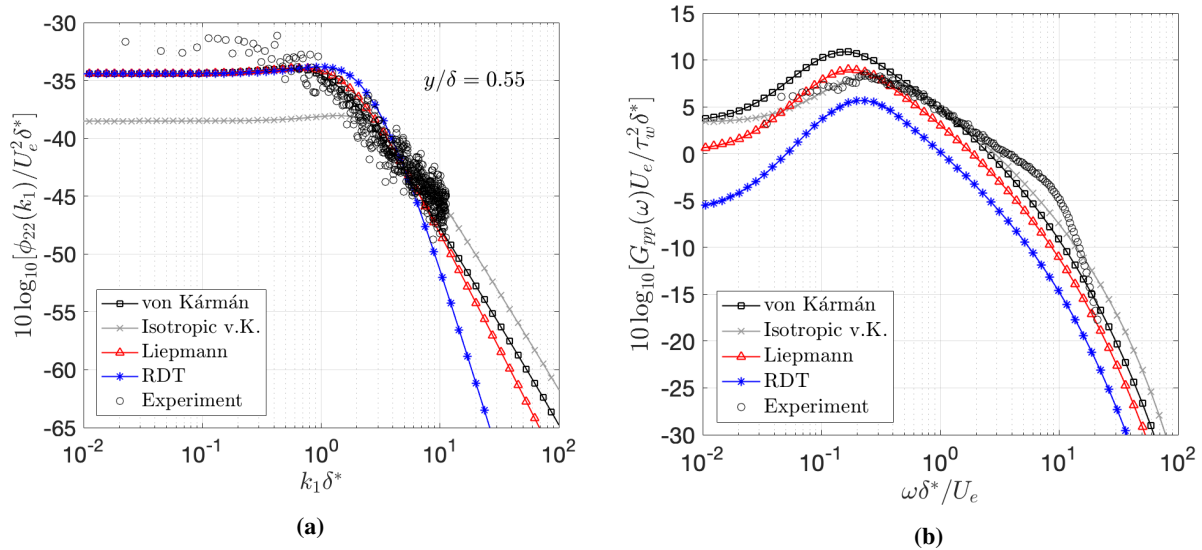


Fig. 14 Velocity spectrum distributions at $y/\delta = 0.55$ (a) and corresponding TNO model spectra (b).

The velocity spectrum effectively has three describable behaviors: the magnitude of the low wavenumber, constant amplitude region and the location and slope of the roll-off. The constant magnitude region is independent of changing ν and only affected by the anisotropy factor, and correlated only with pressure spectrum amplitude in the low frequency region, as observed comparing the isotropic and anisotropic von Kármán models (grey x markers vs. black squares). Increasing ν in the Wilson model pushes the roll-off location to higher wavenumbers and the slope to steeper magnitudes, which is correlated with a decrease in spectral amplitude across the entire frequency range and a shifting to higher frequencies of the entire spectrum.

3. Length Scale

A characteristic length scale is required for the generalized velocity spectrum. For the wall-normal component, ϕ_{22} , this is generally assumed to be a function of the integral length scale of the u_2 - u_2 correlations in the x_2 direction, $\Lambda_{22,2}$. Formally, the integral length scale is defined by the autocorrelation of the desired velocity component:

$$\Lambda_{ii,n} = \int_0^\infty R_{ii}(r_n) dr_n, i = n, i, \in [1, 2, 3] \quad (35)$$

Thus, the characteristic length scale for ϕ_{22} would be:

$$L = \frac{\Gamma(\nu)}{\sqrt{\pi}\Gamma(\nu+0.5)} \Lambda_{22,2} \quad (36)$$

$$\Lambda_{22,2} = \int_0^\infty R_{22}(r_2) dr_2$$

The quantity $\Lambda_{22,2}$ is difficult to estimate from RANS, owing to the lack of correlation data; replication of such length scales from RANS data is impossible for all intents and purposes, but several models have been proposed that are computable from the variables that a RANS model can predict:

k- ω Model Isotropic Length Scale Each turbulence model has an associated integral length scale, which can be taken as a rough estimate of the longitudinal length scale under the assumption of isotropic flow. For k - ω models:

$$\Lambda = C_\mu^{-1/4} \frac{\sqrt{k}}{\omega} \quad (37)$$

where $C_\mu = 0.09$.

Empirical Isotropic Length Scale In general, Λ may be modeled as:

$$\Lambda = C \frac{k^{3/2}}{\epsilon} \quad (38)$$

where C can be taken to be 0.4, based on the characteristic length scale of the von Kármán spectrum ($\nu = 1/3$). The anisotropy of this formulation may be estimated in the same manner as the Reynolds stress, by using some anisotropy factor, f_{aniso} . For the length scale, we will continue to use the anisotropy factor of Kamruzzaman *et al.* (2010) [41].

Kamruzzaman Kamruzzaman *et al.* (2011) proposed a different method of accounting for the anisotropy of the isotropic length scale model, by applying the anisotropy factor to the kinetic energy instead, resulting in a model as a function of the wall-normal stress [43]:

$$\Lambda = 0.748 \frac{\overline{u_2'^2}^{3/2}}{\epsilon} \quad (39)$$

This formulation may be estimated as isotropic or anisotropic depending on the method of calculating $\overline{u_2'^2}$.

Wilcox Wilcox (1993) proposed a formulation for the integral length scale derived from mixing length theory [44]:

$$\Lambda = \frac{1}{\kappa} \sqrt{\frac{|u'v'|}{(\frac{\partial U_1}{\partial x_2})^2}} \quad (40)$$

The Wilcox (1993) formulation is advantageous in that it does not require knowledge of the dissipation rate, meaning it can be employed using a one-equation eddy viscosity model (e.g., Spalart-Allmaras [45]), or a higher order Large Eddy Simulation (LES).

Michel Michel *et al.* (1968) argued that the distribution of the length scale ought to be linear with wall distance in the near-wall region before asymptoting to a constant fraction of the boundary layer thickness [46]:

$$\frac{\Lambda}{\delta} = \frac{\zeta}{\kappa} \tanh\left[\frac{\xi y}{\zeta \delta}\right] \quad (41)$$

where $\zeta = 0.085$ and $\xi = 0.4$.

Figure 15 shows these model length scales and the corresponding model pressure spectra holding all else constant, with an isotropic Reynolds stress ($\overline{u_2'^2} = 2/3k$) and von Kármán velocity spectrum ($\nu = 1/3$). Two experimentally measured length scale distributions are shown: $\Lambda_{22,2}$, since the dependence on the ϕ_{22} spectrum suggests this to be the analytically correct choice, and an estimate of an equivalent isotropic length scale. These are computed from time-resolved, two-dimensional-three-component particle image velocimetry [29]. The wall-normal integral length scale, $\Lambda_{22,2}$, is computed using numerical estimators for the correlation function and Eq. 35. Statistically, a reasonable estimate of the equivalently isotropic scale could be:

$$\Lambda_{iso} = \left[\frac{\Lambda_{11,1}^{2/3} + \Lambda_{22,2}^{2/3} + \Lambda_{33,3}^{2/3}}{3} \right]^{3/2} \quad (42)$$

The issue with this formulation is the difficulty in experimentally measuring all three length scale components. Stereo PIV enables accurate measurement of $\Lambda_{11,1}$ and $\Lambda_{22,2}$, but does not measure sufficient data points in the x_3 direction to integrate to $\Lambda_{33,3}$. This can be handled by assuming a 2D flow and computing:

$$\Lambda_{2D_{iso}} = \left[\frac{\Lambda_{11,1}^{1/2} + \Lambda_{22,2}^{1/2}}{2} \right]^2 \quad (43)$$

None of the length scale models accurately replicates the formally defined integral length scale as measured experimentally with time-resolved PIV. Close to the wall, the experimental results suggest a rapid growth that is similar to the linear growth of the Michel model, but at an even steeper slope. In the outer region, the Michel model is closest to the experimental length. The other models either over-predict or under-predict the experimental values and also exhibit a peak and subsequent decay, which is not seen in the experimental results. However, the experimental results do not show a canonical shape, which previous results suggest ought to demonstrate a large reduction in length scale magnitude in the outer region [47], which most of the model scales do predict.

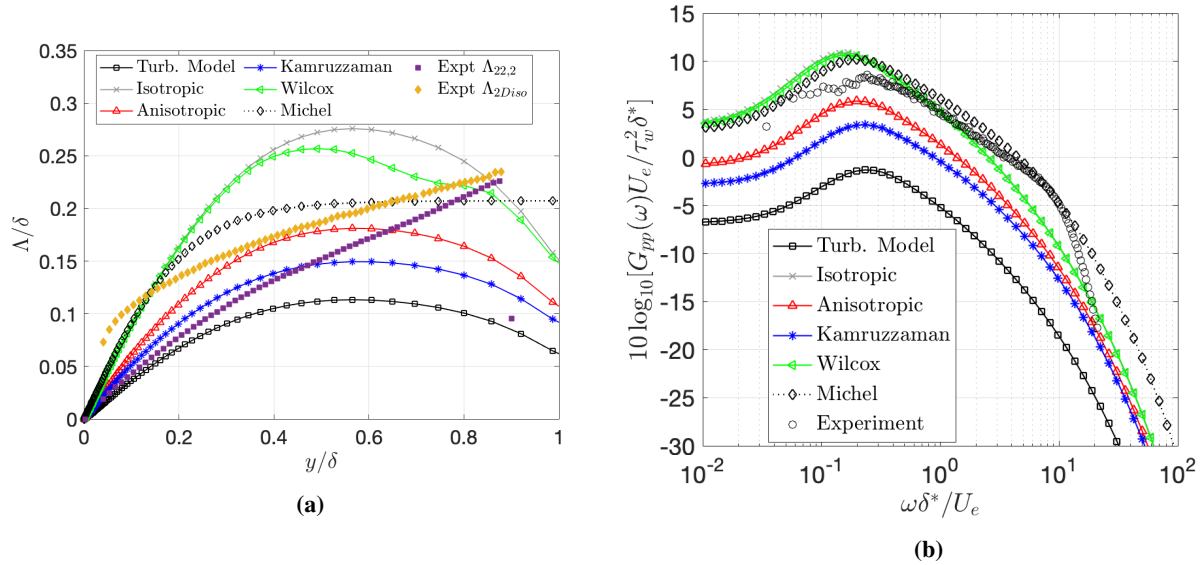


Fig. 15 Length scale distributions (a) and corresponding TNO model spectra (b).

Ultimately, the experimental results are shown only as a point of comparison, the length scale models will be judged based on the output TNO pressure spectra they produce. The SST turbulence model length scales are the smallest of all the various models by a not-insignificant amount and, as a result, the predicted pressure spectrum is the most under-predicted, with a level generally around 10dB less than the experimental profile. In general, larger length scales are correlated with higher dB spectra.

Similar to the Reynolds stress, the length scale magnitude is directly correlated to the model pressure spectrum amplitude and shows a similar inner-to-high-frequency/outer-to-low-frequency regional correlation, which implies the

strength of the pressure fluctuations are largely driven by the size of the pressure imparting eddies, and that structures pass with decreasing frequency when moving further into the boundary layer.

The isotropic, Wilcox, and Michel models all give reasonable estimates of the spectral peak. The good prediction of the peak by the Michel model may be due to the relatively good agreement with experimental length scales overall. However, the isotropic and Wilcox models over-predict the length scale over a wide range of wall distances. This suggests that the TNO formulation is relatively insensitive to the length scale in the outer layer, but rather is largely driven by the behavior in the near-wall region. However, it would also appear that the spectral model formulation is more sensitive to changes in the overall length scale profiles than it is to the input from the Reynolds stress.

4. Convection Velocity

In order to convert the wavenumber spectrum, $\phi_{pp}(K_1, K_3)$, into a frequency spectrum, $G_{pp}(\omega)$, we employ Taylor's hypothesis of frozen turbulence, such that the time frequency, ω , and the spatial frequency, K_1 , are related by a constant convection velocity, i.e., $\omega = K_1 U_c$. The correct interpretation of this convection velocity is somewhat up for debate, but the most likely candidate is the broadband convection velocity of the fluctuating pressure, found by observing how the convection velocity asymptotes to a constant value with increasing correlation separation, around $0.85U_e$ for a typical, canonical ZPG flow. As shown by Fritsch *et al.* (2022) [7], the effect of pressure gradient on the broadband convection velocity in these flow cases is straightforward and largely free of history effects. APG decreases the convection velocity while FPG increases it relative to the local edge velocity. These changes are small in these mild pressure gradients, around $\pm 5\%$ across the full range of observed cases. This enables the relatively simple calculation of the local broadband convection velocity from RANS using Eq. 21. Within the range of $\pm 5\%$, the model is relatively insensitive to changing convection velocity, as shown in Fig. 16, where all else is held constant using the isotropic Reynolds stress, $\overline{u_2'^2} = 2/3k$, von Kármán spectrum ($\nu = 1/3$), and empirical length scale of Eq. 38.

C. Recommended Practices and Performance in Pressure Gradient

Having assessed the various options and their impacts on the model spectra independently, we next turn our attention to finding the combination of sub-models that produces the most accurate and robust pressure spectrum model. The length scale clearly has the greatest effect on the model spectrum, both in its level and shape. The Michel *et al.* (1968) [46] length scale produces the shallowest mid-frequency slope and, consequently, the best agreement with both the currently compared experimental dataset and the expected behavior in this region for these conditions. It was determined via a sensitivity analysis, that this is due to the relatively large magnitude of the length scale in the very-near-wall region. However, the Michel length scale seems less applicable for the outer region, since it provides a fixed plateau value of about $\Lambda/\delta = 0.2$, whereas the length scale in this region is more likely to be a function of the turbulence parameters, as suggested by the other models. In this particular test case, the outer region length scale according to Michel happens to

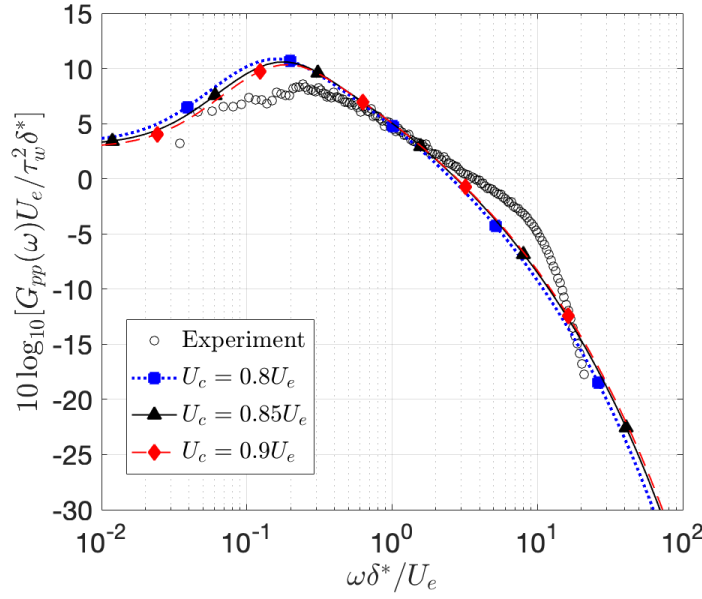


Fig. 16 TNO model spectra with varying U_c .

be similar to the values from the experimental data; however, for a more generally applicable model, the outer region model should depend on the turbulence parameters. It was therefore decided that the length scale distribution that would produce the best results is a hybrid model, employing the Michel distribution near the wall and one of the other considered models in the outer region. We found that either the Wilcox [44] or isotropic models performed well in this role, and the Wilcox model was chosen due to the distinct advantage it offers in lacking a dependence on ϵ , meaning this length scale model can be employed with a one-equation eddy viscosity model or an LES. Additionally, Lane *et al.* (2021) observed that the agreement with this hybrid model was improved by updating the coefficients of the Michel model to $\zeta = 0.06$ and $\xi = 0.51$, which produced better agreement with the length scale as determined from DNS [48] and with the experimentally measured length scales in Fig. 15a. The final recommended length scale model is:

$$\Lambda = \begin{cases} 0.146\delta \tanh[8.5 \frac{y}{\delta}], & \frac{y}{\delta} \leq 0.02 \\ \frac{1}{\kappa} \sqrt{\frac{|u'_1 u'_2|}{(\frac{\partial U_1}{\partial x_2})^2}}, & \frac{y}{\delta} > 0.02 \end{cases} \quad (44)$$

For the Reynolds Stress Transport modeling, the wall-normal Reynolds stress was already established, leaving only the velocity spectrum to be modeled. The wavenumber anisotropy in Eq. 34 appears to be critical, both to matching the experimentally measured velocity spectra and to producing the proper pressure spectrum shape, and so it is employed for all further modeling. By systematically varying the ν parameter in the Wilson [40] model, we observed that the $\nu = 7/6$ "rapid distortion theory" model consistently produced the best results. The RDT velocity spectrum produces a

bottleneck and high frequency roll-off that matches the experimentally measured pressure spectra better than the von Kármán [38] or Liepmann *et al.* [39] models.

The final consideration is the Reynolds stress model for the eddy-viscosity RANS method. The isotropic model outperformed the anisotropic version considerably, the latter under-predicting the pressure spectral levels, particularly in the low frequencies. At first, this was a surprising result, given the agreement observed with the anisotropic RSTM results, but the cause was readily apparent. The RSTM data result in a larger length scale distribution using the Wilcox [44] formulation; the velocity gradients are similar, the difference being in the modeled shear stress, $\overline{u'_1 u'_2}$. This discrepancy makes sense logically, given that it is established that eddy-viscosity models are capable of capturing overall turbulence effects like boundary layer thicknesses, skin friction, and drag with reasonable accuracy, despite having virtually isotropic stresses. The Boussinesq approximation is built on invalid assumptions, which leads to inaccurate prediction of the specifics of a turbulent flow, but these errors are accounted for in the model formulation and tuning such that the turbulent effects are modeled effectively on a global scale. There are two potential approaches for the pressure spectrum modeling; either the simulation results should be taken as is, with no attempt to account for anisotropy, or anisotropy should be accounted for in all variables, the latter of which is difficult at best. These results indicate that, when working with eddy-viscosity models, the best pressure spectrum modeling results will be obtained with the RANS results without attempting to account for anisotropy.

Figure 17 shows the TNO model spectra at all four tested conditions alongside the measured spectra and the Goody model for reference. In the ZPG case (Fig. 17a), the TNO modeling appears to offer little benefit over the Goody model; both model types predict the same peak spectral amplitude and frequency and similar roll-off points, and have seemingly equivalent, if different, errors throughout the spectrum. In the APG case (Fig. 17b), the TNO formulation matches the shape of the spectrum better than the Goody model, but fails to account for the increased peak amplitude, implying that either a) the RANS simulations are failing to capture an increased turbulent stress in the outer region or b) there is an affect of adverse pressure gradient on the pressure spectrum not captured by the associated changes in the model inputs.

In the FPG case (Fig. 17c), the Goody model outperforms the TNO modeling. Neither model seems able to capture the shallowing slope of the mid-frequency region, but the Goody model better matches both the peak and roll-off. The non-equilibrium AGP-FPG case (Fig. 17) is where the TNO model best performs; the combination of the Michel/Lane inner region length scale and RDT velocity spectrum serves to well replicate the bottleneck feature in the mid-frequency region, which none of the empirical models were able to do.

This formulation of the TNO/Grasso *et al.* pressure Poisson equation model is imperfect, but offers several distinct advantages over the range of reviewed empirical models. The analytical formulation proves to be more physically sensitive to changing inputs, able to capture subtle changes in spectral features in response to typical boundary layer inputs. It also has greater flexibility in the output spectral shape. This gives the analytical TNO model a balance between robustness across a wide range of conditions and flexibility through varying Reynolds number and pressure gradient

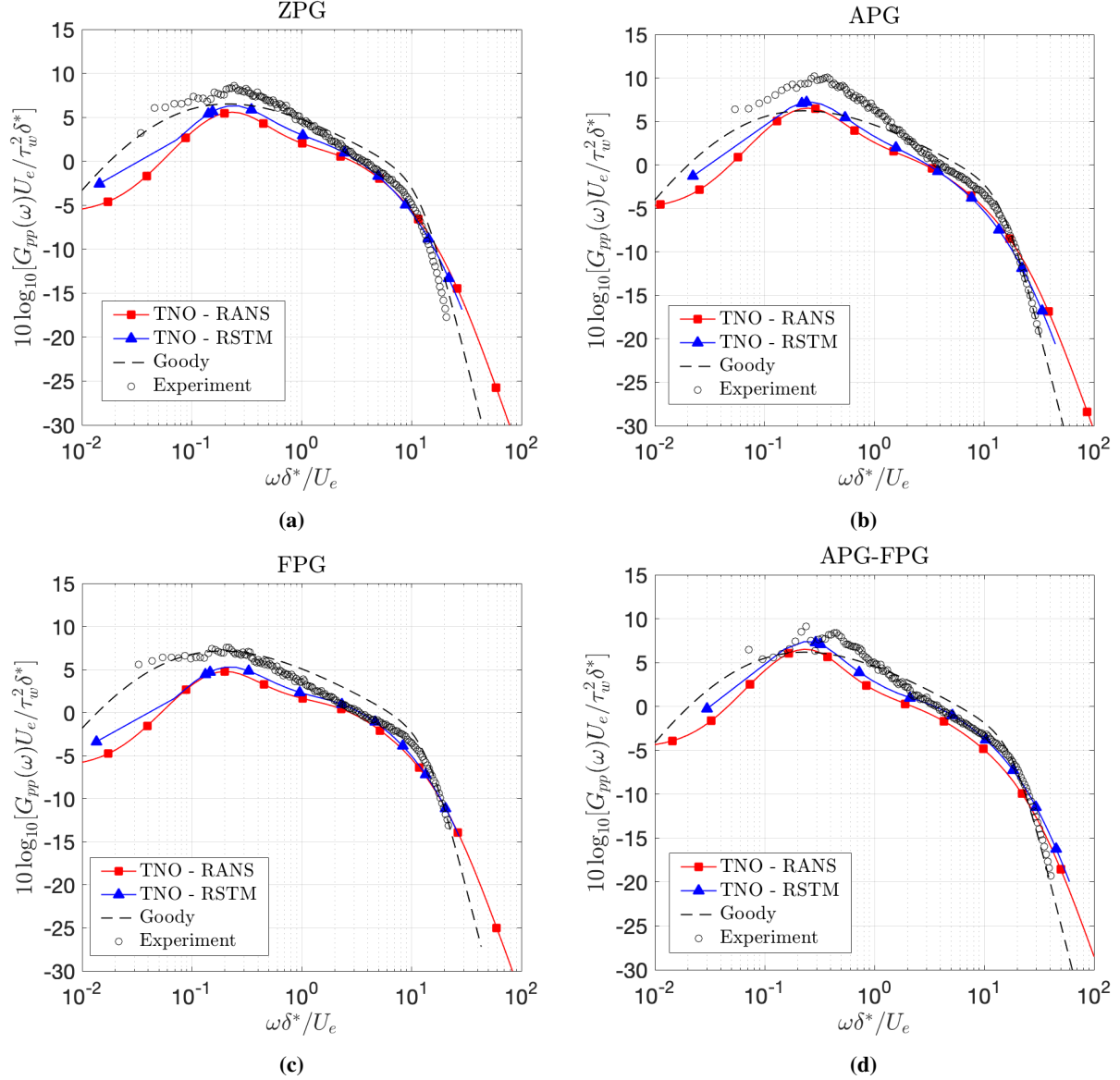


Fig. 17 Pressure spectra at ZPG (a), APG (b), FPG (c), and APG-FPG (d) conditions as predicted using both final TNO models, Goody model, and as measured.

conditions, with the trade-off of increased modeling complexity and computational cost.

There is obviously uncertainty in the utilized RANS data that will filter through the TNO model. We attempt to quantify this from both solver-to-solver uncertainties by comparing the velocity and TKE profiles obtained using the Menter SST model in CREATE-AV Kestrel and ANSYS/Fluent, using the same grids and boundary conditions, and observe errors of approximately $\pm 0.43\%$ in the velocity profiles and $\pm 0.53\%$ in the TKE profiles. Additionally, simulations were run in CREATE-AV Kestrel using the Menter SST, Menter Baseline $k-\omega$ and Spalart-Allmaras (SA) [45] models. TKE was estimated in the SA model using Townsend's structural parameter, the hypothesis that the shear stress vector magnitude and normal stress vector magnitude (i.e., TKE) are related by a constant in 2D flows, such that

$a_1 = \tau/2k = 0.15$, where τ is the shear stress vector magnitude. For a 2D flow, this can be rearranged to show that $k = \frac{10}{3}\overline{u'_1 u'_2}$. Comparing the three models, model-to-model uncertainties were estimated as $\pm 2.3\%$ in the velocity profile and $\pm 5.3\%$ in the TKE profile. The uncertainties in velocity and stress profiles generate an associated uncertainty in the Wilcox length scale. These uncertainties are filtered through the TNO model to estimate the associated uncertainty in the output model spectrum, shown in Fig. 18. The solver and model uncertainty in the RANS data results in an uncertainty in the output pressure spectrum of around $\pm 1dB$.

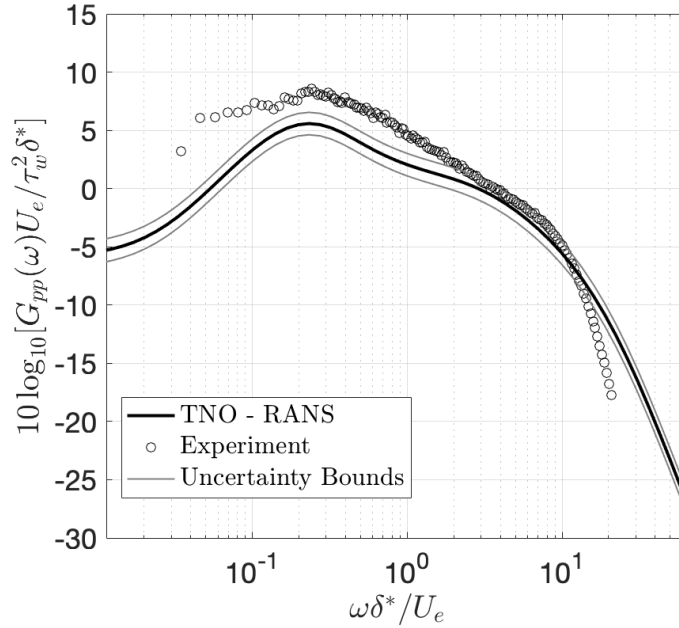


Fig. 18 Pressure spectrum at ZPG conditions as predicted using TNO RANS model showing uncertainty bounds from associated RANS uncertainty in velocity and TKE profiles.

The proposed modeling protocol suffers in two primary ways: an under-prediction of the peak pressure spectrum amplitude and an under-prediction in the high frequency roll-off slope. Based on the sensitivity analysis above, improving prediction of the spectral peak would require an increase in a) the Reynolds stress in the wake region, b) the length scale in the wake region, or c) the wavenumber anisotropy magnitude. Physically, the Reynolds stress and length scale should reduce towards zero approaching the boundary layer edge, thus, increasing one or both in the wake region without producing non-physicality in the input models would be difficult. The most physically consistent correction, then, would be an improvement to the anisotropy model in Eq. 34. This would also be supported by experimental data, based on the under-prediction of the experimentally measured low wavenumber velocity spectrum in Fig. 14a. However, the anisotropy should not simply be tuned to give good agreement with a given dataset; instead the physical behavior ought to be investigated experimentally to develop an improved understanding (and by extension, model) of the α parameter.

The under-prediction of the roll-off slope is more concerning, given it is a benchmark feature of our understanding

of fluctuating wall pressure. Unfortunately, none of the sub-variables observed in the previous sections showed a correlation with the roll-off slope, which showed consistently overly-shallow behavior across Figs. 13-15. Some of the increased magnitude comes from the inclusion of the TT term; the TM term alone shows a steeper roll-off slope, as shown in Fig 19, but is still shallower than ω^{-5} . The under-predicted slope appears to be a relatively fixed feature of the model. Preliminary results suggest that artificially shifting the point at which the pressure fluctuations are generated further from the wall, akin to a rough-wall effect, steepens the slope and improves agreement, but there is little-to-no physical basis for this shift in a smooth wall flow.

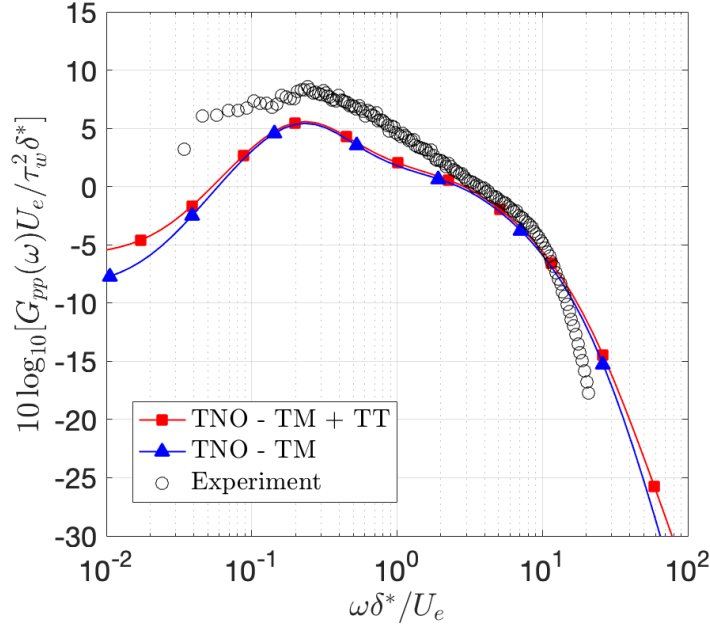


Fig. 19 ZPG spectra predicted from full TNO model and using TM term only.

VI. Conclusions

A variety of methods and models for predicting the surface pressure spectrum beneath turbulent boundary layers have been presented. These models were employed using experimental or CFD data as input to make predictions of the spectra for a high Reynolds number, low Mach number boundary layer flow in zero, adverse, favorable, and mixed adverse-to-favorable pressure gradient conditions. Experimental measurements of these flows have indicated subtle pressure gradient and flow history dependencies in the pressure spectrum that vary between spectral regions, making successful, robust prediction difficult.

A number of empirical, single-equation models were assessed. "Stiff" models, meaning those with few flow-dependent inputs (Chase 1987 [9], Howe 1998 [10] Goody 2004 [11]), were unable to replicate the spectral changes observed between varying pressure gradient conditions, while more "flexible" models (Rozenberg *et al.* 2012 [12],

Kamruzzaman *et al.* 2015 [13], Catlett *et al.* 2016 [14], Hu 2017 [16], Lee 2018 [17]) managed to capture some of the pressure gradient dependencies, particularly in APG, but were shown to produce non-physical results for certain inputs far removed from tuning data, particularly in FPG and non-equilibrium conditions. With these empirical models, there is a trade-off between robustness across varying conditions and response to changing pressure gradient conditions. Despite the weaknesses of empirical models, they are still valuable for their rapid employment and simplicity of required data input, with the caveat that simpler models appear more valuable as they retain physical shape for a wider range of conditions.

New empirical models have been developed using Gene Expression Programming (GEP)-based machine learning. The GEP model is derived from two different sets of boundary layer parameters, one from experiments and the other from corresponding RANS results. The latter is an effort towards a prediction framework with overall low cost, i.e. one that does not require experimental or high-fidelity simulation inputs. Symbolic mathematical expressions are obtained that allow for analysis of the individual terms and the new models obtained from experimental and RANS datasets are tested using both datasets as inputs across various conditions. Both models performed well for both training and testing conditions and improved the accuracy of predictions over existing models throughout the entire frequency range. The GEP models also give better predictions for the low frequency range, although the models are hampered slightly by the lack of training data in this region, the roll-off rate in the mid-frequency range, and the high frequency slope. The results show the excellent prediction of the GEP model at the extreme pressure gradients (both favorable and adverse), which indicates the high potential this method has in developing empirical models.

The analytical TNO-based [21] formulation of Grasso *et al.* (2019) [25] provides a balance between robustness and sensitivity, capturing a wider array of flow-dependent spectral characteristics without developing non-physical behavior, even in non-equilibrium conditions, at the expense of increasing complexity and fidelity of input data and computational cost. A number of inputs to the TNO formulation are difficult to estimate when working with RANS data, therefore, a number of options for these inputs were explored and assessed, as suggested by the literature. The wall-normal Reynolds stress and integral length scale are correlated directly to pressure spectrum amplitude and there is a clear regional dependence from the inner layer to the high frequency and the wake region to the low frequency. A wavenumber anisotropy factor, empirically based on the experimental results of Grasso *et al.* (2019) [25], increases the magnitude of the low wavenumber velocity spectra, agreeing better with experimentally measured ϕ_{22} values, and driving a corresponding increase in peak pressure spectrum amplitude. The inertial roll-off of ϕ_{22} was correlated strongly with both the pressure spectrum amplitude and frequency dependency across the full spectrum.

Based on these results, we recommend the use of a hybrid length scale model composed of the Michel *et al.* (1968) [46] formulation with the coefficients of Lane *et al.* (2021) [48] in the inner region and the Wilcox (1993) [44] model in the outer region; the Wilson (1997) [40] generalized velocity spectrum model with $\nu = 7/6$ (which Grasso *et al.* refer to as the rapid distortion theory model); and for the wall-normal Reynolds stress, either a Reynolds Stress Transport

model or an eddy-viscosity model with the assumption of isotropic flow. This combination of modelling options proves advantageous for a few reasons: the use of the Michel (1968) linear length scale distribution, combined with the RDT velocity spectrum, produces mid-frequency and high frequency roll-off location behavior that matches experimental data more closely than other models. Additionally, the chosen formulation has no dependence on dissipation rate, meaning it can more readily be employed with a one-equation eddy viscosity or LES model. The proposed formulation generally under-predicts the peak spectral amplitude and the roll-off slope of the high frequencies. Based on the sensitivity analyses performed, it is fairly clear what changes to the input behavior would be needed to improve agreement, but challenges remain in physically justifying those changes.

Predictive capability for the surface pressure spectrum beneath turbulent boundary layers has improved in recent years, but several questions remain to be answered. These results strongly indicate a few paths for future research: the development of a toolbox of Goody-style empirical models that incorporate specific flow effects while retaining the robustness of the original model formulation, as opposed to the over-sensitivity of the flow-dependent models; and an advancement of the predictive capability for the inputs to the TNO formulation. In both of these regards, as well as full model development capability, machine learning methods can play an important role.

Acknowledgments

The authors would like thank the NATO Science and Technology Organization for hosting this collaboration.

The authors from Virginia Tech would like thank Dr. Peter Chang and Dr. Julie Young of the U.S. Office of Naval Research (ONR) for their support of experimental work through grant numbers N00014-18-1-2455, N00014-19-1-2109, and N00014-20-1-2821. We would also like to thank the U.S. Department of Defense High Performance Computing Modernization Program (HPCMP) for computational resources.

The authors from the University of Melbourne acknowledge support from the Australian Research Council and the U.S. Office of Naval Research under NICOP Grant N62909-20-1-2046 with program monitors Dr. Julie Young (ONR) and Dr. Elena McCarthy (ONR Global, London).

References

- [1] Ffowcs-Williams, J. E., and Hawkings, D. L., “Sound generation by turbulence and surfaces in arbitrary motion,” *Philosophical Transactions of the Royal Society A*, Vol. 264, 1969, pp. 321–342. <https://doi.org/10.1098/rsta.1969.0031>.
- [2] Glegg, S., and Devenport, W. J., *Aeroacoustics of Low Mach Number Flows*, 1st ed., Academic Press, London, UK, 2017.
- [3] Bull, M. K., “Wall Pressure Fluctuations Beneath Turbulent Boundary Layers: Some Reflections on Forty Years of Research,” *Journal of Sound and Vibration*, Vol. 190, No. 3, 1996, pp. 299–315. <https://doi.org/10.1006/jsvi.1996.0066>.

- [4] Schloemer, H., "Effects of Pressure Gradients on Turbulent Boundary-Layer Wall-Pressure Fluctuations," *US Navy Underwater Sound Laboratory Report*, , No. 747, 1966. <https://doi.org/10.1121/1.1943059>.
- [5] Fritsch, D. J., Vishwanathan, V., Duetsch-Patel, J. E., Gargiulo, A., Lowe, K. T., and Devenport, W. J., "The Pressure Signature of Smooth Wall Turbulent Boundary Layers in Pressure Gradient Family," *AIAA Aviation Forum*, Reno, NV, USA, 15-19 June 2020. <https://doi.org/10.2514/6.2020-3066>.
- [6] Fritsch, D. J., Vishwanathan, V., Lowe, K. T., and Devenport, W. J., "The Space-Time Correlation of Pressure Under High Reynolds Number Smooth Wall Turbulent Boundary Layers in Pressure Gradient Family," *AIAA Science and Technology Forum*, Nashville, TN, USA, 11-21 January 2021. <https://doi.org/10.2514/6.2021-1946>.
- [7] Fritsch, D. J., Vishwanathan, V., Lowe, K. T., and Devenport, W. J., "Fluctuating Pressure Beneath Smooth Wall Boundary Layers in Non-Equilibrium Pressure Gradients," *AIAA Journal*, Vol. 60, No. 8, 2022, pp. 4725–4743. <https://doi.org/10.2514/1.J061431>.
- [8] Chase, D. M., "Modeling the Wavenumber-Frequency Spectrum of Turbulent Boundary Layer Wall Pressure," *Journal of Sound and Vibration*, Vol. 70, No. 1, 1980, pp. 29–67. [https://doi.org/10.1016/0022-460X\(80\)90553-2](https://doi.org/10.1016/0022-460X(80)90553-2).
- [9] Chase, D. M., "The Character of the Turbulent Wall Pressure Spectrum at Subconvective Wavenumbers and a Suggested Comprehensive Model," *Journal of Sound and Vibration*, Vol. 112, No. 1, 1987, pp. 125–147. [https://doi.org/10.1016/S0022-460X\(87\)80098-6](https://doi.org/10.1016/S0022-460X(87)80098-6).
- [10] Howe, M. S., *Acoustics of Fluid-Structure Interactions*, Cambridge University Press, 1998.
- [11] Goody, M., "Empirical Spectral Model of Surface Pressure Fluctuations," *AIAA Journal*, Vol. 49, No. 9, 2004, pp. 1788–1794. <https://doi.org/10.2514/1.9433>.
- [12] Rozenberg, Y., Robert, G., and Moreau, S., "Wall-Pressure Spectral Model Including the Adverse Pressure Gradient Effects," *AIAA Journal*, Vol. 50, No. 10, 2012, pp. 2168–2179. <https://doi.org/10.2514/1.J051500>.
- [13] Kamruzzaman, M., Bekiropoulos, D., Lutz, T., and Würz, W., "A semi-empirical surface pressure spectrum model for airfoil trailing-edge noise prediction," *International Journal of Aeroacoustics*, Vol. 14, 2015. <https://doi.org/10.1260/1475-472X.14.5-6.833>.
- [14] Catlett, M. R., Anderson, J. M., B., F. J., and Stewart, D. O., "Empirical Modeling of Pressure Spectra in Adverse Pressure Gradient Turbulent Boundary Layers," *AIAA Journal*, Vol. 54, No. 2, 2016, pp. 569–587. <https://doi.org/10.2514/1.J054375>.
- [15] Hu, N., and Herr, M., "Characteristics of wall pressure fluctuations for a flat plate turbulent boundary layer with pressure gradients," *22nd AIAA/CEAS Aeroacoustics Conference*, Lyon, France, 30 May - 01 June, 2016. <https://doi.org/10.2514/6.2016-2749>.
- [16] Hu, N., "Empirical spectral model of wall pressure fluctuations including adverse pressure gradient effects," *AIAA Aviation Forum*, Denver, CO, USA, 5-9 June, 2017. <https://doi.org/10.2514/6.2017-3203>.
- [17] Lee, S., "Empirical Wall-Pressure Spectral Modeling for Zero and Adverse Pressure Gradient Flows," *AIAA Journal*, Vol. 56, No. 5, 2018, pp. 1818–1829. <https://doi.org/10.2514/1.J056528>.

- [18] Hu, N., “Empirical model of wall pressure spectra in adverse pressure gradients,” *AIAA Journal*, Vol. 56, No. 9, 2018, pp. 3491–3506. <https://doi.org/10.2514/1.J056666>.
- [19] Balantrapu, N. A., Fritsch, D. J., Millican, A. J., Hickling, C., Gargiulo, A., Vishwanathan, V., Alexander, W. N., and Devenport, W. J., “Wall Pressure Fluctuations in an Axisymmetric Turbulent Boundary Layer,” *AIAA Science and Technology Forum*, Orlando, FL, USA, 6-10 Jan, 2020. <https://doi.org/10.2514/6.2020-0572>.
- [20] Blake, W. K., *Mechanics of Flow-Induced Sound and Vibration*, 1st ed., Academic Press, London, UK, 1986.
- [21] Parchen, R., “Progress Report DRAW: A Prediction Scheme for Trailing-Edge Noise Based on Detailed Boundary-Layer Characteristics,” *TNO Institute of Applied Physics*, , No. 980023, 1998.
- [22] Lee, Y.-T., Blake, W., and Farabee, T., “Modeling of Wall Pressure Fluctuations Based on Time Mean Flow Field,” *Journal of Fluids Engineering*, Vol. 127, 2005, pp. 233–240. <https://doi.org/10.1115/1.1881698>.
- [23] Lutz, T., Herrig, A., Würz, W., Kamruzzaman, M., and Krämer, E., “Design and Wind-Tunnel Verification of Low-Noise Airfoils for Wind Turbines,” *AIAA Journal*, Vol. 45, No. 4, 2007, pp. 779–785. <https://doi.org/10.2514/1.27658>.
- [24] Fischer, A., “Improvements of TNO type trailing edge noise models,” *European Journal of Mechanics B: Fluids*, Vol. 61, 2017, pp. 255–262. <https://doi.org/10.1016/j.euromechflu.2016.09.005>.
- [25] Grasso, G., Jaiswal, P., Wu, H., Moreau, S., and Roger, M., “Analytical Models of the Wall-Pressure Spectrum Under a Turbulent Boundary Layer,” *Journal of Fluid Mechanics*, Vol. 877, 2019, pp. 1007–1062. <https://doi.org/10.1017/jfm.2019.616>.
- [26] Duraisamy, K., “Perspectives on machine learning-augmented Reynolds-averaged and large eddy simulation models of turbulence,” *Phys. Rev. Fluids*, Vol. 6, No. 5, 2021, p. 050504. <https://doi.org/10.1103/PHYSREVFLUIDS.6.050504>.
- [27] Weatheritt, J., and Sandberg, R. D., “A novel evolutionary algorithm applied to algebraic modifications of the RANS stress-strain relationship,” *Journal of Computational Physics*, Vol. 325, 2016, pp. 22–37. <https://doi.org/10.1016/j.jcp.2016.08.015>.
- [28] Dominique, J., Christophe, J., Schram, C., and Sandberg, R. D., “Inferring empirical wall pressure spectral models with Gene Expression Programming,” *Journal of Sound and Vibration*, Vol. 506, 2021, p. 116162. <https://doi.org/10.1016/j.jsv.2021.116162>.
- [29] Vishwanathan, V., Fritsch, D. J., Lowe, K. T., and Devenport, W. J., “Analysis of Coherent Structures Over a Smooth Wall Turbulent Boundary Layer in Pressure Gradient Using Spectral Proper Orthogonal Decomposition,” *AIAA Aviation Forum*, 2-6 August, 2021. <https://doi.org/10.2514/6.2021-2893>.
- [30] Fritsch, D. J., Vishwanathan, V., Roy, C. J., Lowe, K. T., Devenport, W. J., Nishi, Y., Knopp, T., Ströer, P., Krumbein, A., Sandberg, R. D., Lav, C., Bensow, R. E., Eça, L., Toxopeus, S. L., Kerkvliet, M., Slama, M., and Bordier, L., “Experimental and Computational Study of 2D Smooth Wall Turbulent Boundary Layers in Pressure Gradient,” *AIAA Science and Technology Forum*, San Diego, CA, USA, 3-7 January 2022. <https://doi.org/10.2514/6.2022-0696>.

- [31] Fritsch, D. J., Vishwanathan, V., Lowe, K. T., and Devenport, W. J., “Surface Pressure Spectra Beneath High Reynolds Number Smooth and Rough Wall Boundary Layers in Pressure Gradients,” *University Libraries, Virginia Tech*, 2022. <https://doi.org/10.7294/20457189>, dataset.
- [32] McDaniel, D. R., and Tuckey, T. R., “HPCMP CREATE™-AV Kestrel New and Emerging Capabilities,” *AIAA Science and Technology Forum*, Orlando, FL, USA, 6-10 January 2020.
- [33] Menter, F. R., “Two-equation eddy-viscosity turbulence models for engineering applications,” *AIAA Journal*, Vol. 32, 1994, pp. 1598–1605. <https://doi.org/10.2514/3.12149>.
- [34] *ANSYS CFX-Solver Theory Guide*, ANSYS Inc., Canonsburg, PA, USA, 2009. Release 12.0.
- [35] Joseph, L. A., “Pressure Fluctuations in a High-Reynolds-Number Turbulent BOUNDARY Layer over Rough Surfaces of Different Configurations,” Ph.D. thesis, Virginia Polytechnic Institute and State University, 2017.
- [36] Ferreira, C., “Gene Expression Programming: A New Adaptive Algorithm for Solving Problems,” *Complex Systems*, Vol. 13, No. 2, 2001, pp. 87–129. <https://doi.org/10.48550/arXiv.cs/0102027>.
- [37] Gonzalex, A. J., “A Computational Analysis of Bio-Inspired Modified Boundary Layers for Acoustic Pressure Shielding in a Turbulent Wall Jet,” Master’s thesis, Florida Atlantic University, 2019.
- [38] von Kármán, T., “Progress in the statistical theory of turbulence,” *Proceedings of the National Academy of Sciences*, Vol. 34, 1948, pp. 530–539.
- [39] Liepmann, H. W., Laufer, J., and Liepmann, K., “On the spectrum of isentropic turbulence,” *NACA Technical Reports*, 1951.
- [40] Wilson, D. K., “A Three-Dimensional Correlation/Spectral Model for Turbulent Velocities in a Convective Boundary Layer,” *Boundary-Layer Meteorology*, Vol. 85, 1997, pp. 35–52. <https://doi.org/10.1023/A:1000418709945>.
- [41] Kamruzzaman, M., Lutz, T., Herrig, A., and Krämer, E., “Semi-Empirical Modeling of Turbulent Anisotropy for Airfoil Self-Noise Prediction,” *Proceedings of the 16th AIAA/CEAS Aeroacoustics Conference*, Stockholm, Sweden, 7-9 June, 2010. <https://doi.org/10.2514/6.2011-2734>.
- [42] DeGraff, D. B., and Eaton, J. K., “Reynolds-number scaling of the flat-plate turbulent boundary layer,” *Journal of Fluid Mechanics*, Vol. 422, 2000, pp. 319–346. <https://doi.org/10.1017/S0022112000001713>.
- [43] Kamruzzaman, M., Lutz, T., Würz, W., and Krämer, E., “On the Length Scales of Turbulence for Aeroacoustic Applications,” *Proceedings of the 17th AIAA/CEAS Aeroacoustics Conference*, Portland, OR, USA, 5-8 June, 2011. <https://doi.org/10.2514/6.2011-2734>.
- [44] Wilcox, D. C., *Turbulence Modeling for CFD*, 1st ed., DCW Industries, La Cañada, CA, USA, 1993.
- [45] Spalart, P., and Allmaras, S., “A one-equation turbulence model for aerodynamic flows,” *AIAA Sciences Meeting*, American Institute of Aeronautics and Astronautics, 1992. <https://doi.org/10.2514/6.1992-439>.

- [46] Michel, R., Quemard, C., and Durant, R., “Hypotheses on the mixing length and application to the calculation of turbulent boundary layers,” *Proceedings on Computational Turbulent Boundary Layers*, Vol. 1, 1968, pp. 195–207.
- [47] Herr, M., “Broadband Trailing-Edge Noise as a Canonical Problem for Airframe Noise Predictions,” *19th Workshop of the Aeroacoustics Specialists’ Committee of CEAS*, La Rochelle, France, 22 September 2015. URL <https://elib.dlr.de/98665/>.
- [48] Lane, G., Sidebottom, W., and Croaker, P., “Application of Wall-Modelled LES to the Prediction of Turbulent Flow Noise,” *Proceedings of Acoustics 2021*, Wollongong, Australia, 8-10 Nov, 2021.

Chapter 7

Modeling the Surface Pressure Spectrum on Rough Walls in Pressure Gradients

This chapter presents a manuscript currently under review in *AIAA Journal* on the modeling of the pressure spectrum beneath rough wall boundary layers. This is a continuation of Chapter [6](#).

Attributions

Daniel J. Fritsch is the primary contributor and first author. All text and figures are his original work.

Vidya Vishwanthan, K. Todd Lowe, and William J. Devenport supported and advised the gathering of experimental data.

Christopher J. Roy advised the generation of computational data.

Modeling the Surface Pressure Spectrum on Rough Walls in Pressure Gradients

Daniel J. Fritsch*, Vidya Vishwanathan[†], Christopher J. Roy[‡], K. Todd Lowe[†], and William J. Devenport[§]
Virginia Tech, Blacksburg, VA, 24060

Models, both existing and newly proposed, for rough wall boundary layer flows and their underlying surface pressure spectra are assessed, particularly within the framework of spectral prediction from steady, Reynolds-Averaged-Navier-Stokes (RANS) data. Recent updates in roughness boundary conditions for RANS are shown to improve qualitative trends between roughness function and roughness Reynolds number, but model-to-model discrepancies remain and the true sandgrain roughness height does not produce a match in the flow data, requiring *posteriori* adjustment to the boundary condition to match with experiment. Existing empirical models for the surface pressure spectrum show good agreement in some spectral regions, but not all, while a newly proposed model shows good matching across the spectrum in a variety of pressure gradient conditions. Adjustments are made to existing TNO analytical models based on the pressure Poisson equation to incorporate rough wall effects, including changes to the velocity spectrum model and the inclusion of a wall-shift, shown to be independent of local Reynolds number, pressure gradient, or turbulence model. The mathematical character of the rough wall spectrum has been revealed, but challenges remain to implement both flow and spectral modeling with computational fluid dynamics without *a priori* knowledge of the flow.

I. Nomenclature

c_f	=	skin friction coefficient
G_{pp}	=	autospectral density of pressure ((f) Pa^2/Hz , (ω) Pa^2s/rad)
h	=	tunnel height, = $1.85m$
K	=	wavenumber magnitude (m^{-1})
k	=	turbulent kinetic energy (m^2/s^2)
K_i	=	i^{th} wavenumber component (m^{-1})
k_g	=	geometric roughness height (m)

*Graduate Research Assistant, Crofton Dept. Aerospace and Ocean Engineering, AIAA Student Member. Correspondence: dannyf96@vt.edu

[†]Graduate Research Assistant, Crofton Dept. Aerospace and Ocean Engineering, AIAA Student Member.

[‡]Professor, Crofton Dept. Aerospace and Ocean Engineering, AIAA Associate Fellow.

[§]Professor, Crofton Dept. Aerospace and Ocean Engineering, AIAA Fellow.

k_0	= hydrodynamic roughness height (m)
k_s	= equivalent sandgrain roughness height (m)
k^+	= roughness Reynolds number, $= \rho k_s u_\tau / \mu$
p	= pressure (Pa)
q	= dynamic pressure, $= 1/2 \rho U_e^2$ (Pa)
Re	= Reynolds number
R_T	= time scale ratio, $= (\rho \delta u_\tau / \mu) \sqrt{c_f / 2}$
u	= velocity (m/s)
\bar{U}	= Zagarola & Smits velocity scale, $= U_e (1 - \delta^* / \delta)$ (m/s)
U_c	= convection velocity (m/s)
U_e	= edge velocity (m/s)
u_τ	= friction velocity (m/s)
u_v	= modified friction velocity (m/s) [1]
u^+	= viscous normalized velocity, $= u / u_\tau$
x	= spatial coordinate (m)
y	= wall normal coordinate (m)
y^+	= viscous normalized wall distance, $= y u_\tau / \nu$
β	= Clauser parameter, $= (\delta^* / \tau_w) (dp / dx)$
δ	= boundary layer thickness (m)
δ^*	= displacement thickness (m)
Δu^+	= roughness function
θ	= momentum thickness (m)
Λ	= integral length scale (m)
μ	= dynamic viscosity (kg/ms)
$\tilde{\nu}$	= Spalart-Allmaras working variable [2]
ρ	= density (kg/m^3)
ϕ_{ij}	= Spectral density of variables i, j
τ_w	= wall shear stress (Pa)
ω	= specific dissipation rate (s^{-1}) or frequency (rad/s)

II. Introduction

TURBULENT boundary layers are ubiquitous in fluids engineering problems. Beneath a turbulent boundary layer, the immersed surface experiences a fluctuating pressure that is a complex function of the turbulence throughout the flow above, and this fluctuating surface pressure can fatigue that surface and radiate noise both into the structure and outward to the far-field. The statistical behavior of these pressure fluctuations is difficult to understand and model, particularly when considering non-canonical and potentially non-equilibrium effects such as curvature, pressure gradient, and surface roughness, effects that must be considered to extend any modeling capability to real-world problems.

The general effect of surface roughness on the boundary layer is to thicken this region of the flow and intensify the turbulent energy within, increasing the skin friction drag on the surface [3–8]. The roughness effect is primarily characterized by a distinctive downward shift in the viscous-normalized velocity profile, known as the roughness function, Δu^+ . For a fully rough flow, the roughness function is directly proportional to the roughness Reynolds number, k^+ , where flows of $k^+ > 25$ can be considered fully rough [7]. The exact nature of the relationship between a given rough surface and the overlying boundary layer flow is still under investigation, but rough wall flows show certain simplifications that aid in their understanding and modeling, most notably Townsend’s Outer Layer Reynolds Number Similarity Hypothesis, which states that the effect of the roughness is confined to the very-near-wall region (beneath the canopy, within a few roughness heights of the wall), and the boundary layer above will show Reynolds number similarity [9], for which there is a great deal of evidence [8, 10, 11]. The effects of pressure gradient on rough wall flows differ only slightly from those on smooth walls; adverse (increasing) pressure gradient (APG) thickens and intensifies the boundary layer, pushing it towards separation [12, 13] while favorable (decreasing) pressure gradient (FPG) compresses the boundary layer and pushes the turbulence towards re-laminarization; however, in a rough wall flow full re-laminarization is not possible as the acceleration of the flow at the roughness canopy intensifies the near-wall turbulence and effectively makes the flow "rougher" [14–16].

Modeling rough wall flows is notoriously difficult. It is not effective or efficient to geometrically model roughness in the grid for a Reynolds-Averaged-Navier-Stokes (RANS) simulation; instead, the roughness effect is typically modeled by a modification to the wall boundary condition that attempts to correlate the wall-bounded turbulence parameters to the $k^+ \rightarrow \Delta u^+$ relation [17–19]. These models are known to be well correlated to the correct roughness function at lower values of k^+ , but fall off the correct curve at higher values, requiring correction [11, 20, 21]. It is also common, particularly in marine applications, to instead use wall-functions to enforce the "correct" velocity profile over the rough surface, but these models have a variety of issues, particularly in pressure gradient [22, 23].

The effect of roughness on the autospectrum of the surface pressure fluctuations is comparable to that of the turbulence above, characterized most notably by an increase in the peak energy [24, 25]. This increase is correlated with k^+ , but its exact relationship with the roughness geometry is still unclear [1, 26, 27]. It has been repeatedly observed that the high frequency portion of the smooth wall spectrum is universal on viscous scaling [28, 29], and Meyers *et al.*

(2015) postulated that the same ought to be true for a rough wall, but on a modified shear velocity, u_v [1]. The original Meyers *et al.* formulation was limited to *posteriori* matching, but Joseph (2017) showed that u_v exhibits consistent behavior across many rough surfaces and can be predicted *a priori* [27]. The mid-frequency then connects the enlarged peak to the universal high frequency roll-off via a slope that steepens as a function of k_s , though Meyers *et al.* suggest the slope should asymptote to $\omega^{-4/3}$ for fully rough flows [1], which has some experimental support [11, 27]. The effect of pressure gradient on smooth wall pressure spectra is complex and driven by history dependence [29, 30], but is significantly simplified beneath rough wall flows [11]. Fritsch *et al.* (2022) proposed that rough wall pressure spectra in pressure gradient are fully described on a single, outer-variable scaling that accounts for roughness, pressure gradient, and pressure gradient history effects [11].

Modeling the pressure spectrum beneath zero pressure gradient (ZPG) smooth wall flows is fairly straightforward [31, 32]; however, accounting for the complex effects of pressure gradient with empirical models is difficult [32]. Analytical formulations for the pressure spectrum can be derived from the Navier-Stokes momentum equation assuming incompressible flow with no body forces, the boundary layer assumptions, and that the pressure fluctuation sources can be considered to exist in otherwise homogeneous wall-parallel planes, the most common of which is the TNO-Blake model, though updates have been proposed by several authors [33–36], and such models show an enhanced ability to capture pressure gradient effects accurately and robustly [32].

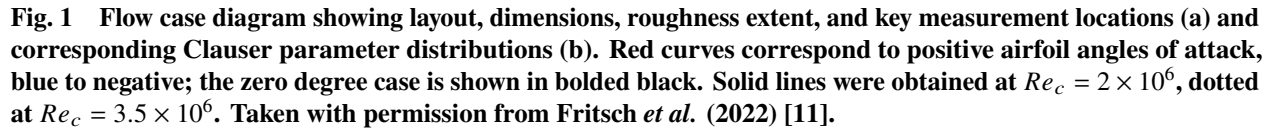
There are fewer models explicitly developed for the pressure spectrum beneath rough walls in the literature. Two empirical models exist that are extensions of the original Goody (2004) formulation [37, 38], however, no significant progress has been made on extending the analytical formulation to rough wall flows.

This paper will explore the predictive modeling of rough wall flows in pressure gradients and their underlying surface pressure spectra. These efforts are centered around a validation database to be discussed in the next section and using the numerical RANS predictions described in Section IV. The modeling of the flow will be discussed in Section V, followed by an extended discussion of pressure spectrum modeling, both empirical in Section VI and analytical in Section VII. Existing models will be assessed for their accuracy and robustness and new modeling ideas are proposed that show improvement over the existing state-of-the-art. Finally, conclusions will be drawn in Section VIII.

III. Flow Case

The flow case to be considered is a nominally 2D rough wall turbulent boundary layer subjected to a systematic family of continually varying, bi-directional pressure gradient cases. These pressure gradient cases are generated experimentally in the Virginia Tech Stability Wind Tunnel (VTSWT) by observing the port side wall boundary layer while a NACA0012 airfoil section is mounted across the full height of the tunnel. The presence of the airfoil generates the pressure gradient distributions on the wall as shown in Fig. 1. Figure 1a shows a diagram of the test layout including the extent of the rough surface, the key dimensions, and the locations of primary measurements and Fig. 1b shows the

The schematic diagram illustrates the experimental setup. A free stream velocity U_∞ flows from left to right. The flow passes through a curved inlet section with a length of 3.58 m, followed by a long straight section of 7.32 m. At the bottom, a rough wall is located at a height of 1.85 m. The roughness elements are represented by vertical bars along the x-axis. The distance from the start of the rough wall to the center of the NACA 0012 airfoil is 3.44 m. The airfoil has a thickness of 0.914 m. The rough wall consists of several rows of roughness elements with varying heights and spacings. The distances between the centers of the roughness elements are labeled as 1.25 m, 1.86 m, 2.47 m, 3.08 m, 3.69 m, 4.30 m, and 4.91 m. The total length of the rough wall section shown is 5.43 m. A trip is indicated at the inlet of the rough wall section.



The rough surface in question is a uniform, staggered array of circular cylinders of height $k_g = 2 \times 10^{-3} m$ and aspect ratio $k_g/d = 0.637$, as described by Fritsch *et al.* (2022) [11]. Based on observations of the roughness function, it was

determined that the surface had a constant, pressure gradient and Reynolds number independent equivalent sandgrain roughness of $k_s = 1.65k_g = 3.3 \times 10^{-3}m$, resulting in a range of roughness Reynolds numbers from $300 < k^+ < 890$. These flows are high k^+ cases, deep into the fully rough asymptotic regime, and representative of the physics of high Reynolds number rough wall flows that might be found on marine vehicles.

By varying flow speed and model angle of attack, a database of 168 pressure spectra were measured on the rough wall, which are available as a public-domain repository [44]. For the sake of brevity, we will focus on four primary cases, all at a free-stream Reynolds number of $Re_c = 2.0 \times 10^6$:

- 1) $x/h = 0.676, \alpha = 12^\circ$: \approx ZPG
- 2) $x/h = 1.34, \alpha = 12^\circ$: APG
- 3) $x/h = 1.34, \alpha = -10^\circ$: FPG
- 4) $x/h = 1.99, \alpha = 12^\circ$: APG-FPG cross-over

IV. Numerical Methods

Compressible, steady RANS simulations were performed in HPCMP-CREATE-AV Kestrel KCFD, an unstructured finite volume solver. The computational domain is a fully structured 2D grid with a no-slip-wall condition on the wall of interest and a slip-wall condition opposite, with the slip-wall set at a 0.46° angle to replicate the background FPG due to the increasing blockage ratio of the tunnel as boundary layers grow on all walls as shown in Fig. 2. The inflow length is a smooth wall condition of a length set to match the boundary layer parameters at the most upstream measurement plane, and the simulated rough wall begins at the same distance upstream of the airfoil model as in the experiment, i.e., beginning at $x = 0$. Computations of the smooth wall have been rigorously assessed [42]. Preliminary rough wall calculations have been performed, but it was clear that changes would be required to the boundary condition modeling for more rigorous assessment [11].

Kestrel uses two types of roughness boundary condition; for two-equation models, a Wilcox-style approach is used, whereby the specific dissipation rate, ω , at the wall is prescribed as a function of k^+ [17, 18]. For the Spalart-Allmaras (SA) [2] model, a modified Boeing approach [19] is used, whereby the wall distance is augmented and changes are made to various model coefficients as a function of k_s .

Each simulation is performed with a uniform, constant stagnation properties inlet ($p_0 = 94.92kPa, T_0 = 284.7K$) and constant static pressure outlet ($p = 94.27kPa$), set to match the experimentally measured Reynolds number at the most upstream measurement plane. Free-stream turbulence levels were defined at 0.02%, based on measurements made in the VTSWT [45]. As described by Fritsch *et al.* (2022), solutions were obtained on five systematically refined grid levels, and the medium grid (level 3 of 5) was used for the bulk of the simulations [42].

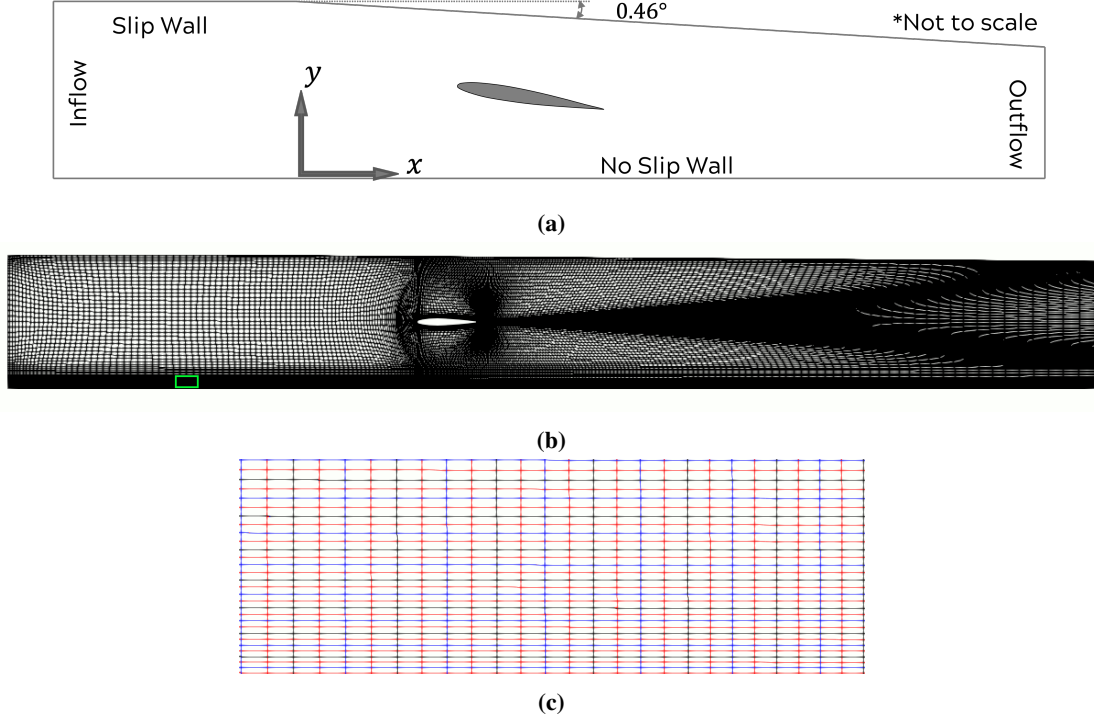


Fig. 2 Computational domain layout (a), coarse grid (b), zoomed view of fine —, medium —, and coarse — grids (c). Taken with permission from Fritsch *et al.* 2022 [42]

V. Flow Modeling

Acceptably accurate flow modeling is a critical aspect of predicting the pressure spectrum. A perfect pressure spectrum model will not give an accurate prediction if the flow-dependent inputs to said model cannot be predicted. Thus, while flow modeling is not the focus of this paper, it deserves careful attention, particularly in light of recent advances in rough wall RANS modeling.

A. Spalart-Allmaras

The original Spalart-Allmaras (SA) roughness modification is given by Aupoix & Spalart (2003) [19]. Aupoix & Spalart's boundary condition modifies some of the SA model coefficients as functions of k_s and changes the boundary condition of the SA working variable, $\tilde{\nu}$, from a constant zero to an enforced wall-normal gradient that is a function of k_s . Results obtained in KCFD using this model are shown in Fig. 3 in the red triangles, and suffer from non-physical asymptotic behavior at high values of $k^+ > 100$. To eliminate the asymptote, and based on the observations of Aupoix (2014) [21], the wall boundary condition is replaced with an enforced value for $\tilde{\nu}$ in the first cell from the wall based on a displaced y^+ value as a function of k^+ . Results obtained using the updated boundary condition are shown in Fig. 3 in blue diamonds and show much improved agreement with the benchmark sandgrain roughness data of Nikuradse (1950) [3] with increasing roughness Reynolds number.

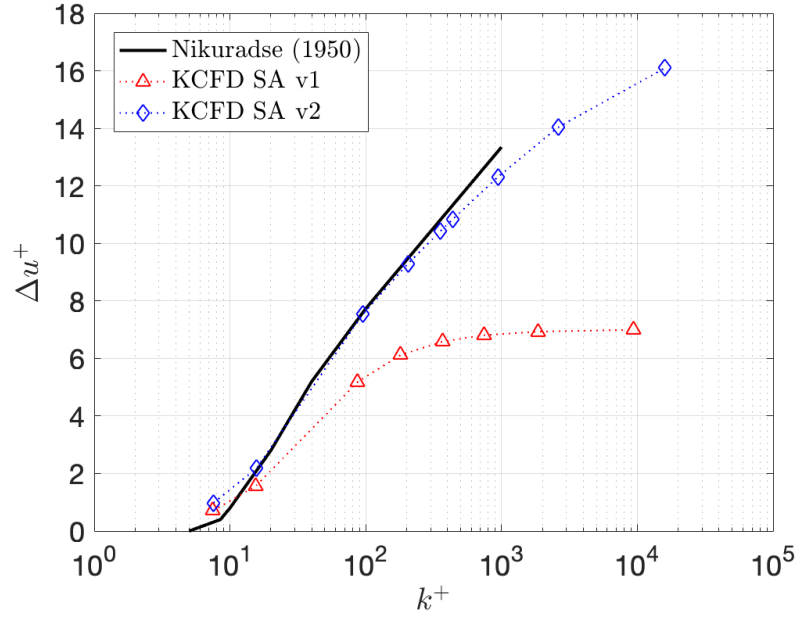


Fig. 3 Roughness function as a function of roughness Reynolds number for new and old Spalart-Allmaras boundary conditions compared with data of Nikuradse (1950) [3].

Roughness Reynolds number sweeps for the ZPG case were performed in two ways: first, by holding the free-stream Reynolds number constant at $Re_c = 2 \times 10^6$ and increasing k_s from $0.05k_g$ to $100k_g$, and then by holding k_s constant at $1.65k_g$ and increasing the Reynolds number from 0.5×10^6 to 5.0×10^6 . These results are shown in Fig. 4; the trend of Δu^+ with k^+ is the same for both manners of increasing k^+ . This consistency is critical for validating that the model captures a true k^+ dependence rather than a k_s or Re dependence that are independent of each other, which would not be consistent with experimental observations of rough wall behavior.

Townsend's Hypothesis [9] suggests that, above the canopy, the velocity profiles over flows of constant k_s should collapse universally on an outer layer defect scaling. Similarly, this implies that the integrated thicknesses, δ^* and θ ought to be Reynolds number independent, and thus the velocity profile should be universal on outer variables, i.e., u/U_e vs. y/δ independent of Reynolds number. As shown in Fig. 5, with sweeping free-stream Reynolds number at constant k_s , the updated SA model shows excellent agreement between all KCFD simulations and the experimental data above $y/\delta = 0.01$. Below this value, which is inside the canopy for all flows, there is some variation in the velocity profiles between Reynolds numbers, but this behavior does not invalidate the results above.

Despite the consistent behavior with Reynolds number, both roughness and free-stream, the SA model does not predict the correct roughness function at the experimentally measured k_s of $1.65k_g$. For the purposes of developing pressure spectrum models, it is important to have simulated data that matches the roughness behavior observed experimentally, and so the simulation k_s value was tuned to produce the correct Δu^+ , and it was found that the associated

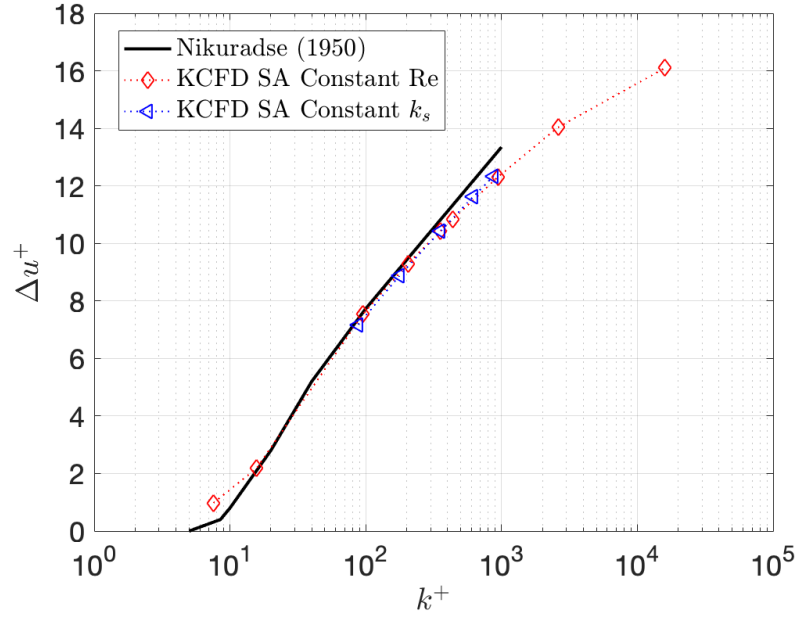


Fig. 4 Roughness function as a function of roughness Reynolds number for constant Reynolds number, increasing k_s and constant k_s , increasing Reynolds number compared with data of Nikuradse (1950) [3].

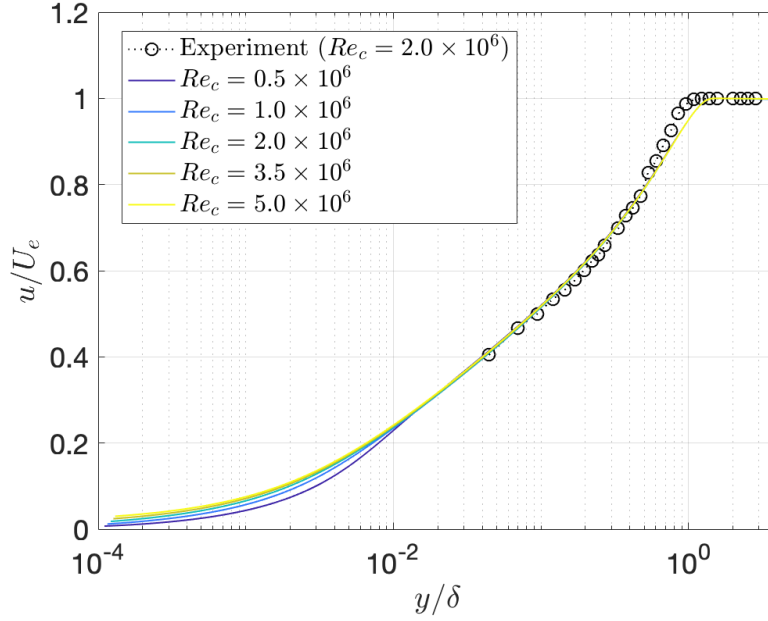


Fig. 5 Outer normalized velocity profiles as measured experimentally and as simulated with SA model with constant k_s and increasing free-stream Reynolds number.

value for k_s was $2.5k_g$. A comparison of the viscous-normalized velocity profiles between the experiment, original KCFD, and tuned KCFD results is shown in Fig. 6.

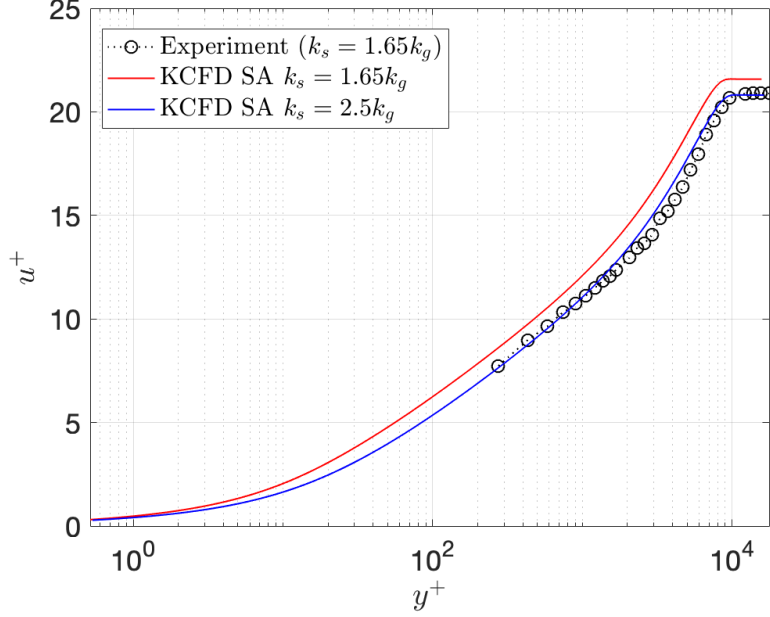


Fig. 6 Viscous normalized velocity profiles as measured experimentally and as simulated with SA model using experimental k_s and k_s tuned to match Δu^+ .

B. Menter SST

The original k - ω roughness boundary condition was given by Wilcox (1988) [17], which was updated in 2006 [18]. The Wilcox model sets a specific dissipation rate wall boundary condition, ω_{wall} , as a function of k^+ . The original KCFD k - ω roughness condition functioned similarly, using a different specific equation for the $\omega_{wall}(k^+)$ relation. As observed by Fritsch *et al.* (2022) [11] and as shown in Fig. 7 in the red circles, this model produced an asymptote at high k^+ similar to the original SA model. The asymptote was eliminated by adopting a modified version of the Aupoix (2014) wall boundary condition [21], which sets a value for ω_{wall} but also shifts the wall by a function of Δu^+ , effectively enforcing a given $\Delta u^+ \propto k^+$ relationship. Results using the updated model are shown in Fig. 7 in the blue squares and show improved behavior at higher k^+ values. Unlike the SA model, the SST model does not match the data of Nikuradse (1950) [3], running parallel to the Nikuradse curve but not falling directly on it. Additionally, at very high k^+ , the SST model loses its constant slope and begins to approach what may be another asymptote, albeit at much higher and less physically relevant values of k^+ .

As with the SA model, a comparison was made of the Δu^+ vs. k^+ relationship when altering k^+ both by changing k_s and by changing Re_c for the ZPG case. Unlike the SA model, the SST model shows varying behavior between the two methods. When holding k_s constant and sweeping Re_c , the curve holds its constant slope to higher values of k^+ and does not show signs of deviating within the tested range.

The SST model does show outer-layer similarity, but only for the three highest tested Reynolds numbers. At the

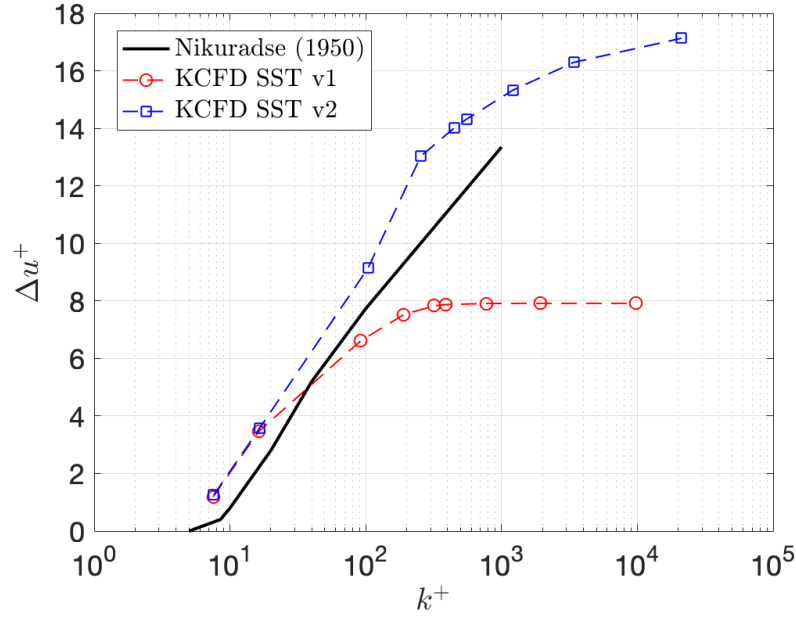


Fig. 7 Roughness function as a function of roughness Reynolds number for new and old Menter SST boundary conditions compared with data of Nikuradse (1950) [3].

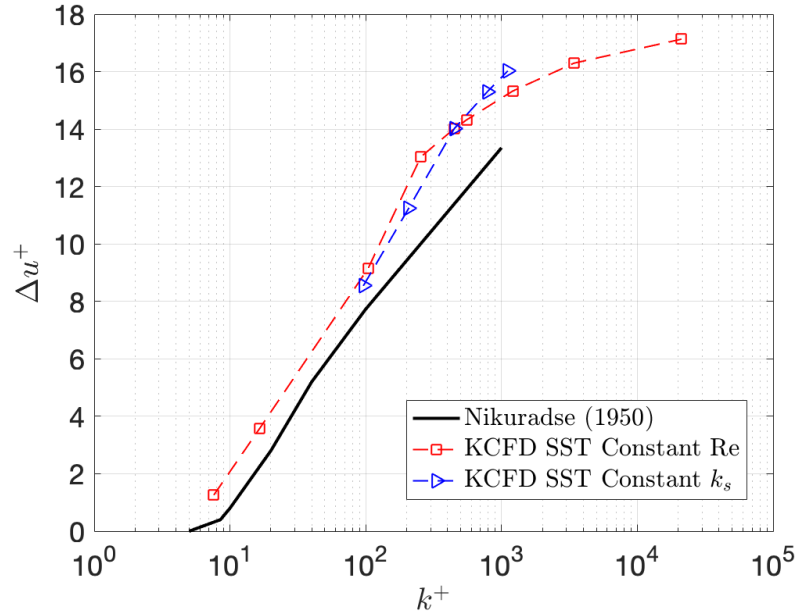


Fig. 8 Roughness function as a function of roughness Reynolds number for constant Reynolds number, increasing k_s and constant k_s , increasing Reynolds number compared with data of Nikuradse (1950) [3].

two lower Reynolds numbers, there remains some outer-normalized Reynolds number dependence. Additionally, the self-similar curve observed at the higher Reynolds numbers does not match with the experimental data as the SA model did, showing lower values of u/U_e for a given value of y/δ .

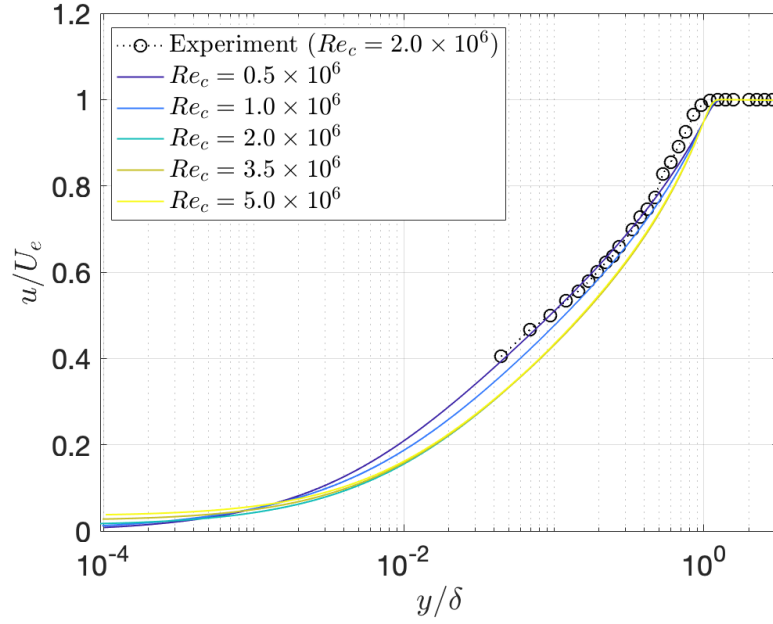


Fig. 9 Outer normalized velocity profiles as measured experimentally and as simulated with SST model with constant k_s and increasing free-stream Reynolds number.

As with the SA model, the roughness function does not match between experiment and simulation at the same value of k_s . The SST model is also tuned to match Δu^+ , achieving this match at a k_s value of $0.85k_g$.

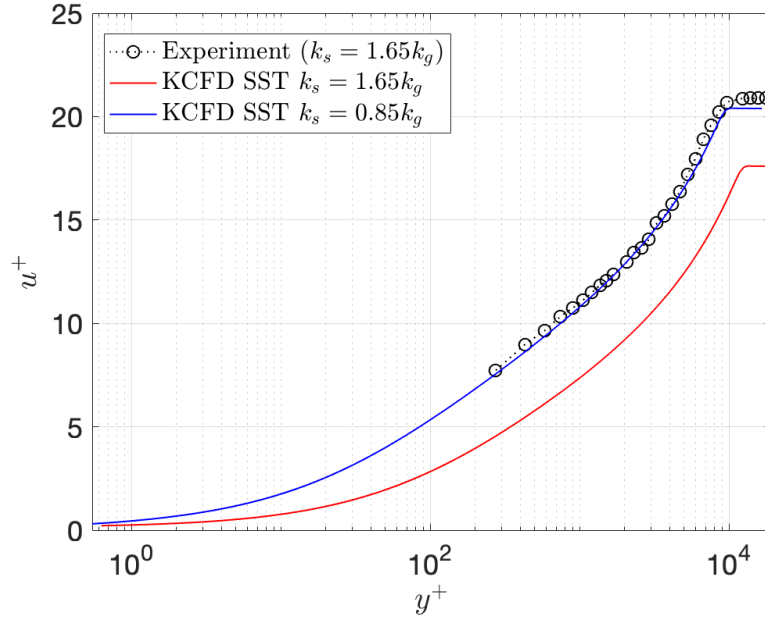


Fig. 10 Viscous normalized velocity profiles as measured experimentally and as simulated with SST model using experimental k_s and k_s tuned to match Δu^+ .

In general, the updated Spalart-Allmaras model shows more accurate and consistent results than the updated Menter SST model. However, analytical pressure spectrum models require details of the Reynolds stress tensor that are more easily obtained using a two-equation model and so both models will be considered in the remainder of the paper.

VI. Empirical Pressure Spectrum Modeling

A. Review of Existing Models

The most well-known empirical spectrum model is that of Goody (2004), which defines a model equation for the classical form of the spectrum [31]. Several empirical models have been proposed that employ the generalized form of Goody's model:

$$G_{pp}(\omega)SS = \frac{a(\omega FS)^b}{[(\omega FS)^c + d]^e + [fR_T^g(\omega FS)]^h} \quad (1)$$

where FS and SS are the frequency and spectral normalizing scalings respectively and $a-h$ are model coefficients. The majority of models in the literature are tuned for smooth walls in adverse pressure gradient, but two models have recently been proposed for rough walls in zero pressure gradient.

Catlett *et al.* (2022) proposed updates to the a , c , d , and f coefficients as functions of the roughness effect, quantified by the parameter $k^+U_e^+$ [37]. They observed that the Goody model coefficients followed roughly power-law behavior with this parameter, enabling the tuning of the coefficients for rough wall flows shown in Table 1.

Joseph *et al.* (2022) observed that predominant effect of roughness was captured in a steepening mid-frequency slope, which was correlated to the Zagarola & Smits velocity scale, \bar{U} [46], and the ratio k_g/δ [38]. Meanwhile, the high frequency behavior was observed to be driven by the Meyers *et al.* modified shear velocity [1]. Correlations observed across a wide variety of rough surfaces were exploited to tune the Goody model coefficients, shown in Table 1.

B. New Model

Fritsch *et al.* (2022) observed that high k^+ rough wall flows scaled on outer variables across the entire spectrum independent of pressure gradient, as shown in Fig. 11 [11]. The existence of such a universal scaling implies the validity of a simple, Goody-style model that fully describes these spectra without the need for flow-dependent coefficients, which are known to come with the risk of non-physical behavior [32].

The a coefficient was reduced from 3.0 to 0.0007 to account for the changing of the pressure scaling from τ_w to q ($0.0007/3 \approx \tau_w^2/q^2$). The b coefficient was reduced from 2.0 to 1.0 both to better match experimental data (though it is not certain if the reduced low frequency slope is a consequence of physics or acoustic contamination) and to facilitate the steepening of the mid-frequency slope. Similarly, the c coefficient was increased from 0.75 to 0.85 to further steepen the slope. The d and e coefficients were unchanged as it was found that adjustment of the c parameter was sufficient to

adjust the mid-frequency slope. No Reynolds number dependence was observed in the high frequency roll-off, and so the Reynolds number dependence was dropped, replacing $f R_T^g$ in the second term of the denominator with a single coefficient set to 0.1183. The lack of Reynolds number dependence on a purely outer scaling is reminiscent of the same observation in the mean velocity profiles (Figs. 5 and 9). This suggests that Townsend's hypothesis holds for the statistics of the fluctuating pressure on the wall for fully rough flows. As shown in Fig. 11, this updated model is well fit to the scaled experimental data.

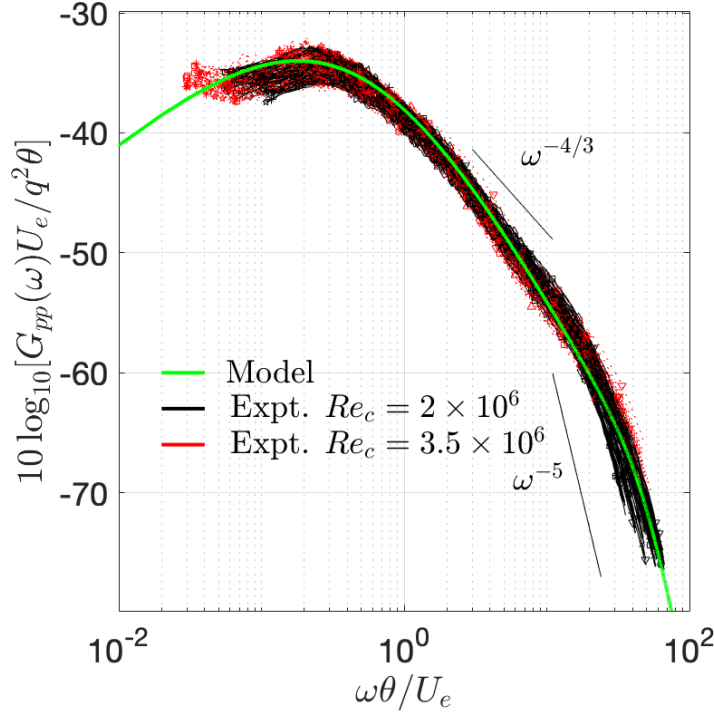


Fig. 11 Proposed empirical pressure spectrum model shown against experimental data of Fritsch *et al.* (2022) [11].

Additionally, the new proposed scaling and subsequent model are compared with the data of Joseph (2017) [27], which represents a large variety of rough surface configurations, in Fig. 12. Data is compared across two Reynolds numbers and three rough surfaces, cylinders, densely-spaced hemispheres, and intermediate-spaced hemispheres. Despite the variety in Reynolds number, roughness shape, and roughness density, the Joseph data shows a similar spread under this scaling as was observed in the current data in Fig. 11 and, thus, the newly proposed model predicts these spectra with comparable accuracy.

C. Results

Figure 13 shows the spectral predictions from all three rough wall empirical models using both turbulence models compared to experimental data for the four primary conditions: ZPG, APG, FPG, and APG-FPG cross. In ZPG, the new

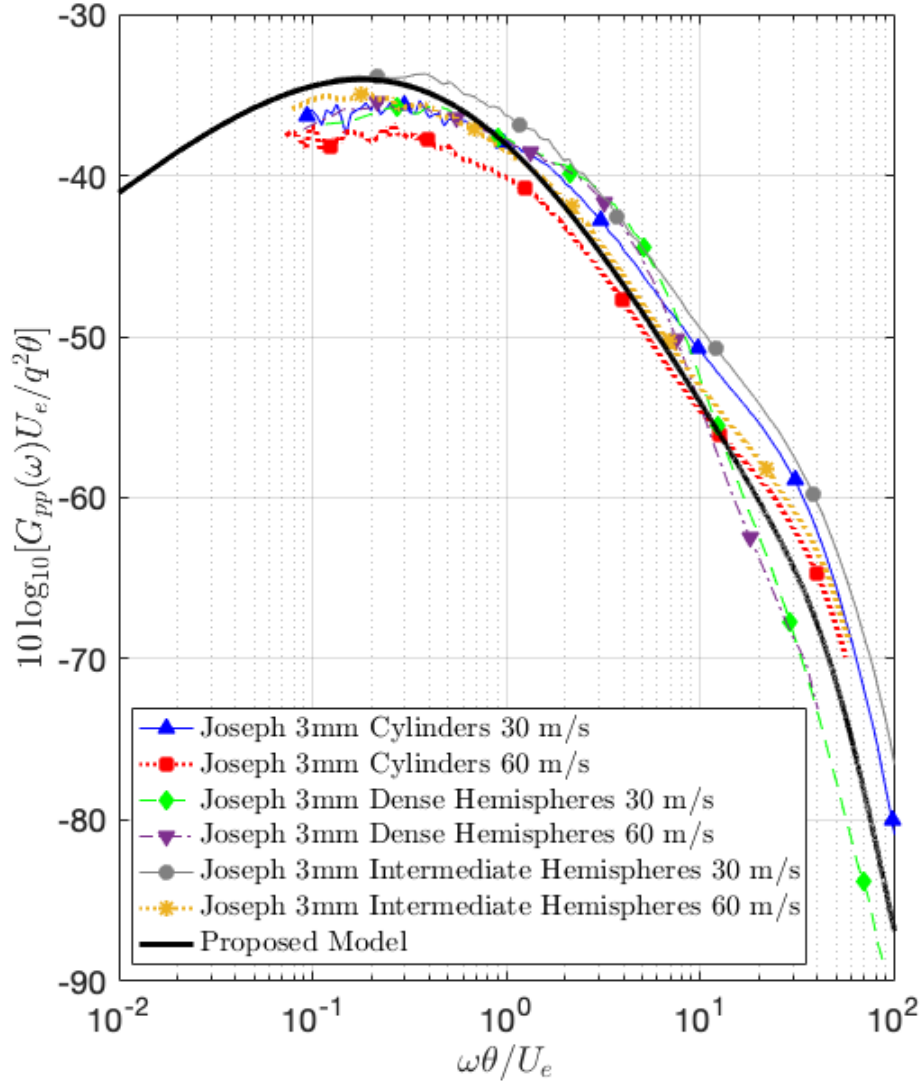


Fig. 12 Newly proposed model compared with data of Joseph (2017) [27] for various rough surfaces and Reynolds numbers.

model shows the most accurate overall prediction, particularly using the SA model, which better matches the peak than SST. The Joseph *et al.* model shows better agreement than the Catlett *et al.* model at low frequencies, but worse at high frequencies. The Catlett *et al.* model is more sensitive to turbulence model at high frequencies than the others. The model-to-model trends are the same in APG.

In FPG, all models suffer compared to the ZPG and APG predictions, which was also observed with smooth wall empirical models in FPG [32]. The peak is suppressed in all models, though the new model with SA data retains the most accurate shape in this region. In FPG, the Catlett *et al.* and Joseph *et al.* models now show the same peak behavior. In the non-equilibrium, APG-FPG cross case, the new model now slightly over-predicts the peak and the Joseph *et al.*

Coefficient	Goody [31]	Catlett [37]	Joseph [38]	New Model
a	3.0	$3.0 + 1.028(k^+ U_e^+)^{0.426}$	$\frac{u_\tau}{U_e - \bar{U}} \frac{u_\tau}{u_v}$	0.0007
b	2.0	2.0	2.0	1.0
c	0.75	$0.75 + 0.059(k^+ U_e^+)^{0.329}$	$0.56(\frac{\bar{U}}{U_e})^{-1.63}$	0.85
d	0.5	$0.5 + 0.126(k^+ U_e^+)^{0.317}$	1.5	0.5
e	3.7	3.7	5.0	3.7
f	1.1	$1.1 + 0.761(k^+ U_e^+)^{0.368}$	$\frac{U_e - \bar{U}}{u_v}$	0.1183
g	$-\frac{4}{7}$	$-\frac{4}{7}$	$-\frac{4}{7} - 0.24(\frac{k_s}{\delta})^{0.16}$	0
h	7.0	7.0	7.0	7.0
FS	δ/U_e	δ/U_e	δ/\bar{U}	θ/U_e
SS	$\frac{U_e}{\tau_w^2 \delta}$	$\frac{U_e}{\tau_w^2 \delta}$	$\frac{\bar{U}}{(U_e - \bar{U})^4 \rho^2 \delta}$	$\frac{U_e}{q^2 \theta}$

Table 1 Coefficients for Goody style model (Eq. 1) for Goody [31], Catlett *et al.* [37], Joseph *et al.* [38], and new proposed models.

model shows the most accurate peak, though the mid-frequency slope is too steep and the accuracy rapidly drops off.

In general, the Catlett *et al.* model is unable to replicate a sufficiently steep mid-frequency slope, but shows good behavior in the high-frequency roll-off when using SST, but not with the SA data. The variation with turbulence model is concerning and is hypothesized to come from the different k_s values required for each model to generate the correct roughness function and the different relationships between the roughness function and Reynolds number. The Joseph *et al.* model shows better behavior at the peak, but over-predicts the mid-frequency slope, which is hypothesized to be due to the very high values of k^+ in this experimental case, higher than those studied by Joseph *et al.*, thus driving up the slope. The new model shows better predictions across all spectral regions and pressure gradient cases, but it must be noted that the model was developed from these data.

VII. Analytical TNO Modeling

The general basis for the following analytical modeling is that of Grasso *et al.* (2019) [36], who presented an updated framework based on the original TNO model of Parchen [34] for modeling the spectrum from the pressure Poisson equation (PPE):

$$\frac{1}{\rho} \nabla^2 p' = -2 \frac{\partial u'_j}{\partial x_i} \frac{\partial U_i}{\partial x_j} - \frac{\partial^2}{\partial x_i \partial x_j} (u'_i u'_j - \overline{u'_i u'_j}) \quad (2)$$

where capital letters represent time-averaged quantities and ' represents fluctuating quantities. The first term on the right hand side is the rapid, turbulence-mean shear interaction. Deriving the spectral contribution of this term is fairly straightforward and has been shown by several authors [34, 35, 47]:

$$\phi_{pp}^{TM}(K) = 4\rho^2 \int_0^\infty \int_0^\infty \frac{K_1^2}{K^2} \exp[-(x_2 + x'_2)K] \frac{\partial U_1}{\partial x_2} \frac{\partial U_1}{\partial x'_2} \phi_{22} dx_2 dx'_2 \quad (3)$$

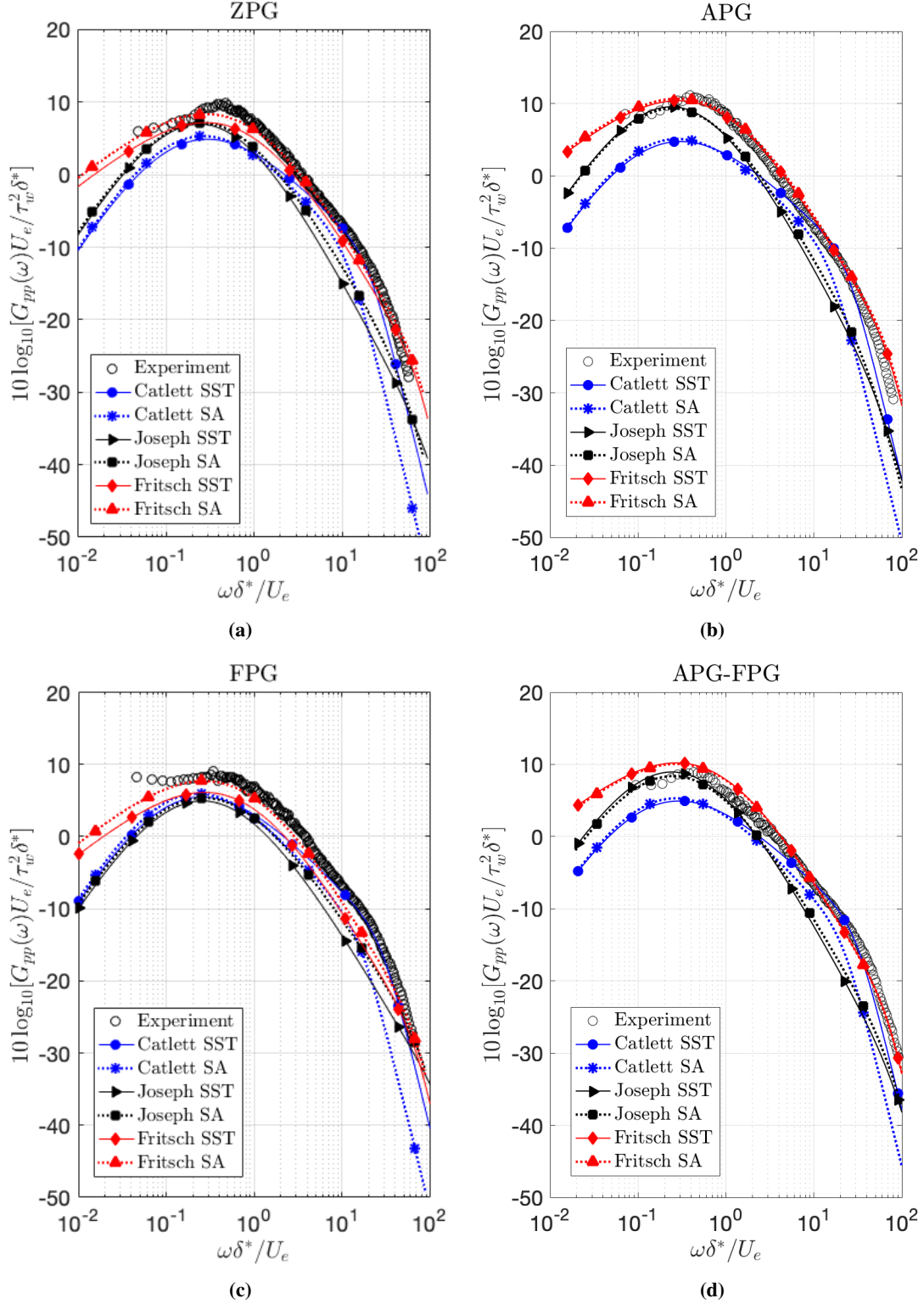


Fig. 13 Empirical models of Catlett *et al.* [37], Joseph *et al.* [38], and proposed model shown against experimental data of Fritsch *et al.* [11] for ZPG (a), APG (b), FPG (c), and APG-FPG cross (d) conditions.

Here, ' represents a secondary spatial domain that appears as a consequence of applying Green's theorem.

The second term of Eq. 2 is the slow, turbulence-turbulence interaction term. Deriving the spectrum of the slow term is significantly less straightforward, requires less valid assumptions, and there is not a widely accepted derivation. We employ the derivation of Grasso *et al.* [36]:

$$\phi_{PP}^{TT}(K) = \frac{\rho^2 L^2}{128\pi} K^2 (28 + L^2 K^2) \exp\left[-\frac{L^2 K^2}{8}\right] \int_0^\infty \int_0^\infty \frac{4}{9} k(x_2) k(x'_2) \exp[-(x_2 + x'_2)K] \mathcal{F}^2 dx_2 dx'_2 \quad (4)$$

where \mathcal{F} is the wall-normal velocity correlation function, assumed to be a Gaussian distribution.

Successful employment of this model formulation requires prediction or sub-modeling for the wall-normal velocity spectrum, ϕ_{22} , and the length scale, L .

A. Baseline Model

Parchen and Grasso *et al.* provide the mathematical basis of the model, but many decisions are left to the end-user on how to employ the model, particularly when working within the inherent limitations of RANS. The baseline RANS-based model to be employed is that of Fritsch *et al.* (2022) [32]. Following the recommendation of Grasso *et al.*, the Wilson (1997) generalized velocity spectrum is used [48]:

$$\begin{aligned} \phi_{22}(K, x_2, x'_2) &= \frac{\sqrt{u_2'^2(x_2) u_2'^2(x'_2)} K^2 L^4 \zeta^{\nu+2}}{\Gamma(\nu) \pi 2^{\nu+1} (1 + L^2 K^2)^{\nu+2}} \mathcal{K}_{\nu+2}(\zeta) \\ \zeta &= \frac{|x_2 - x'_2|}{L} \sqrt{1 + L^2 K^2} \\ L &= \frac{\Lambda}{\sqrt{\pi}} \frac{\Gamma(\nu)}{\Gamma(\nu+0.5)} \end{aligned} \quad (5)$$

Here, \mathcal{K} is the Bessel K function and Γ is the Gamma function. This formulation provides a model for the velocity spectrum knowing the wall-normal Reynolds stress component, $\overline{u_2'^2}$, and the integral length scale, Λ . The amplitude and roll-off behavior of that spectrum is adjustable via the tuning parameter ν . Additionally, Fritsch *et al.* accounted for the wall-normal variation of the wavenumber anisotropy:

$$\begin{aligned} \phi_{22} &= \alpha \phi_{22}^{iso}(\alpha K_1, K_3, x_2, x'_2) \\ \alpha &= \begin{cases} 2.4 \exp[-1.5 \frac{x_2}{\delta}] + 0.355, & \frac{x_2}{\delta} \leq 0.875 \\ 1.0, & \frac{x_2}{\delta} > 0.875 \end{cases} \end{aligned} \quad (6)$$

Fritsch *et al.* found that the most accurate results for smooth walls subjected to pressure gradients were obtained using this anisotropy formulation with the tuning parameter set to $\nu = 7/6$, what Grasso *et al.* referred to as the "Rapid Distortion Theory" (RDT) model. They also proposed a hybrid length scale, blending the Lane *et al.* [49] - Michel [50] length scale in the very near wall region to the Wilcox [51] length scale in the outer region. Finally, they observed that,

when using an eddy viscosity model, the Reynolds stress should be taken as isotropic, i.e., $\overline{u'^2} = 2/3k$.

Figure 14 shows the ZPG spectrum as measured, predicted with the proposed empirical model, and predicted using the analytical modeling protocol of Fritsch *et al.* [32], what will be referred to as the TNO-baseline or TNOBSL model, using both SST and SA input data. For the use of SA, modifications had to be made to account for the lack of turbulent kinetic energy. Predicting k with the SA model was accomplished using Townsend's structural parameter, $a_1 = \tau/2k$, where τ is the magnitude of the shear stress vector [9]. For a 2D flow, there is only one shear stress component, so this simplifies and can be rearranged to show:

$$k_{SA} = \frac{\overline{u'_1 u'_2}}{2a_1} \quad (7)$$

For 2D flows, a_1 can typically be taken as a constant 0.15, leaving:

$$k_{SA} = \frac{10}{3} \overline{u'_1 u'_2} \quad (8)$$

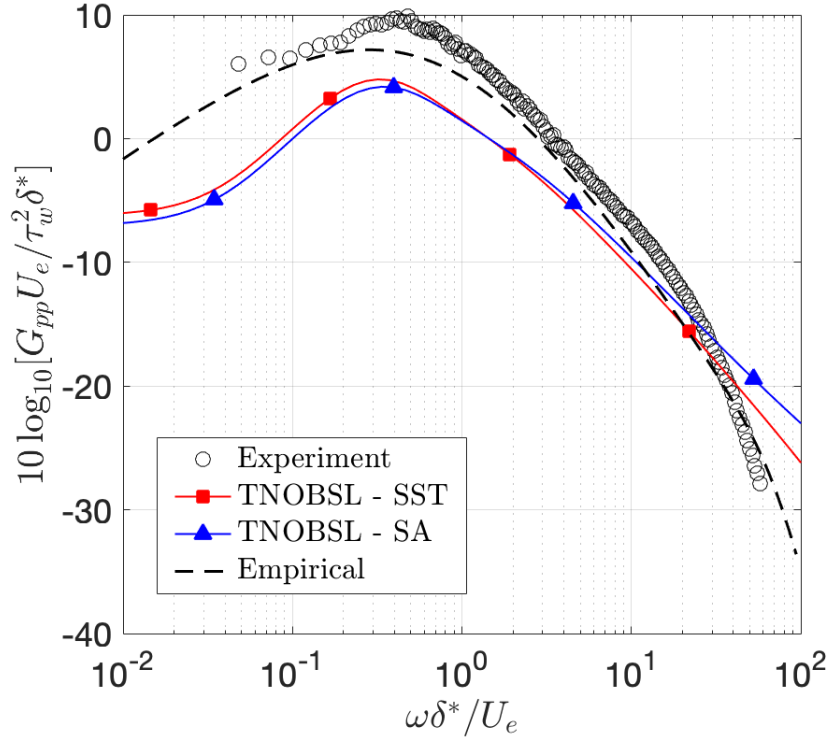


Fig. 14 ZPG spectra predicted using baseline TNO model from Fritsch *et al.* (2022) [32] with SST and SA data and with new empirical model compared against experiment.

With both turbulence models, the baseline TNO model under-predicts the peak spectral density and shows incorrect behavior in both the mid-frequency slope and the high frequency roll-off. The SA results are slightly lower than the SST

in the low frequencies and higher in the high frequencies which appears to be driven by the under-prediction of the Reynolds stress using Eq. 8 and the differences observed in near-wall behavior of the velocity profiles. It is clear that modifications to the formulation of Fritsch *et al.* [32] will be needed for rough wall flows.

B. Adjustments for Roughness

Ideally, the rough and smooth wall models will be as similar as possible. No changes were made to the definition of the Reynolds stress or length scale, both to facilitate overlap between the models and because it was found that there were no logical changes that could be made to these parameters that improved the predictive capability.

The first adjustment is to eliminate the wavenumber anisotropy factor. In the smooth wall model, the benefit of the wavenumber anisotropy was to pull the peak to lower frequencies and to introduce a bottleneck feature around the high frequency roll-off. In the rough wall spectra, this bottleneck is not as present and the peak location is under-, rather than over-predicted.

The second adjustment is to lower the value of the velocity spectrum tuning parameter, ν . In the smooth wall model, pushing ν to higher values shallowed the mid-frequency slope and reduced the peak spectral amplitude, but in the rough wall case the opposite trends are required. ν was reduced to 1/4, which had the effect of steepening the mid-frequency slope and increasing the peak pressure spectrum amplitude.

The final adjustment is to introduce a wall-shift, such that $x_2 = x_2 + \Delta x_2$. Shifting the wall has been shown to produce reasonable predictions of rough wall flows in CFD in the literature [21] and in Section V, and Joseph (2017) observed that the pressure spectrum measured at the canopy top of a rough wall flow is identical to an equivalent smooth wall spectrum [27]. It was desirable that the correct wall-shift be the wall-shift associated with the turbulence model, i.e., $\Delta x_2 = 0.03k_s$ for SA models and $0.2k_s$ for SST, but these shifts did not produce accurate spectra. It was found that the correct shift was the same in dimensional space for both models, $\Delta x_2 = 0.26mm = 0.13k_g$. The two models required differing values of k_s , which implies that the correct wall-shift for the pressure spectrum is not dependent on the simulated value of k_s or the simulation wall-shift, which is not ideal. We hypothesize that the wall-shift in the spectrum is in fact a function of the true k_s and that this would be captured if the CFD models showed the same relationship between k_s and Δu^+ .

Figure 15 shows the predicted spectra using these adjustments compared with experiment, the empirical model, and the baseline method. The adjusted model shows the best agreement with the experiment, best matching all three primary features of the peak location and amplitude, mid-frequency slope, and high frequency roll-off.

C. Rough Wall Analytical Model

The final model for the rough wall can be stated:

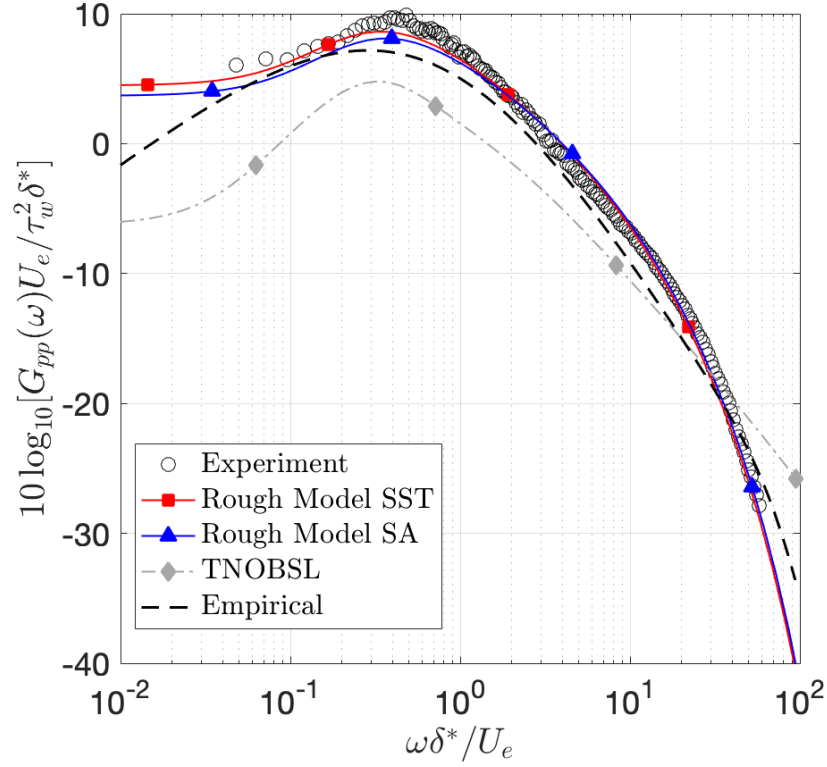


Fig. 15 ZPG spectra predicted using baseline TNO model from Fritsch *et al.* (2022) [32] with SST data and with new empirical model compared against experiment and newly proposed rough wall model using SST and SA data.

$$G_{pp}(\omega) = 2 \frac{\int_{-\infty}^{\infty} \phi_{pp}(K_1 = \omega/U_c, K_3) dK_3}{U_c} \quad (9)$$

$$U_c = \begin{cases} 0.80U_e, & \beta < 0.3 \\ 0.75U_e, & -0.3 \leq \beta \leq 0.3 \\ 0.65U_e, & \beta > 0.3 \end{cases} \quad (10)$$

$$\phi_{pp}(K_1, K_3) = \phi_{pp}^{TM}(K_1, K_3) + \phi_{pp}^{TT}(K_1, K_3) \quad (11)$$

$$\phi_{pp}^{TM}(K_1, K_3) = 4\rho^2 \int_{\Delta x'_2}^{\infty} \int_{\Delta x_2}^{\infty} \frac{K_1^2}{K^2} \exp[-(x_2 + x'_2)K] \frac{\partial U_1}{\partial x_2} \frac{\partial U_1}{\partial x'_2} \phi_{22} d(x_2 + \Delta x_2) d(x'_2 + \Delta x'_2) \quad (12)$$

$$\phi_{22}(K_1, K_3, x_2, x'_2) = \frac{\sqrt{u_2'^2(x_2) u_2'^2(x'_2) K^2 L^4 \zeta^{\nu+2}}}{\Gamma(\nu) \pi 2^{\nu+1} (1 + L^2 K^2)^{\nu+2}} \mathcal{H}_{\nu+2}(\zeta) \quad (13)$$

$$\overline{u_2'^2} = \frac{2}{3}k \quad (14)$$

$$k_{SA} = \frac{10}{3}\overline{u_1' u_2'}$$

$$\nu = 1/4 \quad (15)$$

$$\zeta = \frac{|x_2 - x_2'|}{L} \sqrt{1 + L^2 K^2} \quad (16)$$

$$L = \frac{\Lambda}{\sqrt{\pi}} \frac{\Gamma(\nu)}{\Gamma(\nu + 0.5)} \quad (17)$$

$$\Lambda = \begin{cases} 0.146\delta \tanh[8.5 \frac{x_2}{\delta}], & \frac{x_2}{\delta} \leq 0.02 \\ \frac{1}{\kappa} \sqrt{\frac{|u_1' u_2'|}{(\frac{\partial u_1}{\partial x_2})^2}}, & \frac{x_2}{\delta} > 0.02 \end{cases} \quad (18)$$

$$\phi_{pp}^{TT}(K_1, K_3) = \frac{\rho^2 L^2}{128\pi} K^2 (28 + L^2 K^2) \exp[-\frac{L^2 K^2}{8}] \int_{\Delta x_2}^{\infty} \int_{\Delta x_2}^{\infty} \overline{u_2'^2(x_2)} \overline{u_2'^2(x_2')} \exp[-(x_2 + x_2')K] \mathcal{F}^2 d(x_2 + \Delta x_2) d(x_2' + \Delta x_2') \quad (19)$$

$$\mathcal{F}^2 = \exp[-(x_2 - x_2')^2 / L^2] \quad (20)$$

This model incorporates the analytical framework of the PPE, the limitations and assumptions of RANS flow data, and adjustments for the physics of rough wall flows. The most critical aspect of the model is the correct prediction of the wall shift, Δx_2 . Based on experimental data, it appears that $\Delta x_2 \approx 0.08k_s$, where k_s is the true value that may or may not be related to the simulated value. In the RANS models, k_s is effectively a tuning parameter that obeys qualitatively correct physical trends but does not appear to exhibit an exact quantitative relationship to the true flow k_s .

The order of magnitude of the required wall-shift implies a possible relationship to the hydrodynamic roughness height, k_0 : the height that satisfies the modified log-law:

$$u^+ = \frac{1}{\kappa} \ln\left[\frac{x_2}{k_0}\right] \quad (21)$$

Combined with Nikuradse's roughness function data, $\Delta u^+ = \frac{1}{\kappa} \ln[k^+] - 3.5$, it can be shown that k_0 is a universal function of k_s for fully rough flows, such that:

$$k_0 = k_s \exp[-\kappa(B + 3.5)] \quad (22)$$

which is $0.031k_s$ for $\kappa = 0.41$, $B = 5.0$. The possibility of a dependence on the hydrodynamic roughness is intriguing, both because it is of the same order of magnitude as the "correct" wall-shift, and because it extends back to smooth wall modeling as well. Fritsch *et al.* (2022) observed that the TNO model failed to replicate a ω^{-5} high frequency roll-off and that this did not depend on any of the studied sensitivities [32]. Smooth wall boundary layers have an equivalent hydrodynamic roughness height, albeit much smaller than on a rough wall, which would imply the necessity of a wall-shift for the smooth TNO model as well, steepening the high frequency slope towards the -5 value.

Figure 16 shows the predictions in pressure gradient conditions using this formulation with both turbulence models as well as the empirical model proposed above. In ZPG, the analytical formulation shows better agreement with experiment across the full spectrum, better matching the peak amplitude and location, mid-frequency slope, and high frequency roll-off. In APG, the peak behavior is captured well by both modeling styles, but the empirical model shows a more accurate mid-frequency slope, while the analytical model better captures the high-frequency roll-off.

For the smooth wall empirical and analytical modeling as well as the rough wall empirical modeling, the FPG and APG-FPG cross cases were the most difficult to predict accurately, which remains to be the case here as well. In FPG, the analytical models capture the mid- and high frequency behaviors better than the empirical model, but show a lower spectral peak than what was observed in experiment. In the non-equilibrium pressure gradient cross-over case, the entirety of the predicted spectrum is off from the measured spectrum, though the errors are never larger than $\approx 2dB$.

With the exception of the FPG case, the SA model consistently shows $\approx 1dB$ lower predictions in the low frequencies, attributed to the discrepancies in the methods for estimated the turbulent kinetic energy. Beyond $\omega\delta^*/U_e > 1$, however, the two turbulence models show near-perfect agreement.

VIII. Conclusions

Updates have been made to the rough wall boundary conditions for the Spalart-Allmaras and Menter SST turbulence models and implemented in the HPCMP-CREATE-AV Kestrel KCFD solver, and these updated models show improvements in qualitative trends with increasing roughness Reynolds number, achieved both by holding edge velocity constant and increasing k_s , and by holding k_s constant and increasing U_e . The Spalart-Allmaras model and modified boundary condition shows better agreement with the data of Nikuradse (1950) [3] than the Menter SST model with modified Aupoix [21] boundary condition, the latter showing a bias over-prediction of the roughness function at a given k^+ . Neither turbulence model replicates experimental data when using the experimentally measured value of k_s at the wall, and thus require tuning of the k_s used for the boundary condition.

Two empirical models for the wall pressure spectrum beneath rough wall boundary layers were assessed at zero,

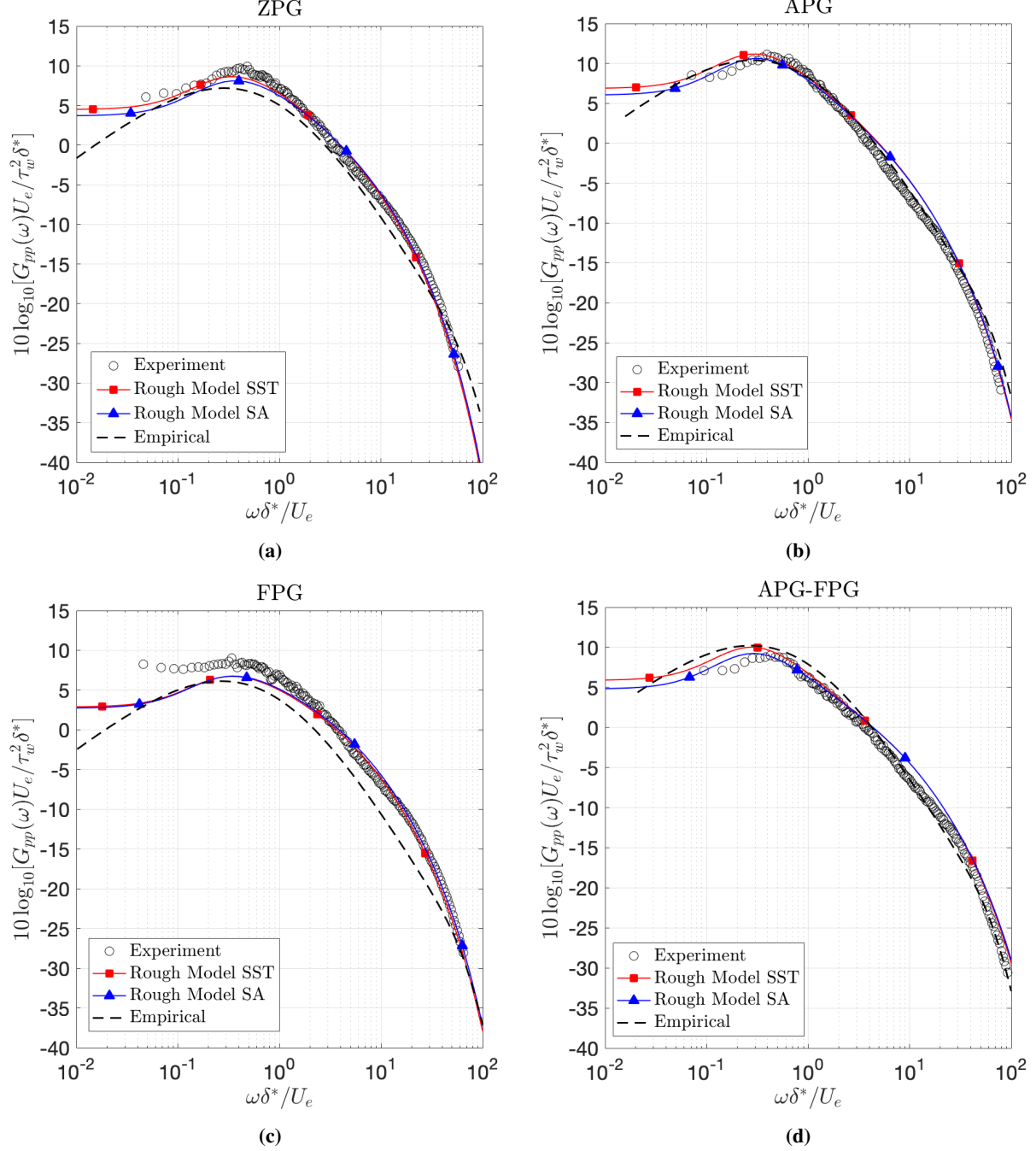


Fig. 16 Pressure spectra as measured and predicted using new rough wall TNO model and new empirical model for ZPG (a), APG (b), FPG (c), and APG-FPG cross (d) conditions.

adverse, favorable, and adverse-to-favorable pressure gradient conditions for their ability to predict the spectrum from RANS data. The model of Catlett *et al.* (2022) captures the high frequency roll-off behavior, but consistently under-predicts the peak amplitude and mid-frequency slope [37]. The model of Joseph *et al.* (2022) shows good agreement with experiment around the peak, but consistently over-predicts the mid-frequency slope, resulting in

under-prediction of the high frequency behavior [38]. The separation of low and high frequency behaviors in the respective models suggests a two-form model consisting of a combination of the Catlett and Joseph models may give superior predictive capability.

A third, new empirical model was proposed based on the observations of Fritsch *et al.* (2022), who observed that rough wall pressure spectra were universal under outer scaling [11]. This results in a simple, flow-independent (aside from scaling factors) model for the spectrum that shows improved predictions over the Catlett *et al.* [37] and Joseph *et al.* [38] models. This new model was also compared against data from Joseph (2017) [27], which was not used in the development of the model, which showed comparable predictive capability. This model may only be applicable to higher k^+ flows, as it incorporates no variation in mid-frequency slope, known to steepen with increasing k_s through the transitional and lower k^+ fully rough regime [1, 27, 38]. The new model contains no Reynolds number dependence on an outer variable scaling, similar to observations made by Fritsch *et al.* (2022) [11] on the overlying velocity profiles, potentially indicating that Townsend’s hypothesis is valid for the surface pressure statistics.

The analytical TNO modeling formulation of Fritsch *et al.* (2022) [32], based on the formulation of Grasso *et al.* (2019) [36], was shown to be a poor predictor for rough wall flows. Adjustments were made to the model to increase the intensity and isotropy of the velocity spectrum and to incorporate a wall-shift akin to that used in the turbulence models. This updated formulation was shown to produce predictions with excellent agreement to experiment from steady RANS data, matching both the general roughness effects as well as the pressure gradient and pressure gradient history effects.

The required wall shift was found to be independent of pressure gradient, local Reynolds number, or turbulence model, which implies that it is a function of the true k_s , which is not necessarily the simulated value. This disconnect between physical and model k_s poses a challenge for *a priori* prediction, although this challenge is not separate from that of the general flow modeling, which suffers from the same disconnect between true and simulated k_s . The required shift is of the same order of magnitude as the hydrodynamic roughness height, and a dependence on that length scale would imply an equivalent wall-shift for the smooth wall TNO model, which would alleviate some of the observed errors in that model as observed by Fritsch *et al.* (2022) [32].

Improvements are still needed in RANS modeling of rough wall flows. With the current state-of-the-art, k_s has little-to-no physical meaning and exists only as an effective tuning parameter. While, as a tuning parameter, k_s shows qualitatively good agreement with experimentally observed trends, quantitatively correct matching requires *a priori* knowledge of the roughness function in order to tune the simulated k_s value correctly, creating a paradox under which the flow cannot be accurately simulated *a priori*. Solving this disconnect will require enhanced knowledge of the relationship between roughness geometry and k_s and new, more physically meaningful boundary condition definitions for RANS simulations.

Acknowledgments

The authors would like to thank Dr. Peter Chang and Dr. Julie Young of the Office of Naval Research for their support under grant numbers N00014-18-1-2455, N00014-19-1-2109, and N00014-20-2821. We would also like to thank the U.S. Department of Defense High Performance Computing Modernization Program (HPCMP) for computational resources. We are extremely grateful for Dr. Robert Nichols for his contributions to roughness model development.

References

- [1] Meyers, T., Forest, J. B., and Devenport, W. J., “The wall-pressure spectrum of high-Reynolds-number turbulent boundary-layer flows over rough surfaces,” *Journal of Fluid Mechanics*, Vol. 768, 2015, pp. 261–293. <https://doi.org/10.1017/jfm.2014.743>.
- [2] Spalart, P., and Allmaras, S., “A one-equation turbulence model for aerodynamic flows,” *AIAA Sciences Meeting*, American Institute of Aeronautics and Astronautics, 1992. <https://doi.org/10.2514/6.1992-439>.
- [3] Nikuradse, J., “Laws of flow in rough pipes,” *NACA Technical Report*, , No. TM 1292, 1950.
- [4] Dvorak, F. A., “Calculation of Turbulent Boundary Layers on Rough Surfaces in Pressure Gradient,” *AIAA Journal*, Vol. 7, No. 9, 1969, pp. 1752–1759. <https://doi.org/10.2514/3.5386>.
- [5] Raupach, M. R., Antonia, R. A., and Rajagopalan, S., “Rough-wall turbulent boundary layers,” *Applied Mechanics Review*, Vol. 44, No. 1, 1991, pp. 1–25. <https://doi.org/10.1115/1.3119492>.
- [6] Krogstad, P. A., Antonia, R. A., and Browne, L. W., “Comparison between rough- and smooth-wall turbulent boundary layers,” *Journal of Fluid Mechanics*, Vol. 245, 1992, pp. 599–617. <https://doi.org/10.1017/S0022112092000594>.
- [7] Jimenez, J., “Turbulent Flows over Rough Walls,” *Annual Review of Fluid Mechanics*, Vol. 36, 2004, pp. 173–196. <https://doi.org/10.1146/annurev.fluid.36.050802.122103>.
- [8] Flack, K. A., and Schultz, M. P., “Roughness effects on wall-bounded turbulence,” *Physics of Fluids*, Vol. 26, 2014, pp. 26–43. <https://doi.org/10.1063/1.4896280>.
- [9] Townsend, A. A., *The Structure of Turbulent Shear Flow*, Cambridge University Press, Cambridge, UK, 1976.
- [10] Flack, K. A., Schultz, M. P., and Shapiro, T. A., “Support for Townsend’s Reynolds number similarity hypothesis on rough walls,” *Physics of Fluids*, Vol. 17, 2005, p. 035102. <https://doi.org/10.1063/1.1843135>.
- [11] Fritsch, D. J., Vishwanathan, V., Roy, C. J., Lowe, K. T., and Devenport, W. J., “Turbulence and pressure fluctuations in rough wall boundary layers in pressure gradients,” *Experiments in Fluids*, 2022. Accepted for Publication.
- [12] Clauser, F. H., “Turbulent Boundary Layers in Adverse Pressure Gradient,” *Journal of the Aeronautical Sciences*, Vol. 21, No. 2, 1954, pp. 91–108. <https://doi.org/10.2514/8.2938>.

- [13] Nagano, Y., Tagawa, M., and Tsuji, T., “Effects of Adverse Pressure Gradients on Mean Flows and Turbulence Statistics in a Boundary Layer,” *8th International Symposium on Turbulent Shear Flows*, Springer-Verlag, New York, USA, Munich, Germany, 9-11 September, 1991. https://doi.org/10.1007/978-3-642-77674-8_2.
- [14] Yuan, J., and Piomelli, U., “Numerical simulations of sink-flow boundary layers over rough surfaces,” *Physics of Fluids*, Vol. 26, No. 1, 2014, p. 015113. <https://doi.org/10.1063/1.4862672>.
- [15] Yuan, J., and Piomelli, U., “Numerical simulation of a spatially developing accelerating boundary layer over roughness,” *Journal of Fluid Mechanics*, Vol. 780, 2015, pp. 192–214. <https://doi.org/10.1017/jfm.2015.437>.
- [16] Devenport, W. J., and Lowe, K. T., “Equilibrium and Non-Equilibrium Turbulent Boundary Layers,” *Progress in Aerospace Sciences*, Vol. 131, 2022, p. 100807. <https://doi.org/10.1016/j.paerosci.2022.100807>.
- [17] Wilcox, D. C., “Reassessment of the scale-determining equation for advanced turbulence models,” *AIAA Journal*, Vol. 46, 1988, pp. 2823–2838. <https://doi.org/10.2514/3.10041>.
- [18] Wilcox, D. C., *Turbulence Modeling for CFD*, 3rd ed., DCW Industries, La Cañada, CA, USA, 2006.
- [19] Aupoix, B., and Spalart, P. R., “Extensions of the Spalart-Allmaras turbulence model to account for wall roughness,” *International Journal of Heat and Fluid Flows*, Vol. 24, 2003. [https://doi.org/10.1016/S0142-727X\(03\)00043-2](https://doi.org/10.1016/S0142-727X(03)00043-2).
- [20] Knopp, T., Eisfeld, B., and Calvo, J. B., “A new extension for k- ω turbulence models to account for wall roughness,” *International Journal of Heat and Fluid Flow*, Vol. 30, 2009, pp. 54–65. <https://doi.org/10.1016/j.ijheatfluidflow.2008.09.009>.
- [21] Aupoix, B., “Wall Roughness Modeling with k- ω SST Model,” *10th International Symposium on Engineering Turbulence Modelling and Measurements*, Marbella, Spain, Sep 2014.
- [22] Apsley, D., “CFD Calculation of Turbulent Flow with Arbitrary Wall Roughness,” *Flow, Turbulence, and Combustion*, Vol. 78, 2007, pp. 153–175. <https://doi.org/10.1007/s10494-006-9059-x>.
- [23] Song, S., Demirel, Y. K., Atlar, M., Dai, S., and Turan, O., “Validation of the CFD approach for modelling roughness effect on ship resistance,” *Ocean Engineering*, Vol. 200, 2020. <https://doi.org/10.1016/j.oceaneng.2020.107029>.
- [24] Blake, W. K., “Turbulent boundary-layer wall-pressure fluctuations on smooth and rough walls,” *Journal of Fluid Mechanics*, Vol. 44, No. 4, 1970, pp. 637–660. <https://doi.org/10.1017/S0022112070002069>.
- [25] Blake, W. K., “Turbulent Velocity and Pressure Fields in Boundary-Layer Flows over Rough Surfaces,” *Symposia on Turbulence in Liquids*, 6 October, 1971.
- [26] Forest, J. B., “The Wall Pressure Spectrum of High Reynolds Number Rough-Wall Turbulent Boundary Layers,” Master’s thesis, Virginia Polytechnic Institute and State University, 2012.
- [27] Joseph, L. A., “Pressure Fluctuations in a High-Reynolds-Number Turbulent Boundary Layer over Rough Surfaces of Different Configurations,” Ph.D. thesis, Virginia Polytechnic Institute and State University, 2017.

- [28] Bull, M. K., "Wall Pressure Fluctuations Beneath Turbulent Boundary Layers: Some Reflections on Forty Years of Research," *Journal of Sound and Vibration*, Vol. 190, No. 3, 1996, pp. 299–315. <https://doi.org/10.1006/jsvi.1996.0066>.
- [29] Fritsch, D. J., Vishwanathan, V., Lowe, K. T., and Devenport, W. J., "Fluctuating Pressure Beneath Smooth Wall Boundary Layers in Non-Equilibrium Pressure Gradients," *AIAA Journal*, 2022. Article in Advance.
- [30] Schloemer, H., "Effects of Pressure Gradients on Turbulent Boundary-Layer Wall-Pressure Fluctuations," *US Navy Underwater Sound Laboratory Report*, , No. 747, 1966. <https://doi.org/10.1121/1.1943059>.
- [31] Goody, M., "Empirical Spectral Model of Surface Pressure Fluctuations," *AIAA Journal*, Vol. 49, No. 9, 2004, pp. 1788–1794. <https://doi.org/10.2514/1.9433>.
- [32] Fritsch, D. J., Vishwanathan, V., Roy, C. J., Lowe, K. T., Devenport, W. J., Croaker, P., Lane, G., Tkachenko, O., Pook, D., Shubham, S., and Sandberg, R. D., "Modeling the Surface Pressure Spectrum Beneath Turbulent Boundary Layers in Pressure Gradients," *28th AIAA/CEAS Aeroacoustics Conference*, Southampton, UK, 14-17 June, 2022. <https://doi.org/10.2514/6.2022-2843>.
- [33] Blake, W. K., *Mechanics of Flow-Induced Sound and Vibration*, 1st ed., Academic Press, London, UK, 1986.
- [34] Parchen, R., "Progress Report DRAW: A Prediction Scheme for Trailing-Edge Noise Based on Detailed Boundary-Layer Characteristics," *TNO Institute of Applied Physics*, , No. 980023, 1998.
- [35] Lee, Y.-T., Blake, W., and Farabee, T., "Modeling of Wall Pressure Fluctuations Based on Time Mean Flow Field," *Journal of Fluids Engineering*, Vol. 127, 2005, pp. 233–240. <https://doi.org/10.1115/1.1881698>.
- [36] Grasso, G., Jaiswal, P., Wu, H., Moreau, S., and Roger, M., "Analytical Models of the Wall-Pressure Spectrum Under a Turbulent Boundary Layer," *Journal of Fluid Mechanics*, Vol. 877, 2019, pp. 1007–1062. <https://doi.org/10.1017/jfm.2019.616>.
- [37] Catlett, M. R., Bryan, B. S., Chang, N., Hemingway, H., and Anderson, J., "Modeling Unsteady Surface Pressure Auto-Spectra for Turbulent Boundary Layer Flow over Small Dense Roughness," *AIAA SciTech Forum*, San Diego, CA, USA, 03-07 Jan, 2022. <https://doi.org/10.2514/6.2022-2560>.
- [38] Joseph, L. A., Devenport, W. J., and Glegg, S., "Empirical Model for Low-Speed Rough-Wall Turbulent Boundary Layer Pressure Spectra," *AIAA Journal*, Vol. 60, No. 4, 2022, pp. 2160–2168. <https://doi.org/10.2514/1.J060965>.
- [39] Fritsch, D. J., Vishwanathan, V., Duetsch-Patel, J. E., Gargiulo, A., Lowe, K. T., and Devenport, W. J., "The Pressure Signature of Smooth Wall Turbulent Boundary Layers in Pressure Gradient Family," *AIAA Aviation Forum*, Reno, NV, USA, 15-19 June 2020. <https://doi.org/10.2514/6.2020-3066>.
- [40] Fritsch, D. J., Vishwanathan, V., Lowe, K. T., and Devenport, W. J., "The Space-Time Correlation of Pressure Under High Reynolds Number Smooth Wall Turbulent Boundary Layers in Pressure Gradient Family," *AIAA Science and Technology Forum*, Nashville, TN, USA, 11-21 January 2021. <https://doi.org/10.2514/6.2021-1946>.

- [41] Vishwanathan, V., Fritsch, D. J., Lowe, K. T., and Devenport, W. J., “Analysis of Coherent Structures Over a Smooth Wall Turbulent Boundary Layer in Pressure Gradient Using Spectral Proper Orthogonal Decomposition,” *AIAA Aviation Forum*, 2-6 August, 2021. <https://doi.org/10.2514/6.2021-2893>.
- [42] Fritsch, D. J., Vishwanathan, V., Roy, C. J., Lowe, K. T., Devenport, W. J., Nishi, Y., Knopp, T., Ströer, P., Krumbein, A., Sandberg, R. D., Lav, C., Bensow, R. E., Eça, L., Toxopeus, S. L., Kerkvliet, M., Slama, M., and Bordier, L., “Experimental and Computational Study of 2D Smooth Wall Turbulent Boundary Layers in Pressure Gradient,” *AIAA Science and Technology Forum*, San Diego, CA, USA, 3-7 January 2022. <https://doi.org/10.2514/6.2022-0696>.
- [43] Vishwanathan, V., Fritsch, D. J., Lowe, K. T., and Devenport, W. J., “History effects and wall similarity of non-equilibrium turbulent boundary layers in varying pressure gradient over rough and smooth surfaces,” *12th International Symposium on Turbulence and Shear Flow Phenomena (TSFP12)*, Osaka, Japan, 19-22 July, 2022.
- [44] Fritsch, D. J., Vishwanathan, V., Lowe, K. T., and Devenport, W. J., “Surface Pressure Spectra Beneath High Reynolds Number Smooth and Rough Wall Boundary Layers in Pressure Gradients,” *University Libraries, Virginia Tech*, 2022. <https://doi.org/10.7294/20457189>, dataset.
- [45] Devenport, W. J., Burdisso, R., Borgoltz, A., Ravetta, P., Barone, M., Brown, K., and Morton, M., “The Kevlar-walled Anechoic Wind Tunnel,” *Journal of Sound and Vibration*, Vol. 332, No. 17, 2013, pp. 3971–3991. <https://doi.org/10.1016/j.jsv.2013.02.043>.
- [46] Zagarola, M. V., and Smits, A. J., “Mean-flow scaling of turbulent pipe flow,” *Journal of Fluid Mechanics*, Vol. 373, 1998, pp. 33–79. <https://doi.org/10.1017/S0022112098002419>.
- [47] Panton, R. L., and Linebarger, J. H., “Wall Pressure Spectra Calculations for Equilibrium Boundary Layers,” *Journal of Fluid Mechanics*, Vol. 65, No. 2, 1974, pp. 261–287. <https://doi.org/10.1017/S0022112074001388>.
- [48] Wilson, D. K., “A Three-Dimensional Correlation/Spectral Model for Turbulent Velocities in a Convective Boundary Layer,” *Boundary-Layer Meteorology*, Vol. 85, 1997, pp. 35–52. <https://doi.org/10.1023/A:1000418709945>.
- [49] Lane, G., Sidebottom, W., and Croaker, P., “Application of Wall-Modelled LES to the Prediction of Turbulent Flow Noise,” *Proceedings of Acoustics 2021*, Wollongong, Australia, 8-10 Nov, 2021.
- [50] Michel, R., Quemard, C., and Durant, R., “Hypotheses on the mixing length and application to the calculation of turbulent boundary layers,” *Proceedings on Computational Turbulent Boundary Layers*, Vol. 1, 1968, pp. 195–207.
- [51] Wilcox, D. C., *Turbulence Modeling for CFD*, 1st ed., DCW Industries, La Cañada, CA, USA, 1993.

Chapter 8

Findings

A rigorous, complete, and comprehensive experimental study of high Reynolds number smooth and rough wall boundary layers beneath systematically varied, continually varying, bi-directional pressure gradients has been performed in the Virginia Tech Stability Wind Tunnel. Measurements were made of the boundary layer parameters and their development as well as the spectra of fluctuating pressure at several locations within the pressure gradient cases. These data were released to the greater turbulence modeling community via NATO AVT-349 and enabled a joint, synergistic computational study of the measured flows. These findings produced the four journal articles, five conference papers, and public domain repository listed below:

Journal Articles

Fritsch, D.J., Vishwanathan, V., Lowe, K.T., and Devenport, W.J., “Fluctuating Pressure Beneath Smooth Wall Boundary Layers in Non-Equilibrium Pressure Gradients,” *AIAA Journal*, 2022, Vol. 60, no. 8, pp. 4725-4743

Fritsch, D.J., Vishwanathan, V., Roy, C.J., Lowe, K.T., and Devenport, W.J., “Turbulence and pressure fluctuations in rough wall turbulent boundary layers in pressure gradients,” *Experiments in Fluids*, 2022, Accepted for Publication

Fritsch, D.J., Vishwanathan, V., Roy, C.J., Lowe, K.T., Devenport, W.J., Croaker, P., Lane, G., Tkachenko, O., Pook, D., Shubham, S., and Sandberg, R.D., “Modeling the Surface Pressure Spectrum Beneath Turbulent Boundary Layers in Pressure Gradients,” *AIAA Journal*, Under Review

Fritsch, D.J., Vishwanathan, V., Roy, C.J., Lowe, K.T., and Devenport, W.J., “Modeling the Surface Pressure Spectrum Beneath Rough Wall Boundary Layers in Pressure Gradient,” 2022, Under Review

Conference Papers

Fritsch, D.J., Vishwanathan, V., Duetsch-Patel, J.E., Gargiulo, A., Lowe, K.T., and Devenport, W.J., “The Pressure Signature of Smooth Wall Turbulent Boundary Layers in Pressure Gradient Family,” *AIAA Aviation Forum*, Reno, NV, USA, 15-19 June 2020

Fritsch, D.J., Vishwanathan, V., Lowe, K.T., and Devenport, W.J., “The Space-Time Correlation of Pressure Under High Reynolds Number Smooth Wall Turbulent Boundary Layers in Pressure Gradient Family,” *AIAA Science and Technology Forum*, Nashville, TN, USA, 11-21 January 2021

Fritsch, D.J., Vishwanathan, V., Lowe, K.T., and Devenport, W.J., “The Effect of Grazing Flow on Pinhole Condenser Microphones,” *AIAA Science and Technology Forum*, Nashville, TN, USA, 11-21 January 2021.

Fritsch, D.J., Vishwanathan, V., Roy, C.J., Lowe, K.T., Devenport, W.J., Nishi, Y., Knopp, T., Ströer, P., Krumbein, A., Sandberg, R.D., Lav, C., Bensow, R.E., Eça, L., Toxopeus, S.L., Kerkvliet, M., Slama, M., and Bordier, L., “Experimental and Computational Study of 2D Smooth Wall Turbulent Boundary Layers in Pressure Gradient,” *AIAA Science and Technology Forum*, San Diego, CA, USA, 3-7 January 2022

Fritsch, D.J., Vishwanathan, V., Roy, C.J., Lowe, K.T., Devenport, W.J., Croaker, P., Lane, G., Tkachenko, O., Pook, D., Shubham, S., and Sandberg, R.D., “Modeling the Surface Pressure Spectrum Beneath Turbulent Boundary Layers in Pressure Gradients,” *28th AIAA/CEAS Aeroacoustics Conference*, Southampton, UK, 14-17 June, 2022

Repository

Fritsch, D.J., Vishwanathan, V., Lowe K.T., and Devenport, W.J., “Surface Pressure Spectra Beneath High Reynolds Number Smooth and Rough Wall Boundary Layers in Pressure Gradients,” *University Libraries, Virginia Tech*, 2022, doi: 10.7294/20457189

The findings of these works are summarized below:

- The effect of pressure gradient on boundary layer development is strongly non-local. Under the presence of continually varying pressure gradient, the boundary layer growth lags downstream of the pressure gradient distribution. This lag appears to be independent of pressure gradient sign or magnitude and of the free-stream Reynolds number, but is dependent on surface treatment; history lags are shortened in rough wall flows. This is most likely due to intensification of inner motions in the rough wall boundary layer, which are shown to respond more rapidly to pressure gradient than their outer layer counterparts.
- The effect of pressure gradient on the smooth wall pressure spectrum is complex and region dependent. The high frequency behavior scales on classical viscous variables and appears largely pressure gradient and history independent. The mid-frequency slope is highly dependent on pressure gradient and features similar lagging behavior to the boundary layer development. This variation was shown to be strongly correlated ($\rho = 0.96$) with the local skin friction coefficient, and it is hypothesized that this is due to the movement towards/-away from the wall of the location of bulk pressure fluctuation sources, which will drive the mid-frequency decay and is strongly dependent on local Reynolds number.
- Standard eddy-viscosity RANS is capable of replicating the effects of continually varying pressure gradient on the boundary layer very accurately if the pressure gradient is captured correctly. However, this is a surprisingly large *if*. Wind tunnel flows are complex, internal, three-dimensional problems that are not as well understood as was once thought. Accurately replicating the pressure gradient in a 2D environment requires careful attention to the meshing and simulation design. This is helped immensely by collaboration between experimental and computational teams from the beginning of the effort. Accurately replicating the flow in 3D requires careful choice of turbulence model; the standard Boussinesq hypothesis appears incapable of replicating corner and juncture flows and should be replaced by the Quadratic Constitutive Relation (QCR).
- Empirical models for smooth walls in pressure gradients fail to balance *flexibility* (accurate

changes with changing pressure gradient behavior) with *robustness* (maintenance of physical behavior across a wide range of flow cases). This is due primarily to the sensitivity of the empirical formulation, which requires the correlation of an infinite dimensional space of flow variables to minute changes in input parameters.

- An analytical formulation for the pressure spectrum can be derived, albeit with questionably valid assumptions. This formulation does not automatically interface well with RANS flow modeling, but new protocols have been proposed for the prediction of Reynolds stresses, velocity spectra, length scales, and anisotropy within the confines of RANS data. These spectral models show improvement in both flexibility and robustness over empirical modeling as well as capturing spectral features that empirical models cannot.
- Rough wall flows in pressure gradients are simplified in many ways compared to equivalent smooth wall flows. They exhibit Reynolds number similarity, shortened history effects (due, it is hypothesized, to the disruption of large-scale turbulent motions and a corresponding reduction in convection speed), and simple pressure spectra with no mid-frequency pressure gradient dependence. The pressure spectra beneath rough walls scale universally on an outer variable scaling, suggesting a dominance of outer motions and their respective pressure gradient effects in combination with a universal viscous behavior and k_s dependence fully describe the pressure fluctuations.
- The modified viscous scaling of Meyers *et al.* (2015) [91] appears to hold validity in pressure gradient and pressure gradient history. The Meyers scale, u_ν , can be interpreted as the shear due to viscous effects, which are un-affected by the presence of roughness, implying that the increase in shear over a rough surface is driven by a new mechanism that is not present in a smooth wall flow. It is hypothesized that this mechanism is the production of turbulent motions at the canopy height.
- RANS simulations of rough wall flows are fundamentally flawed; there is no physical basis for the current state-of-the-art in rough wall boundary condition modeling. This would be acceptable if the existing models produced results that agreed with experimental data across a wide range of cases, but this does not appear true for several widely accepted models. More consistent models have been proposed more recently, but a consistent picture of which models should be employed in which circumstances is lacking.
- A novel empirical model for rough wall pressure spectra is proposed that contains no flow dependent inputs on a classical outer-variable scaling. The lack of Reynolds number dependence on outer scaling is reminiscent of Townsend's hypothesis.
- The analytical pressure spectrum model requires adaptation for rough walls. This comes in two primary changes: an increase in the magnitude of the velocity spectra and a wall shift in the integration, effectively shifting the pressure sources upwards by some function of the roughness height. This formulation proves effective at modeling rough wall pressure spectra, even in pressure gradient, but is difficult to interface with RANS due to a disconnect between the real and simulated values of the roughness height.

Chapter 9

Outlook

Great strides have been made in the past few years across all of the relevant sub-disciplines represented in this work. Our understanding of pressure gradient and roughness effects on boundary layer flows, our ability to model those flows, and our understanding and predictive capability for the underlying surface pressure spectra beneath those flows have all improved. However, many questions still remain. This section will offer some perspective on the outlook for research in these areas in the coming years.

It is quite clear that boundary layer flows subjected to streamwise pressure gradients are dominated by non-local history effects. Quantifying these effects will be critical for improving our understanding of these physics and developing and validating models that correctly capture them. The results presented herein suggest that a reduced order model or partial differential equation that describes these effects ought to exist and be fairly straightforward to develop. The challenge lies in separating the history effects from the local pressure gradient and Reynolds number effects. One way to do this would be to design an experiment that has a double pressure gradient in which the two pressure gradient regions are able to be changed independently. By varying one pressure gradient and leaving the other constant, a picture would emerge of which effects belong to the local conditions and which belong to the upstream history. The desired output of this experiment would be a one- or two-equation algebraic or PDE model for the development of the boundary layer parameters through pressure gradients with history effects.

This work has shown that rough wall flows are in many ways simpler than equivalent smooth wall flows, particularly under pressure gradients, but an understanding of the full dimensional space of roughness effects is sorely lacking. One of the primary issues is the current lack of an understanding of which roughness effects can be considered in or out of equilibrium, because most rough wall experiments in the literature are in a state of non-equilibrium. It is critical in the next phase of rough wall research to develop and rigorously study an equilibrium rough wall flow. This is a significant challenge, and will require careful design-of-experiments and the development of rough surfaces with very exact streamwise distributions of height and density in order to sustain a constant Clauser parameter through the flow. The outputs of this experiment would reveal those roughness effects that exist in equilibrium, allowing them to be separated from those effects that arise due to out-of-equilibrium behavior.

It is clear that the roughness function is the primary variable that describes a rough surface; the equivalent sandgrain roughness simply being a convenient restatement of that roughness function. What is not clear is how the roughness function is related to the geometry of a roughness surface. The Catch-22 of rough wall flows is that the roughness function must be known *a priori* in order to simulate the flow, but the purpose of simulating the flow is to determine the roughness function.

None of the currently proposed roughness geometry-function correlations are universally applicable, but such a correlation should exist, if we can find it, and is fundamentally necessary for meaningful advancement of rough wall modeling. To do this, a large database of highly complete rough wall flows should be brought together and made available to the modeling community, something that has been started by the NATO AVT-349 group.

Wind tunnels are internal, three-dimensional, non-equilibrium flow problems that include complex flow physics in corners and around junctions. The assumption that a wind tunnel model is in “free-stream” flight is poor, and ignored at the detriment to any conclusions or models developed from said experiment. There is a great need throughout the industry for a push to understand, document, and be able to model these effects, and fortunately such an effort has been recently proposed as a NATO AVT group: the Common Research Wind Tunnel. Hopefully, this effort will produce detailed measurements of corner and juncture flows as well as full documentation of tunnel flow uniformity and directivity, and how those details and others develop through the test section as the blockage grows with side-wall boundary layer development. Understanding these behaviors will enable the development and definition of best practices and models for simulating a three-dimensional wind tunnel flow, which will in turn improve digital validation against wind tunnel data.

The current state of the art in roughness modeling is lacking, largely due to a lack of physical understanding of the true effects of roughness on the turbulence model parameters. Improving this understanding is prohibitively difficult; even if detailed turbulence measurements were achievable within the roughness layer, they would not be directly relevant to a RANS simulation in which no roughness geometry is modeled. The current roughness models effectively describe the roughness effect as a wall-normal shift of the boundary layer, but there is another possibility that has not yet been explored. One could interpret the effect of the roughness as a moving wall that moves backwards against the flow at a velocity $\Delta U = u_\tau \Delta u^+$. This would effectively increase the turbulence generation by the boundary layer without changing the outer-layer velocity characteristics, a good approximation of the physics in a rough wall boundary layer. However, this would still require *a priori* knowledge of the roughness function. It is critical that we develop a way to model the roughness from its geometry alone.

Modeling the pressure spectrum beneath turbulent boundary layers is in an excellent place compared to where it was five years ago. A return to emphasis on analytical methods has brought about new protocols for prediction that are far more robust than the library of empirical models proposed between 2012 and 2018. Empirical modeling has a place, but attempted “all-encompassing” models that define coefficients as functions of flow variables should be replaced with a toolbox of robust, inflexible models that are valid under well-defined conditions. Machine learning can be useful in this pursuit.

The analytical modeling protocols presented in this work provide the current state-of-the-art in modeling the spectrum from RANS and have been shown to be robust, flexible, and accurate. Work still remains, however, in three major areas. The turbulence-turbulence term of the pressure Poisson equation is not well understood; the current iterations are passable but incomplete. Improving the derivation of this term could prove groundbreaking. Similarly, the current models are derived from the incompressible Poisson equation, which is unfortunately limiting when considering practical applications. Derivation and implementation of a compressible version is a crucial next

step. Finally, improvements in turbulence modeling, i.e., enhanced predictions of the Reynolds stress tensor, length scales, and velocity spectra, will go a long way in improving upon the current iteration. This would be aided by detailed experimental campaigns aimed at directly measuring the Poisson equation source terms and their sub-model inputs.

Bibliography

- [1] *Environmental Noise Guidelines for the European Region: Executive Summary*. World Health Organization Regional Office for Europe, Copenhagen, Denmark, 2018. URL https://www.euro.who.int/__data/assets/pdf_file/0009/383922/noise-guidelines-exec-sum-eng.pdf.
- [2] R. J. Adrian, C.D. Meinhart, and C.D. Tomkins. Vortex organization in the outer region of the turbulent boundary layer. *Journal of Fluid Mechanics*, 422:1–54. doi: 10.1017/S0022112000001580.
- [3] B-K. Ahn, W. R. Graham, and S. A. Rizzi. Modelling unsteady wall pressures beneath turbulent boundary layers. In *10th AIAA/CEAS Aeroacoustics Conference*, Manchester, UK, 10-12 May, 2004. doi: 10.2514/6.2004-2849.
- [4] R. A. Antonia and P. A. Krogstad. Turbulence structure in boundary layers over different types of surface roughness. *Fluid Dynamics Research*, 28(2):139–157, 2001. doi: 10.1016/S0169-5983(00)00025-3.
- [5] D. Apsley. Cfd calculation of turbulent flow with arbitrary wall roughness. *Flow, Turbulence, and Combustion*, 78:153–175, 2007. doi: 10.1007/s10494-006-9059-x.
- [6] C. D. Aubertine and J. K. Eaton. Turbulence development in a non-equilibrium turbulent boundary layer with mild adverse pressure gradient. *Journal of Fluid Mechanics*, 532:345–364, 2005. doi: 10.1017/S0022112005004143.
- [7] B. Aupoix. Wall roughness modeling with k-w sst model. In *10th International Symposium on Engineering Turbulence Modelling and Measurements*, Marbella, Spain, Sep 2014.
- [8] F. A. Aupperle and R. F. Lambert. Effects of roughness on measured wall-pressure fluctuations beneath a turbulent boundary layer. *Journal of the Acoustical Society of America*, 47: 359–370, 1970. doi: 10.1121/1.1911506.
- [9] N. A. Balantrapu, C. Hickling, W. N. Alexander, and W. J. Devenport. The structure of a highly decelerated axisymmetric turbulent boundary layer. *Journal of Fluid Mechanics*, 929: A9, December 2021. doi: 10.1017/jfm.2021.845.
- [10] N. A. Balantrapu, R. J. Repasky, L. A. Joseph, and W. J. Devenport. The dynamic response of a pinhole microphone under flows of varying shear stress. In *AIAA Aviation Forum*, Alanta, GA, USA, 25-19 June, 2018. doi: 10.2514/6.2018-3933.
- [11] P. R. Bandyopadhyay and R. D. Watson. Structure of rough-wall turbulent boundary layers. *Physics of Fluids*, 31:1877–1883, 1988. doi: 10.1063/1.866686.

- [12] G. I. Barenblatt, A. J. Chorin, and V. M. Prostokishin. A model of a turbulent boundary layer with a nonzero pressure gradient. In *Proceedings of the National Academy of Sciences of the United States of America*, volume 99, pages 5772–5776, 2002. doi: 10.1073/pnas.082117699.
- [13] D. Betterman. Contribution a l’etude de la convection force turbulente le long de plaques rogneuses. *International Journal of Heat and Mass Transfer*, 9:153–164, 1966.
- [14] K. Bhaganagar, G. Coleman, and J. Kim. Effect of roughness on pressure fluctuations in a turbulent channel flow. *Physics of Fluids*, 19, 2007. doi: 10.1063/1.2482883.
- [15] W. K. Blake. Turbulent boundary-layer wall-pressure fluctuations on smooth and rough walls. *Journal of Fluid Mechanics*, 44(4):637–660. doi: 10.1017/S0022112070002069.
- [16] W. K. Blake. *Mechanics of Flow-Induced Sound and Vibration*. Academic Press, London, UK, 1 edition, 1986.
- [17] W. K. Blake. Turbulent velocity and pressure fields in boundary-layer flows over rough surfaces. In *Symposia on Turbulence in Liquids*, 6 October, 1971.
- [18] H. Blasius. Grenzsichten in flüssigkeiten mit kleiner reibung. *Zeitschrift für Angewandte Mathematik und Physik*, 56:1–37, 1908.
- [19] A. Bobke, R. Örtu, R. Vinuesa, and P. Schlatter. History effects and near-equilibrium in adverse-pressure-gradient turbulent boundary layers. *Journal of Fluid Mechanics*, 820:667–692, 2017. doi: 10.1017/jfm.2017.236.
- [20] J. Boussinesq. Essai sur la théorie des eaux courantes. *Mémoires présentés par divers savants à l’Académie des Sciences*, 23(1):1–680, 1987.
- [21] M. K. Bull. Properties of the fluctuating wall-pressure field in a turbulent boundary layer. *NATO Technical Report*, (455), 1963.
- [22] M. K. Bull. Wall pressure fluctuations associated with subsonic turbulent boundary layer flow. *Journal of Fluid Mechanics*, 28(4):719–754, 1967. doi: 10.1017/S0022112067002411.
- [23] M. K. Bull. Wall pressure fluctuations beneath turbulent boundary layers: Some reflections on forty years of research. *Journal of Sound and Vibration*, 190(3):299–315, 1996. doi: 10.1006/jsvi.1996.0066.
- [24] P. Catalano and M. Amato. An evaluation of rans turbulence modelling for aerodynamic applications. *Aerospace Science and Technology*, 7:493–509, 2003. doi: 10.1016/S1270-9638(03)00061-0.
- [25] M. R. Catlett, B. S. Bryan, N. Chang, H. Hemingway, and J. Anderson. Modeling unsteady surface pressure auto-spectra for turbulent boundary layer flow over small dense roughness. In *AIAA SciTech Forum*, San Diego, CA, USA, 03-07 Jan, 2022. doi: 10.2514/6.2022-2560.
- [26] M. R. Catlett, J. M. Anderson, Forest J. B., and D. O. Stewart. Empirical modeling of pressure spectra in adverse pressure gradient turbulent boundary layers. *AIAA Journal*, 54(2):569–587, 2016. doi: 10.2514/1.J054375.

- [27] D. M. Chase. Modeling the wavenumber-frequency spectrum of turbulent boundary layer wall pressure. *Journal of Sound and Vibration*, 70(1):29–67, 1980. doi: 10.1016/0022-460X(80)90553-2.
- [28] D. M. Chase. The character of the turbulent wall pressure spectrum at subconvective wavenumbers and a suggested comprehensive model. *Journal of Sound and Vibration*, 112(1):125–147, 1987. doi: 10.1016/S0022-460X(87)80098-6.
- [29] H. Choi and P. Moin. On the space-time characteristics of wall pressure fluctuations. *Physics of Fluids*, 2(8):1450–1460, 1990. doi: 10.1063/1.857593.
- [30] F. H. Clauser. Turbulent boundary layers in adverse pressure gradient. *Journal of the Aeronautical Sciences*, 21(2):91–108, 1954. doi: 10.2514/8.2938.
- [31] F. H. Clauser. The turbulent boundary layer. *Advances in Applied Mechanics*, 4:1–51, 1956. doi: 10.1016/S0065-2156(08)70370-3.
- [32] D. Coles. The law of the wake in the turbulent boundary layer. *Journal of Fluid Mechanics*, 1(2):191–226, 1956. doi: 10.1017/S0022112056000135.
- [33] G. M. Corcos. Resolution of pressure in turbulence. *Journal of the Acoustical Society of America*, 35:192, 1963. doi: 10.1121/1.1918431.
- [34] G. M. Corcos. The structure of the turbulent pressure field in boundary-layer flows. *Journal of Fluid Mechanics*, 18(3):353–378, 1964. doi: 10.1017/S002211206400026X.
- [35] G. M. Corcos. The resolution of turbulent pressures at the wall of a boundary layer. *Journal of Sound and Vibration*, 6(1):59–70, 1964. doi: 10.1016/0022-460X(67)90158-7.
- [36] W. J. Devenport and K. T. Lowe. Equilibrium and non-equilibrium turbulent boundary layers. *Progress in Aerospace Sciences*, 131:100807, May 2022. doi: 10.1016/j.paerosci.2022.100807.
- [37] K. Duraisamy, P. R. Spalart, and C. L. Rumsey. Status, emerging ideas and future directions of turbulence modeling research in aeronautics. *NASA Report*, 2017. TM-2017-219682.
- [38] F. A. Dvorak. Calculation of turbulent boundary layers on rough surfaces in pressure gradient. *AIAA Journal*, 7(9):1752–1759, 1969. doi: 10.2514/3.5386.
- [39] R. E. Falco. The production of turbulence near a wall. In *AIAA Fluid and Plasma Dynamics Conference*, Snowmass, CO, USA, 14-16 June, 1980. doi: 10.2514/6.1980-1356.
- [40] T. M. Farabee. *An Experimental Investigation of Wall Pressure Fluctuations beneath Non-equilibrium Turbulent Flows*. PhD thesis, Catholic University of America, 1986.
- [41] T. M. Farabee and M. Casarella. Spectral features of wall pressure fluctuations beneath turbulent boundary layers. *Physics of Fluids*, 3:2410–2420, 1991. doi: 10.1063/1.858179.
- [42] A. Fischer. Improvements of two type trailing edge noise models. *European Journal of Mechanics B: Fluids*, 61:255–262, 2017. doi: 10.1016/j.euromechflu.2016.09.005.

- [43] K. A. Flack and M. P. Schultz. Roughness effects on wall-bounded turbulence. *Physics of Fluids*, 26:26–43, 2014. doi: 10.1063/1.4896280.
- [44] K. A. Flack, M. P. Schultz, and T. A. Shapiro. Support for townsend’s reynolds number similarity hypothesis on rough walls. *Physics of Fluids*, 17:035102, 2005. doi: 10.1063/1.1843135.
- [45] J. B. Forest. The wall pressure spectrum of high reynolds number rough-wall turbulent boundary layers. Master’s thesis, Virginia Polytechnic Institute and State University, 2012.
- [46] D. J. Fritsch, V. Vishwanathan, K. T. Lowe, and W. J. Devenport. The effect of grazing flow on pinhole condenser microphones. In *AIAA Science and Technology Forum*, Nashville, TN, USA, 11-21 January 2021. doi: 10.2514/6.2021-0130.
- [47] D. J. Fritsch, V. Vishwanathan, C. J. Roy, K. T. Lowe, W. J. Devenport, P. Croaker, G. Lane, O. Tkachenko, D. Pook, S. Shubham, and R. D. Sandberg. Modeling the surface pressure spectrum beneath turbulent boundary layers in pressure gradients. In *28th AIAA/CEAS Aeroacoustics Conference*, Southampton, UK, 14-17 June, 2022. doi: 10.2514/6.2022-2843.
- [48] D. J. Fritsch, V. Vishwanathan, K. T. Lowe, and W. J. Devenport. Surface pressure spectra beneath high reynolds number smooth and rough wall boundary layers in pressure gradients. *University Libraries, Virginia Tech*, 2022. doi: 10.7294/20457189. Dataset.
- [49] D. J. Fritsch, V. Vishwanathan, K. T. Lowe, and W. J. Devenport. Fluctuating pressure beneath smooth wall boundary layers in non-equilibrium pressure gradients. *AIAA Journal*, 60(8):4725–4743, 2022. doi: 10.2514/1.J061431.
- [50] D. J. Fritsch, V. Vishwanathan, C. J. Roy, K. T. Lowe, and W. J. Devenport. Turbulence and pressure fluctuations in rough wall boundary layers in pressure gradients. *Experiments in Fluids*, 2022. doi: 10.1007/s00348-022-03476-9. Accepted for Publication.
- [51] D. J. Fritsch, V. Vishwanathan, C. J. Roy, K. T. Lowe, W. J. Devenport, Y. Nishi, T. Knopp, P. Ströer, A. Krumbein, R. D. Sandberg, C. Lav, R. E. Bensow, L. Eça, S. L. Toxopeus, M. Kerkvliet, M. Slama, and L. Bordier. Experimental and computational study of 2d smooth wall turbulent boundary layers in pressure gradient. In *AIAA Science and Technology Forum*, San Diego, CA, USA, 3-7 January 2022. doi: 10.2514/6.2022-0696.
- [52] J. R. Gavin. *Unsteady forces and sound caused by boundary layer turbulence entering a turbomachinery rotor*. PhD thesis, The Pennsylvania State University, 2002.
- [53] W. K. George and L. Castillo. Zero-pressure-gradient turbulent boundary layer. *Applied Mechanics Review*, 50(11):689–729, 1997. doi: 10.1115/1.3101858.
- [54] M. Goody. Empirical spectral model of surface pressure fluctuations. *AIAA Journal*, 49(9): 1788–1794, 2004. doi: 10.2514/1.9433.
- [55] W. R. Graham. A comparison of models for the wavenumber-frequency spectrum of turbulent boundary layer pressures. *Journal of Sound and Vibration*, 206(4):541–565, 1997. doi: 10.1006/jsvi.1997.1114.

- [56] A. J. Grass. Structural features of turbulent flow over smooth and rough boundaries. *Journal of Fluid Mechanics*, 50(2):233–255, 1971. doi: 10.1017/S0022112071002556.
- [57] G. Grasso, P. Jaiswal, H. Wu, S. Moreau, and M. Roger. Analytical models of the wall-pressure spectrum under a turbulent boundary layer. *Journal of Fluid Mechanics*, 877:1007–1062, 2019. doi: 10.1017/jfm.2019.616.
- [58] S. Gravante, A. Naguib, C. Wakr, and H. Nagib. Characterization of the pressure fluctuations under a fully developed turbulent boundary layer. *AIAA Journal*, 36(10):1808–1816, 1998. doi: 10.2514/2.296.
- [59] Z. Harun, J. P. Monty, R. Mathis, and I. Marusic. Pressure gradient effects on the large-scale structure of turbulent boundary layers. *Journal of Fluid Mechanics*, 715:477–498, 2013. doi: 10.1017/jfm.2012.531.
- [60] J. Hinze. *Turbulence*. McGraw-Hill, New York, NY, USA, 2 edition, 1975.
- [61] M. S. Howe. *Acoustics of Fluid-Structure Interactions*. Cambridge University Press, 1998.
- [62] N. Hu. Empirical spectral model of wall pressure fluctuations including adverse pressure gradient effects. In *AIAA Aviation Forum*, Denver, CO, USA, 5-9 June, 2017. doi: 10.2514/6.2017-3203.
- [63] N. Hu and M. Herr. Characteristics of wall pressure fluctuations for a flat plate turbulent boundary layer with pressure gradients. In *22nd AIAA/CEAS Aeroacoustics Conference*, Lyon, France, 30 May - 01 June, 2016. doi: 10.2514/6.2016-2749.
- [64] Nan Hu. Empirical model of wall pressure spectra in adverse pressure gradients. *AIAA Journal*, 56(9):3491–3506, 2018.
- [65] M. Hultmark, S. C. C. Bailey, and A. J. Smits. Scaling of near-wall turbulence in pipe flow. *Journal of Fluid Mechanics*, 649:103–113, 2010. doi: 10.1017/S0022112009994071.
- [66] J. Jimenez. Turbulent flows over rough walls. *Annual Review of Fluid Mechanics*, 36:173–196, 2004. doi: 10.1146/annurev.fluid.36.050802.122103.
- [67] L. A. Joseph. *Pressure Fluctuations in a High-Reynolds-Number Turbulent Boundary Layer over Rough Surfaces of Different Configurations*. PhD thesis, Virginia Polytechnic Institute and State University, 2017.
- [68] L. A. Joseph, W. J. Devenport, and S. Glegg. Empirical model for low-speed rough-wall turbulent boundary layer pressure spectra. *AIAA Journal*, 60(4):2160–2168, 2022. doi: 10.2514/1.J060965.
- [69] M. Kamruzzaman, D. Bekiropoulos, T. Lutz, and W. Würz. A semi-empirical surface pressure spectrum model for airfoil trailing-edge noise prediction. *International Journal of Aeroacoustics*, 14, 2015. doi: 10.1260/1475-472X.14.5-6.833.

- [70] M. Kamruzzaman, Th. Lutz, W. Würz, and E. Krämer. On the length scales of turbulence for aeroacoustic applications. In *Proceedings of the 17th AIAA/CEAS Aeroacoustics Conference*, Portland, OR, USA, 5-8 June, 2011. doi: 10.2514/6.2011-2734.
- [71] J. Klewicki, R. Ebner, and X. Wu. Mean dynamics of transitional boundary-layer flow. *Journal of Fluid Mechanics*, 682:617–651, 2011. doi: 10.1017/jfm.2011.253.
- [72] S. J. Kline and W. C. Reynolds. Structure of the turbulent boundary layer on a smooth wall. *Physics of Fluids*, 10, 1967. doi: 10.1017/S0022112067001740.
- [73] T. Knopp, B. Eisfeld, and J. B. Calvo. A new extension for k-w turbulence models to account for wall roughness. *International Journal of Heat and Fluid Flow*, 30:54–65, 2009. doi: 10.1016/j.ijheatfluidflow.2008.09.009.
- [74] N. A. Kolmogorov. The local structure of turbulence in incompressible viscous fluid for very large reynolds numbers. *Proceedings of the Royal Society A: Mathematical, Physical, and Engineering Sciences*, 434(1890), 1941. doi: 10.1098/rspa.1991.0075. Republished 1991.
- [75] R. H. Kraichnan. Pressure fluctuations in turbulent flow over a flat plate. *Journal of the Acoustical Society of America*, 28(3):378–390, 1956. doi: 10.1121/1.1908336.
- [76] P. A. Krogstad, R. A. Antonia, and L. W. Browne. Comparison between rough- and smooth-wall turbulent boundary layers. *Journal of Fluid Mechanics*, 245:599–617, 1992. doi: 10.1017/S0022112092000594.
- [77] G. Lane, W. Sidebottom, and P. Croaker. Application of wall-modelled les to the prediction of turbulent flow noise. In *Proceedings of Acoustics 2021*, Wollongong, Australia, 8-10 Nov, 2021.
- [78] B. E. Launder. Second-moment closure and its use in modelling turbulent industrial flows. *International Journal for Numerical Methods in Fluids*, 9:963–985, 1989. doi: 10.1002/flid.1650090806.
- [79] B. E. Launder, G. J. Reece, and W. Rodi. Progress in the development of a reynolds-stress turbulence closure. *Journal of Fluid Mechanics*, 68(3):537–566, 1975. doi: 10.1017/S0022112075001814.
- [80] J-H. Lee and H. J. Sung. Effects of an adverse pressure gradient on a turbulent boundary layer. *International Journal of Heat and Fluid Flow*, 29:568–578, 2008. doi: 10.1016/j.ijheatfluidflow.2008.01.016.
- [81] S. Lee. Empirical wall-pressure spectral modeling for zero and adverse pressure gradient flows. *AIAA Journal*, 56(5):1818–1829, 2018. doi: 10.2514/1.J056528.
- [82] Y-T. Lee, W.K. Blake, and T.M. Farabee. Modeling of wall pressure fluctuations based on time mean flow field. *Journal of Fluids Engineering*, 127:233–240, 2005. doi: 10.1115/1.1881698.

- [83] H. W. Liepmann, J. Laufer, and K. Liepmann. On the spectrum of isentropic turbulence. *NACA Technical Reports*, 1951.
- [84] P. M. Ligrani and R. J. Moffat. Structure of transitionally rough and fully rough turbulent boundary layers. *Journal of Fluid Mechanics*, 162:69–98, 1986. doi: 10.1017/S0022112086001933.
- [85] G. M. Lilley and T. H. Hodgson. On surface pressure fluctuations in turbulent boundary layers. *NATO Report*, (276), 1960.
- [86] Y. Maciel, T. Wei, A. G. Gungor, and M. P. Simens. Outer scales and parameters of adverse-pressure-gradient turbulent boundary layers. *Journal of Fluid Mechanics*, 844:5–35, 2018. doi: 10.1017/jfm.2018.193.
- [87] B. E. McGrath and R. L. Simpson. Some features of surface pressure fluctuations in turbulent boundary layers with zero and favorable pressure gradient. *NASA Contractor Report*, (4051), 1987.
- [88] F. Mehdi, J. C. Klewicki, and C. M. White. Mean force structure and its scaling in rough-wall turbulent boundary layers. *Journal of Fluid Mechanics*, 731:682–712, 2013. doi: 10.1017/jfm.2013.385.
- [89] G.L. Mellor and D.M. Gibson. Equilibrium turbulent boundary layers. *Journal of Fluid Mechanics*, 24(2):225–253, 1966. doi: 10.1017/S0022112066000612.
- [90] F. R. Menter. Two-equation eddy-viscosity turbulence models for engineering applications. *AIAA Journal*, 32:1598–1605, 1994. doi: 10.2514/3.12149.
- [91] T. Meyers, J. B. Forest, and W. J. Devenport. The wall-pressure spectrum of high-reynolds-number turbulent boundary-layer flows over rough surfaces. *Journal of Fluid Mechanics*, 768: 261–293, 2015. doi: 10.1017/jfm.2014.743.
- [92] R. Michel, C. Quemard, and R. Durant. Hypotheses on the mixing length and application to the calculation of turbulent boundary layers. *Proceedings on Computational Turbulent Boundary Layers*, 1:195–207, 1968.
- [93] Y. Nagano, M. Tagawa, and T. Tsuji. Effects of adverse pressure gradients on mean flows and turbulence statistics in a boundary layer. In *8th International Symposium on Turbulent Shear Flows*, Munich, Germany, 9-11 September, 1991. Springer-Verlag, New York, USA. doi: 10.1007/978-3-642-77674-8_2.
- [94] J. Nikuradse. Laws of flow in rough pipes. *NACA Technical Report*, (TM 1292), 1950.
- [95] W. L. Oberkampf and B. L. Smith. Assessment criteria for computational fluid dynamics model validation experiments. *Journal of Verification, Validation, and Uncertainty Quantification*, 2(3):031002, 2017. doi: 10.1115/1.4037887.

- [96] M. Olazabal-Loumé, F. Danvin, J. Mathiaud, and B. Aupoix. Study on k - ω shear stress transport model corrections applied to rough wall turbulent hypersonic boundary layers. In *7th European Conference for Aeronautics and Space Science (EUCASS)*, Milan, Italy, 2017. doi: 10.13009/EUCASS2017-604.
- [97] R. L. Panton. Scaling turbulent wall layers. *Journal of Fluids Engineering*, 112:425–432, 1990. doi: 10.1115/1.2909420.
- [98] R. L. Panton and J. H. Linebarger. Wall pressure spectra calculations for equilibrium boundary layers. *Journal of Fluid Mechanics*, 65(2):261–287, 1974. doi: 10.1017/S0022112074001388.
- [99] R. Parchen. Progress report draw: A prediction scheme for trailing-edge noise based on detailed boundary-layer characteristics. *TNO Institute of Applied Physics*, (980023), 1998.
- [100] L. J. Peltier and S. A. Hambric. Estimating turbulent-boundary-layer wall-pressure spectra from cfd rans solutions. *Journal of Fluids and Structures*, 23:920–937, 2007. doi: 10.1016/j.jfluidstructs.2007.01.003.
- [101] A. E. Perry, W. H. Schofield, and P. N. Joubert. Rough wall turbulent boundary layers. *Journal of Fluid Mechanics*, 56(2):383–413, 1969. doi: 10.1017/S0022112069000619.
- [102] K. Polhause. Zure näherungsweise integration der defferentialgleichung der laminaren grenzschicht. *Journal of Applied Mathematics and Mechanics*, 1:252–290, 1921.
- [103] L. Prandtl. In *Verhandlungen des dritten internationalen Mathematiker-Kongresses*, page 484, Heidelberg, Germany, 1904. English Translation from Ackroyd, J. A. K., Axcell, B. P., & Ruban, A. I., "Early Developments of Modern Aerodynamics," Butterworth-Heinemann, 2001, Oxford, UK, pp. 77.
- [104] M. R. Raupach. Conditional statistics of reynolds stress in rough-wall and smooth-wall turbulent boundary layers. *Journal of Fluid Mechanics*, 108:363–382, 1981. doi: 10.1017/S0022112081002164.
- [105] M. R. Raupach, R. A. Antonia, and S. Rajagopalan. Rough-wall turbulent boundary layers. *Applied Mechanics Review*, 44(1):1–25, 1991. doi: 10.1115/1.3119492.
- [106] L. F. Richardson. *Weather prediction by numerical process*. Cambridge University Press, Cambridge, UK, 1922.
- [107] S. K. Robinson. A perspective on coherent structures and conceptual models for turbulent boundary layer physics. In *AIAA Fluid and Plasma Dynamics Conference*, Seattle, WA, USA, 18-20 June, 1990.
- [108] Y. Rozenburg, G. Robert, and S. Moreau. Wall-pressure spectral model including the adverse pressure gradient effects. *AIAA Journal*, 50(10):2168–2179, 2012. doi: 10.2514/1.J051500.

- [109] A. E. Samuel and P. N. Joubert. A boundary layer developing in an increasingly adverse pressure gradient. *Journal of Fluid Mechanics*, 66(3):481–505, 1974. doi: 10.1017/S0022112074000322.
- [110] D. M. Schatzman and F. O. Thomas. An experimental investigation of an unsteady adverse pressure gradient turbulent boundary layer. *Journal of Fluid Mechanics*, 815:592–642, 2017. doi: 10.1017/jfm.2017.65.
- [111] J. A. Schetz and R. D.W. Bowersox. *Boundary Layer Analysis*. AIAA Book Series, USA, 2 edition, 2011.
- [112] H. Schlichting. *Boundary Layer Theory*. McGraw-Hill, USA, 1979.
- [113] H. Schloemer. Effects of pressure gradients on turbulent boundary-layer wall-pressure fluctuations. *US Navy Underwater Sound Laboratory Report*, (747), 1966. doi: 10.1121/1.1943059.
- [114] W. H. Schofield. Equilibrium boundary layers in moderate to strong adverse pressure gradients. *Journal of Fluid Mechanics*, 113:91–122, 1981. doi: 10.1017/S002211208100342X.
- [115] M. P. Schultz and K. A. Flack. The rough-wall turbulent boundary layer from the hydraulically smooth to the fully rough regime,. *Journal of Fluid Mechanics*, 580:381–405, 2007. doi: 10.1017/S0022112007005502.
- [116] A. Sigal and J. E. Danberg. New correlation of roughness density effect on the turbulent boundary layer. *AIAA Journal*, 28(3):554–556, 2012. doi: 10.2514/3.10427.
- [117] R. L. Simpson. A generalized correlation of roughness density effects on the turbulent boundary layer. *AIAA Journal*, 11(2):242–244, 1973. doi: 10.2514/3.6736.
- [118] S. Song, Y. K. Demirel, M. Atlar, S. Dai, and O. Turan. Validation of the cfd approach for modelling roughness effect on ship resistance. *Ocean Engineering*, 200, 2020. doi: 10.1016/j.oceaneng.2020.107029.
- [119] P. Spalart and S. Allmaras. A one-equation turbulence model for aerodynamic flows. In *AIAA Sciences Meeting*. American Institute of Aeronautics and Astronautics, Jan 1992. doi: 10.2514/6.1992-439.
- [120] D. B. Spalding. A single formula for the 'law of the wall'. *Journal of Applied Mechanics*, 28(3):455–458, 1961.
- [121] P.R. Splart and S.R. Allmaras. Strategies for turbulence modelling and simulation. *International Journal of Heat and Fluid Flow*, 21(3):252–263, 2000. doi: 10.1016/S0142-727X(00)00007-2.
- [122] G. I. Taylor. *Scientific Papers of Sir Geoffrey Ingram Taylor*, volume 4: Mechanics of Fluids. Cambridge University Press, Cambridge, UK, 1971.
- [123] H. Tennekes and J. L. Lumley. *A First Course in Turbulence*. MIT Press, Cambridge, MA, USA, 1972.

- [124] B. Thwaites. On certain types of boundary-layer flow with continuous surface suction. *HM Stationery Office*, 1946.
- [125] A. A. Townsend. *The Structure of Turbulent Shear Flow*. Cambridge University Press, Cambridge, UK, 1976.
- [126] Y. Tsuji, J. H. M. Fransson, P. H. Afredsson, and A. V. Johansson. Pressure statistics and their scaling in high-reynolds-number turbulent boundary layers. *Journal of Fluid Mechanics*, 585:1–40, 2007. doi: 10.1017/S0022112007006076.
- [127] N. D. Varano. *Fluid Dynamics and Surface Pressure Fluctuations of Turbulent Boundary Layers Over Sparse Roughness*. PhD thesis, Virginia Polytechnic Institute and State University, 2010.
- [128] T. von Kármán. über laminare und turbulente feibung. *Journal of Applied Mathematics and Mechanics*, 1:233–252, 1921.
- [129] T. von Kármán. Mechanische ähnlichkeit und turbulenz. *Sonderdrucke aus den Nachrichten von der Gesellschaft der Wissenschaften zu Göttingen: Mathematisch-Physische Klasse*, 1, 1930.
- [130] T. von Kármán. Progress in the statistical theory of turbulence. In *Proceedings of the National Academy of Sciences*, volume 34, pages 530–539, 1948.
- [131] T. Wei, P. Fife, J. Klewicki, and P. McMurtry. Properties of the mean momentum balance in turbulent boundary layer, pipe, and channel flows. *Journal of Fluid Mechanics*, 522:303–327, 2005. doi: 10.1017/S0022112004001958.
- [132] D. C. Wilcox. Reassessment of the scale-determining equation for advanced turbulence models. *AIAA Journal*, 46:2823–2838, 1988. doi: 10.2514/3.10041.
- [133] D. C. Wilcox. *Turbulence Modeling for CFD*. DCW Industries, La Cañada, CA, USA, 1 edition, 1993.
- [134] D. C. Wilcox. *Turbulence Modeling for CFD*. DCW Industries, La Cañada, CA, USA, 3 edition, 2006.
- [135] W. W. Willmarth. Pressure fluctuations beneath turbulent boundary layers. *Annual Review Fluid Mechanics*, 7:13–36, 1975. doi: 10.1146/annurev.fl.07.010175.000305.
- [136] W. W. Willmarth and C. E. Woolridge. Measurements of the fluctuating pressure at the wall beneath a thick turbulent boundary layer. *Journal of Fluid Mechanics*, 14(2):187–210, 1962. doi: 10.1017/S0022112062001160.
- [137] W. W. Willmartn. Wall pressure fluctuations in a turbulent boundary layer. *Journal of the Acoustical Society of America*, 28(6):1048–1053, 1956. doi: 10.1121/1.1908551.
- [138] D. K. Wilson. A three-dimensional correlation/spectral model for turbulent velocities in a convective boundary layer. *Boundary-Layer Meteorology*, 85:35–52, 1997. doi: 10.1023/A:1000418709945.

- [139] J. M. Witting. A new model of wall pressure fluctuations. *Journal of the Acoustical Society of America*, 80, 1986. doi: 10.1121/1.2023667.
- [140] D. H. Wood and R. A. Antonia. Measurements in a turbulent boundary layer over a d-type surface roughness. *Journal of Applied Mechanics*, 42(3):591–597, 1975. doi: 10.1115/1.3423647.
- [141] Q. Yang and M. Wang. Statistical analysis of acoustic-source field in rough-wall boundary layers. In *17th AIAA/CEAS Aeroacoustics Conference*, Portland, OR, USA, 2011. doi: 10.2514/6.2011-2738.
- [142] M. V. Zagarola and A. J. Smits. Mean-flow scaling of turbulent pipe flow. *Journal of Fluid Mechanics*, 373:33–79, 1998. doi: 10.1017/S0022112098002419.